Entanglement in Ramsey interferometry, optical atomic clocks and trapped ions

Von der QUEST-Leibniz-Forschungsschule
der Gottfried Wilhelm Leibniz Universität Hannover
zur Erlangung des Grades

Doktor der Naturwissenschaften
Dr. rer. nat.

genehmigte Dissertation von

M. Sc. Marius Schulte
geboren am 12. April 1993 in Papenburg

2020

Referent: Prof. Dr. Klemens Hammerer
Institut für theoretische Physik
Leibniz Universität Hannover

Korreferent: Prof. Dr. Piet O. Schmidt
Institut für Quantenoptik
Leibniz Universität Hannover

Korreferent: Prof. Martin Fraas, PhD
Department of Mathematics
University of California, Davis

Tag der Promotion: 11.12.2020

Abstract

This thesis describes new results on the entanglement of atomic spins in Ramsey interferometry, optical atomic clocks and trapped ions. It is divided into three parts:

First, we investigate improvements to conventional Ramsey interferometry with entanglement and adding only rotations of the collective spin to adjust the signal and measurement directions. The geometric degrees of freedom, connected to the rotations, are analytically optimized for a large class of generalized Ramsey protocols to allow efficient optimization of all parameters. Besides a unification of existing approaches, the main result is that there is only one new protocol, where a previously unused double inversion is applied. Studies of the local sensitivity show that this protocol reaches the fundamental quantum Fisher information limit and is yet robust against errors during preparation and measurement.

In the second section we investigate the conditions under which optical atomic clocks exhibit increased long-term stability when applying weakly entangled, spin squeezed states. We discuss the common case of an atomic clock with a single ensemble, typical Brownian frequency noise and finite dead time. Theoretical modelling of the servo loop allows quantitative predictions of the optimal stability for given values of dead time and laser noise, in very good agreement with numerical simulations of the closed feedback loop. The main result is that, even with the current most stable lasers, the clock stability can only be improved for ensembles below a critical atom number of about one thousand in optical Sr lattice clocks. Even with a future improvement of the laser performance by one order of magnitude, the critical atom number still remains below 100,000. In contrast, clocks based on smaller, non-scalable ensembles, such as ion clocks, can already benefit from squeezed states with current clock lasers.

Thus the last section considers the robust generation of entanglement in ion traps. An error budget including relevant experimental error sources is calculated for state-of-the-art quantum gates, driven by oscillating microwave gradients in surface traps. Amplitude modulation of the driving fields is shown to efficiently counteract the current limitations from motional mode instability. The predicted increase of the gate quality was demonstrated by the group of C. Ospelkaus at PTB Braunschweig, who measured gates with errors as low as $\sim 10^{-3}$. In a similar approach, interactions between spin and motion can also be generated by combining oscillating rf-fields with a static magnetic field gradient. Penning traps designed for precision spectroscopy already feature large magnetic field gradients at the edge of a magnetic bottle configuration. We present parameters and conditions under which laser-free coupling of spin and quantized motion for (anti-)protons is possible at these points, in a step towards quantum logic spectroscopy for (anti-)protons.

Keywords: Quantum metrology, Entanglement, Ramsey interferometry, spin squeezing, optical atomic clocks, trapped ions, two-qubit gates

Zusammenfassung

Diese Arbeit beschreibt neue Resultate zur Verschränkung von atomaren Spins in Ramsey Interferometrie, optischen Atomuhren und gefangenen Ionen. Sie ist dementsprechend in drei zentrale Themenbereiche aufgeteilt:

Als erstes wird untersucht wie Verschränkung konventionelle Ramsey Protokolle verbessern kann, allein unter der Hinzunahme kollektiver Spinrotationen zur Anpassung der Signal- und Messrichtungen. Es wird gezeigt, wie die geometrischen Freiheitsgrade der Rotationen in einer Klasse an verallgemeinerten Ramsey Protokollen analytisch optimiert werden können, um somit eine effiziente Optimierung aller Variationsparameter zu erlauben. Neben der Vereinheitlichung bekannter Ansätze ergibt sich als Hauptresultat, dass es nur ein neues Szenario gibt, bei dem eine zuvor ungenutzte doppelte Inversion ausgeführt wird. Untersuchungen der Messgenauigkeit zeigen, dass diese Protokolle die fundamentale quanten-Fisher-Informations Schranke erreichen und zusätzlich robust gegen Fehler in der Präparation und Messung sind.

Im zweiten Abschnitt wird untersucht welche optischen Atomuhren durch leicht verschränkte, spin gequetschte Zustände eine erhöhte Langzeitstabilität aufweisen. Es wird der übliche Fall von Atomuhren mit einem einzelnen Ensemble, typischem Brownschen Frequenzrauschen und endlicher Totzeit diskutiert. Die theoretische Modellierung des Regelkreises erlaubt quantitative Vorhersagen über die optimale Stabilität für gegebene Werte der Totzeit und des Laserrauschens zu treffen, in sehr guter Übereinstimmung mit numerischen Simulationen des geschlossenen Regelkreises. Als wesentliches Resultat ergibt sich, dass selbst mit den aktuell stabilsten Lasern die Uhrenstabilität in optischen Sr Gitteruhren nur für Ensembles unterhalb einer kritischen Atomzahl von etwa tausend Atomen verbessert werden kann. Selbst bei einer zukünftigen Verbesserung des Laserrauschens um eine Größenordnung bleibt die kritische Atomzahl noch immer unter 100.000. Im Gegensatz dazu können Uhren, die auf kleineren, nicht skalierbaren Ensembles basieren, wie z.B. Ionenuhren, bereits mit aktuellen Uhrenlasern von gequetschten Zuständen profitieren.

Somit betrachtet der letzte Abschnitt die Erzeugung von Verschränkung in Ionenfallen. Die Einflüsse relevanter Fehlerquellen in hochmodernen Quantengattern, die von oszillierenden Mikrowellengradienten in Oberflächenfallen getrieben werden, wurden quantifiziert. Modulation der Amplituden reduziert effizient die limitierenden Störeffekte. Die verbesserte Qualität der Gatter wurde durch die Gruppe von C. Ospelkaus an der PTB Braunschweig demonstriert, welche Gatter mit Fehlern $\sim 10^{-3}$ messen konnten. In einem vergleichbaren Ansatz kann Verschränkung auch durch die Kombination oszillierender rf-Felder mit einem statischen Magnetfeldgradienten erzeugt werden. Penningfallen, die für Präzisionsspektroskopie konzipiert wurden, weisen große Magnetfeldgradienten am Rand einer magnetischen Flasche auf. Diese Arbeit identifiziert Parameter und Bedingungen unter denen eine laserfreie Kopplung von Spin und quantisierter Bewegung für (anti-)Protonen an diesen Positionen realisierbar ist, als einen Schritt in Richtung quanten-logik Spektroskopie.

Schlagwörter: Quantenmetrologie, Verschränkung, Ramsey Interferometrie, gequetschte Spinzustände, optische Atomuhren, gefangene Ionen, zwei-qubit Gatter

Author contributions

Parts of this thesis have appeared elsewhere, as peer-reviewed publications or on pre-print servers. Here I summarize my personal contributions to these works. Note that contributions of other co-authors without my involvement are not explicitly listed. In order of the corresponding chapter, they are:

Chapter 2:

M. Schulte, V. J. Martínez-Lahuerta, M. S. Scharnagl, K. Hammerer, *Ramsey interferometry with generalized one-axis twisting echoes*, Quantum 4, 268 (2020)

Author contribution: **MS** contributed considerably to the initial idea and the design of the generalized Ramsey protocols, along with VJML and KH. Most of the analytic calculations and the optimization were performed by **MS** with input from VJML and KH. **MS** developed the comparison to fundamental limits. **MS** and MSS calculated the Wigner functions and developed the visualization of over-un-twisting protocols with considerable contributions from KH. MSS analyzed the extended protocols with supervision by **MS** and KH. **MS** wrote the manuscript with contributions from all authors.

Chapter 3:

M. Schulte, C. Lisdat, P. O. Schmidt, U. Sterr, K. Hammerer, *Prospects and challenges for squeezing-enhanced optical atomic clocks*, arXiv:1911.00882 (2019), accepted at Nature Communications

Author contribution: **MS** contributed to the idea of the manuscript together with all authors. **MS** and KH formulated the stochastic treatment of the feedback stabilization. **MS** calculated the overall instability with contributions from CL and US. **MS** carried out all numerical simulations. **All authors** contributed to the discussion and interpretation of the results. **MS** prepared the manuscript with contributions from all authors.

Chapter 4:

H. Hahn, G. Zarantonello, **M. Schulte**, A. Bautista-Salvador, K. Hammerer, C. Ospelkaus, *Integrated* $^{9}\mathrm{Be}^{+}$ *multi-qubit gate device for the ion-trap quantum computer*, npj Quantum Information 5 (1), 1-5 (2019)

Author contribution: **MS** formulated the theoretical framework for the gate errors, based on the parameters measured by HH and GZ. All analytical calculations and all numerical simulations determining the error budget were performed by **MS**. **MS** contributed significantly to the interpretation of the errors with further contributions by HH and GZ. The manuscript was written mostly by HH with significant contributions from GZ and contributions from **all authors**.

G. Zarantonello, H. Hahn, J. Morgner, **M. Schulte**, A. Bautista-Salvador, R. F. Werner, K. Hammerer, C. Ospelkaus, *Robust and resource-efficient microwave near-field entangling* $^9\mathrm{Be}^+$ *gate*, Physical Review Letters 123 (26), 260503 (2019)

Author contribution: The gate application and infidelity resulting with a $\sin^2$ amplitude modulation was evaluated by **MS** following a proposal by GZ and KH. All analytic calculations comparing the coherent control techniques were performed by **MS**. **MS** contributed considerably to the interpretation and discussion of these results with further contributions from GZ, HH, KH and CO. The manuscript was prepared mostly by GZ with significant contributions from HH and contributions from **all authors**.

D. Nitzschke, **M. Schulte**, M. Niemann, J. M. Cornejo, S. Ulmer, R. Lehnert, C. Ospelkaus, K. Hammerer, *Elementary laser-less quantum logic operations with (anti-) protons in Penning traps*, Advanced Quantum Technologies 2020, 1900133 (2020)

Author contribution: DN calculated the quantum mechanical treatment of the unconventional Penning trap field configuration together with **MS** and KH. DN and **MS** performed all numerical simulations of the sideband dynamics with contributions of KH and input on the parameter values from MN, JMC and CO. **MS** contributed to the interpretation of the results and the preparation of the manuscript along with **all authors**.

For completeness I add that the following articles were published during my time as a PhD student, but they are not included in this thesis as my contributions to these works originated from the subjects of my master thesis:

M. Schulte, N. Lörch, P. O. Schmidt, K. Hammerer, *Photon-recoil spectroscopy: Systematic shifts and nonclassical enhancements*, Physical Review A 98 (6), 063808 (2018)

F. Wolf, C. Shi, J. C. Heip, M. Gessner, L. Pezzè, A. Smerzi, **M. Schulte**, K. Hammerer, P. O. Schmidt, *Motional Fock states for quantum-enhanced amplitude and phase measurements with trapped ions*, Nature Communications 10 (1), 2929 (2019)

Acknowledgements

This work would never have come as far as it did without the support of many other people, whom I would like to thank at this point.

As far as the scientific part is concerned, the first person I would like to thank is, of course, Klemens Hammerer. Since I first set foot into your office a little more than six years ago, looking for a bachelor project at that time, you have been an outstanding supervisor and mentor for me countless times. Originally as a teacher, who had to explain a lot of new things to me, and lately as a constant source of new inspirations. No matter what came up, I could always rely on your support. Your keen appreciation for the physics behind every calculation, a point of view that is very much in line with my own perspective, is what I admire most about you. Thank you for the trust you placed in me over all these years.

Let me also thank Piet Schmidt for, first of all, agreeing to act as one of the referees for my thesis. I am very grateful to you, Piet, for your long-lasting interest in my work, for all your support, and for all the discussions in which you have contributed with your great curiosity and with your clear view for physical phenomena over the years.

I wish to thank Martin Fraas for kindly agreeing to review my thesis and I want to thank Benno Willke for chairing my defense.

Due to the many years I spent in the ‘AG Hammerer’, there are several colleagues I want to acknowledge. Among them are Ondřej, Jonas, Nils, Sergey and Denis, who all welcomed me nicely into the group when I started my work there. They ensured many exciting discussions and entertaining coffee breaks. I would especially like to thank Nils, who helped me learn a lot about quantum optics, Python and simulations in QuTiP. I would also like to thank all current and former members of the research group for the wonderful working atmosphere they created. Apart from the ones mentioned above, these are Victor, Sahand, Kasper, Jan-Niclas, Michael, Florian, Corentin, Jannis, Alexander, Sebastian, Emil and Hashem. I am especially happy to have worked with Victor on various research topics. I would like to thank Nils, Ondrej, Jonas, Jannis, Jan-Niclas, Michael and Kasper, who all shared an office with me at some point. They sparked many interesting debates between the desks. Often about physics but also everything else; from geography and educational policies to personalized diets and fitness plans. Further, I would like to thank the Bachelor and Master students, Timm Kielinski, Simon Eilers, Diana Nitzschke and Maja Scharnagl, for all the work they put into their projects, which often related to my own interests as well. It was a great pleasure diving into these new topics with you.

Another person to thank is Birgit Gemmeke, for handling almost all administrative tasks in the group. Over the years you have taken countless burdens off my shoulders and I am glad your door is always open for advice.

I was in the lucky position to have benefited from the scientific environment of the CRC 1227 (Dq-mat) in Hannover and Braunschweig. This opened up many opportunities and many exciting collaborations for me. In this regard, I would like to thank Christian Lisdat and Uwe Sterr for the nice cooperation, in which they shared their insights on optical lattice clocks and ultra-stable lasers. I thank Fabian Wolf and Jan-Christoph Heip, for providing valuable insights into the daily routine of a trapped ion lab while we worked on metrology with Fock states. Henning Hahn and Giorgio Zarantonello also kindly invited me for a lab rotation. I would like to thank them for the many lively discussions about quantum gates (sometimes even continuing after the second beer, which of course never bothered me) and the great collaboration on our joint publications. Piet Schmidt, Tanja Mehlstäubler, José Crespo and Christian Ospelkaus were kind enough to always invite me to their scientific retreats. It was a great pleasure for me to meet all members of the different groups during these events. I enjoyed the scientific discussions (some of which were still ongoing during the hikes) and exchanging ideas over coffee in the breaks or in the evening when playing games.

For reviewing different parts of this thesis, I highly appreciate the help from Klemens, Victor, Jannis, Henning, Giorgio, Diana, Timm, Maja and Sahand.

I am grateful for the long-standing friendships from Aschendorf, my clique, and the orchestra, for providing welcome distractions during stressful times. Oliver, Christian, Tim and Andreas should be mentioned in particular (almost legally binding), for the tours and many other good times we had.

I would never have come this far without the support of my parents, Maria and Wilhelm, and my brother Andreas. Thank you so much for believing in me and enabling me to pursue my goals. Most of all, I would like to thank my girlfriend, Hanna, who has been able to motivate me and cheer me up time after time. I am very happy to have spent so much of the time writing this thesis together with you.

Contents

1 Introduction 1

2 Ramsey interferometry with generalized one-axis twisting echoes 5

2.1 Motivation and research problem 5
2.2 Spin systems 7
    2.2.1 Collective spin 8
    2.2.2 Visualization via Wigner functions 9
2.3 The conventional Ramsey protocol 11
    2.3.1 Ramsey interferometry with a single qubit 11
    2.3.2 Quantum projection noise (QPN) 14
    2.3.3 Coherent spin states 16
2.4 Previous extensions to Ramsey interferometry 18
    2.4.1 Spin squeezing parameter 19
    2.4.2 One-axis-twisting 20
    2.4.3 Fundamental bounds from quantum metrology 22
    2.4.4 Heisenberg limit 23
    2.4.5 Results on the quantum Fisher information 24
    2.4.6 Estimation from statistical moments 25
2.5 Generalized Ramsey protocols 26
2.6 Geometric optimization 26
2.7 Dephasing noise 31
2.8 Over-un-twisting enhancement 36
2.9 Summary 38
2.10 Outlook 39
    2.10.1 Comments on imperfections 39
    2.10.2 G-asymmetry and information content 39
    2.10.3 Larger variational class 42

3 Prospects and limits of entanglement-enhanced optical atomic clocks 45

3.1 Motivation and research problem 45
3.2 Essential elements of atomic clocks 47
    3.2.1 The local oscillator 48

3.2.2 Atomic reference 59
3.2.3 Servo and feedback application 66
3.3 Limits to the clock stability 67
3.4 Models for noise processes and instability 75
3.4.1 Instability related to the Dick effect 75
3.4.2 Stochastic differential equation approach 77
3.5 Conclusion 90
3.6 Outlook: Further directions for designed quantum states in optical atomic clocks 91
3.6.1 Composite clocks 92
3.6.2 Beating quantum projection noise in atomic clocks 95

4 Designed interactions for quantum metrology with trapped ions 101
4.1 Analysis of error sources in a microwave near-field entangling gate . . 102
4.1.1 Setup and Hamiltonian 102
4.1.2 The Mølmer-Sørensen gate 106
4.1.3 Error budget from experimental parameters 110
4.1.4 Pulse shaping to reduce infidelity 117
4.2 Laser-less quantum logic for (anti-)protons in Penning traps 122
4.2.1 Penning trap with longitudinal magnetic field gradient and transverse oscillating field 123
4.2.2 Numerical case studies 126
4.3 Conclusion and outlook 130

5 Summary and closing statements 133

A Signal and noise from spin characteristic functions 139
A.1 Without dephasing 139
A.2 Expectation values with dephasing 143

B Optimal interrogation time 149

Bibliography 153

Abbreviations and Acronyms

PTB	Physikalisch-Technische Bundesanstalt
LIGO	Laser Interferometer Gravitational-Wave Observatory
OAT	one-axis twisting
SNR	signal-to-noise ratio
OUT	over-un-twisting
CSS	coherent spin state
SSS	spin squeezed state
QPN	quantum projection noise
GHZ	Greenberger-Horne-Zeilinger
QFI	quantum Fisher information
POVM	positive operator-valued measure
SI	Système international d' unités
LO	local oscillator
FF	flicker floor
RW	random walk
CTL	coherence time limit
cL	current laboratory clock laser
pL	projected laboratory clock laser
tL	transportable clock laser
FH	fringe hops
SDE	stochastic differential equation
en	encoding
de	decoding
dbl	double
mfpt	mean first passage time
rf	radio frequency
A.C.	alternating current
ACZS	A.C. Zeeman shift
QuTiP	Quantum toolbox in Python
FWHM	full width at half maximum
CPT	charge, parity, time reversal
mot	motion
RHS	right hand side
h.c.	Hermitian conjugate
m+d	measurement and diffusion

1

Introduction

Currently there are fundamental aspects of physics that are still not understood. For example, the question as to what dark matter and dark energy are, how general relativity and quantum theory can be unified, or even the apparent asymmetry of matter and antimatter. The Standard Model of particle physics, the most complete and tested theory we have to date, is known to be incomplete. It has also not yet been able to solve any of these questions. New theories have been postulated, aimed at explaining some of the unresolved problems. However, so far there have been no direct confirmations on the additional predictions that they make. Designing experiments which can validate these theories, or rule them out, is thus essential for progress.

As there have been relatively few new results in this area from high energy physics, apart from the discovery of the Higgs boson, more and more disciplines of physics have become involved. Driven by this lack of direct observations of new physics at high energy scales (through particle accelerators or cosmology), entirely new systems are now considered in contrast to the established activities. Especially experiments with atomic, molecular and optical systems, operating at much lower energies, allow for complementary observations. In exchange these systems need extremely high accuracy and stability to measure any effects that might indicate new physics. When the masses of new particles are in the TeV range, the size of effects which may be detected in atomic systems (like electric dipole moments or changes of transition frequencies) turn out to be very small. But luckily not so small to be considered completely out of reach. For example, some hypothesized variations of the fine structure constant α are expected to result roughly in a $\dot{\alpha}/\alpha \approx 10^{-19}\,\mathrm{y}^{-1}$ variation with a $\Delta\alpha/\alpha \approx 10^{-20}$ annual modulation. This is only a few orders of magnitude away from the performance of the currently most accurate optical atomic clocks.

One impressive example for the progress in precision measurements is certainly the first measurement of gravitational waves by the optical interferometers in the LIGO collaboration. But also experiments based on the precision spectroscopy of atomic systems, magnetometry, and comparisons between atomic clocks have made significant contributions so far. In particular, new and much stricter constraints on the masses and interaction strengths of postulated particles for dark matter and dark energy were established. Small violations of fundamental symmetries and the validity of the universality of free fall are tested and upper bounds to the temporal variation of natural constants have been calculated from long-term measurements on atomic clocks. Many more results like these are envisioned in the future. Some of the most successful platforms are experiments that involve cold (neutral) atoms, ultra-cold atoms in Bose-Einstein condensates or single to hundreds of trapped ions. This selection is by no means complete, but includes cases which offer significant advantages for precision measurements. For example, all these systems can be well isolated from their environment and simultaneously allow a high degree of control over electronic (internal) and motion (external) degrees of freedom.

The coherent control of individual quantum systems has been a major achievement of the last decades, acknowledged with the Nobel price for D. J. Wineland and S. Haroche in 2012. Modern experiments allow for the creation of strong entanglement between many particles. This also sparked more theoretical research and the general field of quantum metrology arose early on, alongside experiments, from the idea that entangled quantum mechanical systems can be used as sensors with even greater precision than uncorrelated particles. Often, however, highly idealized scenarios were considered in the initial investigations, or the resulting optimizations led to protocols that required manipulation and measurements which are extremely difficult to implement. And still today, almost all high precision measurements focus either on low systematic errors (high accuracy) or low statistical detection noise (high stability). But applications for fundamental research will require improvements in both aspects, which in some cases can only be reached with entanglement. The relevance of designed quantum states for current metrology experiments, beyond proof-of-principle setups, thus remains a pressing open question. This thesis reports our progress on the issue by addressing the following guiding questions:

- Chapter 2: Can Ramsey protocols be robustly enhanced with minimal requirements for measurements and interactions? Are there any alternatives to the known protocols if only specific interactions and measurements are allowed?

- Chapter 3: Under which conditions can the stability of optical atomic clocks (in the simplest architecture) be improved by entanglement? When should entangled states be employed? Can these limits be circumvented by alternative architectures?

- Chapter 4: How can the necessary interactions for improved metrology be faithfully implemented in the case of trapped ions? Can one design readout schemes for exotic particles without optical transitions, like single trapped antiprotons?

The introduction is intentionally kept short at this point. The central research questions of the work were motivated and put into a general framework. However, details on the individual topics are not yet given. This is due to the fact that each of the three major chapters was written with the idea of being largely independent of the other chapters. In this way they can also be read in isolation and hopefully still present the main ideas in a clear and understandable way. Thus, at the beginning of the chapters 2, 3 and 4 there is a separate introduction and motivation. At these points we will pick up the larger framework once again, but also give more background information, especially about the particular issue covered in that chapter.

2

Ramsey interferometry with generalized one-axis twisting echoes

2.1 Motivation and research problem

Atomic sensors are currently among the most accurate measuring apparatuses in the field of quantum metrology. They are used for precision spectroscopy, magnetometry, or as frequency references and Ramsey interferometry is a popular measurement protocol for these applications. One particular advantage of using atoms for metrology is that they are ideal references. All atoms are identical and their transition frequencies are set by the laws of nature. In addition, comparing precision measurements on simple atoms with ab initio theoretical calculations allows for strict tests of our current understanding of the fundamental laws of physics [SBD+18, CSP09]. Due to the high accuracy and precision, reached over years of progress and innovation, those experiments are now envisioned to help detect minute effects which can be indications of new physics [LBY+15, SBD+18]. As an example, we already stated in the introduction that hypothesized variations of the fine structure constant α, having roughly a $\dot{\alpha}/\alpha \approx 10^{-19}\,\mathrm{y}^{-1}$ variation with a $\Delta\alpha/\alpha \approx 10^{-20}$ annual modulation [SBD+18], could soon be investigate with optical atomic clocks.

But using atoms as sensors comes at the cost that, as they are inherently quantum systems, they are also subject to the probabilistic character of measurements in quantum mechanics. In particular, a fundamental limitation for high-precision atomic sensors is given by the quantum projection noise (QPN). In this case, unavoidable quantum fluctuations of the measurement outcomes result in statistical noise, which ultimately limits the precision of the sensor. Fortunately, entanglement between atoms allows these fluctuations to be reduced below what is possible with uncorrelated probes [GLM06]. In the optical domain, squeezed states have already been injected into laser interferometers to enhance the precision [BHS18, T+19, A+19b].

Likewise, significant successes followed in the generation and characterization of non-classical states in atomic physics [PSO+18]. Putting these advances to use in Ramsey interferometry is an essential task to boost the performance of many atomic precision sensors in a similar fashion. However, the biggest problems of entangled states are that strongly correlated systems often require demanding measurements and that increasing sensitivity typically comes at the cost of an increased susceptibility to imperfections. More detailed investigations, taking these effects into account, showed that the actual gain of some entangled states can be significantly lower than in the ideal case [HMP+97, EdMFD11, DDKG12]. Hence the issue of practical quantum metrology protocols arises. The key questions to be answered in this chapter are: How well can extensions of the Ramsey protocol be robustly enhanced with minimal requirements for the measurements and entangling interactions? Are the previous proposals using either squeezed initial states or an interaction based readout complete, or do other possibilities exist? One step towards these goals will be the introduction of variational classes of Ramsey protocols, using entanglement as a resource. These classes form a recurring theme throughout the thesis, in which the complexity of the interactions is adapted at various points to suit the problem at hand.

As all applications mentioned above crucially rely on precise measurements of the energy splitting between two electronic states of an atom or ion, we start this chapter by collecting elementary properties of ensembles of spin-1/2 particles. Standard Ramsey interferometry is introduced in section 2.3 and we summarize some previous results on the one-axis-twisting (OAT) interaction and general phase estimation in sections 2.4.2 and 2.4.3. In the main part of this chapter we consider a large variational class of echo protocols based on OAT operations which, by construction, encompass a number of known protocols. In order to study which protocols give useful enhancements, we also include collective and individual dephasing during the OAT interactions. However, noise during the probe time, i.e. the application of the phase shift, is beyond the scope of this thesis. Related theoretical works include variational optimization algorithms [KSK+19] or inversion protocols using other spin-spin interactions, which are referred to as interaction based readouts [MSP16, Hai18, MNH18, APSK18, HZL+18, NKDW19]. Here we find the maximal amplification of the signal-to-noise ratio (SNR) by analytically optimizing geometric parameters, that is, signal and measurement directions. This allows to provide a complete overview and classification of our echo protocols in terms of the squeezing and un-squeezing strengths at any level of dephasing and arbitrary N. We identify one significant new scenario with a previously unused excess inversion. Such protocol types, which we refer to as 'over-un-twisting' (OUT) protocols, are especially interesting as their sensitivity preserves the optimal Heisenberg scaling of entangled states, SNR $\propto N$, independent of any collective dephasing during the OAT interactions.

2.2 Spin systems

A unified theoretical description of many atomic sensors is possible when the internal electronic structure of each atom is simplified to two energy levels only. Disregarding the presence of other transitions is a common and valid assumption for atoms with spectrally well separated energy levels. Such a two-level system could then constitute, for example, a narrow transition with high stability to external perturbations, as would be favoured for an atomic clock, a transition which allows particularly good coherent control, or any transition with some other favourable properties. Due to the formal equivalence in the mathematical description of a two-level system (qubit) and a pseudospin-1/2 particle, states and operators can be expressed in the latter, well-known form. So any pure state of an atom can be expressed as a superposition $|\psi\rangle = c_0|{\downarrow}\rangle + c_1|{\uparrow}\rangle$. The basis states $|{\uparrow}\rangle \equiv |1\rangle$ and $|{\downarrow}\rangle \equiv |0\rangle$ label the two relevant energy levels of the atom. In terms of the spin-1/2 algebra they are the eigenstates of the Pauli matrix σ_z with eigenvalues $+1$ and -1 respectively. For atoms, $|{\uparrow}\rangle$ and $|{\downarrow}\rangle$ typically correspond to orbitals of the valence electrons with a higher and a lower lying energy. Mixed states of a single qubit are characterized by a density matrix $\rho = (\mathbb{1} + r_1\sigma_x + r_2\sigma_y + r_3\sigma_z)/2 = (\mathbb{1} + \boldsymbol{r}\cdot\boldsymbol{\sigma})/2$ which is given in terms of the three Pauli matrices $\sigma_x, \sigma_y, \sigma_z$ and the 2x2 identity matrix $\mathbb{1}$. The three real coefficients $r_1 = \langle\sigma_x\rangle, r_2 = \langle\sigma_y\rangle, r_3 = \langle\sigma_z\rangle$ form the so called Bloch vector $\boldsymbol{r} = (r_1, r_2, r_3)^T$, with $0 \leq |\boldsymbol{r}| \leq 1$. The Bloch vector fully characterizes the state of a single qubit and gives a geometric interpretation to spin states and their dynamics. See Fig. 2.1 for a picture of the Bloch sphere with markings for the locations of a few example states.

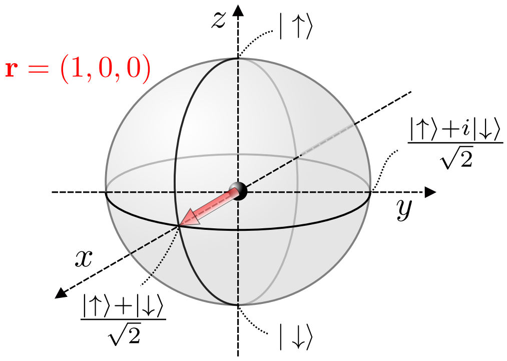
z
$|{\uparrow}\rangle$
$\mathbf{r} = (1,0,0)$
$\frac{|{\uparrow}\rangle + i|{\downarrow}\rangle}{\sqrt{2}}$
y
x
$\frac{|{\uparrow}\rangle + |{\downarrow}\rangle}{\sqrt{2}}$
$|{\downarrow}\rangle$

Figure 2.1: **Bloch sphere visualization:** The Bloch vector $\boldsymbol{r}$ represents the state of a single qubit.

2.2.1 Collective spin

Extending the concepts introduced above, a collection of N two-level systems is described within the tensor product Hilbert space $\mathcal{H} = \bigotimes_{k=1}^{N} \mathbb{C}^2$ of individual qubits. The number of basis states of this space grows as 2^N, making full numerical studies inaccessible for more than a handful of qubits. However, when restricting to interactions and measurements that are symmetric under particle exchange, the complexity can be reduced to a polynomial scaling. Such a symmetry is present for all dynamics considered in this chapter. Under the condition of symmetry all interactions must be some combination of the collective spin operators

$$S_{x,y,z} = \frac{1}{2}\sum_{k=1}^{N} \sigma_{x,y,z}^{(k)} \tag{2.1}$$

where $\sigma_{x,y,z}^{(k)}$ is the respective Pauli matrix for particle k. The collective spin operators fulfill the usual angular momentum commutation relations

$$[S_j, S_k] = i\sum_{l=1}^{3} \epsilon_{jkl} S_l \tag{2.2}$$

where ϵ_{jkl} is the fully antisymmetric tensor.

A basis in the general many-particle case is given by the states $|S, M\rangle$, which are the joint eigenstates of $\boldsymbol{S}^2 = S_x^2 + S_y^2 + S_z^2$ and S_z with $\boldsymbol{S}^2|S, M\rangle = S(S+1)|S, M\rangle$ and $S_z|S, M\rangle = M|S, M\rangle$. The labels are $S \in \{N/2, N/2-1, \ldots, 0 \text{ or } \frac{1}{2}\}$ with the last index depending on N being even or odd and $M \in \{-S, -S+1, \ldots, S-1, S\}$. When dealing with pure states which are symmetric under particle exchange, it suffices to consider only the states with largest total spin $S = N/2$. In that case, the so called Dicke states $|M\rangle \equiv |N/2, M\rangle$ form a basis and thus the dimension of the subspace is only $N+1$. For arbitrary mixed states with exchange symmetry the system can be described in terms of a basis whose number of elements scales $\propto N^3$ [Har16, XTH13, FSKD14, SAL$^+$18]. The Dicke state $|M\rangle$ corresponds to the fully symmetric linear combination of all states with $M + N/2$ excited qubits. For example, the states with lowest M values are [Mes62]

$$|-\frac{N}{2}\rangle = |{\downarrow\downarrow}\ldots{\downarrow}\rangle \tag{2.3}$$

$$|-\frac{N}{2}+1\rangle = \frac{1}{\sqrt{N}}\Big(|{\uparrow\downarrow}\ldots{\downarrow}\rangle + |{\downarrow\uparrow}\ldots{\downarrow}\rangle + \ldots + |{\downarrow\downarrow}\ldots{\uparrow}\rangle\Big) \tag{2.4}$$

$$|-\frac{N}{2}+2\rangle = \frac{1}{2}\binom{N}{2}^{-1/2} \sum_{j\neq k} |{\downarrow}\ldots{\downarrow}{\uparrow_j}{\downarrow}\ldots{\downarrow}{\uparrow_k}{\downarrow}\ldots{\downarrow}\rangle \tag{2.5}$$

and so on. To move between Dicke states of different M-values, the raising and lowering operators

$$S_\pm = S_x \pm i\, S_y \tag{2.6}$$

can be introduced, which obey

$$[S_+, S_-] = 2S_z, \qquad [S_z, S_\pm] = \pm S_\pm. \tag{2.7}$$

Correspondingly, we find

$$S_x = \frac{1}{2}(S_+ + S_-), \qquad S_y = \frac{1}{2i}(S_+ - S_-). \tag{2.8}$$

These ladder operators act like

$$S_\pm |M\rangle = \sqrt{S(S+1) - M(M \pm 1)}\, |M \pm 1\rangle \tag{2.9}$$

and thus increase or decrease the number of excitations by 1.

2.2.2 Visualization via Wigner functions

Whenever we want to gain conceptual insights to some specific measurement protocol involving N qubits, representations of states and operators on the collective Bloch sphere are a useful tool. Specifically, we will focus on the Wigner distribution $W(\theta, \phi)$ for this purpose. The following description is kept along the lines of Refs. [DAS94, Aga81]. The concept is quite general and applies to pure states, mixed states, and spin operators. We outline the construction of Wigner functions using the example of a general mixed state.

General quasi-probability distributions for spin systems, as representations of a quantum state ρ, are based on the decomposition

$$\rho = \sum_{k=0}^{2S} \sum_{q=-k}^{k} \rho_{kq} T_{kq}^{(S)} \tag{2.10}$$

of the density operator into spherical tensor operators $T_{kq}^{(S)}$. The spherical tensor operators (also sometimes referred to as multipole operators) are defined as

$$T_{kq}^{(S)} = \sum_{\mathfrak{m},\mathfrak{m}'=-S}^{S} (-1)^{S-\mathfrak{m}'} \langle S, \mathfrak{m}; S, -\mathfrak{m}' | k, q \rangle |S, \mathfrak{m}\rangle\langle S, \mathfrak{m}'| \tag{2.11}$$

in terms of Clebsch-Gordan coefficients $\langle S, \mathfrak{m}; S, -\mathfrak{m}' | k, q \rangle$ or likewise in terms of the Wigner 3-j symbols with the connection

$$(-1)^{S-\mathfrak{m}'} \langle S, \mathfrak{m}; S, -\mathfrak{m}' | k, q \rangle = (-1)^{S-\mathfrak{m}} \sqrt{2k+1} \begin{pmatrix} S & k & S \\ -\mathfrak{m} & q & \mathfrak{m}' \end{pmatrix}. \tag{2.12}$$

The coefficients ρ_{kq} in the decomposition of Eq. (2.10) are given by

$$\rho_{kq} = \mathrm{tr}\left[(T_{kq}^{(S)})^\dagger \rho\right] \tag{2.13}$$

and the Wigner function associated with ρ is then defined as [DAS94]

$$W(\theta,\phi) = \sum_{k=0}^{2S} \sum_{q=-k}^{k} \rho_{kq} Y_{kq}(\theta,\phi) \tag{2.14}$$

where $Y_{kq}(\theta,\phi)$ are the usual spherical harmonics. This form of the Wigner function is uniquely determined by requiring the two important properties [Aga81]:
(i) Normalization:

$$\mathrm{tr}\,[\rho] = \left(\frac{N+1}{4\pi}\right)^{1/2} \int W(\theta,\phi)\mathrm{d}\Omega, \tag{2.15}$$

where $\mathrm{d}\Omega = \sin(\theta)\,\mathrm{d}\theta\,\mathrm{d}\phi$ is the differential solid angle.
(ii) Traces of operator products become Wigner function overlap integrals:

$$\mathrm{tr}\,[\rho_1\rho_2] = \int W_1(\theta,\phi)W_2(\theta,\phi)\mathrm{d}\Omega, \tag{2.16}$$

where W_1 and W_2 are the Wigner functions for ρ_1, ρ_2 respectively. We highlight again that the above description does not only hold for states ρ but for arbitrary atomic or angular momentum operators. As examples we present a few Wigner functions for states and operators in Fig. 2.2. A collection collection of entangled spin states is later on shown in Fig. 2.6, when discussing one-axis-twisting, and we make further use of the Wigner functions in section 2.8.

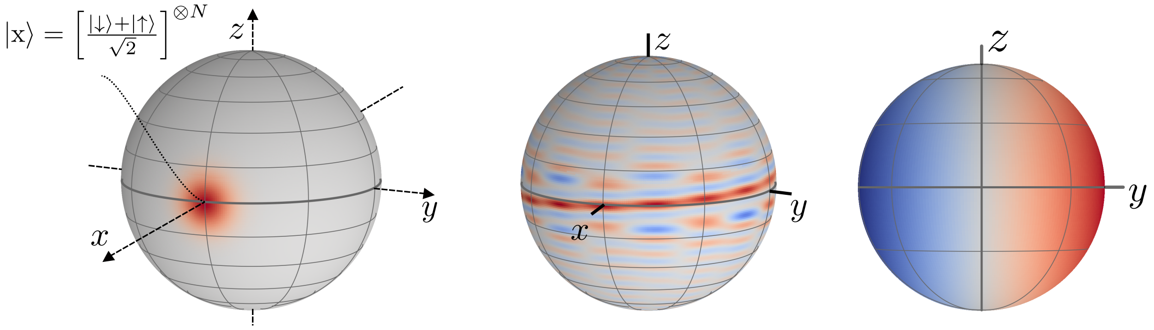

Figure 2.2: **Example Wigner functions:** Examples for different Wigner distributions which give a visual representation for states, operators, and dynamics of many qubits (here, $N = 50$). On the left is the Wigner function for the coherent spin state in x-direction, in the center the one for an entangled state generated via one-axis-twisting, and on the right the Wigner function representing the collective spin operator S_y.

2.3 The conventional Ramsey protocol

After reviewing some elementary aspects of spin systems, this section will now introduce the conventional Ramsey interferometry protocol. Very broadly speaking, the core concept of any interferometer is to detect relative phase shifts between two or more systems, caused e.g. by different propagation phases in the two paths of a Michelson or Mach-Zehnder setup, between atoms and electromagnetic radiation in the conventional Ramsey protocol or between atoms moving along different spatial trajectories in atom interferometry. Historically, optical interferometers performed the phase detection by superimposing electromagnetic fields and measuring the resulting interference, hence the name. The high sensitivity of the interference signal to small phase shifts established interferometry as a powerful tool for precision experiments over the past centuries.

From an abstract point of view, quite general interferometer protocols can be described in the following way: Consider the quantum state

$$\rho_\phi = e^{-i\phi G}\rho_0 e^{i\phi G}, \tag{2.17}$$

which is created by applying a phase shift via the generator G from the initial state ρ_0. The goal of an interferometer is to estimate the unknown phase ϕ as precisely as possible on the basis of ρ_ϕ. Expressing interferometry in this way allows to identify three fundamental parts of any protocol:

(i) Generation of the initial state ρ_0.
(ii) Application of the phase shift, as in Eq. (2.17).
(iii) Measurement on ρ_ϕ to make an estimate of ϕ.

The original Ramsey interrogation is now demonstrated to be one particular case of such a general interferometry protocol.

2.3.1 Ramsey interferometry with a single qubit

Ramsey's method builds upon previous results regarding the Rabi oscillation of atoms, which is a coherent manipulation of the spin state. To this end, let us first consider the interaction of a classical electromagnetic field with the single quantized two-level system introduced before.

Consider an electric field

$$\boldsymbol{E}(t) = \boldsymbol{\epsilon}\mathcal{E}e^{-i(\omega t+\varphi-\pi/2)} + \boldsymbol{\epsilon}^*\mathcal{E}^*e^{i(\omega t+\varphi-\pi/2)} \tag{2.18}$$

at the position of the qubit with polarization $\boldsymbol{\epsilon}$, amplitude $\mathcal{E}$, frequency ω, and phase φ. In a rotating frame with ω, and after applying the rotating wave approximation, the Hamiltonian describing the dynamics is commonly of the form [GZ15]

$$H = \frac{\hbar\Delta\omega}{2}\sigma_z + \frac{\hbar\Omega_\mathrm{R}}{2}\left(\sin(\varphi)\sigma_x - \cos(\varphi)\sigma_y\right) \tag{2.19}$$

where $\Delta\omega := \omega_0 - \omega$ is the detuning between the qubit resonance frequency ω_0 and the oscillation frequency ω of the field and

$$\Omega_\mathrm{R} := \left|\frac{2\mathcal{E}\boldsymbol{d}_{eg}\cdot\boldsymbol{\epsilon}}{\hbar}\right| \tag{2.20}$$

is the Rabi frequency (with the dipole moment $\boldsymbol{d}_{eg}$), expressing the strength of the coherent driving. We further assume that this is a strong, near-resonant drive, meaning that the detuning is the smallest overall frequency, i.e. we assume the hierarchy $|\Delta\omega| \ll \Omega_\mathrm{R} \ll \omega \approx \omega_0$. Without going into detail let us note that this interaction is characteristic for atomic spectroscopy, aimed at measuring the detuning $\Delta\omega$, which is essential to many different applications such as atomic clocks, magnetometers, gravimeters and others. One way to execute spectroscopy protocols, based on the Rabi method, uses continuous irradiation over some fixed time and a measurement of the excitation probability at the end to map out a resonance profile with respect to $\Delta\omega$. However, this has the possible drawback that the probing radiation can perturb the natural transition frequency of the atom while performing the spectroscopy. In this regard, many areas of atomic physics adapted Ramsey interrogation [Ram50], which features two short interaction periods separated by a much longer non-interacting period, due to the inherent reduction of systematic shifts and the reduced influence of inhomogeneities. When operated with a long dark time, Ramsey excitation also produces a narrower Fourier-limited linewidth compared to continuous spectroscopy of the same interrogation time.

The conventional Ramsey protocol for a single qubit is depicted in Fig. 2.3**a** and the approach is conceptually similar to the optical Mach-Zehnder interferometer. Here, the three interferometer steps are:

(i) Beginning from the state $|\downarrow\rangle$, a first atom-light interaction starts the Ramsey interferometer sequence by generating the superposition

$$|\psi_0\rangle = \frac{|\downarrow\rangle + |\uparrow\rangle}{\sqrt{2}} \tag{2.21}$$

of the two qubit states, similar to the action of the first beamsplitter in the analogous Mach-Zehnder interferometer. The state $|\psi_0\rangle$ can be generated with the Hamiltonian from Eq. (2.19) when $\varphi = 0$ as we show now. In the strong driving regime, $|\Delta\omega| \ll \Omega_\mathrm{R}$, effects of the detuning can be neglected and the time evolution for the single qubit is

$$U(t) = e^{-iHt/\hbar} = e^{i\Theta\,\sigma_y} = \cos(\Theta) + i\sigma_y\sin(\Theta) \tag{2.22}$$

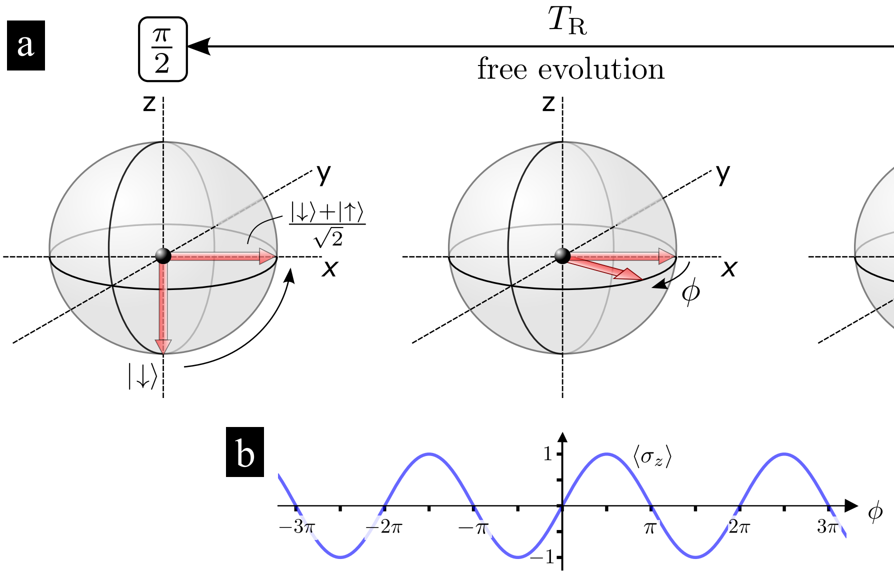
a
$\frac{\pi}{2}$
T_R
free evolution
$\frac{\pi}{2}$
z
y
x
$\frac{|\downarrow\rangle+|\uparrow\rangle}{\sqrt{2}}$
$|\downarrow\rangle$
ϕ
$|\psi_f\rangle$
$\langle\uparrow|$
$\langle\downarrow|$
b
1
$\langle\sigma_z\rangle$
-1
-3π
-2π
$-\pi$
π
2π
3π
ϕ

Figure 2.3: **Single qubit Ramsey protocol: a** Schematic Ramsey interferometry with the single qubit Bloch vector. From left to right this is the preparation of the initial superposition $|\psi_0\rangle$ with the first $\frac{\pi}{2}$ pulse, next the phase shift ϕ is applied during a free evolution time T_R and last a second $\frac{\pi}{2}$ pulse rotates the state back into the x-z-plane, allowing a measurement of σ_z to extract the information about ϕ. **b** Sinusoidal interferometer signal $\langle\sigma_z\rangle(\phi)$.

with $\Theta = \frac{\Omega_R t}{2}$, which generates the desired superposition, Eq. (2.21), when $\Theta = \frac{\pi}{4}$.

(ii) Next, the phase shift results naturally during the Ramsey dark time, where $\Omega_R = 0$. In this interval the time evolution is

$$U(t) = e^{-i\frac{\phi}{2}\sigma_z} \tag{2.23}$$

with the phase $\phi = \Delta\omega\, T_R$, resulting in the state

$$|\psi_{\text{out}}\rangle = \frac{1}{\sqrt{2}}\left(|\downarrow\rangle + e^{-i\phi}|\uparrow\rangle\right) \tag{2.24}$$

up to a global phase. In the rotating frame adopted here, the interaction thus causes the Bloch vector of the qubit to rotate along the equator of the Bloch sphere, as depicted in Fig. 2.3**a**, based on the frequency difference $\Delta\omega$.

(iii) A measurement of the phase signal ends the interferometer sequence. In the conventional Ramsey interferometer this is done by applying another atom-light interaction, as in the creation of the initial state, however now with $\varphi = \frac{\pi}{2}, \Theta = \frac{\pi}{4}$. This closes the interferometer by rotating the Bloch vector around the x-axis and subsequently a measurement of σ_z is performed. The final state prior to the measurement is

$$|\psi_f\rangle = \frac{1}{2}(1 - ie^{-i\phi})|\downarrow\rangle + \frac{1}{2}(e^{-i\phi} - i)|\uparrow\rangle \tag{2.25}$$

so the resulting signal is simply $\langle\sigma_z\rangle = \left|\langle\uparrow|\psi_{\mathrm{f}}\rangle\right|^2 - \left|\langle\downarrow|\psi_{\mathrm{f}}\rangle\right|^2 = \sin(\phi)$, as shown in Fig. 2.3**b**.

2.3.2 Quantum projection noise (QPN)

As mentioned in the motivation of this chapter, interferometry with atoms can not be made with infinite precision. Let us start from the end of the Ramsey interferometry to see what kind of limitations there are, so we first look at the measurement process. It follows from the postulates of quantum mechanics that a measurement of e.g. σ_z on a single qubit can only take two discrete outcomes: Either the particle is measured to be in the ground state $|\downarrow\rangle$ or in the excited state $|\uparrow\rangle$. Assuming a state $|\psi\rangle = c_0|\downarrow\rangle + c_1|\uparrow\rangle$ with complex amplitudes c_0, c_1 such that $|c_0|^2 + |c_1|^2 = 1$, as we had it in the Ramsey interferometer after the phase shift, the measurement detects the particle in $|\uparrow\rangle$ with probability $p_\uparrow = |c_1|^2$ and in $|\downarrow\rangle$ with probability $p_\downarrow = 1 - p_\uparrow = |c_0|^2$. However, no insight on the amplitudes of any superposition can be gained. The binary nature of the measurement outcomes means that generically there will be noise attached to the determination of ϕ based on the fundamental principles of quantum mechanics. Of course a precise knowledge of the excitation probability $p_\uparrow$ would be best for interferometry. In the standard Ramsey protocol from above, $p_\uparrow = \frac{1+\sin(\phi)}{2}$ and precise knowledge of this value would allow a perfect resolution of $\phi \in [-\frac{\pi}{2}, \frac{\pi}{2}]$.

With each spin measurement on the qubit returning only one bit of information, the signal that is encoded in the mean value $\langle\sigma_z\rangle$ is concluded more faithfully from either repeating the measurement multiple times or performing it independently on multiple atoms. One can study the measurement noise that remains for an ensemble of N identically prepared and uncorrelated atoms by looking at a measurement of the number of excited particles

$$\hat{N} = \sum_{i=1}^{N} |\uparrow\rangle_i\, {}_i\langle\uparrow| = S_z + \frac{N}{2}. \tag{2.26}$$

Note that we will use the notation $\hat{A}$ to explicitly refer to quantum mechanical operators only when necessary to avoid confusion. By adding up all results of the σ_z measurements for each individual atom, it can be seen that this observable can only take on one of the integer values between 0 and N in each realization. With the atoms being uncorrelated, the distribution of the outcomes follows a binomial distribution with expectation value $\langle\hat{N}\rangle = Np_\uparrow$ and variance $\left\langle(\Delta\hat{N})^2\right\rangle = Np_\uparrow(1-p_\uparrow)$, cf. Fig. 2.4. This distribution arises from summing up the N independent Bernoulli trials, corresponding to the measurement outcome of each individual qubit. The

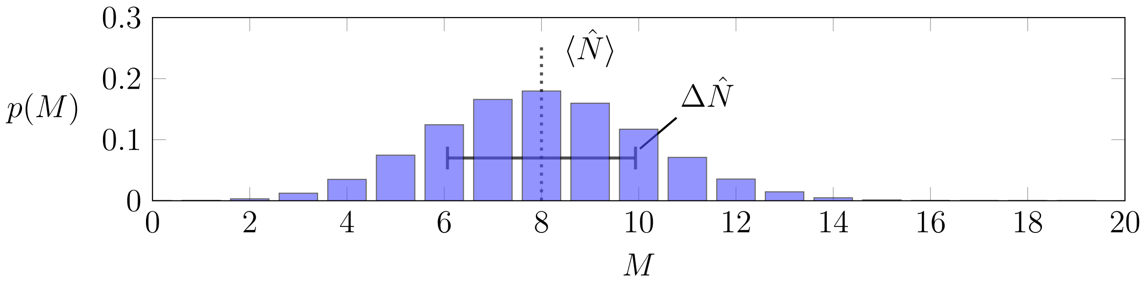

Figure 2.4: **Distribution with QPN:** Due to the probabilistic nature of quantum mechanical measurements, the number of excited qubits can not be determined precisely. For $N = 20$ uncorrelated particles with $p_\uparrow = 0.4$ the distribution of measurement outcomes M is a binomial distribution, centered around $\langle \hat{N} \rangle = 8$ and with standard deviation $\Delta \hat{N} \approx 2.19$.

resulting variance constitutes the fundamental QPN for this state. Although QPN was explained more intuitively in this case, using only σ_z measurements, we point out that the logic remains true for general uncorrelated states and measurements of the collective spin $S_{\boldsymbol{m}}$ in any direction $\boldsymbol{m}$. Note that we will use the notation $S_{\boldsymbol{n}} = \boldsymbol{n} \cdot \boldsymbol{S} = m_1 S_x + m_2 S_y + m_3 S_z$. Even though the value of $p_\uparrow$ changes in general, the overall conclusion remains invariant under a change of basis.

In an interferometer, one now seeks to estimate the probability $p_\uparrow$ according to a particular measurement result M of $\hat{N}$. Choosing $\check{p}_\uparrow = M/N$ gives an unbiased estimator of the excitation probability, as this has $p_\uparrow$ as its mean value. However, looking at Fig. 2.4, the quality of the estimator is clearly limited by the variance of the distribution. When K independent measurements are carried out, the variance of the estimator around the true value scales like

$$\left\langle (\Delta \check{p}_\uparrow)^2 \right\rangle = \frac{\left\langle (\Delta \hat{N})^2 \right\rangle}{K N^2} = \frac{p_\uparrow (1 - p_\uparrow)}{K N}. \tag{2.27}$$

Which reduces the overall uncertainty, but only in the same manner as more (uncorrelated) atoms would do.

More generally, the QPN can be considered a consequence of the uncertainty relation

$$\left\langle (\Delta S_j)^2 \right\rangle \left\langle (\Delta S_k)^2 \right\rangle \geq \frac{|\langle S_l \rangle|^2}{4} \tag{2.28}$$

for the spin components in three orthogonal directions j, k, l. This inequality applies to any state, correlated or not. It thus leads to lower limits on the measurement uncertainties for the components of the total spin for any state with polarization $|\langle S_l \rangle| > 0$. Of course QPN in itself is not the only relevant quantity in metrology, especially as it was introduced here for measurements of collective spin components only. Neither higher moments, individual qubit measurement operators, or other observables were considered. We will follow up with more general limits to the measurement resolution in section 2.4 when we allow for more general observables.

2.3.3 Coherent spin states

Looking back at the initial description of the Ramsey interferometer, we have now seen that the protocol with only a single qubit is severely affected by the resulting quantum projection noise and the use of a larger ensemble of atoms allows to cut down on this noise. In this way we will now briefly adapt the formulation of the Ramsey interferometer from above to the case of multiple atoms. This can be done in a compact manner with the use of coherent spin states (CSS) [ACGT72] and collective spin rotations.

For the study of quantum mechanical fields, such as the quantum mechanical harmonic oscillator, coherent states give the closest analogy to classical oscillations. In a similar way, one can define atomic spin states, which have analogous properties to the coherent states of fields. Let us just consider the initial state of the Ramsey interferometry to motivate this analogy. When we consider N two-level systems, the new initial state before the start of the Ramsey protocol is simply the product state $|\psi_0\rangle = |{\downarrow}\rangle^{\otimes N}$ with all particles in the ground state. Similarly, the results on coherent control of atoms also generalize to the case of many spins by replacing the Pauli matrices with the corresponding collective spin operators. Most important is that equation

$$H = \hbar\Delta\omega S_z + \hbar\Omega_{\mathrm{R}}\left(\sin(\varphi)S_x - \cos(\varphi)S_y\right) \tag{2.29}$$

is the equivalent of Eq. (2.19) for N atoms. The unitary time evolution during such pulses can be expressed as (again neglecting the small influence of the S_z term)

$$R_{\boldsymbol{n}}(\theta) := e^{-i\theta S_{\boldsymbol{n}}} = e^{-i\theta(S_x\sin\varphi - S_y\cos\varphi)} \tag{2.30}$$

where we again use the shorthand notation $S_{\boldsymbol{n}} = \boldsymbol{n}\cdot\boldsymbol{S}$. The operator $R_{\boldsymbol{n}}(\theta)$ describes rotations of the collective spin vector about an axis $\boldsymbol{n} = (\sin(\varphi), -\cos(\varphi), 0)$ in the Cartesian basis, with angle θ. After the rotation, the mean spin vector of the state points along

$$\boldsymbol{s}(\varphi,\theta) = \begin{pmatrix}\langle S_x\rangle\\ \langle S_y\rangle\\ \langle S_z\rangle\end{pmatrix} = \frac{N}{2}\begin{pmatrix}\cos(\varphi)\sin(\theta)\\ \sin(\varphi)\sin(\theta)\\ -\cos(\theta)\end{pmatrix}, \tag{2.31}$$

but the spin variances in any direction orthogonal to $\boldsymbol{s}$ remain unchanged. The value of the orthogonal variances for any rotation are the same as for the initial state $|\psi_0\rangle = |-N/2\rangle = \bigotimes_{k=1}^{N}|{\downarrow}\rangle_k$, which has $\langle S_z\rangle = -N/2$, $\langle S_x\rangle = \langle S_y\rangle = 0$, i.e. is oriented in negative z-direction, and has fluctuations $\left\langle(\Delta S_{\boldsymbol{k}})^2\right\rangle = \left\langle(S_{\boldsymbol{k}} - \langle S_{\boldsymbol{k}}\rangle)^2\right\rangle =$

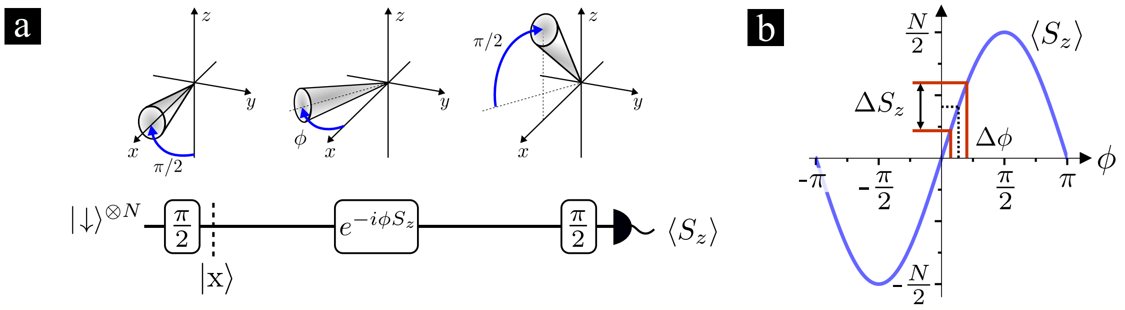

Figure 2.5: **Ramsey interferometer with N atoms: a** Conventional Ramsey measurement where a phase ϕ is imprinted between two $\pi/2$-pulses by rotating the state in the equatorial plane around the z-axis. After the second $\pi/2$-pulse, which rotates the state around the x-axis, the signal in phase is determined from measuring the spin component S_z. Note that alternatively one could discuss the effective observable S_y and leave out the second pulse. Cones visualize mean spin directions and quantum fluctuations of the CSS during the protocol. **b** Measurement signal $\langle S_z\rangle(\phi)$ where we highlight the error propagation from detection noise ΔS_z onto a phase uncertainty $\Delta\phi$.

$N/4$ for all $\boldsymbol{k} \perp \boldsymbol{e}_z$. The fact that each of these states has symmetric, minimal variance according to the Heisenberg uncertainty relation, Eq. (2.28), suggests an analogy to the coherent states of fields. Indeed, in further similarity to the coherent oscillator states $|\alpha\rangle = \mathcal{D}(\alpha)|0\rangle$, which are generated by complex valued displacements $\mathcal{D}(\alpha) = e^{\alpha a^\dagger - \alpha^* a}$ of the vacuum state $|0\rangle$, the most general coherent spin state

$$|\theta, \varphi\rangle = R_{\boldsymbol{n}}(\theta)|-N/2\rangle \tag{2.32}$$

results from a rotation $R_{\boldsymbol{n}}(\theta)$ of the atomic ground state $|-N/2\rangle$. Beyond the formal similarity with coherent field states shown here, a more complete discussion of this topic can be found in Ref. [ACGT72]. This work also includes many additional mathematical relations of the collective spin rotations $R_{\boldsymbol{n}}(\theta)$, among them a highly useful disentangling theorem for angular momentum operators. These relations are particularly valuable for the analytical study of generalized Ramsey protocols as discussed in detail in appendix A.

Given these tools, the Ramsey interferometry with uncorrelated states can be expressed in a compact form, as shown schematically in Fig. 2.5**a**. Picking up the discussion on the initial state from above, we now see that the first $\frac{\pi}{2}$ pulse, starting the interferometer sequence, corresponds to the controlled rotation

$$R_{\boldsymbol{n}}(\Phi) = e^{-i\Phi S_n} \tag{2.33}$$

around $\boldsymbol{n} = \boldsymbol{e}_y$ and with $\Phi = \frac{\pi}{2}$. This generates the coherent spin state

$$|\mathrm{x}\rangle = \left[\frac{|\downarrow\rangle + |\uparrow\rangle}{\sqrt{2}}\right]^{\otimes N}, \tag{2.34}$$

polarized in x-direction. This result can be verified with the property $R_{\boldsymbol{n}}(\Phi) = \bigotimes_{k=1}^{N} e^{-i\frac{\Phi}{2}\sigma_{\boldsymbol{n}}^{(k)}}$, meaning that the rotation splits into the product of single qubit rotations, as $R_{\boldsymbol{n}}(\Phi)$ is linear in the collective spin operator. In the following interaction period, the small phase signal ϕ is imprinted by $e^{-i\phi S_z}$ rotating the state around the z-axis. A second $\pi/2$ rotation, with $\boldsymbol{n} = \boldsymbol{e}_x$, allows to infer ϕ from the measurement result of S_z as shown in Fig. 2.5**b**.

Even though we now include multiple atoms, any finite number N will still give an uncertainty $\Delta\phi$ from spin fluctuations of the CSS, e.g. the detection noise ΔS_z. Note that we will generally make use of the notations

$$(\Delta\hat{A})^2 := \langle\hat{A}^2\rangle - \langle\hat{A}\rangle^2 \tag{2.35}$$

and

$$\Delta\hat{A} := \sqrt{(\Delta\hat{A})^2} \equiv \sqrt{\langle\hat{A}^2\rangle - \langle\hat{A}\rangle^2} \tag{2.36}$$

for the variance and standard deviation of any quantum mechanical operator $\hat{A}$. A natural question at this point is how to progress beyond the QPN limit. Entangling the atoms was proposed as a possible way to reduce the measurement uncertainty. But, given that the entire protocol can be expressed by collective rotations of the uncorrelated initial state and the fact that product states will remain product states under these rotations (as they decompose into individual qubit rotations), no entanglement can be generated in this sequence. In this sense one can regard the standard Ramsey interferometer described here as the most ‘classical’ case. It will be useful to compare the sensitivity of entangled states extending the Ramsey protocol against the uncorrelated coherent spin states. In this way, an advantage over ‘classical’ strategies can be quantified. We will look at some known extensions to the Ramsey protocol in the next section.

2.4 Previous extensions to Ramsey interferometry

Understanding how entanglement has been used so far to enhance the precision of Ramsey interferometry is essential to the results of this chapter. So at this point, we give a short review on advances in quantum metrology which are relevant to Ramsey interferometry. This is intended to help place the upcoming results in the broader context of the field. We will not be able to give a complete discussion of quantum metrology here, but instead rather focus on those results which form a direct basis for our techniques, or those which address closely related research questions.

Extending the conventional Ramsey interferometry means allowing more degrees of freedom in one of the interferometer steps (i)-(iii). As a repeating class of protocols in this thesis, we define extensions of the following form:

(i) Preparation of an initial state $|\psi_0\rangle = \mathcal{U}_{\text{en}}|\text{x}\rangle$. Let the general initial state be some non-classical state, where an entangling interaction $\mathcal{U}_{\text{en}}$ is applied on $|\text{x}\rangle$.

(ii) Imprint of the signal by a phase-dependent rotation of the initial state around the z-axis. This results in $e^{-i\phi S_z}|\psi_0\rangle$ where ϕ is the accumulated phase.

(iii) We allow for an additional decoding operation $\mathcal{U}_{\text{de}}$ to be applied before measuring some component of the collective spin. For more direct correspondence to the classical Ramsey interferometry, let us choose S_y to be the observable.

At the end of the sequence, the average signal is

$$\langle S_y\rangle(\phi) = \langle \text{x}|\mathcal{U}_{\text{en}}^\dagger\, R_z^\dagger(\phi)\,\mathcal{U}_{\text{de}}^\dagger\, S_y\,\mathcal{U}_{\text{de}}\, R_z(\phi)\,\mathcal{U}_{\text{en}}|\text{x}\rangle. \tag{2.37}$$

Note that the choice of the observable may pose no restriction, depending on the generality of $\mathcal{U}_{\text{de}}$. In principle, one could just as well include the application of $\mathcal{U}_{\text{de}}$ into the notion of some new effective measurement operator $\tilde{S}_y = \mathcal{U}_{\text{de}}^\dagger S_y \mathcal{U}_{\text{de}}$. This can alter the direction of the collective spin measurement when a collective spin rotation is taken as the last interaction in $\mathcal{U}_{\text{de}}$.

In the remainder of this section, special cases of the extended protocols are discussed. Adjusting the state preparation only, we will first review the characterisation of sensitivity for collective spin measurement with different initial states in terms of the squeezing parameter. Accompanying that section is a discussion of one-axis-twisted states, which are the relevant entangled states within this thesis. While the phase shift, i.e. step (ii) of a general interferometer, could in principle be adjusted to some nonlinear dynamics, we will consider only collective spin rotations around some axis throughout this entire thesis. Finally, very general optimizations over the measurement, step (iii), are discussed in the section on fundamental metrology bounds.

2.4.1 Spin squeezing parameter

Historically, the quality of an atomic interferometer was first characterized through properties of the applied measurement operator. Either in terms of the spread of the outcomes, as we used it before with $\left\langle(\Delta S_z)^2\right\rangle$ in the discussion of QPN, or as a signal-to-noise ratio around a fixed working point. The latter corresponding to the inverse phase variance $\Delta\phi^{-1}$ depicted in Fig. 2.5**b**. For the spin ensembles introduced above, different forms of so-called squeezing parameters were introduced [MWSN11]. One of the most important definitions goes back to the works of Wineland and colleagues [WBIH94, WBI+92]. They considered an initial state with polarization $\langle S_{\boldsymbol{s}}\rangle$ in $\boldsymbol{s}$-direction, which is rotated on the collective Bloch sphere around a perpendicular axis $\boldsymbol{n} \perp \boldsymbol{s}$ before the spin projection $S_{\boldsymbol{m}}$ is measured in the direction $\boldsymbol{m} \perp \boldsymbol{n}$ and

$\boldsymbol{m} \perp \boldsymbol{s}$, i.e. orthogonal to both. With $\boldsymbol{s} = \boldsymbol{e_x}, \boldsymbol{n} = \boldsymbol{e_z}$ and $\boldsymbol{m} = \boldsymbol{e_y}$, this scenario is exactly the standard Ramsey interrogation, as described above. The spin squeezing parameter

$$\xi^2 = \frac{N\left\langle (\Delta S_{\boldsymbol{m}})^2 \right\rangle}{\langle S_{\boldsymbol{s}} \rangle^2}, \tag{2.38}$$

introduced by Wineland *et al.*, describes the ratio of QPN relative to the mean length $\langle S_{\boldsymbol{s}} \rangle$ of the spin vector in polarization direction. Note that $\langle S_{\boldsymbol{s}} \rangle$ captures the contrast of the measurement in this context. A ratio of $\xi^2 < 1$ denotes spin squeezing, which indicates an improvement in sensitivity compared to the classical coherent spin states. More generally, it can be shown that $\xi < 1$ is a sufficient condition for entanglement [SDCZ01]. Therefore, states with $\xi < 1$ can only be generated by spin-spin interactions which entangle the atoms. For the states that are typically regarded as spin squeezed ($\xi < 1$), the variance of $\left\langle (\Delta S_{\boldsymbol{m}})^2 \right\rangle$ is reduced without violating the uncertainty relation (2.28) by simultaneously increasing the variance $\left\langle (\Delta S_{\boldsymbol{n}})^2 \right\rangle$. However, there are also many other entangled states that can be useful for metrology and for which $\xi < 1$ is not fulfill. Over time, more interactions have been proposed to prepare such metrologically useful states. A comprehensive description of all processes would lead too far and we refer to Ref. [PSO$^+$18] for a collection of the most frequent approaches. Many of these methods have already been tested in experiments and further references to those works can be found in the same review. In this thesis we exclusively make use of the one-axis twisting interaction.

2.4.2 One-axis-twisting

The one-axis-twisting interaction for effective two-level systems allows a uniform description of many setups [KU93]. The necessary Hamiltonian $H = \chi S_z^2$ can be engineered in a variety of metrologically relevant systems. It can be generated through cavity induced spin squeezing of cold atoms [SSLVac10, PSO$^+$18], via laser or microwave driven quantum gates for trapped ions [BW08] and from spin-changing collisions in spinor Bose-Einstein condensates [PSO$^+$18]. In the case of one-axis-twisting, the unitary time evolution

$$T_\mu := e^{-i\chi t S_z^2} = e^{-i\frac{\mu}{2} S_z^2} \tag{2.39}$$

with $\mu = 2\chi t$ generates a large variety of spin squeezed states, see Fig. 2.6. For small squeezing strengths, $\mu < 4/\sqrt{N}$, the generated entanglement is reflected by reduced fluctuations of the mean spin [KU93, PSO$^+$18] (see top row). With increasing μ, greater levels of multi-particle entanglement are generated. At $\mu = \pi$, rotated versions of the N-particle correlated Greenberger-Horne-Zeilinger (GHZ) state $\left[|\downarrow\rangle^{\otimes N} + |\uparrow\rangle^{\otimes N}\right]/\sqrt{2}$, aligned along the x axis if N is even or along the y axis if N is odd, are created and the dynamic reverses afterwards [PSO$^+$18] (see last panel).

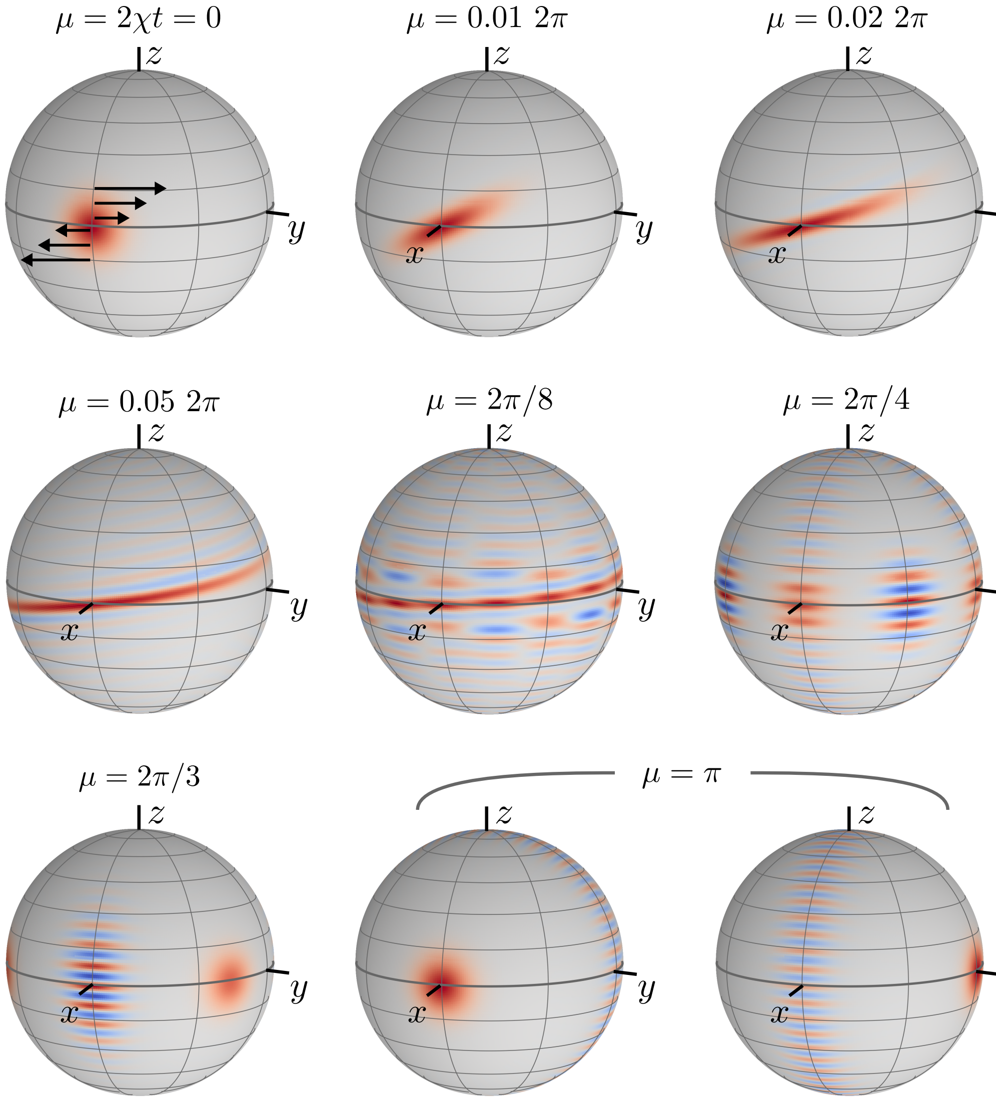

Figure 2.6: **Overview of one-axis-twisting states:** States generated via the one-axis-twisting interaction for increasing squeezing strength $\mu = 2\chi t$. In this visualization the interaction has the form of a shearing force around the z-axis (see first panel). Starting from the coherent spin state ($\mu = 0$), one finds first the generation of weakly squeezed spin states with the noise ellipse rotated depending on the value of μ. For increasing μ, the states transform to oversqueezed states, superpositions of multiple coherent spin states and finally to a GHZ state in the x or y basis. We used $N = 50$ for all Wigner functions except for the last panel where $N = 51$ to represent the difference between even and odd particle number which is relevant for this state.

A few specific Ramsey protocols using such states are already known. Among them is the use of maximally entangled GHZ states [BIWH96] and optimized moderately squeezed states [ASL04]. Recently, experiments in which simple but well-controlled interactions were used several times, in the form of an 'echo', achieved excellent results in a range of precision measurements [HKEK16, LBS+04, LSM+16, BSB+19]. By applying the inverse OAT interaction before measuring a spin projection, even stronger squeezed states can be used without the typical limitation from the loss of contrast. These echo protocols, also called 'interaction based readout', attracted great interest not only because they allow amplified sensitivity for simple measurements, but also as they can ease the required resolution in the detection. A variety of such protocols has been proposed, see for example Refs. [DBSS16, FSD16, NSH17, APSK18, MSP16, HZL+18, NKDW19]. Notably, Haine [Hai18] identified optimal interaction based readout strategies which maximize the classical Fisher information (see below) under the influence of detection noise.

2.4.3 Fundamental bounds from quantum metrology

Apart from these specific protocols, much more universal statements can be made about the resolution of phase shifts when optimizing over all measurements that could be performed in step (iii). In this way limits to the uncertainty of phase estimation were obtained by applying results from classical parameter estimation theory and quantum information theory. For example, the Cramér-Rao bound

$$\left\langle (\Delta\check{\phi})^2 \right\rangle \geq \left\langle (\Delta\check{\phi}_{\mathrm{CR}})^2 \right\rangle = \frac{1}{F(\phi)}, \tag{2.40}$$

for unbiased estimators $\check{\phi}$, can be considered as a quantum mechanical restriction when the conditional probabilities $p(M|\phi)$ in the Fisher information

$$F(\phi) = \sum_M \frac{1}{p(M|\phi)} \left(\frac{\partial p(M|\phi)}{\partial \phi} \right)^2 \tag{2.41}$$

reflect the measurement statistics of a quantum mechanical observable. Meaning $p(M|\phi) = \mathrm{tr}\left[\rho_\phi E(M)\right]$ is the probability to obtain result M for the observable $E(M)$.

Generalized measurements We have applied here the concept of positive operator-valued measures (POVMs) to describe generic observables [NC09]. With this notion any measurement outcome M of a detector is identified with a positive, Hermitian operator $E(M)$. A POVM is then given by the complete set $\{E(M), M \in \mathcal{M}\}$ with the defining properties $E(M) \geq 0$ and $\sum_M E(M) = \mathbb{1}$, so they resolve the identity operator. They constitute the most general measurements possible in quantum mechanics, extending the usual projective measurements and also allowing for indirect measurements in which a system interacts first with another probe system before the measurement is performed on the probe. POVMs are motivated based on general statistical theories and the Born rule so that the defining properties from above ensures positive probabilities $p(M|\phi) \geq 0$ with proper normalization $\sum_M p(M|\phi) = 1$.

It should be noted that the classical Cramér-Rao limit, Eq. (2.40), includes an optimization over all unbiased estimators but still depends on the selected observable. In a second step, the bound can be lowered by maximizing the Fisher information over all observables. This results in the so-called quantum Cramér-Rao bound [Hel69]

$$\left\langle (\Delta\phi_{\mathrm{CR}})^2 \right\rangle \geq \left\langle (\Delta\phi_{\mathrm{QCR}})^2 \right\rangle = \frac{1}{\mathcal{F}_Q[\rho_\phi]}, \tag{2.42}$$

where the quantum Fisher information (QFI) $\mathcal{F}_Q[\rho_\phi] = \max_E F(\phi)$ is the maximization of Eq. (2.41) over all generalized measurements E. For some reviews on the topic, see e.g. Refs. [GLM11, Par09]. The QFI, and thus the quantum Cramér-Rao limit, are completely characterized by the final state ρ_ϕ. Thus, one obtains with Eq. (2.42) a limit that only depends on the initial state ρ_0 and the interferometer transformation, as e.g. in Eq. (2.17).

2.4.4 Heisenberg limit

The largest QFI for any generator $G = S_{\boldsymbol{n}}$, linear in the collective spin operators, and arbitrary N-qubit states ρ is [PS09]

$$\mathcal{F}_Q[\rho, S_{\boldsymbol{n}}] \leq N^2. \tag{2.43}$$

In combination with Eq. (2.42) this defines the Heisenberg limit [GLM06]

$$\left\langle (\Delta\phi_{\mathrm{H}})^2 \right\rangle = \frac{1}{KN^2} \tag{2.44}$$

as the lowest value to the estimation variance. Here we allowed for K independent repetitions of the measurement process. The name 'Heisenberg limit' originates from the heuristic phase-number uncertainty relation $\Delta\phi\Delta N \geq 1$ and was termed by Holland and Burnett [HB93]. We will refer to *Heisenberg scaling* whenever $\Delta\phi \propto N^{-1}$. Note that the Heisenberg limit presented in Eq. (2.44) can still be outperformed by non-linear interactions [Lui04, BFCG07, RB08, BDF$^+$08] or multi-pass protocols [HBB$^+$07].

2.4.5 Results on the quantum Fisher information

Interestingly, it has also been shown that the QFI is connected to the separation of states under the interferometer transformation [BC94]. Looking at the Bures distance [Bur69, Hüb92]

$$d_{\mathrm{B}}^2(\rho_0, \rho_\phi) = 1 - \mathscr{F}(\rho_0, \rho_\phi), \tag{2.45}$$

where $\mathscr{F}(\rho_0, \rho_\phi) = \mathrm{tr}\left[\sqrt{\sqrt{\rho_\phi}\rho_0\sqrt{\rho_\phi}}\right]$ is the general quantum fidelity [Uhl76, Joz94] between two states, a Taylor expansion around small values of ϕ gives [PSO+18]

$$d_{\mathrm{B}}^2(\rho_0, \rho_\phi) = \frac{\mathcal{F}_Q[\rho_0]}{8}\phi^2 + \mathcal{O}(\phi^3). \tag{2.46}$$

Thus the QFI corresponds to the speed at which the transformed state ρ_ϕ separates from ρ_0. Not only does this give a geometric perspective to the QFI, but it also allows the derivation of useful ways to calculate the QFI in particular instances. Essential for this work is the case of a general mixed state with spectral decomposition $\rho_\phi = \sum_\kappa q_\kappa |\kappa\rangle\langle\kappa|$, which can result from a mixed initial state after the unitary interferometer transformation with generator G. Here, the spectral decomposition has $q_\kappa \geq 0$ for the eigenvalues and $|\kappa\rangle$ denote the associated eigenvectors. In this case the QFI is [BC94, PSO+18]

$$\mathcal{F}_Q[\rho_0, G] = 2 \sum_{\substack{\kappa,\kappa' \\ q_\kappa + q_{\kappa'} > 0}} \frac{(q_\kappa - q_{\kappa'})^2}{q_\kappa + q_{\kappa'}} |\langle\kappa'|G|\kappa\rangle|^2. \tag{2.47}$$

An important simplification of equation (2.47) follows for pure states $\rho_0 = |\psi\rangle\langle\psi|$. In that case

$$\mathcal{F}_Q[\rho_0, G] = 4\big\langle(\Delta G)^2\big\rangle, \tag{2.48}$$

causing the QFI to depend entirely on the variance of the generating Hamiltonian. Although the optimal measurements can be determined in principle [BC94], this often results in complicated solutions, which generally depend on the true value of the parameter ϕ. So reaching the full QFI is often impossible or very complicated at best. Nonetheless, it is important as a useful limit to compare to. Thus the QFI has been studied on its own for a variety of states and interferometer interactions. For states created by one-axis twisting and transformed by collective spin rotations, one has [PS09]

$$\max_{\boldsymbol{n}} \mathcal{F}_Q[\rho_0, S_{\boldsymbol{n}}] = \max\left\{ N + \frac{N(N-1)}{4}\left(A + \sqrt{A^2 + B^2}\right), \right. \\ \left. N^2\left(1 - \cos^{2N-2}(\mu/2)\right) - \frac{N(N-1)A}{2} \right\} \tag{2.49}$$

with $A = 1 - \cos^{N-2}(\mu)$ and $B = 4\sin(\mu/2)\cos^{N-2}(\mu/2)$.

2.4.6 Estimation from statistical moments

A relation between the general bounds introduced above and the standard phase resolution or the well-known squeezing parameter ξ can be established by the method of moments [PSO+18]. In this approach, the change of collective properties of the measurement statistics, such as the mean value $\overline{M}(\phi)$ or the variance $\langle(\Delta M)^2\rangle(\phi)$, is used to detect the phase ϕ. The method is briefly explained here, using the example of the mean value. Consider an observable for which the outcomes $M_1, \dots, M_K$ are obtained in K independent repetitions with the true phase value ϕ_0. The experimentally determined mean value is $\overline{M}_{\text{ex}} = \frac{1}{K}\sum_{j=1}^{K} M_j$. If the functional relation $\overline{M} = f(\phi)$ between the phase and the mean value is known, then the value $\check{\phi} = f^{-1}(\overline{M}_{\text{ex}})$ is chosen as the estimator. In this way, $\check{\phi}$ corresponds to that value of ϕ which would give the measured mean value $\overline{M}_{\text{ex}}$. In a small region around a fixed value ϕ_0, the variance of this estimator is calculated by error propagation to be

$$\Delta\phi_{\text{mom}} = \frac{\Delta M(\phi_0)}{\sqrt{K}|\mathrm{d}\overline{M}/\mathrm{d}\phi|\big|_{\phi_0}}. \tag{2.50}$$

Since the Fisher information is bounded from below by the variation of the mean value [PS09], i.e.

$$F(\phi) \geq \frac{1}{\langle(\Delta M)^2\rangle(\phi_0)} \left(\frac{\partial\overline{M}}{\partial\phi}\Big|_{\phi_0}\right)^2, \tag{2.51}$$

it follows that

$$\Delta\phi_{\text{mom}} \geq \frac{1}{\sqrt{K}\sqrt{F(\phi)}} \geq \frac{1}{\sqrt{K}\sqrt{\mathcal{F}_Q[\rho, G]}}. \tag{2.52}$$

Finally, in the case of spin squeezing, one has

$$\frac{N}{\mathcal{F}_Q[\rho_0, S_{\boldsymbol{n}}]} \leq \xi^2. \tag{2.53}$$

The method of moments is often favoured, due to its simplicity in determining the phase sensitivity of interferometers. Note, however, that it is generally not optimal, since $\Delta\phi_{\text{mom}} < \Delta\phi_{\text{CR}}$. Furthermore, the procedure can only be applied in a range of parameters, for which the relationship $\overline{M} = f(\phi)$ is unambiguous and the inversion of $f(\phi)$ is possible. In section 2.7, we will make use of the bounds (2.52) and (2.53) as a benchmark for the generalized echo protocols developed hereafter.

2.5 Generalized Ramsey protocols

Motivated by the conventional Ramsey scheme, introduced in section 2.3 and displayed for comparison in Fig. 2.7**a**, we now consider the generalized echo protocols, shown schematically in Fig. 2.7**b**. Starting again from the coherent spin state $|\mathrm{x}\rangle$, present after the first $\pi/2$ pulse, a squeezed spin state is initiated via the non-linear OAT interaction $T_\mu = e^{-i\frac{\mu}{2}S_z^2}$, with strength μ. For the following signal imprint we now consider the more general case of a rotation of the collective spin around an arbitrary axis $\boldsymbol{n}$. Note that the physical rotation around the z-axis may be converted to a rotation around $\boldsymbol{n}$ by appropriate single qubit rotations R (in the form of Eq. (2.33)) before and after the phase imprint such that $R_{\boldsymbol{n}}(\phi) = e^{-i\phi S_{\boldsymbol{n}}} = R^{-1}e^{-i\phi S_z}R$, meaning that $S_{\boldsymbol{n}} = R^{-1}S_z R$. Prior to the measurement, we allow for another OAT interaction with strength $\nu - \mu$. With this definition, ν describes the deviation from an exact inversion of the initial OAT. This choice is based on an appearing symmetry around exact echo protocols at $\nu = 0$, cf. Fig. 2.7**c**. We assume inversion of the OAT is possible by reversing the sign of the interaction strength, as already demonstrated for cold atoms [HKEK16], spinor Bose-Einstein condensates [LSM$^+$16] and trapped ions [LBS$^+$04, GBSN$^+$17]. At the end of our protocols, the collective spin $S_{\boldsymbol{m}}$ in an arbitrary direction $\boldsymbol{m}$ is measured. Again, this can be implemented with a measurement of S_z by preceding an appropriate rotation of the collective spin. Overall, the generalized echo protocols have a measurement signal

$$\langle S_{\boldsymbol{m}}\rangle(\phi) = \langle \mathrm{x}|T_\mu^\dagger\, R_{\boldsymbol{n}}^\dagger(\phi)\, T_{\nu-\mu}^\dagger\, S_{\boldsymbol{m}}\, T_{\nu-\mu}\, R_{\boldsymbol{n}}(\phi)\, T_\mu|\mathrm{x}\rangle, \tag{2.54}$$

characterized by parameters μ, ν for squeezing and un-squeezing, and directions $\boldsymbol{n}, \boldsymbol{m}$ for signal and measurement. This is now one particular refinement of the general extensions which were introduced in section 2.4. We highlight that the generalized echo protocols include some common squeezing protocols as limiting cases: For $\nu = \mu$, i.e. no un-twisting, we find standard Ramsey interrogation with a spin squeezed initial state [ASL04]. In this case, the SNR is enhanced by reducing projection noise at a constant signal. More recently, protocols with exact inversion, i.e. $\nu = 0$, were suggested for application in quantum metrology [DBSS16, FSD16, NSH17]. There, amplification of the signal at constant measurement noise occurs.

2.6 Geometric optimization

In the following we quantify metrological sensitivity by the inferred phase deviation

$$\Delta\phi(\mu, \nu, \boldsymbol{n}, \boldsymbol{m}) = \Delta S_{\boldsymbol{m}}|_{\phi=0} \Big/ \left|\frac{\partial\langle S_{\boldsymbol{m}}\rangle}{\partial\phi}\Big|_{\phi=0}\right| \tag{2.55}$$

around the working point $\phi = 0$. As motivated before, this is a useful measure for atomic sensors limited by quantum projection noise. For $\nu = \mu$, i.e. no interaction preceding the measurement, the phase deviation is connected to the squeezing parameter as $\Delta\phi = \frac{\xi}{\sqrt{N}}$ when $\boldsymbol{n} \perp \boldsymbol{m}$ and both are in the y-z plane. However, for $\nu \neq \mu$, $\Delta\phi$ is a true extension of ξ by also considering effectively nonlinear spin observables. We will now show that the essential optimization with respect to the signal and measurement directions can be solved analytically. The method described here corresponds exactly to the method first described in a related work by Gessner *et al.* in Ref. [GSP19]. While in that case the authors were able to systematically

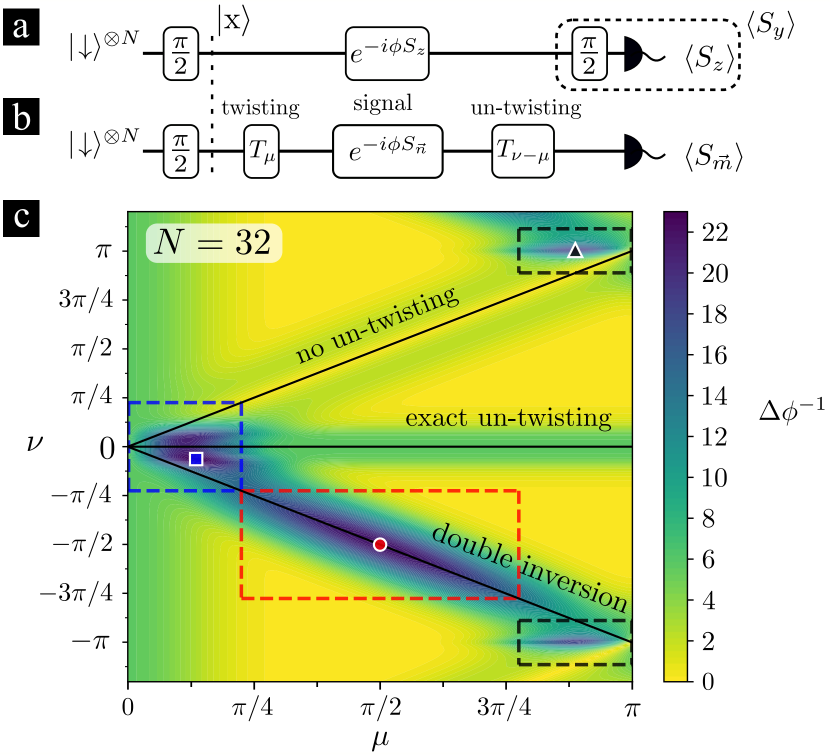

Figure 2.7: **Generalized Ramsey protocols:** **a** Conventional Ramsey interferometry. **b** Generalized Ramsey protocols with additional one-axis twisting T_μ and un-twisting $T_{\nu-\mu}$ dynamics, as well as arbitrary directions $\boldsymbol{n}$, $\boldsymbol{m}$ for the signal and measurement respectively. Optimizing over $\boldsymbol{n}$, $\boldsymbol{m}$ allows to extract the largest sensitivity, characterized by the initial squeezing strength μ and the inversion ν only. **c** Example of an optimized sensitivity landscape for the inverse phase variance $\Delta\phi^{-1}$ around $\phi = 0$ with $N = 32$. The boxes (dashed lines) highlight three distinct types of protocols we identified. At small μ the 'squeezing protocols' (blue), and at large squeezing strength the 'GHZ protocols' (black), which are known in the literature. In between, at an unusual double inversion of squeezing for $\nu = -\mu$, we find a new class of 'over-un-twisting protocols' (red). Colored symbols denote the local maxima in each class, the squeezing protocols (square), the OUT protocols (circle), and the GHZ protocols (triangle). Figure adapted from Schulte *et al.* [SMLSH20].

optimize general nonlinear measurement operators, we use the method in our work to find the optimal geometric factors for generalized echo protocols. It is interesting to note that only by this means the metrological gain of strongly entangled states, such as non-Gaussian states, could be shown in both works.

First, we re-express the two contributions, signal and noise, separately. For the signal strength we find

$$\left|\frac{\partial\langle S_{\boldsymbol{m}}\rangle}{\partial\phi}\Big|_{\phi=0}\right| = \boldsymbol{n}^T M \boldsymbol{m} \tag{2.56}$$

with $M_{kl} = i\langle[S_k(\mu), S_l(\nu)]\rangle_{|\phi=0}$, where we denoted transformed spin operators by $S_k(\mu) = T_\mu^\dagger S_k T_\mu$. Taking the absolute value in Eq. (2.56) comes with no loss of generality when optimizing the directions, as the sign of the slope can always be flipped by changing either $\boldsymbol{n} \to -\boldsymbol{n}$ or $\boldsymbol{m} \to -\boldsymbol{m}$. Likewise, the measurement variance can be expressed as

$$\left\langle(\Delta S_{\boldsymbol{m}})^2\right\rangle\Big|_{\phi=0} = \langle S_{\boldsymbol{m}}^2(\nu) - \langle S_{\boldsymbol{m}}(\nu)\rangle^2\rangle\Big|_{\phi=0} = \boldsymbol{m}^T Q \boldsymbol{m} \tag{2.57}$$

with $Q_{kl} = \left\langle\frac{1}{2}(S_k(\nu)S_l(\nu) + S_l(\nu)S_k(\nu)) - \langle S_k(\nu)\rangle\langle S_l(\nu)\rangle\right\rangle\Big|_{\phi=0}$. The matrices M and Q can be obtained analytically. The calculations in Appendix A give

$$M = \begin{pmatrix} \frac{1}{2}(n_1+n_2) & 0 & 0 \\ 0 & \frac{1}{2}(n_1-n_2) & n_3 \\ 0 & n_4 & 0 \end{pmatrix} \tag{2.58}$$

with

$$n_1 = \frac{N(N-1)}{2}\sin\left(\frac{\mu-\nu}{2}\right)\cos^{N-2}\left(\frac{\mu-\nu}{2}\right), \tag{2.59}$$

$$n_2 = -\frac{N(N-1)}{2}\sin\left(\frac{\mu-\nu}{2}\right)\cos^{N-2}\left(\frac{\mu+\nu}{2}\right), \tag{2.60}$$

$$n_3 = -\frac{N}{2}\cos^{N-1}\left(\frac{\mu}{2}\right),\ n_4 = \frac{N}{2}\cos^{N-1}\left(\frac{\nu}{2}\right). \tag{2.61}$$

For the spin covariances, the respective matrix is

$$Q = \begin{pmatrix} \frac{1}{2}(q_1+q_2) - q_0^2 & 0 & 0 \\ 0 & \frac{1}{2}(q_1-q_2) & q_3 \\ 0 & q_3 & q_4 \end{pmatrix} \tag{2.62}$$

with

$$q_0 = \frac{N}{2}\cos^{N-1}\left(\frac{\nu}{2}\right),\ q_1 = \frac{N(N+1)}{4},\ q_2 = \frac{N(N-1)}{4}\cos^{N-2}(\nu), \tag{2.63}$$

$$q_3 = \frac{N(N-1)}{4}\sin\left(\frac{\nu}{2}\right)\cos^{N-2}\left(\frac{\nu}{2}\right),\ q_4 = \frac{N}{4} \tag{2.64}$$

While seemingly a rather technical point, the fact that M and Q can be calculated exactly is crucial to an efficient optimization for arbitrary particle number N.

For a minimization of $\Delta\phi$ we instead aim to maximize the inverse phase deviation, i.e. the SNR, which is expressed as

$$\Delta\phi^{-1} = \frac{\boldsymbol{n}^T M \boldsymbol{m}}{\sqrt{\boldsymbol{m}^T Q \boldsymbol{m}}} \,. \tag{2.65}$$

Because Q is a positive semi-definite spin co-variance matrix, we can define the vector $\boldsymbol{v} = Q^{1/2}\boldsymbol{m}$ with $||\boldsymbol{v}|| = \sqrt{\boldsymbol{m}^T Q \boldsymbol{m}}$ and correspondingly $\boldsymbol{m} = Q^{-1/2}\boldsymbol{v}$. Note that Q is singular for $\nu = 0$ only. In this case, the optimization of rotation and measurement directions can be restricted to the plane perpendicular to the initial spin polarization. With the unit vector $\boldsymbol{u} = \boldsymbol{v}/||\boldsymbol{v}||$, the sensitivity is

$$\Delta\phi^{-1} = \boldsymbol{n}^T\, M\, Q^{-1/2}\, \boldsymbol{u}. \tag{2.66}$$

The right hand side of Eq. (2.66) can be optimized over all signal directions $\boldsymbol{n}$ and measurement directions $\boldsymbol{m}$ by a singular value decomposition $M\,Q^{-1/2} = U\mathbb{S}V^\dagger$, where U and V are orthogonal matrices and $\mathbb{S} = \mathrm{diag}(s_1, s_2, s_3)$ is the diagonal matrix containing the singular values. After this step, the optimized sensitivity depends exclusively on the initial squeezing strength μ and excess inversion ν. The maximal SNR is just the largest singular value and the ideal directions for signal and measurement, at each point (μ, ν), can be inferred from the two orthogonal matrices U and V. An example landscape of the optimal SNR

$$\Delta\phi^{-1}(\mu, \nu) = \max_{\boldsymbol{n},\boldsymbol{m}} \Delta\phi^{-1}(\mu, \nu, \boldsymbol{n}, \boldsymbol{m}) \tag{2.67}$$

is shown in Fig. 2.7**c**. We point out that the relatively small particle number, $N = 32$, is motivated to easily highlight important features of the landscape. With the analytic expressions, computational time is independent of N and we show the landscapes for different values of N, up to $N = 1024$, in Fig. 2.8.

In view of Fig. 2.7**c** mainly three separate regions exist in which an amplified SNR is achieved: *(i)* The first region (blue box) includes protocols with small squeezing strengths $|\mu|, |\nu| \lesssim 4/\sqrt{N}$. We refer to such cases as ‘squeezing protocols’, because this is the only region that contains initial states exhibiting reduced spin fluctuations while still maintaining significant polarization (see section 2.4.2). Note however that this usual intuition is no longer exclusive for all states contained in the ‘squeezing protocols’. Already at $\mu \gtrsim 2/\sqrt{N}$ the states generated by OAT enter the regime of so called oversqueezed states, which wrap around the Bloch sphere. From this point on spin squeezing is lost according to the Wineland squeezing parameter, i.e. $\xi > 1$ [WBI+92, WBIH94]. Again, ξ is connected to our figure of merit without any echo

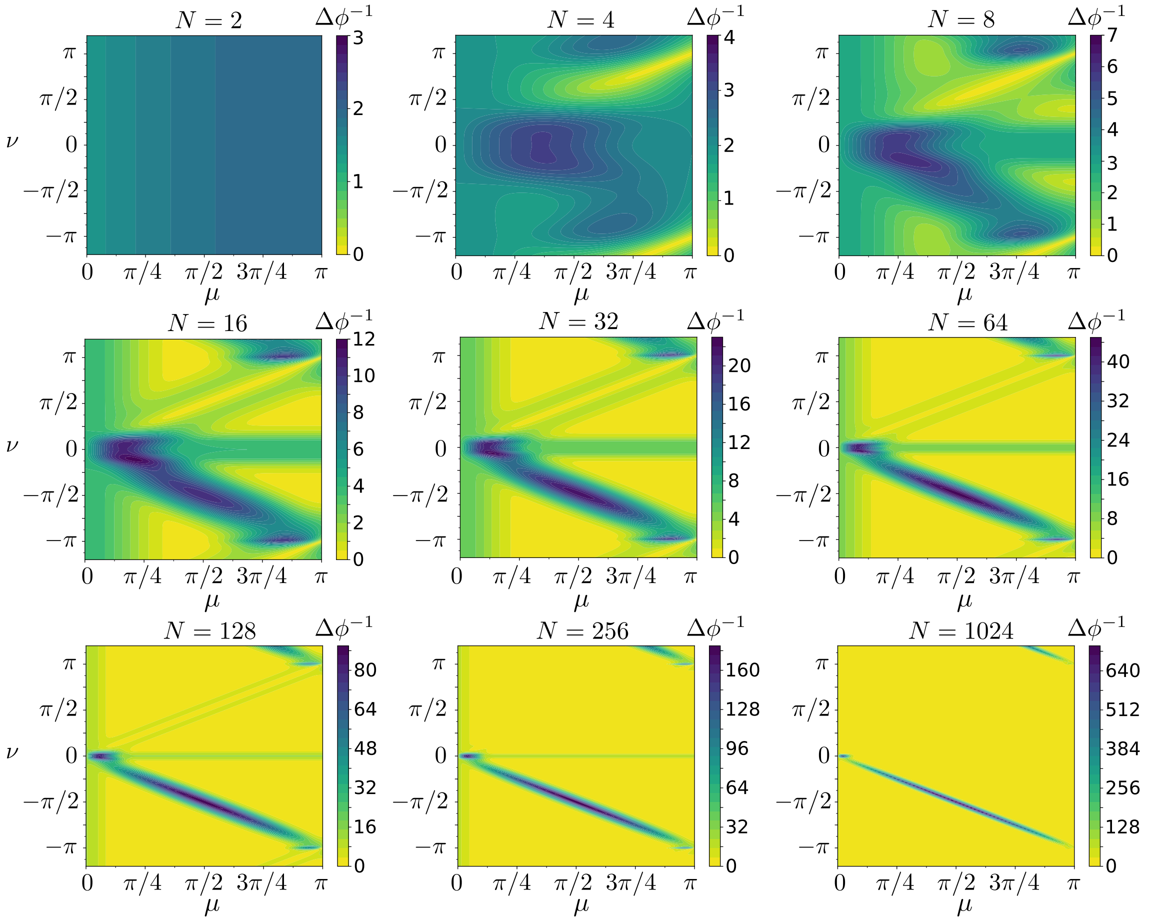

Figure 2.8: **Landscapes for larger N:** Generalized Ramsey protocols for $N = 2 - 1024$.

($\nu = \mu$) by $\xi^2 = N\Delta\phi^2(\mu, \mu)$. While the original classification, based on the squeezing parameter ξ, fails with the application of echoes, we find that the characteristic scaling $\mu \sim 1/\sqrt{N}$ of the squeezing region remains valid for the generalized protocols. Note that the failure of the usual argument is also visible in the μ-ν-landscapes we show. Compare for example the position of maximum sensitivity along the $\nu = \mu$ line with the local maximum over all squeezing protocols (blue square) in Fig. 2.7 **c**. The additional factor of two in the condition $|\mu|, |\nu| \lesssim 4/\sqrt{N}$ was introduced here to place the cutoff close to the minimum that lies between the local maximum at small squeezing strength and the broad maximum around $\mu = \pi/2$.

As a special case of ‘squeezing protocols’ we recover the classic Ramsey protocols with squeezed initial states and no un-squeezing ($\nu = \mu$) along with their known optimal signal and measurement directions [KU93]. We also find optimized exact echo protocols, on the horizontal line at $\nu = 0$, for initial squeezing strengths $\mu \sim 2/\sqrt{N}$.

The optimal directions converge to $\boldsymbol{n} = \boldsymbol{e}_y$ and $\boldsymbol{m} = \boldsymbol{e}_y$ for $N \gg 1$.[1] This proves optimality for the choices of signals and measurements made by Davis *et al.* [DBSS16]. Interestingly, we find that within the class of squeezing protocols the local maximum in sensitivity is reached at values of ν which do not correspond to either of these known protocols. It rather lies at an intermediate value of ν. *(ii)* The second region (black box) exhibiting enhanced sensitivity exists at large squeezing strength, $\pi - 4/\sqrt{N} \leq \mu \leq \pi$. It contains highly entangled states, close to the GHZ state, so that we refer to these as 'GHZ protocols'. Note that the enhancement of GHZ states is ideally obtained with parity measurements. Recently, approaches using the measurement of spin projections and an additional squeezing interaction were discussed by Leibfried *et al.* [LBS+04, L+05b]. *(iii)* Finally, we find exactly one more region (red box, with $4/\sqrt{N} < \mu < \pi - 4/\sqrt{N}$), corresponding to a new type of protocols that are characterized by a double inversion of the OAT, at $\nu = -\mu$. We refer to these as 'over-un-twisting' (OUT) protocols. The enhancing mechanism there is conceptually different from the squeezing protocols and is discussed further below. The initial states in this class are regarded as oversqueezed or non-Gaussian states [SML+14]. So far, the entanglement in this region was first captured by the quantum Fisher information [PS09] or later in terms of nonlinear squeezing parameters [GSP19].

Closing the discussion of special cases we note that one does not see the standard GHZ interferometry at $\mu = \pi$, $\nu = 0$ in Fig. 2.7 **c**. This is due to the fact that within our variational class the signals of these protocols, oscillating as $\langle S_{\boldsymbol{m}} \rangle(\phi) \propto \cos(N\phi)$, have a local maximum at $\phi = 0$. The standard GHZ interferometry can, on paper, compensate for the vanishing slope with an also vanishing QPN such that the SNR in the limit $\phi \to 0$ is still a finite value. However, for numerical stability of the singular value decomposition, we have prohibited 0 variance by adding a tiny offset to the variance of any spin projection. This also makes sense from a practical point of view as a vanishing projection noise would require perfect measurement contrast. In experiments, this problem is bypassed by placing the observed signal at mid fringe with an additional controlled rotation, causing $\phi \to \phi - \frac{\pi}{2N}$. But such a static phase shift lies beyond the possibilities of the variational class defined here. However, it can be done with even further generalization of the protocols (see section 2.10.3).

2.7 Dephasing noise

To see which protocols actually correspond to a robust enhancement, we now add dephasing during the OAT. In the presence of collective dephasing, at a rate $\gamma_C > 0$, the dynamics of the system will be governed by the master equation

---

[1] Deviations from these directions are basically insignificant, even at low particle numbers N. They are, for example, on the order of $\boldsymbol{n} = (0, 0.93, 0.37)^T$ and $\boldsymbol{m} = (0, 0.98, -0.22)^T$ at $N = 16$.

$$\dot{\rho} = -i[H, \rho] + \gamma_C \mathcal{L}_C[\rho] \tag{2.68}$$

with $H = \chi S_z^2$ and $\mathcal{L}_C[\rho] = S_z \rho S_z - \frac{1}{2} S_z^2 \rho - \frac{1}{2} \rho S_z^2$. The noise strength is quantified by the dimensionless parameter $\sigma = |\gamma_C|/|\chi|$. In cavity induced squeezing of atoms, dephasing of this kind happens due to photon shot noise [DBSS16], causing fluctuations in the direction of the states' collective spin vector. For quantum gates with trapped ions, dephasing occurs through random variations of the transition frequency from stray fields or from frequency noise of the driving fields. When uniform over the extend of the ion string, both result in collective dephasing [KMR+01, RCK+06]. With spinor Bose-Einstein condensates, collective dephasing may also arise from magnetic field fluctuations [PSO+18].

The geometrical optimization with respect to $\boldsymbol{n}$ and $\boldsymbol{m}$ can still be performed analytically, also when including dephasing. See appendix A.2 for the technical details. Figure 2.9 **a** shows the sensitivity including collective dephasing with $\sigma = 0.1$. Compared to the ideal case, shown in Fig. 2.7 **c**, we see that any enhancement of the GHZ protocols is strongly suppressed by the noise. Furthermore, within the squeezing protocols a bias towards $\nu \approx \mu$ is developing, as protocols with reduced additional inversion suffer less from dephasing. Surprisingly, the large maximum of OUT protocols remains only weakly affected by preparation noise and still offers large enhancement. To emphasize this, Fig. 2.9 **b** displays the measurement-optimized sensitivity, $\max_\nu (\Delta\phi^{-2}(\mu, \nu)/N)$, as a function of the initial squeezing for various levels of dephasing. Performing the optimization over all measurements within our protocols also allows to compare the obtained SNR to fundamental limits of quantum metrology (see section 2.4.3). Most notably, Eq. (2.52) implies

$$\max_\nu \Delta\phi^{-2}(\mu, \nu) \leq \mathcal{F}_Q, \tag{2.69}$$

following from the quantum Cramér-Rao bound. The upper limit $\mathcal{F}_Q$ is the quantum Fisher information, which quantifies the maximum information about the phase ϕ that can possibly be inferred from the initial state and the interferometer transformation with $S_{\boldsymbol{n}}$. The quantum Fisher information thereby includes an optimization over all measurements, containing weak measurements, individual operations on each particle, parity and others, which go beyond what is possible with the resources considered here. The black, solid line in Fig. 2.9 **b** shows the quantum Fisher information limit, given by Eq. (2.49) for OAT, in comparison to the SNR. As a function of the squeezing strength, $\mathcal{F}_\mathrm{Q}$ increases from the standard quantum limit $\mathcal{F}_\mathrm{Q} = N$ of uncorrelated particles, at $\mu = 0$, up to the Heisenberg limit $\mathcal{F}_\mathrm{Q} = N^2$, at $\mu = \pi$. Even though the quantum Fisher information constitutes a true extension over the capabilities of the

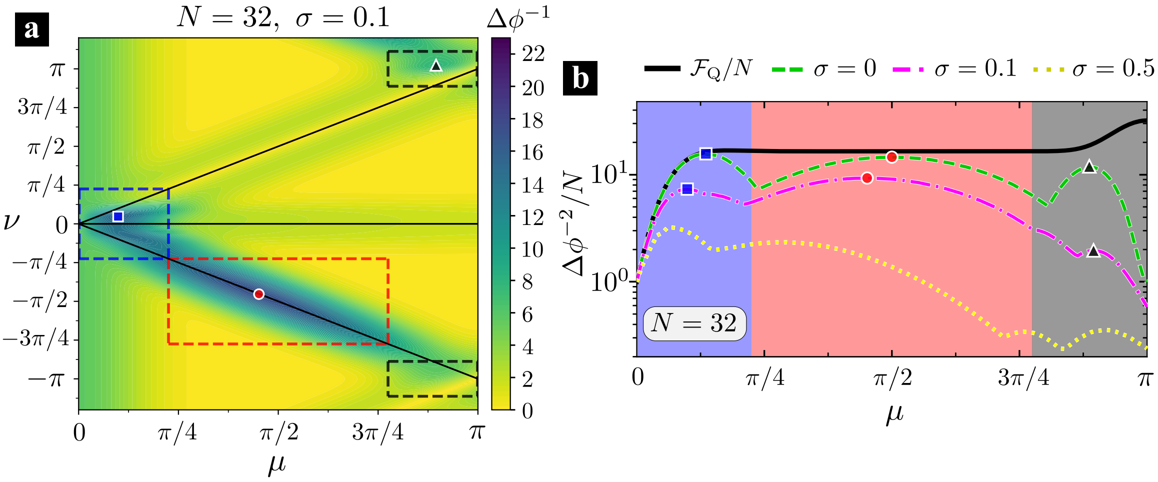

Figure 2.9: **Sensitivity with dephasing:** **a** Sensitivity $\Delta\phi^{-1}$ for $N = 32$ with $\sigma = 0.1$ collective dephasing noise during the state preparation and inversion. As compared to Fig. 2.7 **c**, changes in the positions of optimal protocols (symbols) as well as an overall reduction in sensitivity can be observed. **b** SNR with optimized inversion, $\max_\nu \Delta\phi^{-2}(\mu,\nu)/N$, for different levels of collective dephasing noise $\sigma = 0,\ 0.1,\ 0.5$. Colored areas mark the squeezing, OUT and GHZ protocol types. The black line is the scaled quantum Fisher information $\mathcal{F}_Q/N$ of the ideal initial squeezed state, i.e. $\sigma = 0$. We find three peaks corresponding to the optimal squeezing, over-un-twisting and GHZ protocols. Symbols on the green dashed line represent the optimal protocols of Fig. 2.7 **c** while symbols on the magenta dash-dotted line correspond to part **a**. Figure adapted from Schulte *et al.* [SMLSH20].

protocols considered here, we nevertheless find that the OUT protocols actually reach the quantum Fisher information bound with increasing N. This feature persists for small collective dephasing as well. The only other case where this holds true is for $\mu \ll 1$. However, at extreme levels of noise also the OUT protocols fall short compared to the quantum Fisher information limit. Figure 2.10 illustrates the comparison to fundamental limits for different N, adding also the QFI for an initial state with some collective dephasing. In the case of collective qubit dephasing, in the form of the master equation (2.68), the density matrix can be expressed in the Dicke basis as

$$\rho = \sum_{m,m'=-N/2}^{N/2} e^{-i(m^2-m'^2)\mu/2-\sigma(m-m')^2|\mu|/4}\, c_m(\theta,\varphi)c^*_{m'}(\theta,\varphi)\,|m\rangle\langle m'| \tag{2.70}$$

with the coefficients [ACGT72]

$$c_m(\theta,\varphi) = \binom{N}{N/2+m}^{1/2} \sin^{N/2+m}(\theta/2)\cos^{N/2-m}(\theta/2)e^{-i(N/2+m)\varphi} \tag{2.71}$$

of the coherent spin state $|\theta,\varphi\rangle$. Now the quantum Fisher information for the dephased initial state can be evaluated by numerically diagonalizing ρ based on

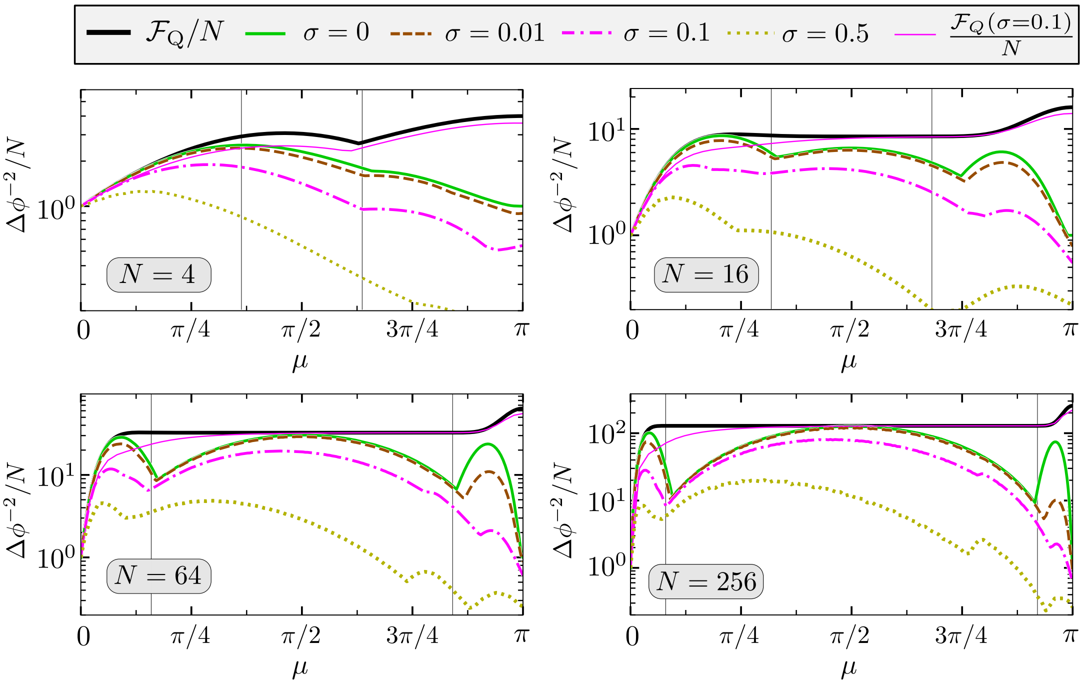

Figure 2.10: **Overview of sensitivity with collective dephasing:** The solid black line is the quantum Fisher information for an ideal OAT state, while the thin magenta line is the quantum Fisher information of the state with collective dephasing $\sigma = 0.1$ in the initial state preparation. This shows that the noisy quantum Fisher information limit is reached for stronger dephasing only at $\mu \ll 1$. Vertical lines mark the transitions from the squeezing region to the OUT region and to the GHZ region.

Eq. (2.70) and optimizing the right hand side of Eq. (2.47), with $H = S_{\boldsymbol{n}}$, over all directions $\boldsymbol{n}$.

Due to the exact optimization, established in section 2.6, we are also able to efficiently examine the influence of dephasing on the particle number scaling of the sensitivity. Figure 2.11 **a-c** show the scalings for $\sigma = 0, 0.01, 0.5$. Symbols mark the best sensitivity within each protocol type, while lines show numerical fits to an asymptotic scaling $\Delta\phi^{-1} = cN^{\alpha}$ with fitting parameters c and α. The green region reflects sensitivity beyond the Heisenberg limit $\Delta\phi^{-2} > N^2$ and the grey region sensitivity below the standard quantum limit $\Delta\phi^{-2} < N$. We find that, remarkably, the OUT protocols always exhibit Heisenberg scaling, $\Delta\phi^{-1} \propto N$, independent of the dephasing. On the other hand the GHZ protocols quickly drop to the classical scaling, showcasing their increased susceptibility in this regard. The dependence of the exponent α on the noise strength is shown in Fig. 2.11**d**, highlighting the characteristic differences regarding the influence of collective dephasing. Although the squeezing protocols have a reduced scaling exponent compared to OUT protocols, they may still be the overall best protocols when limited to small ensembles and larger

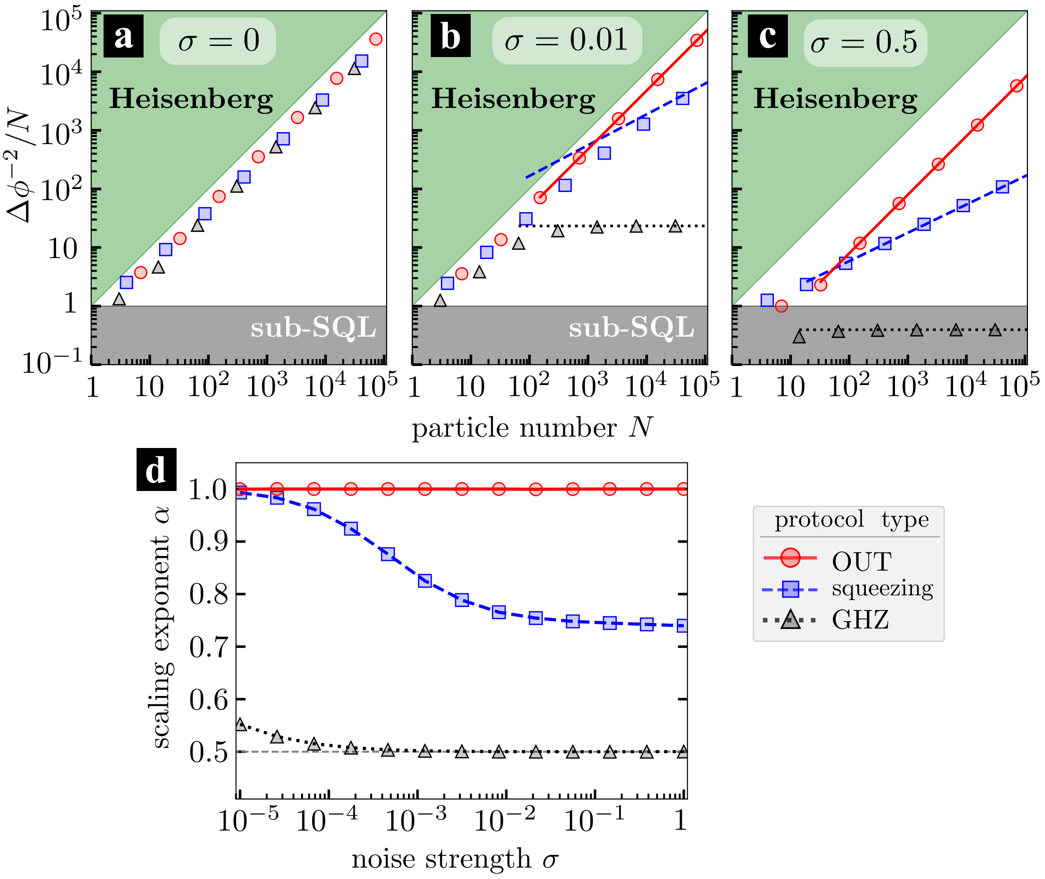

Figure 2.11: **Scaling of the sensitivity with N: a-c** Sensitivity under collective dephasing, with $\sigma = 0, 0.01, 0.5$, for squeezing (blue), OUT (red) and GHZ (black) protocols as a function of the particle number N. The green region shows sensitivity beyond the Heisenberg limit, $\Delta\phi^{-2} > N^2$, and the grey region sensitivity below the standard quantum limit, $\Delta\phi^{-2} < N$. Lines are fits of the local optima to an asymptotic scalings $\Delta\phi^{-1} = c\,N^{\alpha}$ at large N. Note that a flat line thus still means improvement with N, however, only at the classical scaling $\Delta\phi^{-2} \propto N$. **d** Scaling exponent α as a function of noise strength. Figure adapted from Ref. [SMLSH20].

dephasing, cf. Fig. 2.11**c**. Our findings also show that initially the scaling may deviate significantly from the asymptotic case, even up to ensembles of considerable size.

In addition to collective dephasing, we further study individual dephasing during the OAT interactions. Compared to Eq. (2.68), the master equation is

$$\dot{\rho} = -i[H, \rho] + \gamma_I \mathcal{L}_I[\rho], \tag{2.72}$$

where $\mathcal{L}_I[\rho] = \sum_{k=1}^{N} \sigma_z^{(k)} \rho \sigma_z^{(k)} - \rho$. This describes individual, but symmetric, dephasing of each atom at a rate $\gamma_I > 0$, and we likewise define $\Sigma = |\gamma_I|/|\chi|$. It turns out that individual dephasing results in a less stringent restriction on sensitivity than collective dephasing of the same strength. The sensitivity for all protocol types scales asymptotically linearly in N, independent of the value of Σ, as shown in Fig. 2.12. In this case, the squeezing protocols are optimal, as the prefactor to their scaling is least affected by the individual dephasing.

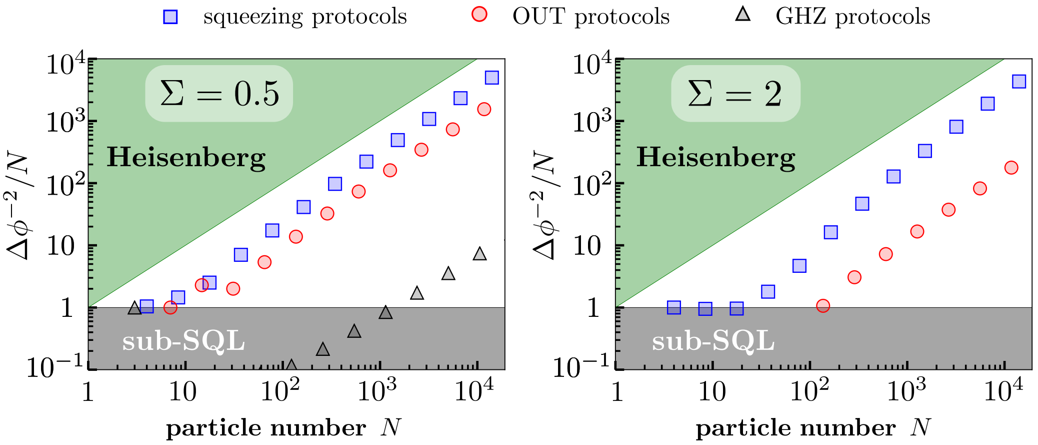

Figure 2.12: **Effects of individual dephasing:** Sensitivity versus particle number for individual dephasing during the OAT interactions with strength $\Sigma = 0.5$ and extreme dephasing at $\Sigma = 2$. Figure reproduced from Schulte *et al.* [SMLSH20].

2.8 Over-un-twisting enhancement

In this last section we give an explanation of the mechanism underlying the OUT protocols. To visualize the sensitivity enhancement we split the protocols into a state evolution and an effective measurement part. As shown in the schematic of Fig. 2.13, we group one half of the double inversion to the state evolution and the other half to the measurement. Now, for the optimal OUT protocol, first a superposition of four coherent spin states along the equator of the collective Bloch sphere is generated by T_μ with $\mu = \frac{\pi}{2}$ [APS97]. The corresponding Wigner function is shown in the top row of Fig. 2.13. A small rotation around the y-axis perturbs the following exact inversion of OAT in such a way that interference patterns remain on the sides of a large polarization contribution in x-direction. The absolute values of these patterns increase for larger rotation angles ϕ, or with increasing N, when keeping $\phi \ll 1$ fixed. The signs of the interference patterns change only when rotating in the opposite direction, i.e. $R_y(-\phi)$ instead of $R_y(\phi)$. The second part of the OUT protocols can be viewed as a transformation of the applied measurement. The bottom row in Fig. 2.13 shows that the twisting dynamics on S_y leads to a Wigner function for the operator $P := T^\dagger_{\pi/2} S_y T_{\pi/2}$ with rapid sign changes, wrapping around the Bloch sphere. Larger values of N have narrower spacing of the interference patterns with increased maximal and minimal values of the Wigner function, thus giving an enhanced signal, cf.

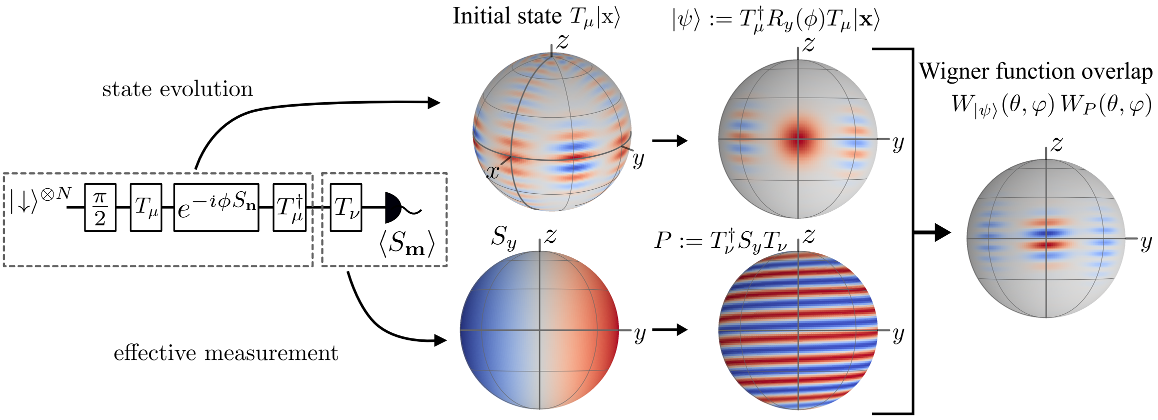
state evolution
$|\downarrow\rangle^{\otimes N}$
$\frac{\pi}{2}$
T_μ
$e^{-i\phi S_{\mathbf{n}}}$
$T_\mu^\dagger$
T_ν
$\langle S_{\mathbf{m}}\rangle$
effective measurement
Initial state $T_\mu|\mathrm{x}\rangle$
$|\psi\rangle := T_\mu^\dagger R_y(\phi) T_\mu |\mathbf{x}\rangle$
Wigner function overlap
$W_{|\psi\rangle}(\theta,\varphi)\, W_P(\theta,\varphi)$
S_y
$P := T_\nu^\dagger S_y T_\nu$
z
x
y

Figure 2.13: **Illustration of over-un-twisting protocols:** Wigner function representation for the optimal over-un-twisting protocol at $\mu = \frac{\pi}{2}$, $\nu = -\frac{\pi}{2}$, here with $N = 32$. Half the OAT inversion is assigned to the state evolution, the other half to the measurement operator. State evolution (top): Starting from the superposition of four coherent states along the equator, a small rotation around $\boldsymbol{n} = \boldsymbol{e_y}$ (here $\phi = -0.02$), followed by exact OAT inversion, leads to the state $|\psi\rangle$ with large polarization in x-direction and residual interference patterns due to the disturbance of the rotation. Effective measurement (bottom): OAT of the optimal measurement direction $S_{\boldsymbol{m}} \approx S_y$ creates dense sequences of positive and negative values in its Wigner function. These match exactly the pattern on $|\psi\rangle$, so that in the overlap of the two Wigner functions the interference patterns are either all positive or all negative, depending on the sign of ϕ. Integrating the overlap over the sphere results in the measurement signal $\langle S_y\rangle(\phi)$. Figure adapted from Schulte *et al.* [SMLSH20].

Fig. 2.14 **a**. The density of patterns increases in the same way with N for both the state $|\psi\rangle$ and the measurement operator P. So, importantly, the interference patterns of the two Wigner functions match exactly. It is interesting to note that the Wigner functions show similarities to a Moiré pattern as well as Gottesman-Kitaev-Preskill states [GKP01, DTW17]. Due to the matching Wigner functions, in the product all oscillations contribute with either a positive or a negative sign, depending on the sign of the rotation. The mean value $\langle S_y\rangle = \int_0^\pi \mathrm{d}\theta \int_0^{2\pi} \mathrm{d}\varphi \sin(\theta) W_{|\psi\rangle}(\theta,\varphi) W_P(\theta,\varphi)$ then corresponds to the integral over the sphere for the product of the Wigner functions [Aga81, DAS94]. This shows N times faster oscillations, compared to uncorrelated atoms, for even N. For odd N, the signal has a sharp initial incline, before vanishing after a few oscillations, see Fig. 2.14 **b**. Although this distinction is relevant for larger phases, away from $\phi = 0$, the sensitivity $\Delta\phi$, the optimal signal direction, and the optimal measurement direction all remain a continuous function of N. Thus, for the OUT protocols no additional information about the particle number is necessary. This is a consequence of the fact that we study and optimize the sensitivity at $\phi = 0$.

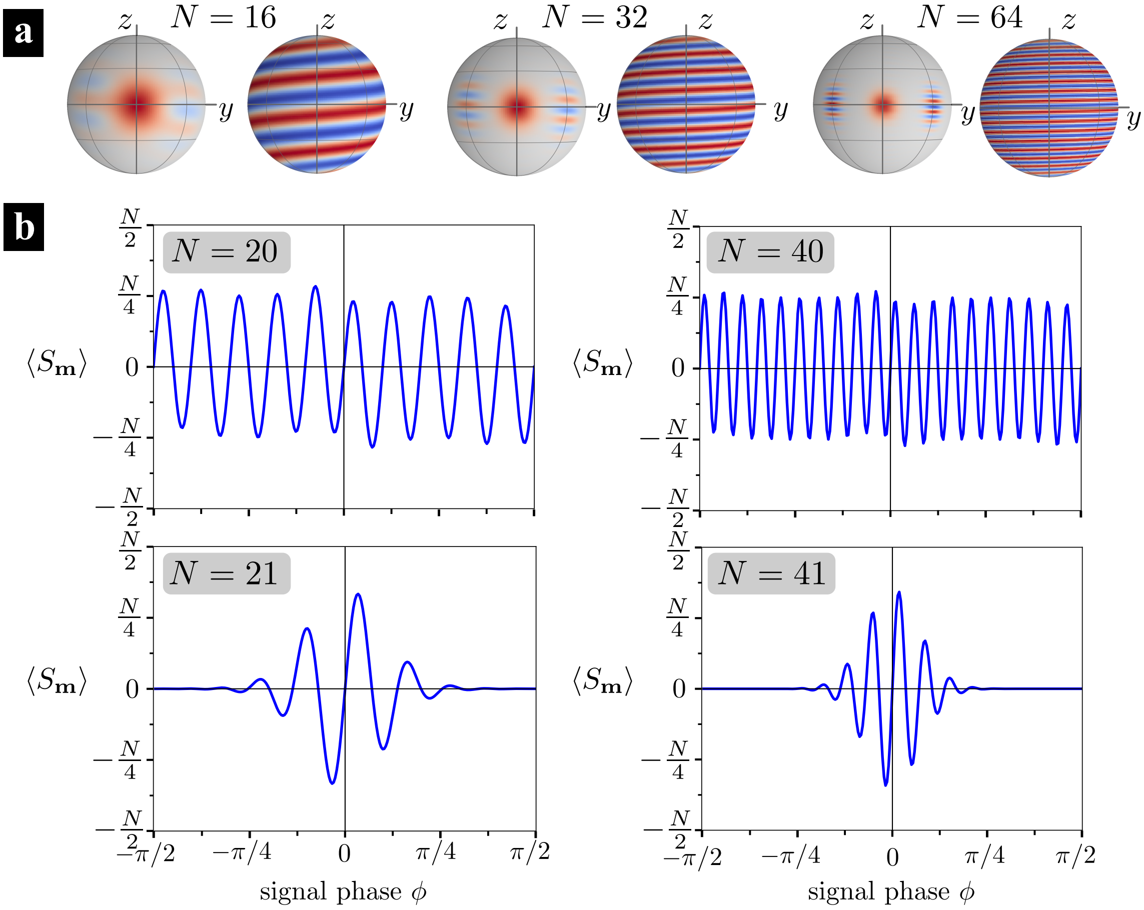

Figure 2.14: **Over-un-twisting signal:** **a** Finer features appear on the Wigner functions for the state $|\psi\rangle = T^{\dagger}_{\pi/2} R_y(\phi) T_{\pi/2} |\mathrm{x}\rangle$ (always left) and the measurement operator $T^{\dagger}_{-\pi/2} S_y T_{-\pi/2}$ (always right) when increasing N. **b** OUT signals beyond $\phi \ll 1$. Even particle numbers show an N-fold increased oscillation frequency, whereas odd particle numbers experience a large slope at $\phi = 0$ and subsequent attenuation.

2.9 Summary

In conclusion, we presented an analytic theory for the geometric optimization of generalized echo protocols at any particle number and dephasing. The method of optimization was already treated in Ref. [GSP19] by Gessner, Smerzi and Pezzè. Using these results, we are able to give a comprehensive overview and characterization of the variational class of echo protocols in terms of the (un-)squeezing strengths. We find that only one new protocol exists. This protocol, the over-un-twisting protocol, stands out as it exhibits Heisenberg scaling in the sensitivity even for strong dephasings during the OAT interaction. Remarkably, the effectively nonlinear readout performs almost as well as the quantum Fisher information limit in this case. This can be considered one of the most important findings of this chapter. In a broader context, our results provide a route towards quantum enhanced measurements away from the typical squeezing regime or GHZ states, while still using measurements of spin projections only.

2.10 Outlook

2.10.1 Comments on imperfections

Beyond the scope of this thesis, non-ideal signal and measurement directions or the impact of other imperfections, such as noise during the phase imprint, can be studied. The former is not expected to reduce sensitivity much for directions close to the optimal ones, due to the predominant contribution of the largest singular value. The exact consequences of the latter often depend on a number of other factors and would require additional modelling. For example, a more precise modelling of the physical system at hand, the duration of the Ramsey dark time, as well as the type and strength of the noise. It is known that beyond some critical ensemble size, noise during the signal acquisition reduces the scaling of quantum metrological amplification to the standard (classical) scaling of independent particles [EdMFD11, DDKG12]. This behavior is also expected for our protocols, most notably for the highly entangled states beyond the squeezing regime. In most cases, however, it is the absolute performance at a given N which matters and not the scaling. We therefore believe that the trade-off between quantum projection noise and technical noise, specific to each sensor, must be studied to understand in which cases entanglement is actually useful for metrological improvements [SLS$^+$19]. One example of this is the detailed modelling of noise sources and limitations in optical atomic clocks, which we discuss in chapter 3.

2.10.2 G-asymmetry and information content

A key assumption of the measures of sensitivity considered so far is locality in the sense that only variances and derivatives at $\phi = 0$ are evaluated. This is true for the squeezing parameter ξ, the phase variance $\Delta\phi$, and the (quantum) Fisher information. They all result from an analysis of the estimation process around a fixed working point. This closely relates to a scenario with an unknown but constant phase ϕ. For such a static estimation problem it is possible to get prior information about the approximate value of ϕ, for example through previous measurements with lower resolution. Using that prior information allows to perform the final measurement with highest accuracy always under the assumption of locality. The ultimate precision in this scenario would therefore be indeed well represented by the squeezing parameter or the (quantum) Fisher information. However, there are often cases where the phase cannot be considered stationary. Important applications of this are phase tracking and waveform estimation in optical interferometers [Y+12, TWC11, BHW13], which is used in the detection of gravitational waves, or the closed feedback loop in atomic clocks. In these cases the trade-off between measurement precision and bandwidth has to be considered. Nevertheless, general limits have been developed for fluctuating parameters in analogy to the quantum Cramér-Rao limit. With methods from (quantum) information theory, it can be shown that the average estimation error is limited by a combination of (i) an entropic measure of the degree to which the probe state ρ_ϕ can encode a phase value, called the G-asymmetry, and (ii) any prior information about the phase shift [HW12]. We briefly recapitulate the logic presented in that work.

Let Φ be a shift parameter which for a specific value ϕ generates the state $\rho_\phi = e^{-i\phi G}\rho_0 e^{i\phi G}$, as given by the general interferometer transformation (2.17). For any estimate $\check{\Phi}$, the average estimation error is defined as

$$\epsilon_{\text{av}} = \sqrt{\mathbb{E}[(\check{\Phi} - \Phi)^2]}, \tag{2.73}$$

where the expectation value is

$$\mathbb{E}[(\check{\Phi} - \Phi)^2] := \int_{-\infty}^{\infty} \mathrm{d}\phi \, \mathrm{d}\check{\phi} \; (\check{\phi} - \phi)^2 \; p(\check{\phi}|\phi) \; \mathscr{P}(\phi). \tag{2.74}$$

Here $p(\check{\phi}|\phi)$ is the conditional probability of the estimate $\check{\phi}$ for a specific phase shift $\Phi = \phi$, and $\mathscr{P}(\phi)$ denotes the prior distribution of the phase shift parameter. Conceptually ϵ_{av} is related to an average of the local sensitivity $\Delta\phi$ over the prior distribution. A quantum information bound on the resolution of phase shifts is given by [HW12]

$$\epsilon_{\text{av}} \geq (2\pi e)^{-1/2} e^{\mathscr{H}[\Phi]} e^{-A_G[\rho_0]}, \tag{2.75}$$

where $\mathscr{H}[\Phi] = -\int_{-\infty}^{\infty} \mathscr{P}(\phi) \ln(\mathscr{P}(\phi)) \, \mathrm{d}\phi$ denotes the differential entropy of the prior distribution and $A_G[\rho_0]$ is the asymmetry of the state ρ_0 with respect to the unitary group G. Explicitly, the G-asymmetry is defined as

$$A_G[\rho_0] := \mathcal{S}\left(\sum_g \Pi_g \rho_0 \Pi_g\right) - \mathcal{S}(\rho_0), \tag{2.76}$$

where $\mathcal{S}(\rho) = -\mathrm{tr}[\rho \ln(\rho)]$ denotes the von Neumann entropy, and Π_g is the projection operator onto the eigenspace corresponding to eigenvalue g of G. Using the Holevo bound [NC09] and properties of the von Neumann entropy, it can be shown that the

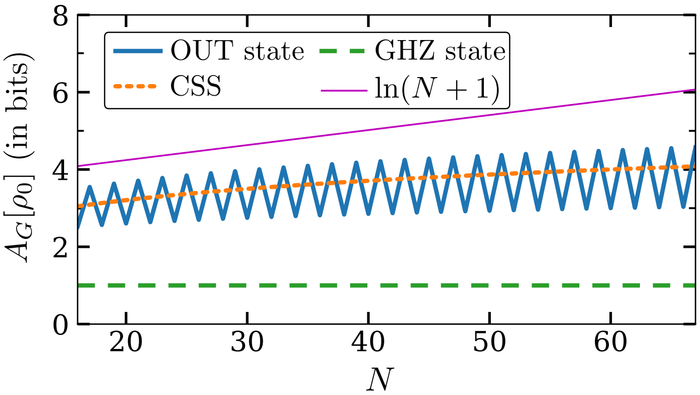

Figure 2.15: **G-asymmetry:** Comparison of the G-asymmetry for the OUT protocol, a coherent spin state (CSS) and the GHZ state. As an additional reference value $\ln(N+1)$ is shown. This is the largest possible asymmetry, as $A_G[\rho_0] \leq \ln(N+1)$ for any state ρ_0.

G-asymmetry is an upper bound to the mutual information $H(\check{\Phi} : \Phi)$ between the phase shift parameter and its estimate, i.e.

$$H(\check{\Phi} : \Phi) \leq A_G[\rho_0]. \tag{2.77}$$

This bound holds for any generator G with a discrete spectrum [HW12]. It is this step where an implicit optimization over all estimation strategies and all POVM elements, describing generalized measurements, is done. Note the similarity to the two-step optimization of the quantum Cramér-Rao bound combined with the quantum Fisher information, described in section 2.4.3, for local estimation. Equation (2.77) also gives an interpretation to the G-asymmetry by being an upper bound to the average information gained per estimate, as quantified by the mutual information $H(\check{\Phi} : \Phi)$.

Looking at Eq. (2.75), one can see that a small average estimation error is only attainable with both a narrow prior and a large G-asymmetry. The bound also nicely shows the exchange between the average information obtained per estimate and the required prior information. For example if one considers the GHZ state $|\psi_0\rangle = \frac{|-N/2\rangle + |N/2\rangle}{\sqrt{2}}$ under a transformation with $G = S_z$, the asymmetry $A_G[\rho_0] = \ln(2)$ results [HW12], or $A_G[\rho_0] = \log_2(2)\,\text{bits} = 1\,\text{bit}$ in units of information. So in this case, only one classical bit of information is gained per measurement. The only possibility to achieve an uncertainty $\sim N^{-1}$ in Eq. (2.75) for the GHZ state is then if $-\mathscr{H}[\Phi] \sim \ln N$, i.e. the known prior already determines the parameter to N bits. In contrast, the quantum Cramér-Rao bound in Eq. (2.42) only implies that the phase can be estimated around a fixed point with high precision due to the large QFI, $\mathcal{F}_Q = N^2$ for the GHZ state. Note, however, that Eq. (2.75) has no immediate implication for the case of a fixed phase, i.e when looking at the limit of very narrow priors. This can be seen by considering a Gaussian prior $\mathscr{P}(\phi) = \frac{1}{\sqrt{2\pi s^2}} e^{-\frac{\phi^2}{2s^2}}$ with variance s. In this case, the differential entropy $\mathscr{H}[\Phi] = \ln(s) + \frac{1}{2}(\ln(2\pi)+1)$ tends to $-\infty$ for $s \to 0$ and gives the trivial bound $\epsilon_{\mathrm{av}} \geq 0$ in Eq. (2.75), independent of what $A_G[\rho_0]$ is. This is why large G-asymmetry is not a necessary requirement for good local precision and even the low information content of a single bit of information of the GHZ state still suffices for local measurements.

Having seen that the OUT protocols achieve a similar N-fold increase in the oscillation frequency of the measurement signal as GHZ-state-based protocols, but without requiring parity measurements, suggests that the state conveys much more information than a single bit. To quantify this conjecture, the upper bound $A_G[\rho_0]$ is evaluated for OUT protocols with $G = S_y$, which is close to the optimal direction for increased N. The results can be seen in Fig. 2.15. We find that the information content is similar to what is achieved with coherent spin states and in stark contrast to GHZ states, which return only a single bit of information. The fact that we find an increased information gain, as well as a large local sensitivity, is a compelling property of this novel type of protocol. Interestingly, $A_G[\rho_0]$ depends on even and odd particle number for the OUT protocol, similar to the oscillating features of the full measurement signal. Even though the optimal directions do not change this drastically between even and odd N. Compared to the upper limit $\max_{\rho_0} A_G[\rho_0] = \ln(N+1)$ that the G-asymmetry can take, all states compared here still fall short.

2.10.3 Larger variational class

The selected variational class, presented first in section 2.5, proved to be quite general and convenient, due to the fully analytical optimization. But it still allows to add more degrees of freedom, which we explore briefly at this point. This can be viewed again as a broader specification for the general encoding and decoding operations $\mathcal{U}_{\mathrm{en}}, \mathcal{U}_{\mathrm{de}}$, introduced in section 2.4. Sticking to the usual OAT initial states, one has e.g. the option of adding another collective spin rotation before or after the phase imprint. This would generate signals with

$$\langle S_{\boldsymbol{m}} \rangle(\phi) = \langle \mathrm{x} | T_\mu^\dagger \, R_{\boldsymbol{v}}^\dagger \, R_{\boldsymbol{n}}^\dagger(\phi) \, T_{\mu_2}^\dagger \, S_{\boldsymbol{m}} \, T_{\mu_2} \, R_{\boldsymbol{n}}(\phi) \, R_{\boldsymbol{v}} \, T_\mu | \mathrm{x} \rangle \tag{2.78}$$

or

$$\langle S_{\boldsymbol{m}} \rangle(\phi) = \langle \mathrm{x} | T_\mu^\dagger \, R_{\boldsymbol{n}}^\dagger(\phi) \, R_{\boldsymbol{v}}^\dagger \, T_{\mu_2}^\dagger \, S_{\boldsymbol{m}} \, T_{\mu_2} \, R_{\boldsymbol{v}} \, R_{\boldsymbol{n}}(\phi) \, T_\mu | \mathrm{x} \rangle \tag{2.79}$$

with some additional rotation $R_{\boldsymbol{v}}$ (see Fig. 2.16**a**). Coming back to the typical GHZ protocols, we remark that these extensions now enable the required shifts of the working point $\phi \to \tilde{\phi}$, by choosing $\boldsymbol{v} = \boldsymbol{n}$ and the correct rotation angle. Both scenarios, Eq. (2.78) and Eq. (2.79), are mathematically equivalent to a rotation

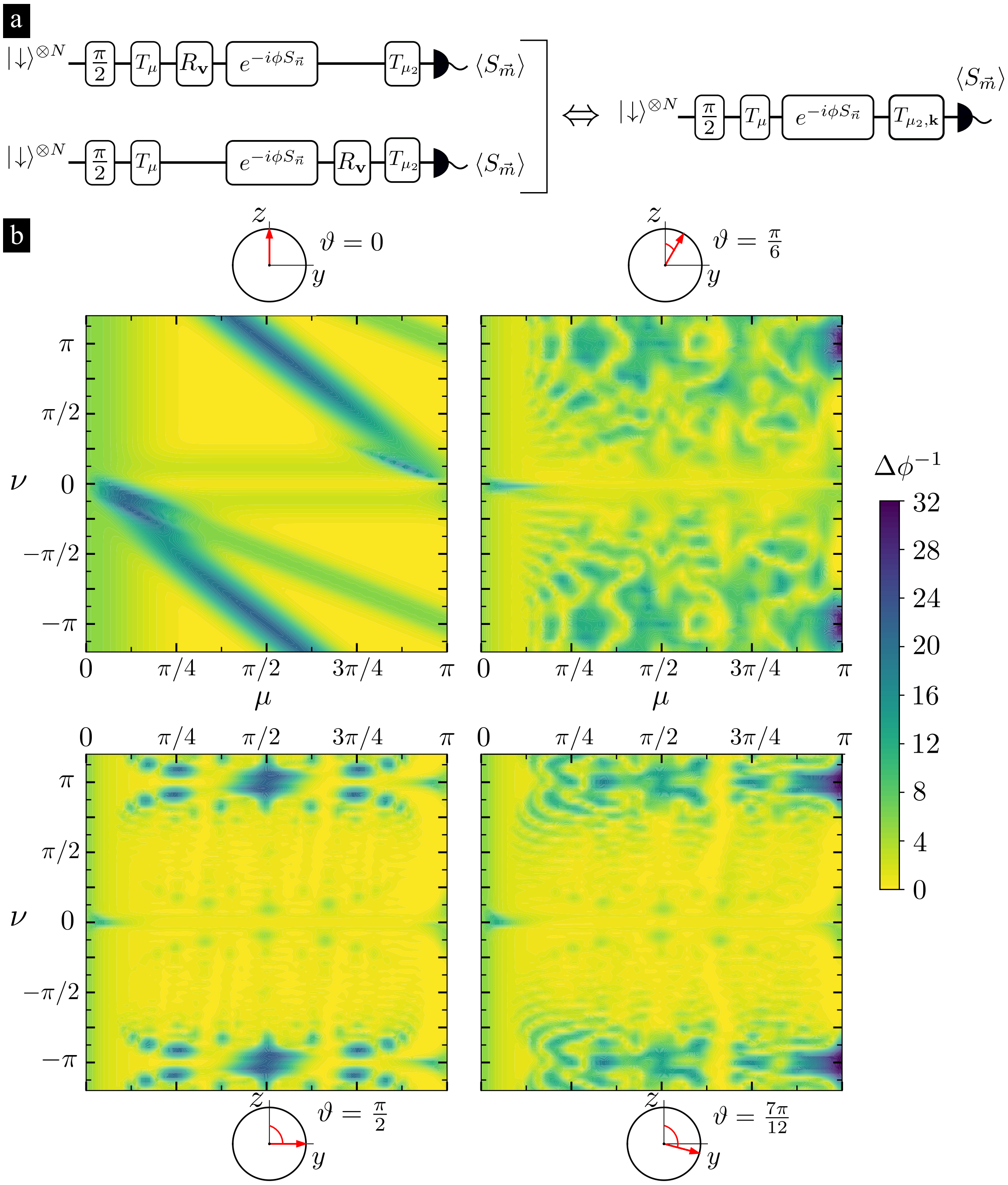

Figure 2.16: **Extended Protocols: a** Schematics of the protocols. Adding an additional collective spin rotation $R_{\boldsymbol{v}}$ (the two choices on the left), is equivalent to a rotated basis for the second OAT interaction (shown on the right). **b** Overview of the achieved sensitivity for $N = 32$. Here $T_{\mu_2,\boldsymbol{k}} = e^{-i\frac{\mu_2}{2}(\cos\vartheta S_z + \sin\vartheta S_y)^2}$ with the axis rotated in the z-y-plane (as indicated by the arrows). The Heisenberg limit $\Delta\phi^{-1} = N$ is reached for the top right and bottom right panel.

of the basis for the second OAT interaction and adjusted signal and measurement directions. In light of the geometric optimization, the changes of the signal and measurement directions are irrelevant. So one may resort to studying

$$\langle S_{\boldsymbol{m}} \rangle(\phi) = \langle \mathrm{x}| T_\mu^\dagger \, R_{\boldsymbol{n}}^\dagger(\phi) \, T_{\mu_2,\boldsymbol{k}}^\dagger \, S_{\boldsymbol{m}} \, T_{\mu_2,\boldsymbol{k}} \, R_{\boldsymbol{n}}(\phi) \, T_\mu |\mathrm{x}\rangle \tag{2.80}$$

with the OAT interaction $T_{\mu_2,\boldsymbol{k}} = e^{-i\frac{\mu_2}{2}S_{\boldsymbol{k}}^2}$ around an axis $\boldsymbol{k}$. Note that we have also removed the symmetry around exact inversion, as there is no more reason to assume that such a symmetry exists in the extended class. Unfortunately, we have not found a way to solve this case analytically, so numerical evaluation of the matrix elements in M and Q is needed, which makes this study less efficient. Looking at the landscapes of Fig. 2.16**b**, rich but complex structures appear when moving away from the usual $T_{\mu_2,\boldsymbol{e_z}}$ OAT (top left panel). Also, with the typical GHZ protocols included, it is not surprising to find that the exact Heisenberg limit is reached for some directions $\boldsymbol{k}$. But, again, the susceptibility of the different protocols achieving the Heisenberg limit without noise needs to be taken into account. In preliminary results, a constant offset from the Heisenberg limit was found when including collective dephasing during OAT interactions. However, a complete study of these protocols is beyond the scope of this thesis. At last, note that there is still more room to adjust the protocols. Another possible diversification is with the use of sequential variational protocols, which have so far been explored for state preparation, by applying $n_{\mathrm{en}} \in \mathbb{N}$ stages of entangling interactions and collective rotations onto the initial state, i.e. giving more layers to $\mathcal{U}_{\mathrm{en}}$ [KSK+19]. In accord with the interaction based readouts, one could also include $n_{\mathrm{de}} \in \mathbb{N}$ stages in $\mathcal{U}_{\mathrm{de}}$ to decode the phase information into some simple observable. All protocols considered here remain in a subclass with overall low order, specifically $n_{\mathrm{en}} = 1$ and $n_{\mathrm{de}} = 1$. Using more layers would be a promising approach to optimize interrogation protocols specifically when considering more complicated cost functions, in contrast to the standard phase uncertainty $\Delta\phi$ studied here.

3

Prospects and limits of entanglement-enhanced optical atomic clocks

3.1 Motivation and research problem

In recent years, atomic clocks based on optical transitions [LBY+15] have achieved unprecedented levels in accuracy and stability as frequency references [N+15, M+19, HSL+16, BCH+19]. Apart from a redefinition of the SI second, this also facilitates new tests of physics beyond the Standard Model [D+17, SHL+19, R+20, SBD+18] and opens up the field of relativistic geodesy [DL13, G+18, MGL+18]. For these applications, high clock stability is vital in order to reach a given frequency uncertainty in the shortest possible time. Accordingly, approaches from quantum metrology [PSO+18] are being pursued which promise to achieve an improvement through the use of entangled atoms. In particular, spin squeezed states [WBI+92, KU93, WBIH94] received much attention due to their practicability and noise resilience [MWSN11, PSO+18]. As already mentioned in chapter 2, spin squeezed states can be generated with trapped ions [MRK+01, LBS+04] or in cold atomic gases [TFNT09, LSSVac10a, CGWT16], and have already been used in proof-of-principle experiments to demonstrate a reduction of QPN in measurements of small phases on microwave transitions [LSSVac10b, BCN+14, HEKK16, B+19b]. The realization of such tailored entangled states on optical clock transitions is a major challenge for experiment [VBE+17, B+19b] and theory [MYH08, WBD10, GMB+14, MSP16, LSNC+18, HPM+19]. At the time of writing this thesis, there is only one work reporting entanglement enhanced phase measurements on an optical transition with weakly squeezed spin states [P+20], as it would be relevant for an optical atomic clock. So understanding the prospects and limitations of entangled states in typical architectures for an optical atomic clock is an important current ambition.

In view of these advances, it is important to note that under practical conditions, optical atomic clocks are not exclusively limited by QPN. Indeed, the operating point of a clock at which maximum stability is achieved is determined by a balance of QPN and other noise processes, such as laser phase noise and dead time effects [HMP+97, LSH+17, BKV18, LWL+11]. While the instability due to dead time can be considered a merely technical problem, we emphasize that laser phase noise must not be treated as such. Indeed, the suppression of laser noise by locking on an atomic reference is the central objective of an optical atomic clock. To dismiss this noise as a technical imperfection would render the problem trivial. Laser noise arises fundamentally in optical atomic clocks due to thermal noise [NKC04] or quantum noise [ST58]. On the other hand, atomic spontaneous decay can be neglected for the most advanced clocks which employ clock transitions with upper state lifetimes way beyond the laser coherence times [LBY+15]. In this chapter we assess the prospects for improving the stability of optical atomic clocks using spin squeezing under these conditions. Our main result is that at a given level of dead time and laser phase noise, spin squeezing can only offer an advantage for atomic ensembles below a certain critical number of clock atoms. For state-of-the-art high-quality clock lasers, this critical atomic number is smaller than the size that can realistically be reached in optical lattice clocks without being limited by density effects. Thus, in lattice clocks spin squeezing can only provide an advantage with significant improvements in dead time and phase noise of next generation clock lasers. In contrast, in atomic clocks based on platforms whose atomic number cannot be easily scaled, such as multi-ion traps [KKB+19, KBK+19, SMS+18, TKA+19] or tweezer arrays [L+19, NYE+19, MCS+19, SWGT19], spin squeezing can offer a relevant advantage. We would like to stress that this limitation applies to single atomic clocks with conventional (Ramsey) interrogation sequences with squeezed input states. The limitation could be avoided with schemes achieving dead-time-free interrogation or overcoming laser phase noise [BS13a, RL13, KKB+14, HL16, TTK11, S+16, CHT+11]. We briefly discuss the case of cascaded ensembles in the outlook of this chapter. The potential gain from entanglement should then be assessed by an appropriate analysis, incorporating the trade-offs discussed here. In the following, we will first introduce some elementary concepts underlying the model of an optical atomic clock. Afterwards, we describe our main result more quantitatively, highlighting the key findings, before presenting the details of the model. We conclude by looking at some possible future directions, extending this work.

3.2 Essential elements of atomic clocks

In optical atomic clocks a laser of very high but finite coherence time is stabilized by a control loop to an atomic transition of frequency ν_0, see Fig. 3.1 **a**. The laser frequency is compared to the atomic transition in a sequence of interrogation cycles, each of duration T_C. In the following we consider Ramsey interrogations with interrogation time T_R, and cycles with a dead time $T_\mathrm{D} = T_\mathrm{C} - T_\mathrm{R}$, see Fig. 3.1 **b**. At the end of an interrogation cycle, the collective atomic spin is measured along a projection, which we take as S_y, providing information about the deviation of the laser from the atomic transition frequency, see Fig. 3.1 **c**. The measurement result is converted into an error signal that is used to correct the laser frequency. Finally, the clock signal is obtained from the stabilized laser with the help of a frequency comb. The clock instability achieved in this way after averaging over a time $\tau \gg T_\mathrm{C}$ is measured in terms of the Allan deviation $\sigma_y(\tau)$ for fractional frequency fluctuations [LBY+15]. A detailed discussion of the essential components of an atomic clock and measures of the stability is provided in the remainder of this section. We will look in particular

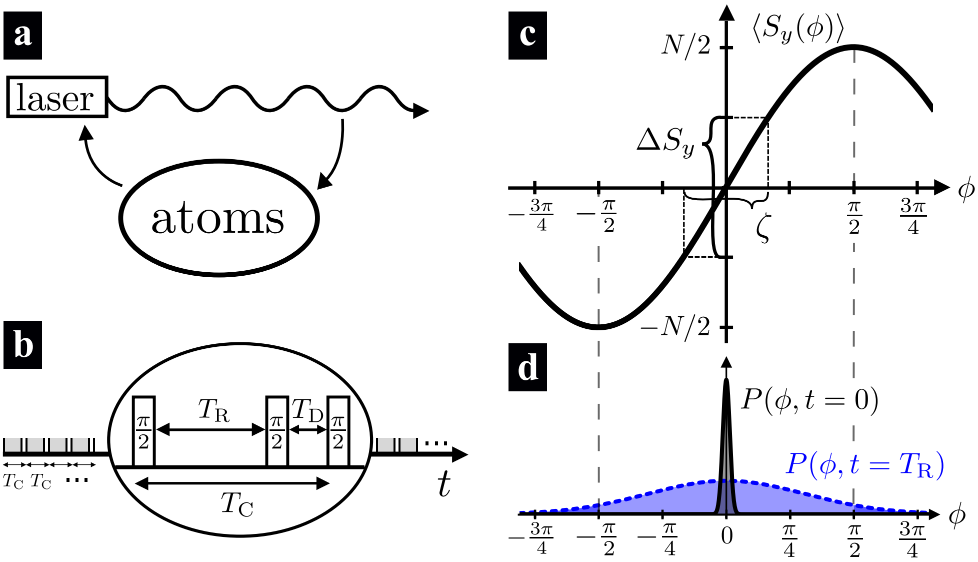
a
laser
atoms
b
T_R
T_D
$\frac{\pi}{2}$
$\frac{\pi}{2}$
$\frac{\pi}{2}$
T_C
T_C T_C ...
t
c
$\langle S_y(\phi)\rangle$
$N/2$
$-N/2$
ΔS_y
ζ
ϕ
$-\frac{3\pi}{4}$ $-\frac{\pi}{2}$ $\frac{\pi}{2}$ $\frac{3\pi}{4}$
d
$P(\phi, t=0)$
$P(\phi, t=T_\mathrm{R})$
ϕ
$-\frac{3\pi}{4}$ $-\frac{\pi}{2}$ $-\frac{\pi}{4}$ 0 $\frac{\pi}{4}$ $\frac{\pi}{2}$ $\frac{3\pi}{4}$

Figure 3.1: **Setup and noise processes: a** Measurement and feedback loop to stabilize the laser frequency to an atomic transition. **b** Periodic measurements with Ramsey time T_R and dead time T_D in each cycle of total time T_C lead to increased instability from the Dick effect. **c** Quantum projection noise ΔS_y limits the clock stability for short interrogation times but can be decreased with squeezed states thus reducing the inferred phase uncertainty $\zeta = \xi/\sqrt{N}$ where ξ is the Wineland spin squeezing parameter. **d** For longer T_R the distribution of phases broadens substantially due the laser's decoherence. Inefficient feedback for phases outside the $[-\frac{\pi}{2}, \frac{\pi}{2}]$ interval gives the coherence time limit.

at the local oscillator, the atomic reference, and the servo. A combined treatment of all three components, analyzing the full feedback process is presented in section 3.4.

3.2.1 The local oscillator

Any atomic clock we consider in this work has two oscillators at their core. One oscillation is provided by two electronic energy levels within an atom or ion which, without external perturbations, provides an ideal frequency reference at the natural transition frequency ν_0. The other is an electromagnetic field

$$E(x,t) = E_0(x,t)\cos\big(\phi(x,t)\big), \tag{3.1}$$

with amplitude $E_0(x,t)$ and phase $\phi(x,t)$ which interacts with the atoms. This field constitutes the local oscillator which is required to count the atomic oscillations, a task that can not be done directly from the atoms. It also allows to further distribute the frequency standard. We had seen in chapter 2 how the atom-light interaction can be used to measure the frequency difference between the local oscillator and ν_0. Repeated applications of Ramsey interferometry can thus be used to stabilize the local oscillator to the reference frequency. With the invention of the optical frequency comb, even oscillations of a local oscillator in the optical (THz) regime can be counted to derive the frequency signal. Overall, the stabilized local oscillator signal allows for the comparison of different clocks, relativistic geodesy, contributing to the universal coordinated time, and applications in fundamental science.

To model the operation of atomic clocks it is thus essential that we take a closer look at the local oscillator and its properties. At first, we have that the (angular) frequency of an oscillator at time t is defined as the rate of change of its phase, meaning

$$\omega(t) = \frac{\partial\phi}{\partial t}. \tag{3.2}$$

In turn this leads to the explicit expression

$$\phi(t) = \int_{t_0}^{t} \omega(t')\mathrm{d}t' + \phi(t_0) \tag{3.3}$$

for the accumulated phase between t_0 and t, starting from $\phi(t_0)$.

A phase analysis like this is useful when studying frequency differences between oscillators. To see this, we assume two oscillators with the same initial phase at $t_0 = 0$ but with different frequencies $\omega_1(t)$ and $\omega_2(t)$. This condition is fulfilled, either if both oscillators are initialized identically or if one oscillator determines the induces the phase of the other, as was the case for standard Ramsey interrogation. Under these assumptions, the phases of the oscillators after a time T are

$$\begin{aligned}\phi_1(T) &= \int_0^T \omega_1(t')\mathrm{d}t' + \phi(0)\,,\\ \phi_2(T) &= \int_0^T \omega_2(t')\mathrm{d}t' + \phi(0).\end{aligned}$$

So in general the phase difference

$$\Delta\phi(T) = \phi_1(T) - \phi_2(T) = \int_0^T \left[\omega_1(t') - \omega_2(t')\right]\mathrm{d}t' \tag{3.4}$$

is independent of the initial phase value and can be used to infer frequency deviations between the two oscillators. For example, with constant frequencies $\omega_1(t') = \omega_1$ and $\omega_2(t') = \omega_2$ over the timescale T one finds $\omega_1 - \omega_2 = \frac{\Delta\phi}{T}$ for the frequency difference. At this point we can clearly see the connection to Ramsey protocols as introduced in section 2.3. When one of the frequencies corresponds to the noisy laser frequency and the other to the ideal (thus time independent) transition frequency $\omega_0 = 2\pi\nu_0$, we see that

$$\Delta\phi(T_\mathrm{R}) = \int_0^{T_\mathrm{R}} \left[\omega_\mathrm{LO}(t') - \omega_0\right]\mathrm{d}t' \tag{3.5}$$

is exactly the phase around which a state is rotated in the Ramsey protocol. While previously we were interested in optimizing sensitivity, at $\phi = 0$ only, a discussion of optical atomic clocks necessarily involves phases away from this point as they arise from the fluctuations of the local oscillator frequency. This point becomes more pressing when we try to predict the overall stability of an atomic clock. For now we will restrict this study to a free-running local oscillator, on the basis of which we introduce measures of stability and describe the relevant frequency noise. In doing so we disregard any measurement of the frequency deviation using the atomic ensemble as well as any feedback control.

Atomic clocks in the optical regime feature an ultra-stable laser as their local oscillator. The frequency noise of these lasers is largely dependent on their realization. Most clock lasers achieve a high stability by locking the light to an ultra-stable reference cavity. For a Fabry-Pérot cavity the resonant frequencies to which the laser can be locked are $\nu_q = q\frac{c}{2L}$ with the mode number q and L the length between the cavity mirrors. In this way small frequency fluctuations $\Delta\nu$ around one of the resonances (denoted simply as ν) directly connect to changes of L. As

$$\frac{\Delta\nu}{\nu} = -\frac{\Delta L}{L} \tag{3.6}$$

applies for small variations ΔL of the cavity length, one can see that a major effort must be put into keeping the length as stable as possible. Among today's best designs are room-temperature glass cavities based on ultra-low-expansion materials or single-crystal silicon cavities in a cryostat. Despite the tremendous level of stability achieved in this way, residual technical imperfections can limit the resulting laser coherence [A$^+$19a] and at some point even fundamental noise processes may give the overall limit [NKC04, ST58]. Taking a more abstract point of view, this thesis will only consider three types of laser noise. They are distinguished by their contribution to the spectral noise density of the laser. In other words, by the temporal correlations of the frequency fluctuations they cause. We consider white frequency noise, flicker (or $1/f$-noise) frequency noise and random walk frequency noise. These are the most relevant contributions in many ultra-stable clock lasers. Especially flicker frequency noise due to thermal fluctuations is a notorious limit to the stability. The next section presents methods how to characterize and quantify the laser noise.

Stability measure To compare the quality of oscillators across a variety of frequencies one considers relative frequency differences rather than absolute differences. We therefore introduce the fractional frequency deviation

$$y(t) = \frac{\omega_{\mathrm{LO}}(t) - \omega_0}{\omega_0} \tag{3.7}$$

of an oscillator with frequency $\omega_{\mathrm{LO}}(t)$ with respect to an ideal reference at ω_0. We express the definition in this way in anticipation of later studying the frequency deviation of the clock laser against the atomic reference. There, we will be interested in the resulting phase fluctuations of the laser when close to ν_0. In principle, however, the relative frequency deviation can be calculated for any nominal laser frequency and reference value. One advantage of the relative deviations is exactly that the absolute noise level at any frequency can be inferred from them. For example, this is useful when the short term fractional frequency stability of the clock laser, interrogating the atoms, is transferred by a frequency locking scheme from some other ultra-stable laser at a different frequency.

Phase differences and absolute frequency deviations are linked as well, via

$$\Delta\phi(T) = T\,\overline{\Delta\omega} = \omega_0\,T\,\overline{y}. \tag{3.8}$$

This connects both to the time averaged fractional frequency deviation

$$\overline{y} = \frac{1}{T}\int_0^T \frac{\omega_{\mathrm{LO}}(t) - \omega_0}{\omega_0}\,\mathrm{d}t\,. \tag{3.9}$$

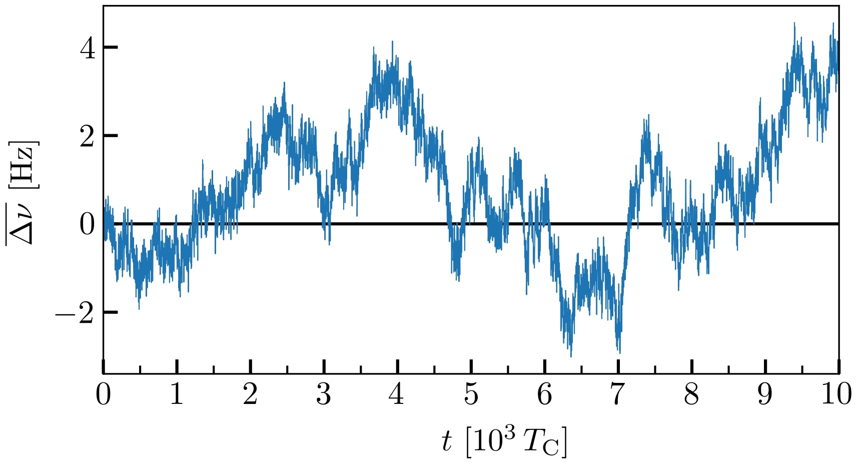

Figure 3.2: **A typical noisy signal:** Fluctuating frequency deviations $\overline{\Delta\nu}(t)$ over the course of 10^4 measurement cycles. The signal has contributions from white, flicker and random walk frequency noise.

The time averaged frequency deviations are defined analogously, as

$$\overline{\Delta\omega} = \frac{1}{T}\int_0^T [\omega_\mathrm{LO}(t) - \omega_0]\,\mathrm{d}t \quad \text{and} \quad \overline{\Delta\nu} = \frac{\overline{\Delta\omega}}{2\pi}\,. \tag{3.10}$$

Note that all these equations are exact and no approximations regarding the noise were needed.

Every laser we consider will produce a noisy signal $y(t)$ such as the one shown in Fig. 3.2. A priori the fractional frequency deviation will be a time continuous stochastic process. But for a typical measurement record, e.g. as measured by a frequency counter, a discrete sequence of frequency readings would be returned. Also in the case of continuous feedback control the sequence of averaged values

$$\overline{y}_k = \frac{1}{T}\int_{(k-1)T}^{kT} y(t)\,\mathrm{d}t \tag{3.11}$$

during measurement interval k (this is the frequency reading at the end of the kth cycle) will be what is relevant. Here we divided time into equal intervals of length T as in the cyclic feedback loop. When including dead time one would make the grid finer and have consecutive averages with T_D and T_R repeatedly. Note that the series $\overline{y}_k$ can again be regarded as a time continuous process after many cycles, i.e. $k \gg 1$. We will make use of this feature in section 3.4.2, when presenting a stochastic differential equation model for the clock stability.

To study the accuracy and stability of an oscillator, with respect to the reference, one would now typically study first and second statistical moments of $\overline{y}_k$. However, simply looking at the variance is not sufficient here as it is non-convergent for some noise types [Ril08]. Since the typical noise is correlated, additional statistical tools are needed to identify the different features of the external perturbations. To this end a number of N-sample variances were introduced [Rie06, Rut78]. In the context of atomic clocks the agreed upon convention is to use the 2-sample variance, also called Allan variance. The Allan variance [All66, Ril08]

$$\sigma_y^2(\tau) = \frac{1}{2}\left\langle(\overline{y}_{j+1} - \overline{y}_j)^2\right\rangle = \frac{1}{2}\left\langle\left(\frac{1}{\tau}\int_{j\tau}^{(j+1)\tau} y(t)\,\mathrm{d}t - \frac{1}{\tau}\int_{(j-1)\tau}^{j\tau} y(t)\,\mathrm{d}t\right)^2\right\rangle \tag{3.12}$$

is based on the difference of two averages $\overline{y}_j, \overline{y}_{j+1}$ with integration time $\tau = n\tau_0$, $n \in \mathbb{N}$. When evaluated in the context of atomic clocks the base integration time τ_0 will always be the cycle time, i.e. $\tau_0 = T_\mathrm{C}$. The brackets $\langle\cdot\rangle$ in Eq. (3.12) denote a statistical average. This can be either over many independent clock runs or (as done in this thesis) over subsets of a single realization which then needs sufficiently many cycles of operation.

For a numerical calculation of the Allan variance from a finite data set we assume that the mean fractional frequency deviation $\overline{y}_k$ (with $T \equiv T_\mathrm{C}$ and $k = 1, \ldots, M_\mathrm{tot}$) was measured in a total of M_tot observation cycles. If the Allan variance is then to be evaluated at the averaging times $\tau = nT_\mathrm{C}$, the entire data set contains exactly $M_n = \left\lfloor \frac{M_\mathrm{tot}}{n} \right\rfloor$ consecutive intervals of length n (see e.g. Fig. 3.3). The averaging factor n thus serves to determine the time averages

$$\overline{y}_j = \frac{1}{n}\sum_{k=(j-1)n}^{jn} \overline{y}_k = \frac{1}{nT_\mathrm{C}}\sum_{k=(j-1)n}^{jn}\int_{(k-1)T_\mathrm{C}}^{kT_\mathrm{C}} y(t)\mathrm{d}t \tag{3.13}$$

in Eq. (3.12) for each interval $j = 1, \ldots, M_n$ of length τ. The number M_n on the other hand indicates with how many samples the statistical average $\langle\cdot\rangle$ in Eq. (3.12) can be calculated. In this way

$$\sigma_y^2(\tau) = \frac{1}{2(M_n - 1)}\sum_{j=1}^{M_n-1}(\overline{y}_{j+1} - \overline{y}_j)^2 \tag{3.14}$$

is a finite size estimate to the Allan variance [Ril08].

In contrast to the original definition of the Allan variance, Eq. (3.14), there also exists a more robust version, the overlapping Allan variance. Though the two are equal for large samples, the overlapping Allan variance is more efficient by utilizing all possible combinations of the data set [Ril08]. In this way, more precise values are obtained at the same sample size and error bars are reduced at a faster rate. Because of the fact that in the end both values are the same we refrain from stating the

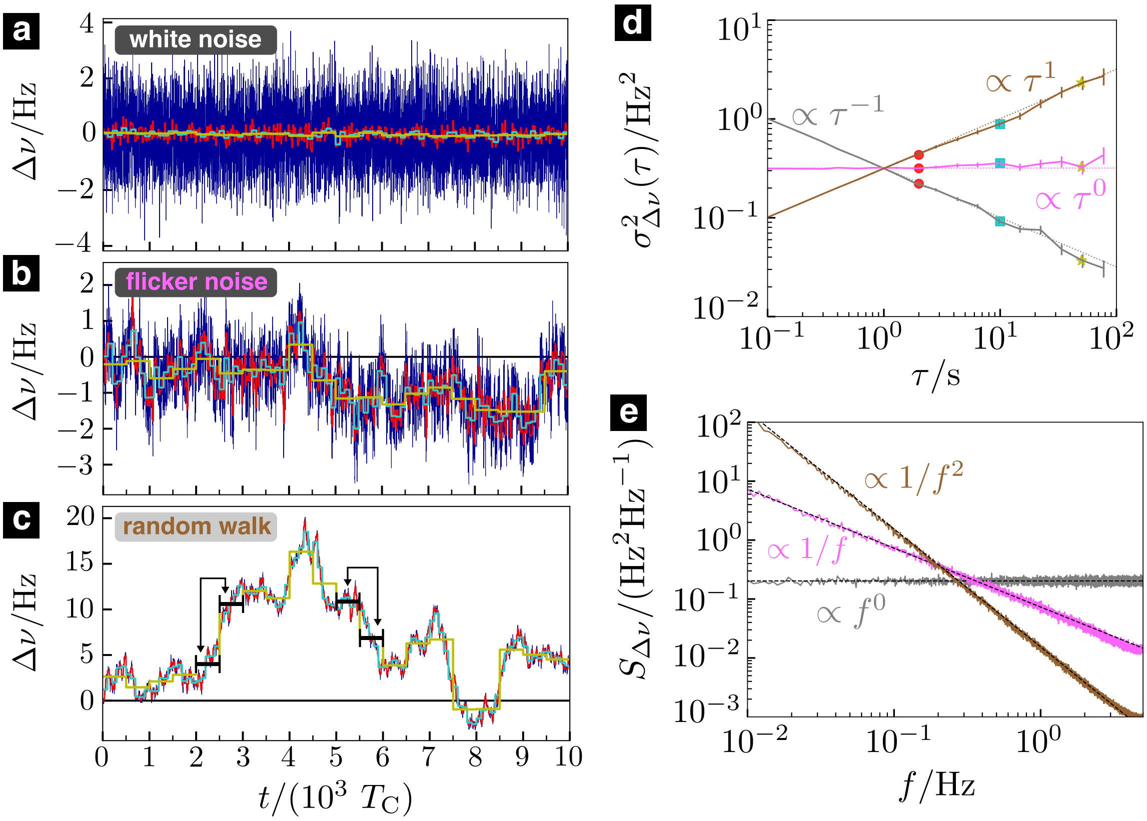

Figure 3.3: **Stability analysis: a-c** Time traces simulated over 10^4 cycles of operation for the three noise classes that are considered in this thesis. In each part the dark blue trace is the noise in each cycle. Colors denote averages over multiple cycles with $\tau = 20\,T_\mathrm{C}$ (red), $\tau = 100\,T_\mathrm{C}$ (cyan) and $\tau = 500\,T_\mathrm{C}$ (yellow). These averages are used to characterize noise in the time domain. The Allan deviation calculates the fluctuations between sequential averages, e.g. $\overline{\Delta\nu}_6 - \overline{\Delta\nu}_5$ or $\overline{\Delta\nu}_{12} - \overline{\Delta\nu}_{11}$ as marked in **c** when $\tau = 500\,T_\mathrm{C}$. The variance is small at shorter averaging times (red and cyan) compared to the longer averaging times (yellow) due to temporal correlations in the random walk noise. This is in contrast to the white noise shown in **a**, where the variance for long averaging is so small that it is hardly visible. The statistical averaging contained in $\sigma_y^2(\tau)$ is obtained by averaging the fluctuations between all pairs $\overline{\Delta\nu}_{i+1}$ and $\overline{\Delta\nu}_i$, always shifting the index by one. In **d** we show the resulting time domain stability in terms of the Allan deviation. Symbols mark the averaging duration of the correspondingly colored averages in **a-c**. For example, the yellow star results from using all 20 pairs of averages with length $\tau = 500\,T_\mathrm{C}$. Error bars arise from the finite size of the sample and resulting finite averaging. In addition to the numerically computed Allan deviations we show the analytic τ-scaling by the dashed lines. Part **e** shows the frequency domain stability in terms of the noise spectrum $S_{\Delta\nu}(f)$, highlighting the characteristic frequency scaling of the three noise processes.

explicit definition of the overlapping Allan deviation here. It can be found in suitable references, such as the 'Handbook of frequency stability analysis' by Riley [Ril08]. Frequent use of the overlapping Allan deviation is made in the numerical simulations.

Evaluating fluctuations in the time domain, via the Allan variance, is a practical way to differentiate several noise types. As mentioned before, in this work we consider white frequency noise, flicker frequency noise and random walk frequency noise. Each of those has a power-law scaling $\sigma_y^2(\tau) \propto \tau^\gamma$ in the Allan variance with a characteristic exponent γ and a related power-law scaling in its spectral density $S_y(f) \propto f^\alpha$. The specific scaling laws will be derived later, see e.g. Eq. (3.24). Specifically white, flicker, and random walk frequency noise are treated here as they are the most common noise types for current day laboratory clock lasers and will likely remain so in the near future. This is because they are the typical consequences for many relevant physical causes of cavity length fluctuations [NKC04].

For the sake of completeness we note that a detailed characterization of ultra-stable lasers often includes other noise sources beyond the ones introduced so far. Those are white phase noise, flicker phase noise, and a slow frequency drift. These effects are neglected in this thesis because on the one hand the contributions of white phase noise and flicker phase noise are only relevant on very short time scales and on the other hand we assume that a deterministic drift can be corrected out. Thus, for our investigation concerning optimal interrogations of non-classical ensembles with time scales $\sim 100\,\mu\mathrm{s}$ - $10\,\mathrm{s}$, they generally have no influence. Stochastic noise with even longer correlation times than the random walk noise is of no concern for the same reason. The timescales where this would become relevant are so long that it is typically referred to as an 'aging' effect.

Although the Allan variance already provides a good overview of the various noise components, the averaging process it contains can cause small details of the noise to be lost. A more detailed picture is given by the spectral noise density $S_y(f)$. For most 'well-behaved' noise types the spectral noise density (single-sided power spectral density) can be calculated as

$$S_y(f) = 2 \lim_{\mathcal{T}\to\infty} \frac{1}{\mathcal{T}} \left| \int_0^{\mathcal{T}} y(t) e^{-i\,2\pi f t}\,\mathrm{d}t \right|^2 \tag{3.15}$$

where $\mathcal{T}$ is the length of the signal $y(t)$. Alternatively, representations using the auto-correlation function

$$R_y(\tau) = \langle y(t+\tau) y(t) \rangle = \lim_{\mathcal{T}\to\infty} \frac{1}{2\mathcal{T}} \int_{-\mathcal{T}}^{\mathcal{T}} y(t+\tau) y(t)\,\mathrm{d}t \tag{3.16}$$

of the noise exist. From the Wiener-Khinchin theorem follows

$$S_y(f) = 2 \int_{-\infty}^{\infty} R_y(\tau) e^{-i\,2\pi f \tau} \mathrm{d}\tau. \tag{3.17}$$

The spectral noise density $S_y(f)$ for the fractional frequency fluctuation $y(t)$ is particularly instructive, since it allows oscillators with different carrier frequencies ν_c to be compared very easily. Spectral noise densities of related quantities can also be derived from $S_y(f)$. In particular,

$$S_{\Delta\nu}(f) = \nu_c^2\, S_y(f) \tag{3.18}$$

holds for absolute frequency deviations, in which $[S_{\Delta\nu}(f)] = \mathrm{Hz}^2\,\mathrm{Hz}^{-1}$. For phase noise,

$$S_{\Delta\phi}(f) = \left(\frac{\nu_c}{f}\right)^2 S_y(f) \tag{3.19}$$

applies, where we used that $2\pi\Delta\nu(t) = \frac{\mathrm{d}\Delta\phi(t)}{\mathrm{d}t}$.

From frequency domain to time domain Let us assume that we would like to infer the time domain description of the noise, in terms of the Allan deviation $\sigma_y^2(\tau)$, from a known spectral density $S_y(f)$. Since the spectral density contains more information we know that this conversion should always be possible. One way of deriving the relation between the two domains is by first expressing the Allan variance from Eq. (3.12) as

$$\sigma_y^2(\tau) = \left\langle \left(\int_{-\infty}^{\infty} y(t')\, h_\tau(\tau - t')\, \mathrm{d}t' \right)^2 \right\rangle \tag{3.20}$$

with

$$h_\tau(t) = \begin{cases} -\frac{1}{\sqrt{2}\tau} & -\tau < t < 0 \\ \frac{1}{\sqrt{2}\tau} & 0 \le t < \tau \\ 0 & \text{else} \end{cases} \tag{3.21}$$

as a filter function. Equation (3.20) is recognized as a convolution between $y(t)$ and $h_\tau(t)$. This motivates to express the Allan deviation in terms of the Fourier representations of the two constituents. So the desired relation is

$$\sigma_y^2(\tau) = \int_0^{\infty} S_y(f) |H_\tau(f)|^2\, \mathrm{d}f \tag{3.22}$$

where $S_y(f)$ is again the power spectral density and $H_\tau(f)$ is the Fourier transform of $h_\tau(t)$, namely

$$|H_\tau(f)|^2 = 2\frac{\sin^4(\pi\tau f)}{(\pi\tau f)^2}\,. \tag{3.23}$$

A detailed proof of this relation was given by Barnes *et al.* [B+71]. Using Eq. (3.22) one can directly compute the characteristic scalings

$$\sigma_y^2(\tau) \propto \tau^\gamma \tag{3.24}$$

of the Allan variance. For spectral noise densities $S_y(f) \propto f^\alpha$ the scaling exponent is $\gamma = -\alpha - 1$. So for white, flicker and random walk noise, with $\alpha = 0, -1, -2$ respectively, the scaling exponents are $\gamma = -1, 0, 1$. More precisely, a spectral noise density $S_y(f) = b_0 f^0 + b_{-1} f^{-1} + b_{-2} f^{-2}$ results in

$$\sigma_y^2(\tau) = \frac{b_0}{2}\frac{1}{\tau} + 2\ln(2)\, b_{-1} + b_{-2}\frac{(2\pi)^2}{6}\tau.$$

The pre-factors b_α specify the bandwidth of the noise. We summarize the transformation properties in Table 3.1.

Type of noise	$S_y(f)$	$\sigma_y^2(\tau)$
white frequency noise	$b_0 f^0$	$\frac{b_0}{2}\,\tau^{-1}$
flicker frequency noise	$b_{-1} f^{-1}$	$2\ln(2)\, b_{-1}$
random walk frequency noise	$b_{-2} f^{-2}$	$b_{-2}\frac{(2\pi)^2}{6}\,\tau$

Table 3.1: **Noise contributions to the Allan variance:** For a given power law scaling in the Fourier frequency f of the one-sided spectral density $S_y(f)$ one finds the corresponding contributions to the τ scaling of the Allan variance $\sigma_y^2(\tau)$.

Laser coherence time With the characterization of laser noise as introduced above, a single timescale expressing the coherence of the laser can be given. There are multiple ways how to introduce such a notion, typically motivated by the desired application in different fields of physics [TMS17, M+17]. Within this thesis we chose

$$\sigma_{y,\mathrm{LO}}(Z_c) 2\pi\nu_0 Z = 1\,\mathrm{rad} \tag{3.25}$$

as the implicit definition for the laser coherence time Z, following [LSH+17]. Here $\sigma_{y,\mathrm{LO}}(Z_c)$ is the local oscillator Allan deviation at the cycle time $Z_c = Z + T_\mathrm{D}$. See Fig. 3.4 for an illustration of this definition. Introducing Z allows to compare the performance of clocks with a variety of underlying local oscillators in terms of the dimensionless ratio T/Z of the probe time T and the laser coherence time Z. Note, however, that while the noise characteristic $\sigma_{y,\mathrm{LO}}$ uniquely defines Z, the inverse is not true. In particular, two lasers limited by different noise types may still give rise to the same coherence time. As an intuitive description, the laser coherence time is the interrogation time at which the Allan deviation of the laser coincides with the quantum projection noise limited stability $\sigma_y(Z) = \frac{1}{\omega_0 Z}\sqrt{\frac{Z_c}{Z}}$ of a single atom, following Eq. (3.43). A related definition [M+17, A+19a], up to a factor of $\sqrt{2}$, has also connected Z to the root-mean-square phase deviations in a two-pulse Ramsey

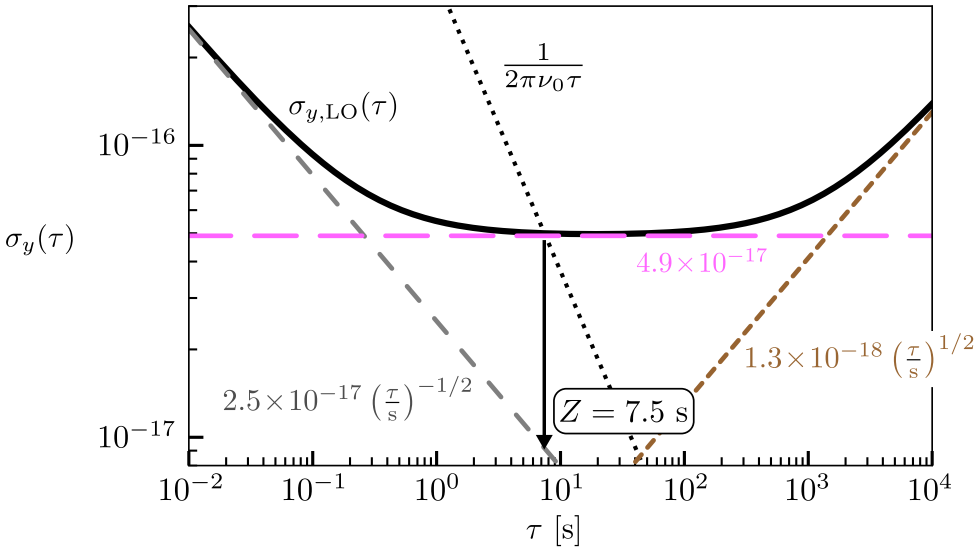

Figure 3.4: **Example clock laser stability:** Allan deviation $\sigma_{y,\mathrm{LO}}(\tau)$ for state-of-the-art laboratory clock lasers (cL). Dashed lines show the individual noise contributions σ_{W}, σ_{FF} and σ_{RW}. Intersecting the dotted line with $\sigma_{y,\mathrm{LO}}(\tau)$ determines the laser coherence time Z. We use $\nu_0 = 429.228\,\mathrm{THz}$.

interrogation of atoms but will not be applied here. With current laser technology, where $\sigma_{y,\mathrm{LO}} \sim 10^{-16}$, the coherence time is limited to a few seconds (see the following paragraph and Table 3.2 for specific parameters).

Example laser parameters To give an intuition into what the current state-of-the-art technology for clock lasers is, we now present a small collection of example parameters. Four kinds of lasers are considered in this thesis, as summarized in Table 3.2: The first kind (second row) is the currently best laboratory clock laser (cL), which is limited on the relevant timescales by flicker frequency noise at an Allan deviation of $\sigma_{\mathrm{FF}} = 4.9\times10^{-17}$ [M+17]. We also consider two future generation clock lasers with projected improved noise spectra limited by $\sigma_{\mathrm{FF}} = 10^{-17}$ and $\sigma_{\mathrm{FF}} = 3\times10^{-18}$ respectively, which we refer to as pL1 and pL2. Such lasers require vast improvements over state-of-the-art systems. They could possibly be achieved in a combination of low temperature cryogenic systems with pure crystalline components of the cavity, which are envisioned of achieving a fundamental noise limit in the low 10^{-18} range [A+19a]. For comparison, we also include a laser for transportable atomic clocks (tL) whose stability is reduced due to shorter cavities and stronger environmental perturbations compared to the laboratory setting [HHV+20]. We consider here an ambitious design, limited by flicker frequency noise at $\sigma_{\mathrm{FF}} = 10^{-16}$. See Table 3.2 for the detailed characterizations of all lasers. When projecting laser parameters based on the current record laboratory laser we choose to always scale the entire noise spectrum (or

Laser type	Abbr.	$\sigma_{\mathrm{W}}(\tau = 1\,\mathrm{s})$	$\sigma_{\mathrm{FF}}(\tau = 1\,\mathrm{s})$	$\sigma_{\mathrm{RW}}(\tau = 1\,\mathrm{s})$	$Z\,[s]$
projected transportable clock laser	tL	5.2×10^{-17}	1.0×10^{-16}	2.6×10^{-18}	3.6
current record laboratory clock laser	cL	2.5×10^{-17}	4.9×10^{-17}	1.3×10^{-18}	7.5
projected laboratory clock laser 1	pL1	5.2×10^{-18}	1.0×10^{-17}	2.6×10^{-19}	36.5
projected laboratory clock laser 2	pL2	1.6×10^{-18}	3.0×10^{-18}	7.8×10^{-20}	118.8

Table 3.2: **Laser parameters:** Specification of the four types of clock lasers considered in this thesis. Stability is given in terms of white (σ_{W}), flicker (σ_{FF}) and random walk (σ_{RW}) frequency noise at an averaging time $\tau = 1\,\mathrm{s}$. Then with $\nu_0 = 429.228\,\mathrm{THz}$ the coherence time Z is determined as defined in the main text.

consequently the entire Allan deviation). Thus the form of the example laser stability shown in Fig. 3.4 is valid for all kinds of lasers we consider here and the curve would simply move up or down with the overall stability being reduced or improved.

Numerical simulation of noise traces At many places in this chapter will we refer to the results of numerical Monte Carlo simulations of an atomic clock. To simulate the underlying laser, traces of the noise signal have to be generated. Since only fixed protocols are considered in this thesis, where the interrogation times are not changed throughout the stabilization process, the average frequency deviation in each cycle can be simulated separately in advance. The noise in each cycle, consisting of the mean differential frequency noise $\overline{\Delta\nu}$ in an interval of length T_{D} and subsequent interval of duration T_{R}, is generated by the discrete stochastic processes described in the following. After the free-running noise traces are generated, the complete feedback cycle can be performed by simulating the atomic error signal and adding the servo corrections to the previously calculated frequency trace of the laser. Time traces of correlated noise with arbitrary spectral noise density $S_y \propto 1/f^{\alpha}$ can generally be obtained by simulating uncorrelated noise in frequency space at the given Fourier frequencies and subsequent Fourier transformation. However, for long traces this method can lead to lengthy runtimes due to the application of the fast Fourier transformation algorithm. In the simulations of the laser applied in this thesis, a different method is used to generate the three characteristic noise types introduced above. The original implementation for the simulations was set up by I.D. Leroux and was first utilized in Ref. [LSH+17]:

(i) White frequency noise corresponds to independent Gaussian distributed random numbers $\overline{\Delta\nu}_k = \mathcal{N}(0, s^2)$ with a variance $s^2 = \frac{s_\mathrm{W}}{\Delta t_k}$, which scales inversely with the length Δt_k of the k-th time interval. As expected, the auto-correlation function is $\langle \overline{\Delta\nu}_k, \overline{\Delta\nu}_j \rangle = s^2\delta_{kj}$ so that the spectral density $S_{\Delta\nu}(f) = s_\mathrm{W}$ is white.

(ii) random walk frequency noise is described as integrated white noise. The frequency deviation at the end of each simulated time interval is calculated as a running sum of all previous values of normally distributed random numbers with variance $s^2 = s_\mathrm{RW}\Delta t_k$. Formally, the frequency deviation at the end of the i-th interval is recursively defined as $\Delta\nu(t_{k+1}) = \Delta\nu(t_k) + \mathcal{N}(0, s^2)$. The mean frequency deviation in one time step is then the average deviation between its value at the start and end of the interval, i.e. $\overline{\Delta\nu}_k = \frac{\Delta\nu(t_k)+\Delta\nu(t_{k+1})}{2}$. An additional white noise component describes deviations of the noise from this mean value due to fast components of the random walk.

(iii) Flicker frequency noise is approximated by a sum of damped random walks. If the damping rates are chosen correctly, noise with a $1/f$ spectrum over all relevant time scales of the simulation is obtained [Kae90]. The final implementation, which was build by I. D. Leroux [LSH+17], is lengthy and complex, so therefore no exact representation will be given here.

3.2.2 Atomic reference

Looking back at the schematics of an atomic clock, presented in Fig. 3.1**a**, we have so far explored one of the two essential components of an optical atomic clock in detail, namely the local oscillator, in the form of ultra-stable clock lasers. Let us now turn our attention to the atomic reference, constituting the other essential part of the clock.

Requirements for clock transitions The first point to discuss is the selection of atoms and clock transitions. This choice should be motivated by the central goals of atomic clocks, which are to provide precise and stable frequency references. In this context, 'precise' means that one really exploits the fact that, in complete isolation, all atoms of the same species are exactly alike and have the same electronic structure. One of these unperturbed transition frequencies should be the output of the clock. Errors to the precision of a realistic reference then, of course, come from the practical impossibility of perfect isolation. Typical atomic clock experiments feature a number of external perturbations, which can cause systematic shifts of the transition frequency [LBY+15]. For example, motion of the atoms, relative to the interrogation laser, results in Doppler shifts. To diminish this effect, the atoms are trapped spatially and their motion is cooled to near the ground state, both of which typically requires the application of external electric and magnetic fields. However, these fields can induce Stark shifts and Zeeman shifts on the transition. The same shifts are caused by the interaction with the clock laser and with blackbody radiation from the surrounding apparatus. Employing larger ensembles with many atoms can cause frequency shifts from collisions among the atoms and even single atoms may be disturbed by collisions with background gas particles. This list is just a short illustration of the possible systematic shifts in optical atomic clocks. One could now naively argue that the best clock transitions are those, for which the frequency is least disturbed by any perturbation. In the end, however, the selection of atoms and transitions, based on their achievable precision, is not quite as simple. Mainly because not all shifts contribute equally to the overall systematic shift. Some of them may be determined very well, by precise calibration, so that their influence on the inferred natural transition frequency is negligible, even though the atomic transition may react strongly to that particular perturbation. In this sense, there are often many technical details to consider, which may lead to favoring a particular atomic species and transition [A$^+$19a]. For the theoretical study of stability improvements, performed in this thesis, we neglect any systematic shifts and assume ideal atomic references. Nevertheless, a more complete description on systematic shifts can be found e.g. in the review [LBY$^+$15], including the most common atomic clock species and showcasing recent achievements of both, lattice clocks and single ion clocks, reaching fractional frequency uncertainties $\sim 10^{-18}$ or below.

In contrast to the precision, which relates to measurements of the absolute frequency, the notion of stability for an optical atomic clock relates to fluctuations of the stabilized frequency. Within each cycle of the feedback process, errors remain, when estimating the frequency differences $\overline{\Delta\nu}$ between the laser and the atomic transition from a noisy signal. The fluctuations of this estimate then transfer to the stabilized frequency trace, causing the output of the clock to fluctuate over time around the true atomic resonance frequency.

Before going into a detailed discussion of the overall clock stability, as we will do in section 3.3, let us briefly connect the notion of clock stability to the quantum projection noise (QPN), as treated intensely in chapter 2, and identify what are some key parameters that modify the stability. In general, there are different methods to construct the interrogation scheme, which links the laser and the atoms. Within this thesis we consider only Ramsey interferometry in each cycle, although other protocols, such as Rabi interrogation, are also commonly applied [LBY$^+$15]. To later on allow the construction of the analytic model, underlying the results of this chapter, another restriction to the general entangled interferometer protocols, presented in chapter 2, is made. Only squeezed initial states are considered, such that $\mathcal{U}_{\text{en}} = R_x(\theta_0)T_\mu$, and no additional inversion before the measurement shall be applied for now, i.e. $\mathcal{U}_{\mathrm{de}} = \mathbb{1}$. The additional spin rotation $R_x(\theta_0)$ after the entangling one-axis-twisting interaction in $\mathcal{U}_{\mathrm{en}}$ is there to align the reduced spin variance with the measurement direction S_y [KU93]. Reviewing results of chapter 2, the Ramsey sequence proceeds as follows: (i) Preparation of the initial coherent spin state $|\psi_0\rangle = \mathcal{U}_{\mathrm{en}}|\mathrm{x}\rangle$. (ii) Imprint of the signal by a rotation $e^{-i\phi_k S_z}|\psi_0\rangle$ where $\phi_k \equiv \Delta\phi_k$ is the accumulated phase in cycle k. (iii) Measurement of S_y. Note that the signal of this protocol is $\langle S_y\rangle(\phi) = \langle\psi_0|S_x|\psi_0\rangle\,\sin(\phi)$, which is in close resemblance to the Ramsey interferometer with uncorrelated atoms as long as $\mu \lesssim \frac{2}{\sqrt{N}}$.

At this point, conceptual insight into the stability of an atomic clock can be gained by looking at the residual error in a single feedback cycle. Assuming cancellation of the local oscillator noise, by completely subtracting $\check{\overline{\Delta\nu}}$ in the feedback, the residual fractional frequency error can be expressed as

$$\overline{y}_1 = \frac{\overline{\Delta\nu_1} - \check{\overline{\Delta\nu_1}}}{\nu_0} = \frac{\phi_1 - \check{\phi}_1}{2\pi\nu_0 T_{\mathrm{R}}}. \tag{3.26}$$

Based on the sinusoidal Ramsey signal $\langle S_y\rangle(\phi)$, the phase estimate in cycle k can be expressed as

$$\check{\phi}_k = \frac{1}{2\pi T_{\mathrm{R}}} \frac{\mathcal{S}_{y,k}(\phi_k)}{\frac{\mathrm{d}\langle S_y\rangle}{\mathrm{d}\phi}\Big|_{\phi=0}} \tag{3.27}$$

where $\mathcal{S}_{y,k}(\phi_k)$ is the random outcome of the S_y measurement in cycle k. Thus the frequency estimate has $\check{\overline{\Delta\nu}}_k = \frac{\check{\phi}_k}{2\pi T_{\mathrm{R}}}$ as long as $\phi_k \ll 1$ for all k. Under this condition, the estimate also satisfies $\left\langle \check{\overline{\Delta\nu}}_k \right\rangle = \overline{\Delta\nu_k}$ and the standard deviation for $\overline{y}_k$ is

$$\langle\Delta\overline{y}_k\rangle = \frac{1}{2\pi\nu_0 T_{\mathrm{R}}} \frac{\langle\Delta S_y\rangle(\phi_k)}{\frac{\mathrm{d}\langle S_y\rangle}{\mathrm{d}\phi}\Big|_{\phi=0}}. \tag{3.28}$$

With $\phi_k \ll 1$ as above, this clearly shows the appearance of the standard phase variance $\Delta\phi = \frac{\langle\Delta S_y\rangle}{\frac{\mathrm{d}\langle S_y\rangle}{\mathrm{d}\phi}\big|_{\phi=0}}$, expressing QPN, as defined in chapter 2. Assuming that the residual noise is dominated by the white atomic projection noise, the fractional frequency deviations are uncorrelated from cycle to cycle, i.e. $\langle\Delta\overline{y}_k\Delta\overline{y}_n\rangle = \delta_{kn}$. In this case, performing τ/T_{C} repeated independent measurements over an averaging time τ gives

$$\sigma_y(\tau) = \frac{1}{2\pi\nu_0 T_{\mathrm{R}}}\sqrt{\frac{T_{\mathrm{C}}}{\tau}} \int_{-\infty}^{\infty} \mathrm{d}\phi\,(\phi - \check{\phi})^2 \mathscr{P}(\phi) \approx \frac{\Delta\phi}{2\pi\nu_0 T_{\mathrm{R}}}\sqrt{\frac{T_{\mathrm{C}}}{\tau}} \tag{3.29}$$

for the long-term clock stability, i.e. when $\tau \gg T_{\mathrm{C}}$. We have assumed that the phases are identically distributed in each cycle, following the distribution $\mathscr{P}(\phi)$, and the final approximation holds for narrow phase distributions. Note that Eq. (3.29) reflects only the instability contribution from projection noise. Other contributions need to be considered as well to obtain the full instability of the clock.

Equation (3.29) provides several important insights: First, it motivates the use of high-frequency transitions, e.g. in the optical regime, as the stability of the clock improves with ν_0^{-1}. While $\sigma_y \propto \nu_0^{-1}$ was derived here specifically for Ramsey interrogation, the statement remains true for general signals [Rie06, LBY$^+$15]. Looking towards the future, even transitions in the ultraviolet and beyond can be envisioned [LBY$^+$15]. However, clocks in this frequency regime are currently limited by the lack of suitable spectrally narrow local oscillators and means to count the fast oscillations, which was enabled for optical clocks by the optical frequency comb. Apart from the high atomic oscillation frequency, one also needs to consider the coherence properties of the two oscillators, the laser and the atoms, involved in the clock. In general, dephasing will eventually reduce the validity for the derivation of Eq. (3.29) and, as the condition of small phases is broken, cause a loss of stability. Since the measurement determines only differential phases, at which point this trade-off sets in depends on which oscillator dephases first and thus limits the stability. Narrow optical transitions, which reach long coherence times due to particularly long lifetimes of the two clock states, have been identified from precision spectroscopy [CHT$^+$11, MHG$^+$18, NYE$^+$19]. Those are some of the transitions that are commonly aimed for as clock transitions. The long atomic coherence time, however, means that for clocks of the highest quality, it is actually the laser phase noise, which is limiting. Giving even more emphasis to the discussion of section 3.2.1.

Modeling and simulating measurement noise Looking further at Eq. (3.29) we can see that knowing quantities like the mean signal $\langle S_y\rangle(\phi)$ and the variance $(\Delta S_y)^2(\phi)$ of the measurement, as functions of the phase, will be important to model the stability of an atomic clock. However, if we aim to describe the actual process that takes place in each clock cycle, it is not enough to know only these two statistical moments. In each cycle the detection process will return one particular realization out of the spectrum of measurement outcomes. Therefore the full distributions are relevant. Calculating the distributions and sampling the outcomes can be expressed even for the general extended protocols with expectation values in the form of Eq. (2.37) and not just under the restriction to weakly squeezed states. As we feel that such a description is instructive for future simulations of extended clock protocols, that notation will be used in the following. In the case of a measurement of S_y the outcomes $M \in \left\{-\frac{N}{2}, -\frac{N}{2}+1, \ldots, \frac{N}{2}-2, \frac{N}{2}-1, \frac{N}{2}\right\}$ can occur and we denote

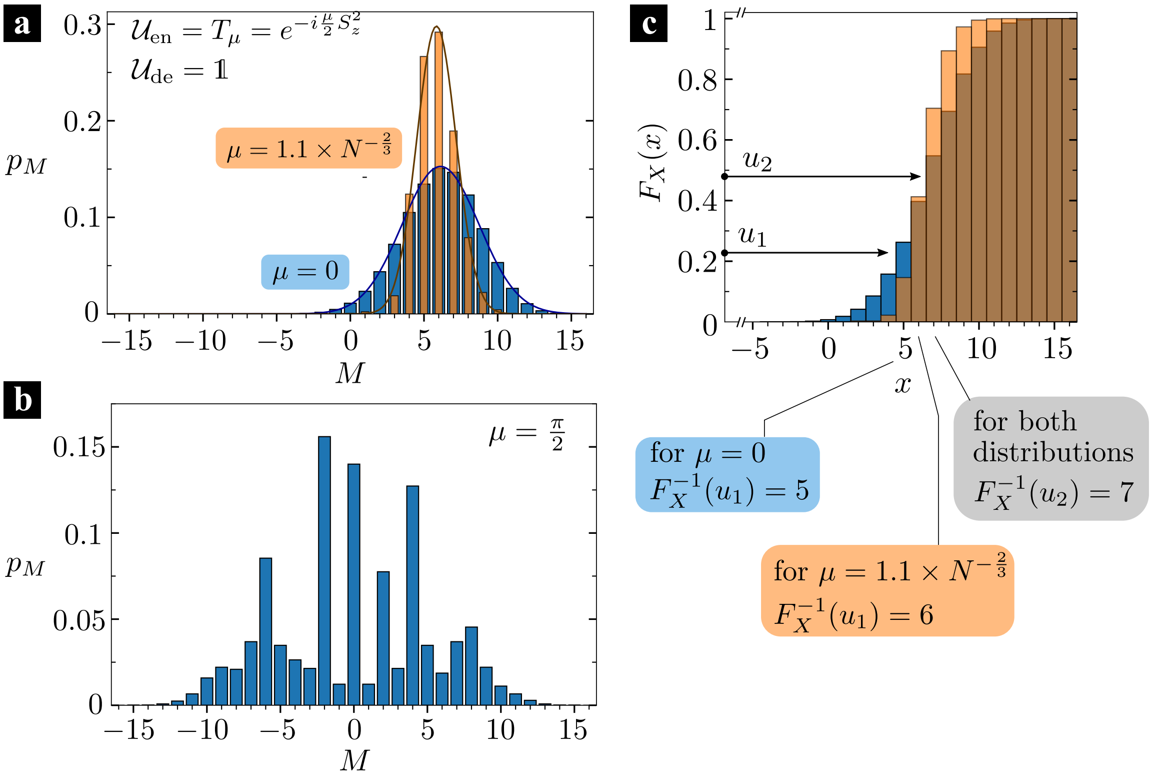

Figure 3.5: **Measurement distributions and sampling: a** Probability distribution p_M for measurement outcome M given an optimally squeezed state (orange) or uncorrelated atoms (blue). In both cases $N = 32$. Each initial state is rotated by $\phi = \frac{\pi}{8}$ to show the impact of a phase signal. Full lines are Gaussian normal distributions with mean and variance according to Eq. (3.36) and Eq. (3.37). **b** Distribution for an over-squeezed state at $\mu = \frac{\pi}{2}$, again with $\phi = \frac{\pi}{8}$. **c** Cumulative distribution function $F_X(x)$ for the two distributions displayed in **a**. When sampling random uniform numbers u_1, u_2, random measurement results with the correct statistics are obtained by calculating $F_X^{-1}(u_{1,2})$.

the corresponding eigenstates (Dicke state in the y-basis) by $|M\rangle_y$. The probability of detecting measurement result M at the end of cycle k is then by the Born rule

$$p_M = \left|\, {}_y\langle M|\psi(\phi_k)\rangle \,\right|^2, \tag{3.30}$$

where $|\psi(\phi_k)\rangle = \mathcal{U}_{\text{de}}\, R_z(\phi_k)\, \mathcal{U}_{\text{en}} |\text{x}\rangle$. Collecting the results for each M value will give distributions like the one shown in Fig. 3.5**a**-**b**. We have already encountered such distributions for uncorrelated atoms when first discussing quantum projection noise. Depending on the acquired phase ϕ_k, the statistics will then change. In the simplest case, the mean value $\overline{M}$ of the distribution bears the dependence of ϕ_k. This means that an estimate about the phase difference can be derived from a single measurement result of S_y, see also Ref. [PSO+18] and the method of moments introduced in section 2.4.6. If the dependency of the phase is contained solely in higher moments of the distribution, nonlinear measurements of the spin components or a reconstruction of the statistics from many repetitions of identical measurements are necessary. The first option is technically demanding and the latter option is difficult to perform reliably in atomic clocks due to the fluctuating nature of ϕ_k. It is therefore desirable to keep the dependence on ϕ_k on the mean of the distribution and ideally the functional dependence is simple.

During the numerical simulation of quantum mechanical states in the clock cycle, a random result is sampled in each cycle according to the distribution which results for the simulated differential phase $\phi_k = 2\pi\overline{\Delta\nu}_k T_{\mathrm{R}}$ of the free-running laser. For the purpose of generating random outcomes, inverse transform sampling [Dev86] can be used: Let

$$F_X(x) = \Pr[X \leq x] \tag{3.31}$$

be the cumulative distribution function for the random variable X. This function takes as input a value x of the outcomes for X and returns the probability $P_x = \Pr[X \leq x]$ that a random variable of the distribution takes a value $X \leq x$. For example, when X is the discrete random measurement outcome of S_y, then $x \in \left\{-\frac{N}{2}, -\frac{N}{2}+1, \ldots, \frac{N}{2}-1, \frac{N}{2}\right\}$ and P_x is the probability to detect at most x excited qubits in the y-basis. Of course $0 \leq F_X \leq 1$. Expressed in terms of the probability density $f_X(x)$ (or p_M for discrete outcomes), the cumulative distribution function is

$$F_X(x) = \int_{-\infty}^{x} f_X(t)\,\mathrm{d}t \quad \text{or} \quad F_X(x) = \sum_{k=-\frac{N}{2}}^{x} p_k \tag{3.32}$$

for continuous or discrete random variables, respectively. The domain of the discrete distribution are the eigenvalues of the observable. Now the inverse function to the cumulative distribution function can be defined as

$$F_X^{-1}(u) = \inf\left\{x \mid F_X(x) \geq u\right\}. \tag{3.33}$$

If Unif$[0,1]$ is the uniform distribution on the interval $[0,1]$, then $F_X^{-1}(\mathrm{Unif}[0,1])$ has F_X as its cumulative distribution function [Dev86]. Thus, when generating a random number u of Unif$[0,1]$, one obtains directly, via $F_X^{-1}(u)$, a realization of the quantum mechanical measurement according to its corresponding distribution. The procedure is illustrated in Fig. 3.5**c**. This method can be used for the general distributions, which we are concerned with here. Note that for the particular case of uncorrelated atoms the sampling can also be simplified. In that case, one can do sampling on the individual particle: For atom j (where each atom has excitation probability p in the specific basis), draw a random number u_j with uniform distribution and assign the value $v_j = 0$ when $u < p$ or $v_j = 1$ when $u \geq p$. Calculating $\sum_{j=1}^{N} v_j$ gives a random sample for measuring the number of excited qubits in that basis.

While the procedure outlined above enables a complete numerical treatment, using the full quantum statistics is not practical for making analytic estimations of the long term stability. However, this can be achieved when assuming weakly squeezed states only. With $\mathcal{U}_{\mathrm{de}} = \mathbb{1}$, one can include the signal rotation as part of the measurement step to simplify the description. Formally, the expectation value in this case is

$$\begin{aligned} \langle S_y \rangle(\phi) &= \langle \mathrm{x} | \mathcal{U}_{\mathrm{en}}^{\dagger} \, R_z^{\dagger}(\phi) \, S_y \, R_z(\phi) \, \mathcal{U}_{\mathrm{en}} | \mathrm{x} \rangle \\ &= \langle \mathrm{x} | \mathcal{U}_{\mathrm{en}}^{\dagger} \, (S_y \cos\phi + S_x \sin\phi) \, \mathcal{U}_{\mathrm{en}} | \mathrm{x} \rangle \\ &= \langle S_y \rangle \cos(\phi) + \langle S_x \rangle \sin(\phi) \, . \end{aligned} \tag{3.34}$$

Similarly, the variance is

$$\begin{aligned} \langle (\Delta S_y)^2 \rangle(\phi) = \cos^2(\phi) \langle (\Delta S_y)^2 \rangle + \sin^2(\phi) \langle (\Delta S_x)^2 \rangle \\ + \cos(\phi) \sin(\phi) \left(\langle S_y S_x + S_x S_y \rangle - 2 \langle S_y \rangle \langle S_x \rangle \right) . \end{aligned} \tag{3.35}$$

The above transformations are useful, as now all expectation values and variances are in relation to the initial state $|\psi_0\rangle$ only. With $|\psi_0\rangle = \mathcal{U}_{\mathrm{en}} |\mathrm{x}\rangle \equiv R_x(\theta_0) T_\mu |\mathrm{x}\rangle$, Eq. (3.34) and Eq. (3.35) simplify to

$$\langle S_y \rangle(\phi) = \langle \psi_0 | S_x | \psi_0 \rangle \, \sin(\phi) \tag{3.36}$$

and

$$\langle (\Delta S_y)^2 \rangle(\phi) = \cos^2(\phi) \, \langle \psi_0 | (\Delta S_y)^2 | \psi_0 \rangle + \sin^2(\phi) \, \langle \psi_0 | (\Delta S_x)^2 | \psi_0 \rangle \, . \tag{3.37}$$

Here we used that $\langle \psi_0 | S_y | \psi_0 \rangle = \langle \psi_0 | S_z | \psi_0 \rangle = 0$ and

$$\langle \psi_0 | S_y S_x + S_x S_y | \psi_0 \rangle = \langle \psi_0 | S_z S_x + S_x S_z | \psi_0 \rangle = 0, \tag{3.38}$$

as can be directly inferred from Eq. (A.31) and Eq. (2.58). With the reduced variance aligned along the measurement direction S_y, the exact expressions for the variances are [KU93]

$$\langle (\Delta S_y)^2 \rangle = \frac{N}{4} \left(1 + \frac{1}{4} (N-1) (A - \sqrt{A^2 + B^2}) \right) \tag{3.39}$$

and

$$\langle (\Delta S_x)^2 \rangle = \frac{N}{4} \left(N \left(1 - \cos^{2N-2}\left(\frac{\mu}{2}\right) \right) - \left(\frac{N}{2} - \frac{1}{2} \right) A \right) \tag{3.40}$$

with $A = 1 - \cos^{N-2}(\mu)$, $B = 4 \sin(\frac{\mu}{2}) \cos^{N-2}(\frac{\mu}{2})$. The measurement contrast decays as

$$\langle S_x \rangle = \frac{N}{2} \cos^{N-1}\left(\frac{\mu}{2}\right) . \tag{3.41}$$

Working in the small squeezing strength regime, we are able to approximate the stochastic measurement outcomes for $N \gg 1$ by Gaussian random variables. This means that we neglect any cumulants of order three or higher in the probability distributions for measurement results of $S_{x,y,z}$. Already in Fig. 3.5**a** the close resemblance of the distributions p_M with the Gaussian distributions is visible. Due to the vanishing correlations between S_x and S_y for OAT states, see Eq. (3.38), the measurement outcomes can be further separated as a linear combination of two independent Gaussian random variables, describing the results of S_x and S_y respectively. The random measurement outcome for the weakly squeezed state in cycle k is then approximated by the continuous random variable

$$\mathcal{S}_{y,k} = \langle S_x \rangle \left[\left(1 + \frac{\Delta S_x}{\langle S_x \rangle} \mathcal{N} \right) \sin(\phi_k) + \frac{\Delta S_y}{\langle S_x \rangle} \mathcal{N} \cos(\phi_k) \right] \tag{3.42}$$

where $\mathcal{N}$ are standard-normally distributed random variables with expectation value 0 and variance 1. Standard deviations $\Delta S_y := \sqrt{\langle (\Delta S_y)^2 \rangle}$ and $\Delta S_x := \sqrt{\langle (\Delta S_x)^2 \rangle}$ can be inferred from Eqs. (3.39)-(3.40). The outcomes in the numerical simulation are constrained by the fact that their value range may not exceed $-N/2$ to $N/2$ and each result is statistically independent from all others. Making the Gaussian approximation is vital to formulate the stochastic differential equation and finally obtain an analytic estimation on the stability, see section 3.4.2.

3.2.3 Servo and feedback application

Apart from the phase measurement, the servo is the other part which connects the atomic reference with the laser by performing the feedback corrections in each cycle. Different modes of feedback are available for atomic clocks and a more complete theoretical treatment falls in the category of control theory. It turns out that the particular choice of the servo has an impact on the short term stability and can affect the long term stability as well. The former has been studied e.g. by comparing a simple integrator and a generalized linear integrator [LSH⁺17], so we will not dwell on it here. In regard to the latter, one important point is that in order to cancel out the strongly correlated random walk noise or correcting deterministic frequency drifts, the feedback of the servo must be adapted. If an integrator is used as the servo, then a second stage of the integrator must be included for the strongly correlated noise. The necessity will be shown directly in the analytic model developed in section 3.4. This thesis does not consider general feedback strategies but rather focuses on an integrating servo only. Therefore more in-depth studies of other control schemes remain an open problem. Also for all numerical simulations presented in this chapter an integrating servo was used.

3.3 Limits to the clock stability

Having introduced the basic components of an optical atomic clock, we will now continue by evaluating which processes constitute the most relevant limitation to the long term stability in simple architectures. Under the assumption of ideal atoms, without systematic errors on ν_0, this becomes a study at the interplay of quantum mechanical measurement noise and quantum metrological phase estimation as well as classical control theory and laser phase noise.

For an atomic clock whose stability is exclusively limited by the QPN of the spin measurements ΔS_y, the Allan deviation would asymptotically be [WBI+92]

$$\sigma_{\mathrm{QPN}}(\tau) = \frac{1}{2\pi\nu_0 T_{\mathrm{R}}}\sqrt{\frac{T_{\mathrm{C}}}{\tau}}\frac{\xi}{\sqrt{N}}, \tag{3.43}$$

as motivated before. Here N is the number of clock atoms and $\xi = \sqrt{N}\Delta S_y/\langle S_x\rangle$ is the Wineland spin squeezing parameter [WBI+92]. For uncorrelated atoms in a coherent spin state with mean spin polarization $\langle S_x\rangle \approx N/2, \langle S_y\rangle = \langle S_z\rangle = 0$, where $\xi = 1$, the QPN limited phase uncertainty $\Delta\phi = \xi/\sqrt{N}$ scales as $\Delta\phi = 1/\sqrt{N}$, the standard quantum limit. Correlated states of atoms with $\xi < 1$ can optimally change this scaling up to $1/N$ [PSO+18]. In particular spin squeezed states can reduce the QPN while maintaining a strong spin polarization, thus lowering ξ and ultimately σ_{QPN}. This was demonstrated explicitly for OAT states in chapter 2.

As Eq. (3.43) suggests, the stability can also be improved by increasing the interrogation time T_{R}, provided the QPN still remains the dominant noise process. Obviously, it will be beneficial to increase T_{R} to a point where this is no longer the case, and the QPN is reduced to a level where other processes contributing to the clock instability become comparable. Which other noise processes become relevant first depends on the type of atomic clock. For the extremely narrow-band transitions that can be used in optical atomic clocks it is the finite coherence time of the clock laser rather than that of the atoms that is the limiting factor. Laser phase noise affects clock stability in two ways: Firstly, by phase diffusion during dead time (see Fig. 3.1 **b**), the so-called Dick effect [Dic88] whose contribution to the Allan deviation σ_{Dick} is well known and summarized in section 3.4.1. Second, by phase diffusion during the interrogation, causing the distribution of phases prior to the measurement to become wider. When the Ramsey dark time T_{R} becomes comparable to the laser coherence time, the differential phase noise between laser and atomic reference can exceed the invertible domain of the Ramsey signal and thus no unambiguous estimate based on the measurement result is possible, as illustrated in Fig. 3.1 **d**. At this point, the feedback loop becomes ineffective, compromising stability in two ways: First, the finite laser coherence time contributes to the Allan deviation in the form of an additional diffusion process, which we refer to in the following as the laser coherence time limit (CTL). Building on previous work by Leroux *et al.* [LSH+17] and André *et al.* [ASL04, And05], we develop in section 3.4.2 a detailed stochastic model of the CTL from which we can infer its contribution to the Allan deviation σ_{CTL}. Second, laser phase noise can also result in an abrupt loss of clock stability when the stabilization passes to an adjacent fringe, causing the clock to run permanently wrong. We will show that the resulting limitation of the Ramsey time can be understood quantitatively in the framework of our stochastic model as a first escape time, giving good agreement with previous phenomenological estimates [LSH+17]. We find that in the regime of a good atomic clock, i.e. long laser coherence time and small dead time, fringe-hops and the CTL contribute either at a similar level or the diffusive process σ_{CTL} constitutes the more stringent limitation for the Ramsey interrogation, so that we concentrate the discussion on the diffusive process.

Incorporating these additional effects, the optimal operating point of the control loop has to be determined from a trade-off between QPN, Dick effect, and CTL, by minimizing the combined instability

$$\sigma_y(\tau) = \sqrt{\sigma^2_{\mathrm{QPN}}(\tau) + \sigma^2_{\mathrm{Dick}}(\tau) + \sigma^2_{\mathrm{CTL}}(\tau)}. \tag{3.44}$$

At this point a remark on the asymptotic stability is in order: Throughout this chapter, we will typically refer to Allan deviations at $\tau = 1\,\mathrm{s}$ only. What is meant by this is that we look for the pre-factor to the asymptotic $\sigma_y(\tau) \propto 1/\sqrt{\tau}$ scaling, found e.g. by extrapolating the Allan deviation from a regime with $\tau \gg T_{\mathrm{C}}$ back to $\tau = 1\,\mathrm{s}$, (see Fig. 3.6).[1] Even though the actual stability of the clock at $\tau = 1\,\mathrm{s}$ may be different, e.g. due to the transient response of the feedback loop, this quantity still provides us with a useful measure to compare the long term stability of different clocks without limitations based on their specific mode of operation. In particular as the long term stability is largely independent of the level of laser noise.

Now without already going into the specific functional dependence of σ_{Dick} and σ_{CTL} on the parameters that characterize the atomic clock, we can highlight the most important features of Eq. (3.44), most of which are intuitive to understand: Just as the QPN, the Dick noise is monotonically decreasing with longer Ramsey time as the relative weight of the dead time T_{D} goes down (we assume here that T_{D} and T_{R} are not dependent on each other). However, the CTL will increase with T_{R}, as explained above from the spread of the phase distribution. In contrast to QPN, both Dick and CTL noise do not depend on the size of the atomic ensemble N. This should be clear

---

[1] The asymptotic scaling is reached typically after a few thousand cycles of clock operations in simulations with a total of 8×10^5 cycles.

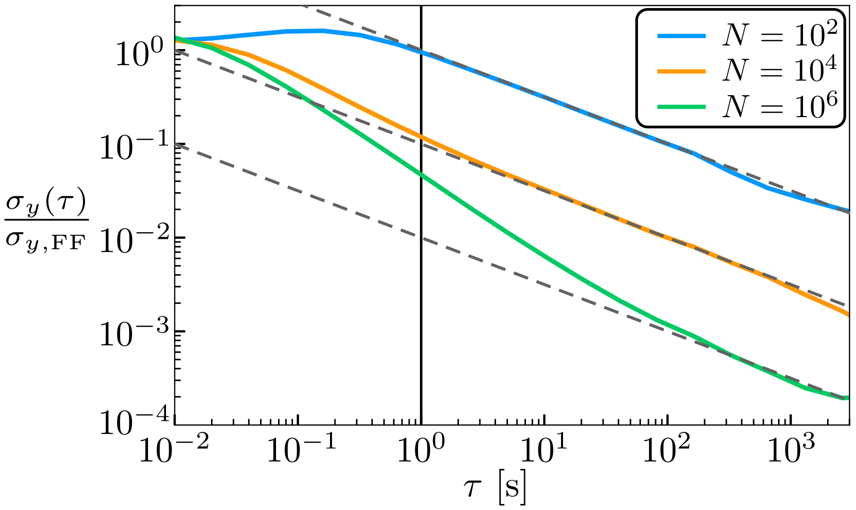

Figure 3.6: **Asymptotic stability:** Clock stability $\sigma_y(\tau)$ compared to the underlying local oscillator stability $\sigma_{y,\mathrm{FF}}$. For long averaging times $\tau \gg 1\,\mathrm{s}$ the clock stability reaches an asymptotic scaling $\propto \tau^{-1/2}$ (dashed lines). This can correspond to white atomic measurement noise or to the Dick effect (see section 3.4.1). Given this scaling, the long term stability is thus entirely determined by the pre-factor, i.e. the stability at $\tau = 1\,\mathrm{s}$. For simplicity we choose the parameters such that $Z = 1\,\mathrm{s}$.

for the Dick effect, which is determined by the laser noise, T_D and T_R only. The fact that the CTL does not depend on N is not so obvious, and will be shown below. For the weakly squeezed states this is related to the fact that the form of the Ramsey signal is most important for the CTL and this is independent of N. These scalings are visible in Fig. 3.7 which shows the combined Allan deviation, Eq. (3.44), and all three contributing noise processes versus Ramsey time for a small ensemble ($N = 10$, blue solid line) and a larger ensemble of atoms ($N = 2000$, red solid line) in a coherent spin state. Solid lines in Fig. 3.7 correspond to the analytical models, symbols show the results of numerical simulations of the closed feedback loop in excellent agreement with the theoretical curves. For all simulation results presented in this section we used moderate feedback with $g = 0.4$ and the squeezing strength was optimized beforehand for each N to give the lowest instability without dead time.

In view of Fig. 3.7, which concerns uncorrelated atoms in coherent spin states, several observations can be made: First, the instability will attain a minimum for a certain interrogation time T_opt. We assume for now that the clock can operate at this optimal time without running into technical problems such as optical path length fluctuations and others. Second, an important distinction has to be made with regard to the particle number N. For small ensembles, where QPN dominates over the Dick effect, the minimal instability is set by a trade-off between QPN and the CTL (cf. blue line in Fig. 3.7). This minimum depends on N. However, for large ensembles,

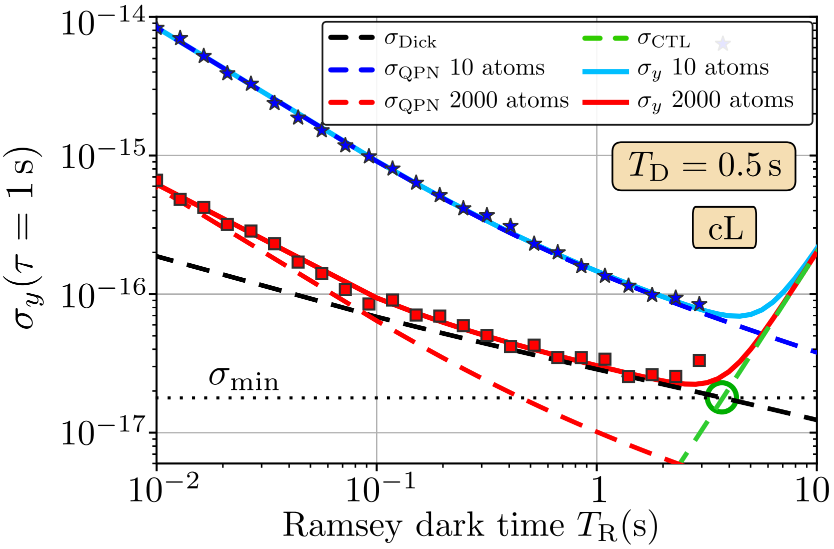

Figure 3.7: **A lower bound to the clock stability:** Allan deviation of an optical atomic clock at averaging time $\tau = 1\,\mathrm{s}$ as a function of Ramsey dark time T_{R} assuming a dead time $T_{\mathrm{D}} = 0.5\,\mathrm{s}$ and laser noise corresponding to the currently best ultra-stable clock lasers (cL) as characterized in Table 3.2. Solid lines are instabilities from the full noise model, Eq. (3.44), with $N = 10$ (blue) and $N = 2000$ (red) uncorrelated clock atoms. Dashed lines show the three contributing noise processes: QPN (blue and red), CTL (green), and the Dick noise (black). Symbols are numerical simulations of the closed feedback loop in agreement with the analytic model until the onset of fringe-hops leads to a sudden, strong increase in instability.

where the Dick effect dominates over QPN, the minimal instability is set by a trade-off between the Dick effect and the CTL (cf. red line in Fig. 3.7). This minimum does not depend on N and is determined only by laser noise and dead time. Minor deviations result from details of the feedback loop, gain factor and measurement contrast. In particular there exists a time T_{R}^* where both of these processes contribute equally, i.e. $\sigma_{\mathrm{Dick}}|_{T_{\mathrm{R}}^*} = \sigma_{\mathrm{CTL}}|_{T_{\mathrm{R}}^*} \equiv \sigma_{\mathrm{min}}$, cf. green circle in Fig. 3.7. This sets a lower bound for the combined Allan deviation $\sigma_y(\tau = 1\,\mathrm{s}) \geq \sigma_{\mathrm{min}}$ which is independent of the size N of the ensemble. How closely this bound can be saturated depends on the exact scaling of σ_{Dick} and σ_{CTL} with T_{R}. However, in the worst case σ_{min} lies only a factor $\sqrt{2}$ below the true minimum if both terms contribute equally. In Fig. 3.8 we show the minimal instability σ_{min} as a function of dead time T_{D} for four types of lasers, as summarized in Table 3.2: Again, one is the currently best laboratory clock laser (cL) which is limited by flicker frequency noise at an Allan deviation $\sigma_{\mathrm{FF}} = 4.9 \times 10^{-17}$ [M$^+$17]. The others are two future generation clock lasers, pL1 and pL2, with projected improved noise spectra and last is a laser for transportable atomic clocks (tL) whose stability is reduced compared to the laboratory clock lasers. For all types of lasers an almost universal behaviour emerges, as shown in the inset

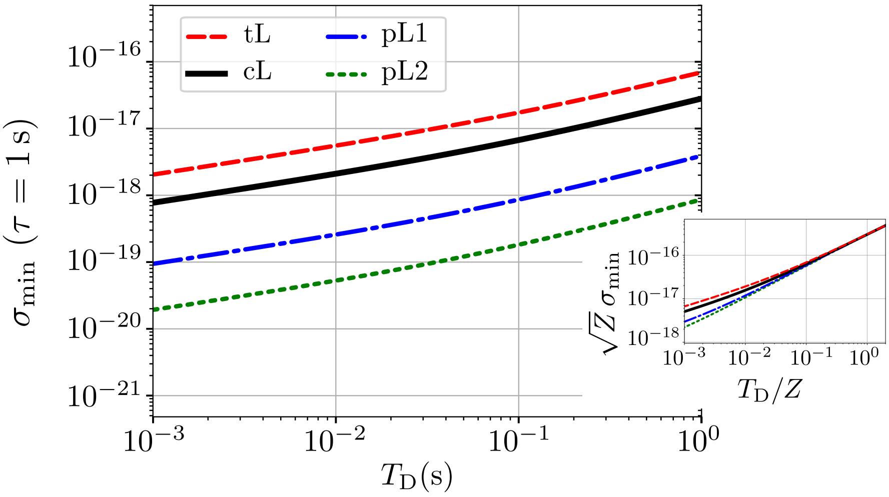

Figure 3.8: **Minimal clock stability:** Lower bound $\sigma_{\rm min}$ to the minimal instability as a function of dead time for four different types of clock lasers (tL, cL, pL1, pL2) as defined in Table 3.2. Inset: Normalizing by the laser coherence time Z (as defined in section 3.2 and given in Table 3.2) reveals an almost universal scaling with $\sqrt{Z}\sigma_{\rm min} = 3.0\ 10^{-16}\,(T_{\rm D}/Z)^{0.7}$ at longer dead times. We use the transition frequency $\nu_0 \approx 429.228\,$THz of ^{87}Sr for calculations.

of Fig. 3.8, upon re-scaling $T_{\rm D}$ and $\sigma_{\rm min}$ by the laser coherence time Z. Deviations from this behaviour are likely due to the complicated dependence of $\sigma_{\rm Dick}$ on the duty factor $T_{\rm R}/T_{\rm C}$. Note also that at $T_{\rm D} < 10^{-3}\,$s contributions to the Dick effect from neglected technical high frequency noise, at Fourier frequencies $f \geq 1\,$kHz, can become significant compared to the noise sources considered in this thesis. The laser coherence time Z is as introduced in section 3.2, see also Table 3.2 for the values corresponding to the lasers compared here.

So far, all statements referred to uncorrelated atoms. Provided we perform Ramsey interrogation of a single ensemble of atoms, under which conditions can the clock stability be improved by employing squeezed spin states? First, it is clear that the limitation due to dead time in form of the Dick effect will not be reduced by atomic correlations. On the contrary, additional preparation time may even lead to an increase in instability there. Strongly squeezed or other highly entangled states will result in a more restrictive CTL and are unfavorable also for several other reasons (stronger decoherence, unfeasible requirements on measurements etc.). We had observed the steep incline of the signals at $\phi = 0$ in chapter 2. With a reduced range of unambiguous phase estimation these protocols will suffer from an increased CTL and earlier fringe-hops. Therefore we consider here only moderately squeezed states which maintain the fringe width and contrast, leaving the CTL largely at the level of coherent states [ASL04]. Specifically, we assume states generated via the unitary one-axis twisting interaction $e^{-i(\mu/2)S_z^2}$ for which the squeezing strength, $\mu \approx 1.1\, N^{-2/3}$, was independently optimized beforehand to give the lowest instability for a given particle number N in the dead time free case. Compared to chapter 2, this choice corresponds to squeezing protocols without the additional echo. Also the scaling of the optimal values for μ is the same as for the local minima along the $\nu = \mu$ line in the landscapes calculated there. Since a new preparation of the initial state is the only necessary requirement, this reduced variational class is comparatively easy to implement and robust against errors in the squeezing interactions. The resulting optimal spin squeezing parameter in this case is $\xi^2 = \mathcal{O}(N^{-2/3})$. Further improvements to the squeezing parameter using the one-axis twisting interaction would need modifications of the protocols with additional control interactions. For example with more elaborate interactions $\mathcal{U}_{\text{en}}, \mathcal{U}_{\text{de}}$ in the very general Ramsey interferometry of chapter 2 or some nonlinear measurements [GSP19]. Comments on the use of more complex variational Ramsey protocols for optical atomic clocks will be provided in section 3.6.2.

Considering the weakly squeezed initial states, we thus arrive at the important conclusion that – with CTL and Dick noise being unchanged – the combined instability is limited by σ_{min}, independently of the degree of squeezing. This limit will eventually be met when the QPN is reduced below σ_{min}, either by means of spin squeezing (reducing ξ) or using a larger ensemble of atoms. Figure 3.9 shows the Allan deviation versus particle number for various levels of dead time when using coherent spin states (CSS) or optimized spin squeezed states (SSS). This reflects precisely the aforementioned approach to the limit σ_{min} in both cases. For sufficiently large ensembles, CSS and SSS approach the same limit given by σ_{min}. From the illustration of the crossover between the two regimes, with N below and above N_{min}, one can infer on the one hand the gain that squeezing provides at small ensemble sizes while it is clear that nothing can be gained by squeezing ensembles with $N > N_{\text{min}}$. Additionally, Fig. 3.9 shows that N_{min} cannot represent a sharp threshold value, but should rather be understood in the context of the asymptotic approach to σ_{min} depicted there.

We infer that, especially for large ensembles, squeezing can provide a gain in stability only for quite challenging levels of dead time. These conclusions also imply that the asymptotic (large N) scaling of phase sensitivity in quantum metrology is largely irrelevant in the setting considered here. As a caveat we again note that our statements are based on the assumption of Ramsey or similar conventional interrogations of a single ensemble and spin projection measurements. More exotic protocols may be subject to different limitations (for better or worse). Of course the asymptotic scaling would also be relevant again in the special case $T_{\text{D}} = 0$. The critical number of particles N_{min}, which is required to achieve the minimal instability for a given dead

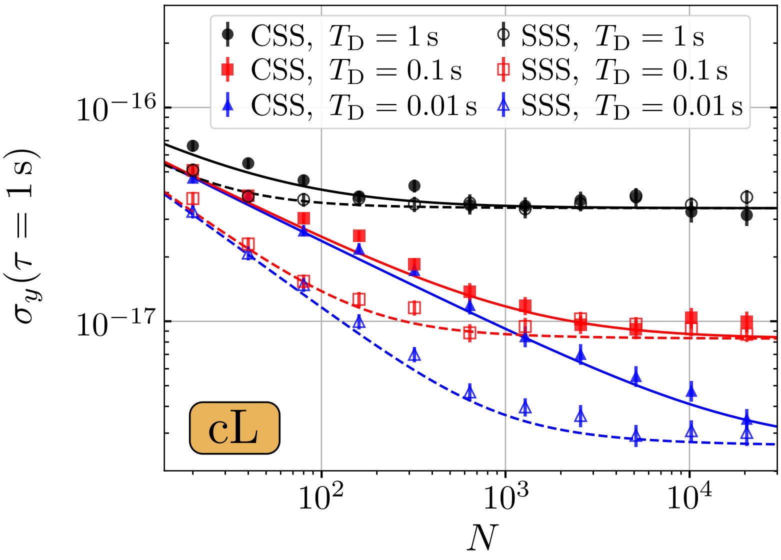

Figure 3.9: **Approaching the optimal stability:** Particle number scaling towards the lower bound $\sigma_{\min}$ for $T_D = 1\,$s, $0.1\,$s, $0.01\,$s. The stability for each N is optimized over the Ramsey time. Compared are uncorrelated atoms in a coherent spin state (CSS, full lines and symbols) and squeezed spin states (SSS, dashed lines and empty symbols).

time, laser stability, and degree of squeezing ξ, is set by the condition that the QPN dives below $\sigma_{\min}$, that is

$$N_{\min} = \min_N \{ \sigma_{\mathrm{QPN}}|_{N,T_R^*} \leq \sigma_{\min} \} . \tag{3.45}$$

Note that for $T_D = 0$, the Dick effects contribution in Eq. (3.44), being the only one that cannot be reduced by larger N, vanishes and the definition of $N_{\min}$ is no longer meaningful. In that case also $\sigma_{\min} \to 0$, and the stability of a clock with a finite ensemble size would depend on N and Z only [ASL04, LSH+17]. For $T_D = 0$ one should employ weakly squeezed states for any particle number as the trade-off in Eq. (3.44) is between QPN and CTL only. The definition in Eq. (3.45) is equally valid for uncorrelated as well as squeezed spin states. In Fig. 3.10 **a** we show $N_{\min}$ for uncorrelated particles (full lines) and squeezed states (dashed) versus T_D. At small dead times this shows the expected significant reduction $N_{\min}^{(\mathrm{SSS})} < N_{\min}^{(\mathrm{CSS})}$ for squeezed states, which results from the reduction of the squeezing parameter. We conclude that an increased stability using spin squeezed states is only possible in small ensembles with particle numbers $N < N_{\min}^{(\mathrm{CSS})}$ for a given T_D and laser noise. This result highlights how the envisioned improvements in the laser coherence time will eventually make larger ensembles or squeezed states in lattice clocks necessary. In order to assess the long-term perspectives of squeezed states, we show in Fig. 3.10 **b** the critical particle number $N_{\min}$ as a function of laser instability. In this case we

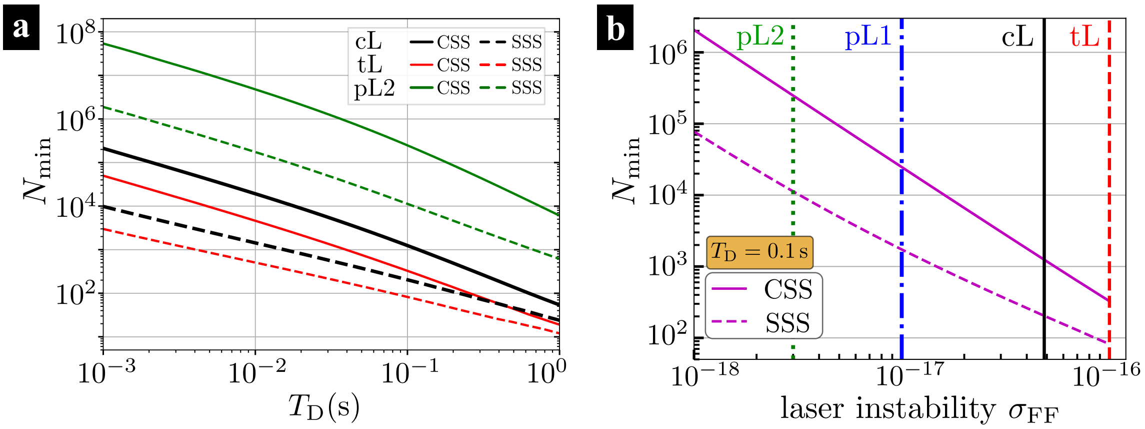

Figure 3.10: **Scaling of the critical particle number:** **a** Minimal required particle number for reaching the stability limit with uncorrelated particles (full lines) or spin squeezed initial states (dashed lines). **b** Increase of the critical particle number N_{min} with improved laser stability for coherent spin states and squeezed spin states. Vertical lines show the four highlighted laser types described in the main text. The labels (tL, cL, pL1, pL2) denote the respective laser phase noise, as specified in Table 3.2, in all parts of the figure.

considered lasers which are dominantly limited by flicker frequency noise and then scale the entire noise spectrum. The respective value for σ_{FF} serves as an indicator for the stability. Comparing the two curves shows a slowly increasing separation with reduced instability. The results predict a significant reduction of the required particle numbers when using squeezed states, compared to reaching the same stability with uncorrelated particles, only at high laser quality. Thus, the model allows to identify concrete conditions of laser stability, from which point on squeezing becomes relevant even for relatively larger ensembles as used in lattice clocks. However, the required laser stability goes far beyond the currently best technical achievements (vertical solid line) and requires considerable improvement of the clock lasers (corresponding to green or blue dashed lines).

Finally, the results presented above may be altered if there exists some additional process which places an upper bound T_{max} to the Ramsey time. This could occur due to coherence losses from collisions, photon scattering, a limited natural lifetime or others. Of course, in the case $T_{\mathrm{R}}^* \leq T_{\mathrm{max}}$, i.e. where T_{max} is larger than the optimal interrogation time T_{R}^* identified above, our results are unchanged. In this case the additional constraint T_{max} would only be relevant after the optimal interrogation time is already reached. When $T_{\mathrm{R}}^* \geq T_{\mathrm{max}}$ one can define the new critical particle number

$$\tilde{N}_{\mathrm{min}}(T_{\mathrm{max}}) = \min_{N}\{\sigma_{\mathrm{QPN}}|_{N,T_{\mathrm{max}}} \leq \sigma_{\mathrm{Dick}}|_{T_{\mathrm{max}}}\}\,. \tag{3.46}$$

For example, at $T_{\mathrm{D}} = 0.1\,\mathrm{s}$ and assuming the laser cL, we find that the critical particle number changes only from $N_{\text{min}} = 1244$ to $\tilde{N}_{\text{min}}(T_{\text{max}} = 0.1\,\text{s}) = 3504$, $\tilde{N}_{\text{min}}(T_{\text{max}} = 1\,\text{s}) = 1475$ and remains unchanged if $T_{\text{max}} > 2.6\,\text{s}$. T_{R}^* is on the order of a few seconds for cL, see App. B and is expected to increase by a factor of 5 and 16 for the improved laser parameters pL1 and pL2 respectively.

The logic presented above so far neglected the effects of fringe hops, which might preclude a stable clock operation at the optimal Ramsey time T_{R}^* for a clock comprised of N_{min} atoms. To assure the validity of our results we therefore compare T_{R}^* with the Ramsey time T_{FH} at which fringe-hops appear with probability 1 per total number of clock cycles ($\sim 10^6$ in the numerical simulations performed here). We are able to determine T_{FH} by extending the stochastic differential equation formalism to an equivalent Fokker-Planck equation (see section 3.4.2). From this, a mean first escape time for the phase of the stabilized laser can be calculated. We find that fringe-hops set in once the escape time from the interval $[-\pi, \pi]$ reaches the total number of clock cycles. Our results are in agreement with a previous phenomenological guide $T_{\text{FH}} = (0.4 - 0.15 N^{-1/3}) Z$ [LSH+17]. In this way we found that the minimal instability can be achieved prior to being limited by fringe-hops, i.e. $T_{\text{R}}^* < T_{\text{FH}}$, with exceptions only in regimes of short laser coherence times and long dead times, as will be shown later in Fig. 3.12.

3.4 Models for noise processes and instability

In this section we will provide more technical background for the description of the different instability contributions: The Dick effect as well as QPN and the CTL with the latter two being inferred by the study of a stochastic differential equation model for the clock feedback cycle.

3.4.1 Instability related to the Dick effect

For typical atomic clocks with cyclic operation, there is a contribution to the overall instability resulting from any dead time in which the frequency deviation from the atomic reference is not probed. Dead time commonly occurs in atomic frequency standards, e.g. when loading and preparing atoms or from the detection process. While shorter dead times are usually possible in ion based clocks, optical lattice clocks relying on destructive imaging techniques for state detection often operate with longer dead times in which the atomic sample has to be reloaded. The resulting instability can be understood conceptually from the fact that dead time leads to a loss of information about the fluctuating laser frequency and an aliasing effect of the laser noise. The discrete sampling process during clock operation converts high-frequency noise of the laser to additional noise at the frequency of the clock cycle. This so called

Dick effect has been known in atomic clocks since the earlier microwave frequency standards through the seminal works of G. J. Dick [Dic88]. It remains relevant for optical atomic clocks and has been a major practical limitation especially for current optical lattice clocks. Thorough evaluations of the Dick effect and its effect on clock stability for different schemes of operation has been developed before [DPGM90, SAM+98]. The resulting instability can be stated in terms of the noise spectral density of the laser and a function characterizing the sensitivity to phase shifts during the clock cycle, which includes the dead time and the applied measurement protocol. For example, in the case of Ramsey interrogation with infinitely short $\pi/2$ pulses, the sensitivity function is simply [Dic88]

$$w(t) = \begin{cases} 0 & 0 \leq t < T_\mathrm{D} \\ 1 & T_\mathrm{D} \leq t \leq T_\mathrm{C} \end{cases} . \tag{3.47}$$

Evaluating the low frequency component of the locked oscillator spectrum translates to an instability contribution [Dic88]

$$\sigma^2_{y,\mathrm{Dick}}(\tau) = \frac{1}{\tau} \sum_{k=1}^{\infty} S_{y,\mathrm{LO}}\left(\frac{k}{T_\mathrm{C}}\right) \left|\frac{g_k}{g_0}\right|^2 \tag{3.48}$$

for $\tau \gg T_\mathrm{C}$ and where

$$g_k = \frac{1}{T_\mathrm{C}} \int_0^{T_\mathrm{C}} w(t) e^{-2\pi i k t/T_\mathrm{C}}\,\mathrm{d}t \tag{3.49}$$

are the Fourier components of the sensitivity function and $S_{y,\mathrm{LO}}(f)$ is the laser's single-sided fractional frequency noise power spectral density. For the idealized Ramsey pulse we thus find

$$\sigma^2_{y,\mathrm{Dick}}(\tau) = \frac{1}{\tau} \frac{T_\mathrm{C}^2}{T_\mathrm{R}^2} \sum_{k=1}^{\infty} S_{y,\mathrm{LO}}\left(\frac{k}{T_\mathrm{C}}\right) \frac{\sin^2(\pi k T_\mathrm{R}/T_\mathrm{C})}{\pi^2 k^2} . \tag{3.50}$$

Within this thesis we assume $S_{y,\mathrm{LO}}(f) = \sum_{k=-2}^{0} b_k f^k$ with $b_{-2} = 2.4 \times 10^{-37}\,\mathrm{Hz}$, $b_{-1} = 1.7 \times 10^{-33}$, $b_0 = 1.3 \times 10^{-33}\,\mathrm{Hz}^{-1}$ for the state-of-the-art laboratory clock laser cL (see Table 3.2). To represent the other lasers of varying quality, the entire spectral density is scaled accordingly. For calculations we use $\nu_0 \approx 429.228\,\mathrm{THz}$ based on the clock transition in ^{87}Sr.

As emphasized in the above study of squeezing in clocks with finite dead time (see section 3.3), the Dick effect depends on parameter values of the clock operation: Increasing the portion of the clock cycle during which the atoms are probed, i.e. increasing the duty factor $T_\mathrm{R}/T_\mathrm{C}$, reduces the efficiency of the down-sampling. To harness this gain, one possibility for optical lattice clocks would be the implementation of non-destructive readout schemes [VBE+17]. Similarly, better lasers reduce the impact of the Dick effect when the spectral noise density is reduced. These two aspects can be directly inferred from Eq. (3.50).

Beyond the standard clock setup we considered in this study, there are also ways to reduce the Dick effect by increasing the complexity of the setup. Using two ensembles of atoms with anti-synchronized interrogation of the same laser enables a dead time free tracking of the noisy clock frequency. In this way, the composite setup constitutes an atomic clock which is basically free of the Dick effect noise. Though technically challenging, these techniques will need to be implemented, and extensions including correlated quantum states need to be developed, when operating with large ensembles, where the Dick noise is otherwise limiting. First proof of principle demonstrations have been shown, however without any quantum correlations. There, a high quality clock laser enabled interrogation times which were long enough to cover the dead time of the second ensemble [S+16].

3.4.2 Stochastic differential equation approach

For modeling the CTL we build on Refs. [ASL04, And05, LSH+17], and infer the instability due to measurement noise and ineffective feedback based on a stochastic differential equation (SDE). In a nutshell, the SDE describes the evolution of the stabilized laser frequency, driven by noise from the free-running laser but cyclically corrected using information from the measurements which includes quantum projection noise. The perturbative solution of the SDE, in powers of the laser phase variance, allows to describe the effects of finite laser coherence in lowest order. The CTL results as a contribution in third order of the laser phase variance. If the free-running laser stability is dominated by power-law noise, i.e. $\sigma^2_{\mathrm{LO}}(\tau) \propto \tau^\gamma$ with $\gamma = -1, 0, 1$ corresponding to white frequency, flicker frequency and random walk frequency noise respectively, the laser phase variance

$$V_\phi = \chi(\gamma)\,(T_{\mathrm{R}}/Z)^{2+\gamma} \tag{3.51}$$

scales at specific powers of T_{R}/Z and with $\chi(\gamma)$ of order unity. As a main result, the SDE gives

$$\sigma^2_{\mathrm{m+d}}(\tau) = V_{\mathrm{m+d}} T_{\mathrm{C}}/(2\pi\nu_0 T_{\mathrm{R}}\sqrt{\tau})^2 \tag{3.52}$$

where $V_{\mathrm{m+d}}$ is the variance of measurement outcomes when the dynamics is affected by laser phase diffusion. As this is a combined effect of measurement noise, leading to QPN, and phase diffusion, leading to the CTL, both contributions are inferred from $V_{\mathrm{m+d}}$ as we show in this section. Based on the SDE model, we will see that $V_{\mathrm{m+d}} = V_0 + V_1 + \mathcal{O}(V_\phi^4)$ with [And05]

$$V_0 = \frac{\Delta S_y^2}{\langle S_x\rangle^2} + \frac{\Delta S_x^2}{\langle S_x\rangle^2} V_\phi + \frac{3(1-c)^2}{8}\frac{\Delta S_y^2}{\langle S_x\rangle^2} V_\phi^2 \tag{3.53}$$

and

$$V_1 = (1/6 - c/2 + 4c^2/9)V_\phi^3. \tag{3.54}$$

Here $c = g\langle S_x\rangle/N$ and g is the gain factor of an integrating servo in the feedback loop. This result holds for Ramsey interrogation with weakly squeezed initial states, where measurement statistics are approximated by Gaussian distributions (as introduced in section 3.2.2). Now, $\sigma^2_{\mathrm{m+d}}$ can be separated in the following way: All terms in V_0 contain spin variances and $V_0 = \xi^2/N$ for $T_R \ll Z$. In this limit they reproduce the QPN, so

$$\sigma^2_{\mathrm{QPN}}(\tau) = V_0 T_{\mathrm{C}}/(2\pi\nu_0 T_{\mathrm{R}}\sqrt{\tau})^2. \tag{3.55}$$

The CTL is

$$\sigma^2_{\mathrm{CTL}}(\tau) = V_1 T_{\mathrm{C}}/(2\pi\nu_0 T_{\mathrm{R}}\sqrt{\tau})^2 \tag{3.56}$$

as V_1 is the lowest order with an N-independent contribution. This term results conceptually from the lowest order (cubic) non-linearity of the sinusoidal Ramsey signal. In the remainder of this section we will review the previous model for the clock dynamics, along with new results regarding the necessary feedback and ways to include fringe-hops. Most notably we discuss the effects of using a two-stage integrating servo to correct out local oscillator fluctuations in particular for more strongly correlated laser noise. Afterwards, we review how the nonlinear SDE can be solved approximately to generate the expression $\sigma_{\mathrm{m+d}}$ for the resulting clock instability in orders of the phase variances. Finally, we discuss the onset of fringe-hops and motivate a possible description via the mean first passage time.

Modeling the closed feedback loop In the following we consider an optical atomic clock which operates in repeated, identical cycles of duration T_{C} as introduced in section 3.2. Again, each cycle contains a Ramsey dark time $T_{\mathrm{R}} \equiv T$ as well as some dead time $T_{\mathrm{D}} = T_{\mathrm{C}} - T_{\mathrm{R}}$. Three frequencies are relevant to describe the clock operation:

(i) The ideal atomic transition frequency ν_0, which we assume is constant for all times.

(ii) The free-running laser frequency $\nu_{\mathrm{LO}}(t)$ as introduced in section 3.2. The stochastic fractional frequency noise has a noise power spectral density $S_{y,\mathrm{LO}}(f) = b_\alpha f^\alpha$ with $\alpha = -2, -1, 0$.

(iii) The stabilized laser frequency $\nu(t)$ which results from the periodic feedback corrections on the free running laser. The error signal for the feedback application is derived from probing the atomic ensemble within each cycle via Ramsey interferometry with a weakly squeezed state, cf. section 3.2.2.

In order to derive the long term stability of the clock, we start by discussing the evolution of the stabilized frequency $\nu(t)$ between successive interrogation intervals. Let us review from section 3.2 that the average stabilized frequency difference during the Ramsey dark time of cycle k is

$$\overline{\Delta\nu}_k = \frac{1}{T}\int_{(k-1)T_\mathrm{C}}^{(k-1)T_\mathrm{C}+T} (\nu(t)-\nu_0)\,\mathrm{d}t. \tag{3.57}$$

This gives rise to a differential phase

$$\phi_k = 2\pi\int_{(k-1)T_\mathrm{C}}^{(k-1)T_\mathrm{C}+T} (\nu(t)-\nu_0)\,\mathrm{d}t = 2\pi\,\overline{\Delta\nu}_k\,T \tag{3.58}$$

before the measurement at time $(k-1)T_\mathrm{C}+T$. Using the information about ϕ_{k-1}, and accordingly also $\overline{\Delta\nu}_{k-1}$, a feedback correction is applied to the free-running laser frequency at the end of each cycle. Due to the recursive nature of the feedback, the stabilized frequency difference in the following cycle can then be expressed as

$$\overline{\Delta\nu}_k = \overline{\Delta\nu}_{\mathrm{LO},k} - p_{k-1}. \tag{3.59}$$

The first term on the right hand side, $\overline{\Delta\nu}_{\mathrm{LO},k}$, is the average frequency difference contributed by the free-running laser in cycle k, whereas p_{k-1} is the frequency correction of the servo applied at the end of the previous cycle. Likewise, for the differential phase

$$\phi_k = 2\pi\,\overline{\Delta\nu}_k\,T = 2\pi\,T\,\overline{\Delta\nu}_{\mathrm{LO},k} - 2\pi\,T\,p_{k-1} \tag{3.60}$$

applies. The specific form of the servo correction p_{k-1} depends on the design of the control loop. A frequently used method of feedback is to have an integrator as the servo. In this case, the correction is constructed as

$$p_{k-1} = \frac{g}{2\pi T}\left(\check{\phi}_{k-1} + \frac{2\pi T}{g}p_{k-2}\right) = \frac{g}{2\pi T}\check{\phi}_{k-1} + p_{k-2}. \tag{3.61}$$

Here g is the gain factor and $\check{\phi}_{k-1}$ an estimator for the accumulated phase during the Ramsey interrogation in the previous cycle. The phase estimate is based on the outcome of the measurement, e.g. in the simplest case the estimator is just the measurement result itself. Combining Eq. (3.61) with Eq. (3.60) gives the coupled stochastic difference equations

$$\overline{\Delta\nu}_k - \overline{\Delta\nu}_{k-1} = \overline{\Delta\nu}_{\mathrm{LO},k} - \overline{\Delta\nu}_{\mathrm{LO},k-1} - \frac{g}{2\pi T}\check{\phi}_{k-1} \tag{3.62}$$

$$\phi_k - \phi_{k-1} = \phi_{\mathrm{LO},k} - \phi_{\mathrm{LO},k-1} - g\check{\phi}_{k-1} \tag{3.63}$$

for the average frequency difference and the phase. We now focus on the phase evolution, Eq. (3.63). Before we are able to treat these stochastic difference equations in detail we will need to again take a look at the atomic measurements which are contained within the phase estimates $\check{\phi}_k$.

Atomic noise Let us just briefly refresh the relevant results from section 3.2.2. In the case of Ramsey interferometry with weakly squeezed initial states it was found that the random measurement outcome in each cycle k can be approximated by the continuous random variable

$$\mathcal{S}_{y,k} = \langle S_x \rangle \left[\left(1 + \frac{\Delta S_x}{\langle S_x \rangle} \mathcal{N} \right) \sin(\phi_k) + \frac{\Delta S_y}{\langle S_x \rangle} \mathcal{N} \cos(\phi_k) \right] \tag{3.64}$$

where $\mathcal{N}$ are standard-normally distributed random variables with expectation value 0 and variance 1. The standard deviations $\Delta S_y := \sqrt{\langle (\Delta S_y)^2 \rangle}$ and $\Delta S_x := \sqrt{\langle (\Delta S_x)^2 \rangle}$ can be inferred from Eqs. (3.39)-(3.40).

Phase estimation to servo the laser frequency In the stochastic difference equation for the phase of the stabilized laser, Eq. (3.63), information about the frequency deviations of previous steps comes in via the estimate $\check{\phi}_{k-1}$. The fact that $\langle S_y \rangle(\phi) = \langle S_x \rangle \sin(\phi)$ shows that, on average, the measurement outcome of S_y is simply linear in ϕ as long as $\phi \ll 1$. So

$$\check{\phi}_{k-1} = \frac{\mathcal{S}_{y,k-1}}{S} \tag{3.65}$$

is an unbiased estimator in this regime. We denote by $\mathcal{S}_{y,k-1}$ the particular measurement outcome at the end of cycle $k-1$, see Eq. (3.64). Note that here the full measurement contrast $S = N/2$ was used for the phase estimation rather than the reduced contrast, which may not be precisely known beforehand. The linear estimation strategy, Eq. (3.65), is conceptually easy and well suited for analytic calculations. In the regime of small particle numbers it gives results which are basically indistinguishable from other non-linear estimation strategies. However, to reach the optimal scaling of the long-term stability with N for large particle numbers, $N \gtrsim 10^4$, non-linear estimation strategies such as

$$\check{\phi}_{k-1} = \arcsin\left(\frac{\mathcal{S}_{y,k-1}}{S} \right) \tag{3.66}$$

are necessary [ASL04]. The non-linear estimation strategy would ensure an unbiased estimation of the phase everywhere between $-\frac{\pi}{2}$ and $\frac{\pi}{2}$. Instead of classical post-processing of the measurement results in the form of non-linear estimation, the same result could also be achieved with an appropriate choice of $\mathcal{U}_{\mathrm{de}}$. In the case of weakly squeezed states, where the measurement outcomes $\mathcal{S}_{y,k-1}$ are Gaussian, the phase estimate reduces to

$$\begin{aligned} \check{\phi}_{k-1} = & \frac{\kappa}{T} \sin(\phi_{k-1}) \mathrm{d}t + \frac{\kappa}{\sqrt{T}} \frac{\Delta S_x}{\langle S_x \rangle} \sin(\phi_{k-1}) \, \mathrm{d}W_{x,k} \\ & + \frac{\kappa}{\sqrt{T}} \frac{\Delta S_y}{\langle S_x \rangle} \cos(\phi_{k-1}) \, \mathrm{d}W_{y,k} \end{aligned} \tag{3.67}$$

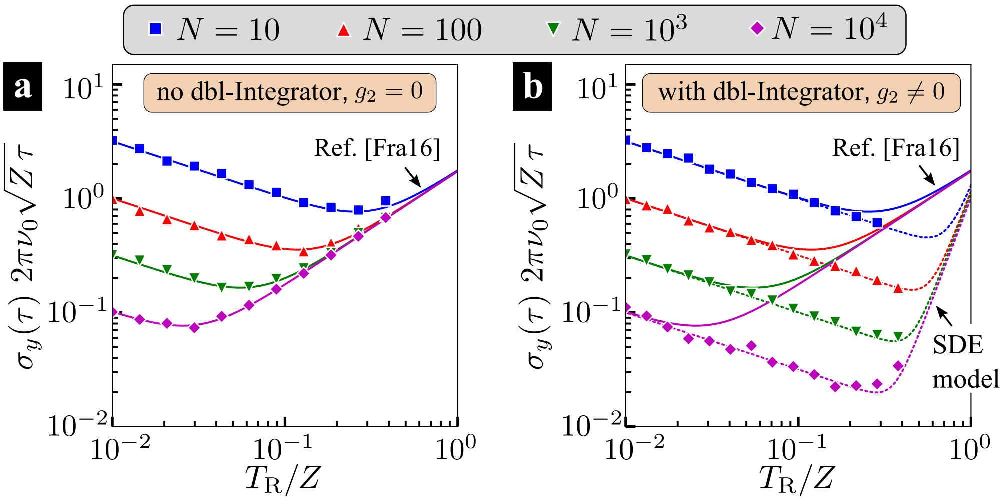

Figure 3.11: **Stability with and without a double integrator:** Rescaled long-term clock instability as a function of normalized Ramsey time T_R/Z. The underlying laser has random walk frequency noise only. **a** No double integrator (see main text) was used for the numerical simulations (symbols). Full lines are the stability limit according to Eq. (3.69), based on Fraas [Fra16]. **b** Stability with a double integrator for the numerical simulations. The predicted stability based on the stochastic differential equation is shown as dotted lines. Solid lines are the same as in **a** for better comparison.

where $\kappa = \langle S_x \rangle / S$ quantifies the measurement contrast and at this stage $\mathrm{d}W_{\langle x,y\rangle,k}$ are random numbers with a normal distribution, such that

$$\langle \mathrm{d}W_{\alpha,k} \rangle = 0, \qquad \langle \mathrm{d}W_{\alpha,j}\, \mathrm{d}W_{\beta,k} \rangle = T\, \delta_{\alpha\beta}\, \delta_{jk} \tag{3.68}$$

with δ_{ij} being the Kronecker-Delta for both, the spin projections $\alpha, \beta \in \{x, y\}$ and the cycle indices j, k. The elements $\mathrm{d}W_{(x,y),k}$ thus represent fluctuations of the kth measurement outcome for $S_{(x,y)}$ around their mean values. The differential time increment $\mathrm{d}t = T$ in the first term on the RHS corresponds to the Ramsey duration as we are interested in studying the phase evolution over the course of many interrogation cycles. When going to time continuous stochastic differential equations, $W_{(x,y)}$ will become standard Wiener processes, adding measurement noise, hence the notation. For the same reason we also did not cancel the factors T in the first term on the RHS in order to highlight the correspondence to the continuous stochastic differential equation.

As a first result we now show that the single integrator described above is not sufficient to suppress all relevant laser noise types, even under otherwise ideal conditions. Especially for stronger temporal correlations, as is the case for random walk frequency noise, this particular choice of the servo can not fully correct out all fluctuations of the laser frequency. Thus the design of the servo control can influence the overall stability of the clock and, importantly, it must be considered when deriving fundamental limits to the stability. A previous - mathematically more rigorous - approach by Fraas [Fra16] was able to to identify lower bounds on the stability which are expected to hold for white frequency and flicker frequency noise. However, as that theory is based on a regular integrating servo, the bounds should not be expected to hold for random walk or more strongly correlated noise of the local oscillator. We show here that, for lasers with those noise characteristics, the limits can be overcome with a different choice of servo. Figure 3.11**a** displays the long-term stability for uncorrelated atoms as a function of Ramsey time in the case of a standard integrating servo according to Eq. (3.61). If T_R/Z is increased, it can be seen that the stabilized signal contains a white noise term which represents a stricter limitation than the QPN. In this case the fundamental limit

$$\sigma_y(\tau)\, 2\pi\nu_0\sqrt{Z\tau} = \sqrt{\frac{Z}{T_\mathrm{R}}}\sqrt{\frac{1}{N} + 3\left(\frac{Z}{T_\mathrm{R}}\right)^3} \tag{3.69}$$

from Ref. [Fra16] (full lines in Fig. 3.11**a**) accurately describes the simulated stability (symbols), up to the emergence of fringe hops, which are not included in the analytical model. Note that we set $g = 1$ as the gain factor and used that the Fisher information is $\frac{1}{N}$ for uncorrelated atoms (explicitly $F_T = \frac{T^2}{N}$ in Ref. [Fra16]). The comparison with Fig. 3.11**b** shows that the additional white noise is not due to the coherence properties of the laser. Here, the laser noise can be further suppressed by adding a second stage of the servo which operates at a lower gain $g_2 \ll g$. It is only the CTL, evaluated from the SDE, or the onset of fringe-hops which ultimately limits the stability in that case.

For a quantitative analysis of the argument given above, we will have to change the way that the feedback corrections are applied. Modifying the servo is easily possible in the recursive relations of Eq. (3.59) and Eq. (3.60) by adapting the corrections p_{k-1}. Instead of the regular integrator, Eq. (3.61), consider now a double-integrator with

$$p_{k-1} = p_{k-2} + \frac{g}{2\pi T}\check{\phi}_{k-1} + \frac{g_2}{2\pi T}\sum_{n=1}^{k}\check{\phi}_{k-n} \tag{3.70}$$

including longer averages of estimates $\check{\phi}$ with the secondary gain factor $g_2 \ll g$. Such secondary integrator stages already find applications in the operation of atomic clocks to also counteract slow deterministic drifts of the laser frequency [PST05]. Alternatively, servos employing optimized general linear predictors have also been considered in the literature [SJA$^+$16, LSH$^+$17]. The effect on the stochastic difference equation is straightforward, changing Eq. (3.63) to

$$\phi_k - \phi_{k-1} = \left(\phi_{\mathrm{LO},k} - \phi_{\mathrm{LO},k-1}\right) - \left(g\check{\phi}_{k-1} + g_2 \sum_{n=1}^{k} \check{\phi}_{k-n}\right). \tag{3.71}$$

This fully determines the evolution of phase differences between the stabilized laser and the atomic reference during a clock run. To evaluate the suppression of laser noise via the double integrator we transform this finite stochastic difference equation into a system of two coupled stochastic differential equations (note that this disregards dead times):

$$\mathrm{d}\phi = \mathrm{d}\phi_{\mathrm{LO}} - g\frac{\kappa}{T}\,\phi(t)\,\mathrm{d}t - g\frac{\kappa}{T^{1/2}}\frac{\Delta S_y}{\langle S_x\rangle}\,\mathrm{d}W_y(t) - \frac{g_2}{T}\,\psi\,\mathrm{d}t\,, \tag{3.72}$$

$$\mathrm{d}\psi = \frac{\kappa}{T}\,\phi(t)\,\mathrm{d}t + \frac{\kappa}{T^{1/2}}\frac{\Delta S_y}{\langle S_x\rangle}\,\mathrm{d}W_y(t)\,. \tag{3.73}$$

Here the additional variable $\psi(t)$ was introduced, which in general is defined as

$$\psi(t) = \int_0^t \left[\frac{\kappa}{T}\sin(\phi(t'))\mathrm{d}t' + \frac{\kappa}{\sqrt{T}}\frac{\Delta S_x}{\langle S_x\rangle}\sin(\phi(t'))\,\mathrm{d}W_x(t') + \frac{\kappa}{\sqrt{T}}\frac{\Delta S_y}{\langle S_x\rangle}\cos(\phi(t'))\,\mathrm{d}W_y(t')\right]. \tag{3.74}$$

Equations (3.72) and (3.73) are derived from Eq. (3.71) in the long time limit where an individual interrogation cycle gives the differential time step $\mathrm{d}t = T$. Thus the finite differences $\phi_k - \phi_{k-1}$ approach the differential $\mathrm{d}\phi(t)$, so we define $\dot{\phi}(t) = \frac{\mathrm{d}\phi(t)}{\mathrm{d}t}$ and likewise $\dot{\phi}_{\mathrm{LO}}(t) = \frac{\phi_{\mathrm{LO}}(t)}{\mathrm{d}t}$. On the other hand, the finite differences $\mathrm{d}W_{(x,y),k}$ become the differential Wiener elements $\mathrm{d}W_{(x,y)}(t)$ with the analogous properties

$$\langle \mathrm{d}W_\alpha(t)\rangle = 0, \qquad \langle \mathrm{d}W_\alpha(t)\,\mathrm{d}W_\beta(t')\rangle = \delta_{\alpha\beta}\,\delta(t-t')\,\mathrm{d}t. \tag{3.75}$$

To simplify the coupled stochastic differential equations, Eq. (3.72) and Eq. (3.73), all functions of ϕ in the phase estimation, Eq. (3.67) were expanded up to linear order only. Furthermore, terms involving products of different variables, such as $\phi(t)\,\mathrm{d}W_x(t')$ are also neglected. Of course, these assumptions can only be justified for small phase variations $\phi \ll 1$. If the instability of the atomic clock is to be optimized over the Ramsey time $T_{\mathrm{R}} \equiv T$, these terms must be considered, as we will do again after evaluating the effect of the double integrator.

For now, the linearized system of stochastic differential equations can be expressed more compactly as

$$\mathrm{d}\boldsymbol{w} = M\boldsymbol{w}\mathrm{d}t + \mathrm{d}\boldsymbol{f}(t) \tag{3.76}$$

with

$$\boldsymbol{w}(t) = \begin{pmatrix}\phi(t)\\ \psi(t)\end{pmatrix}, \quad M = \begin{pmatrix}-g\frac{\kappa}{T} & -\frac{g_2}{T}\\ \frac{\kappa}{T} & 0\end{pmatrix}, \quad \mathrm{d}\boldsymbol{f}(t) = \begin{pmatrix}\mathrm{d}\phi_{\mathrm{LO}}(t) - g\frac{\kappa}{T^{1/2}}\frac{\Delta S_y}{\langle S_x\rangle}\mathrm{d}W_y(t)\\ \frac{\kappa}{T^{1/2}}\frac{\Delta S_y}{\langle S_x\rangle}\mathrm{d}W_y(t)\end{pmatrix}. \tag{3.77}$$

An equivalent equation stochastic differential equation for $\dot{\boldsymbol{w}} = \frac{\mathrm{d}\boldsymbol{w}}{\mathrm{d}t}$ could be formulated from this as well. Equation (3.76) can be solved formally via Fourier transform resulting in

$$\boldsymbol{w}(\omega) = (i\omega\mathbb{1} - M)^{-1}\boldsymbol{g} \tag{3.78}$$

where

$$\boldsymbol{g} = \begin{pmatrix} i\omega\phi_{\mathrm{LO}}(\omega) - g\frac{\kappa}{T^{3/2}}\frac{\Delta S_y}{\langle S_x\rangle}\,\mathrm{d}W_y(\omega) \\ \frac{\kappa}{T^{3/2}}\frac{\Delta S_y}{\langle S_x\rangle}\,\mathrm{d}W_y(\omega) \end{pmatrix}. \tag{3.79}$$

Based on the solution $\boldsymbol{w}(\omega)$ we calculate the spectrum matrix

$$S_{\boldsymbol{w}}(\omega) = \langle \boldsymbol{w}(\omega)\,\boldsymbol{w}^{\dagger}(\omega)\rangle = (i\omega\mathbb{1} - M)^{-1}\boldsymbol{g}\,\boldsymbol{g}^{\dagger}(-i\omega\mathbb{1} - M^{\dagger})^{-1}. \tag{3.80}$$

As one element of the matrix we find the spectrum of the stabilized phase

$$S_{\phi}(\omega) = \frac{S_{\mathrm{LO}}(\omega) + \left[\frac{g_2^2\kappa^2}{\omega^4T^5} + \frac{g^2\kappa^2}{\omega^2T^3}\right]\frac{\Delta S_y^2}{\langle S_x\rangle^2}S_{\mathrm{d}W_y}(\omega)}{1 + (g^2\kappa^2 - 2g_2\kappa)/(\omega T)^2 + g_2^2\kappa^2/(\omega T)^4}, \tag{3.81}$$

where we used that the laser noise ϕ_{LO} is independent from the atomic noise $\mathrm{d}W_y$. As we are interested in the long term stability of atomic clocks, at $\tau \gg T_{\mathrm{C}}$, we thus expand $S_{\phi}(\omega)$ in lowest orders of ω. In the limit $\omega T/g_2 \ll 1$, which can be reached at some sufficiently low Fourier frequencies ω for any given values of T and g_2, Eq. (3.81) reduces in an intermediate step to

$$S_{\phi}(\omega) = \frac{(\omega T)^4}{g_2^2\kappa^2}S_{\mathrm{LO}}(\omega) + \left[1 + \frac{g^2}{g_2^2}(\omega T)^2\right]\frac{1}{T}\frac{\Delta S_y^2}{\langle S_x\rangle^2}. \tag{3.82}$$

This expression was further simplified by inserting the white spectrum $S_{\mathrm{d}W_y}(\omega) = \omega^0$ of the measurement noise. The intermediate result of Eq. (3.82) is presented, as it highlights that the local oscillator noise $S_{\mathrm{LO}}(\omega)$ is now suppressed for all correlations considered in this thesis. This includes a scaling of the spectral density with $S_{\mathrm{LO}}(\omega) \propto 1$, $S_{\mathrm{LO}}(\omega) \propto 1/\omega$ and $S_{\mathrm{LO}}(\omega) \propto 1/\omega^2$. Especially in the case of random walk frequency noise the same would not hold for a servo without the second integration stage. This can be seen by first setting $g_2 = 0$ in Eq. (3.81), which then reads

$$S_{\phi}(\omega) = \frac{S_{\mathrm{LO}}(\omega) + \frac{g^2\kappa^2}{\omega^2T^3}\frac{\Delta S_y^2}{\langle S_x\rangle^2}S_{\mathrm{d}W_y}(\omega)}{1 + g^2\kappa^2/(\omega T)^2}. \tag{3.83}$$

With this, the corresponding low frequency limit

$$S_{\phi}(\omega) = \frac{(\omega T)^2}{g^2\kappa^2}S_{\mathrm{LO}}(\omega) + \frac{1}{T}\frac{\Delta S_y^2}{\langle S_x\rangle^2} \tag{3.84}$$

has an additional white noise contribution $\frac{b_2T^2}{g^2\kappa^2}$ when $S_{\mathrm{LO}}(\omega) = b_2\omega^{-2}$ from the first term on the right hand side. This is local oscillator noise which is not fully corrected out by the servo and the remaining instability contribution competes with the atomic noise, i.e. the QPN. For small Ramsey times T, QPN dominates but with increasing T the uncorrected laser noise takes over. Looking again at Fig. 3.11, the features we derived are precisely what was observed there. Only with $g_2 \neq 0$ will the dominant contribution at long averaging times be the white atomic noise. In the results presented here, this is made evident as the stabilized noise in the low frequency limit is

$$\lim_{\omega \to 0} S_\phi(\omega) = \frac{\Delta S_y^2}{T \left\langle S_x \right\rangle^2} \,. \tag{3.85}$$

This remains true for any T until the onset of fringe-hops at long interrogations times. In the derivation so far this effect is however not captured as we disregarded any non-linear contribution to the phase estimates which cause the fringe hops. We will drop that approximation in the following part, showing the emergence of the CTL and discuss fringe-hops as a first escape time problem. To capture these features in the numerical treatment as well, all numerical results we refer to (symbols in Fig. 3.7, Fig. 3.9 and Fig. 3.13) come from simulations of the stochastic difference equations

$$\overline{\Delta\nu}_k - \overline{\Delta\nu}_{k-1} = \overline{\Delta\nu}_{\mathrm{LO},k} - \overline{\Delta\nu}_{k-1} - \frac{g}{2\pi T}\check{\phi}_{k-1} \tag{3.86}$$

$$\phi_k - \phi_{k-1} = \phi_{\mathrm{LO},k} - \phi_{\mathrm{LO},k-1} - g\check{\phi}_{k-1} \tag{3.87}$$

with the true (non-Markovian) local oscillator noise and with the full (non-linear) phase estimation as given in Eq. (3.67). The only difference between Eq. (3.86)-(3.87) and Eq. (3.62)-(3.63) are the terms proportional to g_2 from applying the double integrator, as stated in Eq. (3.70).

How the analytic expression for the CTL follows from the stochastic differential equation without the linear approximation is discussed next.

Approximate solution to the SDE - determining the CTL Based on the results of the previous paragraph, we infer that the double integrating servo completely corrects frequency errors and removes correlations between phases in different measurement cycles. Therefore, we approximate from now on the local oscillator driven phases $\mathrm{d}\phi_{\mathrm{LO}}$ in each cycle as uncorrelated Wiener increments. The variance

$$V_\phi = \chi(\gamma) \left(\frac{T_\mathrm{R}}{Z} \right)^{2+\gamma} \tag{3.88}$$

of $\mathrm{d}\phi_{\mathrm{LO}}$ within each interrogation cycle scales at characteristic powers with T_R/Z, given the specific noise type, and has $\chi = 1,\ 1.8,\ 2$ for $\gamma = -1,\ 0,\ 1$. Note that for small ensembles and short Ramsey times V_ϕ may be increased due to the influence of quantum projection noise [LSH+17]. For this paragraph we neglect the influence of the second integrator, given that $g_2 \ll g$, and we are only interested in evaluating the consequences of the non-linear terms in the phase estimate. Thus, using the full phase estimate $\check{\phi}_{k-1}$ of Eq. (3.67), the stochastic difference equation, Eq. (3.63), becomes the single stochastic differential equation

$$\mathrm{d}\phi = \sqrt{V_\phi}\mathrm{d}\phi_{\mathrm{LO}} - g\frac{\kappa}{T}\sin(\phi)\mathrm{d}t - g\frac{\kappa}{\sqrt{T}}\frac{\Delta S_x}{\langle S_x\rangle}\sin(\phi)\mathrm{d}W_x - g\frac{\kappa}{\sqrt{T}}\cos(\phi)\frac{\Delta S_y}{\langle S_x\rangle}\mathrm{d}W_y \tag{3.89}$$

in the continuum limit over many clock cycles. An approximate solution to this non-linear SDE can be constructed from a power series ansatz [And05]

$$\phi(t) = \sum_{n=1}^{\infty}\epsilon_1^n\phi_{1,n}(t) + \epsilon_2\sum_{n=0}^{\infty}\epsilon_1^n\phi_{2,n}(t) + \epsilon_3\sum_{n=0}^{\infty}\epsilon_1^n\phi_{3,n}(t), \tag{3.90}$$

assuming small perturbation parameters $\epsilon_1 = \sqrt{V_\phi}$, $\epsilon_2 = \frac{\Delta S_y}{\langle S_x\rangle}$ and $\epsilon_3 = \frac{\Delta S_x}{\langle S_x\rangle}$. Here the variance V_ϕ quantifies again the width of the phase distribution prior to each measurement. The greater the correlations in the laser noise, the faster the width V_ϕ of the phase distribution increases with the Ramsey time. For details on the further steps we refer to Ref. [And05], which provides a specific calculation of the Allan variance resulting from the approximate solution $\phi(t)$ when restricting to terms of at most first order in ϵ_2, ϵ_3 and at most third order in ϵ_1. Note, however, that the result stated here also includes a term proportional to $\epsilon_2\epsilon_1^2$ which was not treated in the original work. The resulting Allan variance, to lowest orders in the perturbation parameters, is

$$\sigma^2_{\mathrm{m+d}}(\tau) = \frac{1}{(2\pi\nu_0 T_{\mathrm{R}})^2}\frac{T_{\mathrm{C}}}{\tau}V_{\mathrm{m+d}} \tag{3.91}$$

with

$$V_{\mathrm{m+d}} = \frac{\Delta S_y^2}{\langle S_x\rangle^2} + \frac{\Delta S_x^2}{\langle S_x\rangle^2}V_\phi + \frac{3(1-c)^2}{8}\frac{\Delta S_y^2}{\langle S_x\rangle^2}V_\phi^2 + \frac{1-3c+8c^2/3}{6}V_\phi^3 + \mathcal{O}(V_\phi^4) \tag{3.92}$$

and

$$c = \frac{1}{2}\frac{\langle S_x\rangle}{S}g \tag{3.93}$$

as applied in section 3.3.

Fringe-hops as a first passage time problem Finally, it is worth noting that just evaluating the Allan variance often does not correctly reflect the appearance of fringe-hops. While we find that the minimal stability is not affected by fringe-hops in the case of small dead times and long coherence times, as we will see, there may still be parameter regimes where fringe-hops are the relevant constraint. Upper limits for safe Ramsey times, within which less than 1 fringe-hop per 10^6 clock cycles occurs,

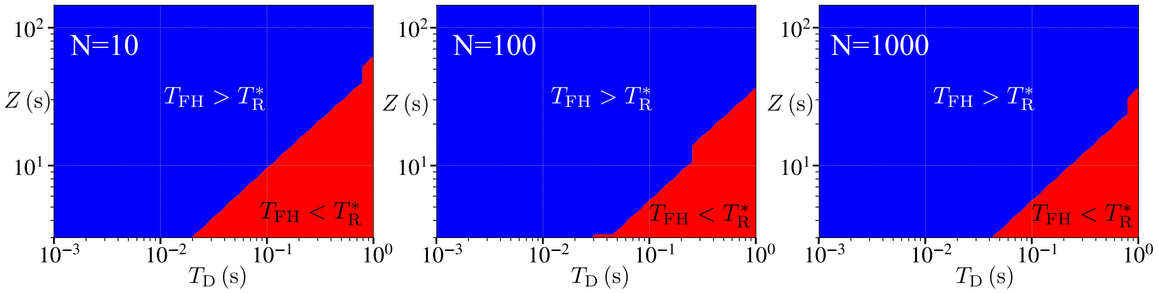

Figure 3.12: **Fringe-hops and interrogation time:** Comparison between the safe interrogation times T_{FH} (without fringe-hops) and the time T_{R}^* for minimal instability as a function of laser coherence time Z and dead time T_{D}. Based on this study we can identify regions in which the minimum between Dick effect and CTL can be safely reached (blue) and regions in which additionally the occurrence of fringe-hops has to be investigated in detail (red). By comparing $N = 10, 100$ and 1000 one finds that the red region is largest for small ensembles, short coherence times and larger dead times and decreases in size with increased particle numbers.

have so far only been determined phenomenological by numerical simulations of the full stochastic process for uncorrelated atoms [LSH+17]. According to that study,

$$T_{\mathrm{FH}} = (0.4 - 0.15N^{-1/3})Z \tag{3.94}$$

and

$$T_{\mathrm{FH}} = (0.4 - 0.25N^{-1/3})Z \tag{3.95}$$

were suggested as guides for safe interrogation times in the case of flicker frequency and random walk frequency noise respectively. As described in section 3.3, this guide can be used to estimate for which parameters fringe-hops may occur before reaching the intersection of Dick effect and CTL. Figure 3.12 shows corresponding parameter landscapes illustrating the relation of the two time scales, T_{FH} and the optimal Ramsey time T_{R}^*, against laser coherence time Z and dead time T_{D}. By evalutating the landscapes for different N, it can also be seen that the region with $T_{\mathrm{FH}} < T_{\mathrm{R}}^*$ reduces for increasing particle numbers.

In contrast to the numerically motivated guides above, the onset of fringe-hops can also be predicted by further investigation of the SDE. This may also allow a better understanding of the underlying processes in the future. First, we observe that the SDE in Eq. (3.89) may be expressed more compactly as

$$\mathrm{d}\phi = A(\phi)\mathrm{d}t + \boldsymbol{b}(\phi) \cdot \mathbf{d}\boldsymbol{W}(t) \tag{3.96}$$

with

$$A(\phi) = -g\frac{\kappa}{T}\sin(\phi), \tag{3.97}$$

and the coefficients

$$\boldsymbol{b}(\phi) = \begin{pmatrix} \sqrt{V_\phi} \\ -g\frac{\kappa}{\sqrt{T}}\frac{\Delta S_x}{\langle S_x\rangle}\sin(\phi) \\ -g\frac{\kappa}{\sqrt{T}}\cos(\phi)\frac{\Delta S_y}{\langle S_x\rangle} \end{pmatrix} \tag{3.98}$$

to the three independent Wiener processes

$$\mathbf{d}\boldsymbol{W} = \begin{pmatrix} \mathrm{d}\phi_{\mathrm{LO}} \\ \mathrm{d}W_x \\ \mathrm{d}W_y \end{pmatrix}. \tag{3.99}$$

Generally, a stochastic differential equation in the form of Eq. (3.96) can be re-expressed in an equivalent Fokker-Planck equation [Gar09] for the probability distribution $P(\phi, t)$ of the stabilized phase at time t, which in this case reads

$$\frac{\partial P(\phi,t)}{\partial t} = \left[-\frac{\partial A(\phi)}{\partial\phi} + \frac{1}{2}\frac{\partial^2 B(\phi)}{\partial\phi^2}\right] P(\phi,t). \tag{3.100}$$

Again, we remind that time is in multiples of the interrogation time T here. The drift and diffusion coefficient are

$$A(\phi) = -q\sin\phi, \quad B(\phi) = \boldsymbol{b}\,\boldsymbol{b}^T = r + s\cos^2\phi \tag{3.101}$$

respectively, where

$$q = -\frac{g\kappa}{T}, \tag{3.102}$$

$$r = V_\phi + \frac{g^2\kappa^2}{T}\frac{\Delta S_x^2}{\langle S_x\rangle^2}, \tag{3.103}$$

$$s = \frac{g^2\kappa^2}{T}\left(\frac{\Delta S_y^2}{\langle S_x\rangle^2} - \frac{\Delta S_x^2}{\langle S_x\rangle^2}\right). \tag{3.104}$$

The idea for connecting this to fringe-hops is to consider the so-called mean first passage time (mfpt). The mean first passage time describes the average duration over which a random variable (here the stabilized phase) remains within an interval $[a, b]$. Note that the passage time in this cases is again to be regarded as a multiple of the feedback cycle duration. In order to calculate the mfpt we use established tools within the field of stochastic methods [Gar09]. A useful function in the context of the mfpt is

$$\begin{aligned}\Psi(x) &= \exp\left\{\int_0^x \mathrm{d}x' \frac{2A(x')}{B(x')}\right\} \\ &= \exp\left\{\frac{2q}{\sqrt{r\,s}}\left[\arctan\left(\sqrt{\frac{s}{r}}\cos(x)\right) - \arctan\left(\sqrt{\frac{s}{r}}\right)\right]\right\}.\end{aligned}$$

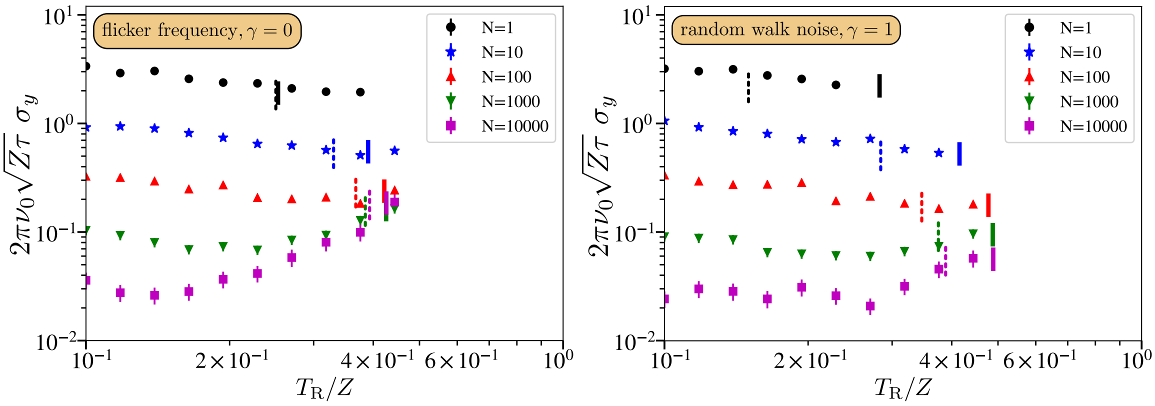

Figure 3.13: **Modeling fringe-hops:** Numerically simulated clock instability (symbols) for a comparison to the predicted onset of fringe-hops, based on a mean first escape time (solid bars) as well as the safe interrogation times (dashed bars) suggested by Eq. (3.94) and (3.95). For both, flicker frequency noise and random walk frequency noise, we find that the predictions based on the mean first escape time reproduce the observed sudden increase in instability well. To include different noise strengths, we normalized all time scales to the laser coherence time Z (see main text).

From $\Psi(x)$ the mean first time to escape the symmetric interval $[-a, a]$, assuming the laser phase starts with $\phi = 0$ at $t = 0$, is given by [Gar09]

$$T_\mathrm{mfpt} = \frac{2\left[\left(\int_{-a}^{0}\frac{\mathrm{d}z}{\Psi(z)}\right)\int_0^a\frac{\mathrm{d}x}{\Psi(x)}\int_{-a}^{x}\mathrm{d}y\frac{\Psi(y)}{B(y)} - \left(\int_0^a\frac{\mathrm{d}z}{\Psi(z)}\right)\int_{-a}^{0}\frac{\mathrm{d}x}{\Psi(x)}\int_{-a}^{x}\mathrm{d}y\frac{\Psi(y)}{B(y)}\right]}{\int_{-a}^{a}\frac{\mathrm{d}z}{\Psi(z)}}.$$

Which can be further simplified to the double integral

$$T_\mathrm{mfpt} = \int_{-a}^{a}\mathrm{d}x\int_{-a}^{x}\mathrm{d}y\,[2\Theta(x)-1]\,\frac{\Psi(y)}{\Psi(x)}\frac{1}{B(y)} \qquad (3.105)$$

where $\Theta(x)$ is the Heaviside function, by using the symmetry $\Psi(x) = \Psi(-x)$.

A maximum Ramsey time T_FH without fringe-hops can be specified by requesting that the stabilized phase should not leave the interval $[-\pi, \pi]$, in which it is corrected back to the original reference point $\phi = 0$, within the simulated $\sim 10^6$ cycles of clock operation. So $T_\mathrm{mfpt}(T_\mathrm{R}) \leq 10^6$ for $T_\mathrm{R} \leq T_\mathrm{FH}$, where the functional dependence $T_\mathrm{mfpt}(T_\mathrm{R})$ in terms of the Ramsey duration is implicit through the parameters q, r and s, which depend on T_R. In the case of flicker frequency noise this procedure led to a good agreement with the onset of fringe-hops observed in numerical simulations. For random walk noise we achieved slightly better agreements when assuming the interval $[-\frac{\pi}{2}, \frac{\pi}{2}]$ for the calculation of the mean first passage time. We found that this stronger requirement is more applicable here due to the increased temporal correlations which already cause fringe-hops in a regime where the feedback, though insufficient, is not on paper stabilizing the frequency to a different fringe. Figure 3.13 compares T_{FH} as based on the mfpt with results from numerical simulations of the full clock operation as well as the phenomenological guides in Eq. (3.94) and Eq. (3.95) in the case of uncorrelated atoms. For both flicker frequency and random walk frequency noise the prediction of the mfpt exhibits an almost constant cutoff for large N and reduced T_{FH} for smaller ensembles which is in qualitative and quantitative agreement with the phaenomenological guides as well as the numerical results. Except the escape interval, as mentioned above, all calculations are without free parameters. For very small ensembles, e.g. $N = 1$, our theory falls short in accurately predicting T_{FH} as it uses the assumption of phases with variance V_ϕ for each interrogation, which in this regime is assumed to break down.

3.5 Conclusion

In conclusion, we would like to emphasize that the theoretical and experimental progress in manipulating the QPN in quantum metrological measurements with entangled states represents an important and exciting challenge. In the context of atomic clocks, however, a reduction in the QPN does not automatically mean an improvement in statistical uncertainty. A possible gain through entangled states therefore requires an evaluation that is detailed to the specific conditions of an atomic clock. Frequency estimation using GHZ states which is limited by QPN and atomic decoherence was already considered quite some time ago by Huelga *et al.* [HMP+97]. Here, we have extended this idea to discuss the stability of optical atomic clocks with squeezed states. The model we developed allows a comprehensive and quantitative investigation of limitations to the overall clock stability. It thus shows in which parameter regimes laser noise is not the most stringent limitation, so squeezing can improve the stability, and in which cases laser noise is dominant and needs to be overcome by other means before squeezing provides an advantage. Although we showed that current improvements are limited to small systems only, our results also indicate that after challenging improvements in laser stability and dead time reduction, spin squeezing will become relevant for optical lattice clocks as well. In order to promote the use of entanglement in optical clocks, a number of further aspects should be considered in a similar way: Excess anti-squeezing due to imperfect state preparation has been considered in Ref. [BKV18], and shown to reduce clock stability for white frequency noise. It would be desirable to incorporate excess anti-squeezing to our model which deals with realistic colored laser noise. To what extent other measurement methods besides Ramsey interrogation are subject to similar restrictions or in which cases they can be circumvented remains open. Rabi interrogation is not expected to give improvements over the limits presented here due to its increased QPN and enhanced Dick effect [WLL10], even though it allows for slightly longer interrogation times than Ramsey protocols. The limitations described here, valid for single ensemble clocks with cyclic Ramsey interrogation and dead time, may be overcome with more sophisticated clock architectures: The laser coherence limit can be tackled with adaptive measurement schemes [BS13b] or cascaded systems with multiple ensembles of atoms [BS13a, RL13, KKB$^+$14] (see also the outlook). However, we suspect at least for the adaptive scheme that including dead time to these studies would still show the existence of a critical ensemble size, limiting the useful regime of squeezed states, similar to what was presented here. Although one should note that the overall stability would improve on what we have presented. Dead time free laser stabilization, basically eliminating the Dick effect, was constructed by anti-synchronized interrogations of two atomic clocks [S$^+$16]. It is then expected that spin squeezing will again increase the stability for any N but comes at the cost of keeping low systematic shifts for two ensembles. While the underlying method has been demonstrated, showing an improvement through squeezed states remains an open challenge in this setting. Conceptually different approaches that may evade the presented limitations when applied without dead time are based on continuously tracking the atomic phase via weak measurements [ST12, SGW$^+$19, KBC$^+$15].

3.6 Outlook: Further directions for designed quantum states in optical atomic clocks

The detailed model for an optical atomic clock, described in this chapter, has shown that the overall stability transitions between two different limitations, depending on the operating parameters and especially the number of reference atoms. For large ensembles, no gain through quantum correlations between the atoms can be expected. While small ensembles will necessarily require quantum correlations to reduce QPN. Separate strategies are in order to improve atomic clocks in the two regimes. We will comment on future perspectives in both cases, accompanied with our own novel results:

Composite clocks, consisting of cascaded interrogation with multiple atomic ensembles, are envisioned to overcome the coherence time limited operation. We review previous results in this direction in section 3.6.1 and show that even asymmetric designs featuring ensembles of different atom numbers will result in an atomic clock with improved stability under more realistic conditions.

Interrogation protocols with entangled quantum states and observables are the only way to operate small atomic clocks with a sensitivity beyond the standard quantum limit. However, finding the right interactions and controls becomes a non-trivial problem. In section 3.6.2 we motivate an easy to optimize quantity, which extends the conventional squeezing parameter, for an improved description of phase estimation protocols within the feedback process of an atomic clock. Applying this quantity as a cost function then allows the treatment of clock protocols with well-established quantum gates as a variational optimization problem. New insights in this direction have resulted from a collaboration with R. Kaubruegger, D. Vasilyev and P. Zoller. In the end it is shown that new protocols, which were determined beforehand by variational minimisation of the average variance for a phase estimator, provide a stable improvement even in simulations of the full clock operation at constant variational complexity.

3.6.1 Composite clocks

One idea to beat the CTL is to cascade several atomic ensembles in the stabilization process [BS13a, RL13]. Borregaard and Sørensen [BS13a] have shown that m ensembles, each of size N, can stabilize a noisy local oscillator to

$$\sigma_y(\tau) \propto \frac{1}{2\pi\nu_0\sqrt{\tau}}\frac{1}{N^{m/2}} \tag{3.106}$$

with an exponential improvement in the number of ensembles. The basic principle is that the first ensemble, operating at a relatively short Ramsey time $T_1 \ll Z$, will pre-stabilize the laser noise seen by the second ensemble, which operates at longer Ramsey time $T_2 = nT_1$ ($n \in \mathbb{N}$), this further reduces the laser noise seen by the third ensemble, operating with $T_3 = \tilde{n}T_2$, and so forth for all further ensembles (see Fig. 3.14**b**). In addition, before each measurement is applied in later ensembles, a reference phase value is provided from the previous ensembles in the cascade. This reference value is basically the (roughly) estimated phase difference determined from measurements of the previous ensembles. It is needed to place the later, finer Ramsey measurement on the correct fringe. Forwarding this information about the expected phase is crucial to the correct operation of the clock and provides a means to beat the CTL.

In our study we find that also an asymmetric setting can be used to improve the stability assuming state-of-the-art laser parameters. By combining a large ensemble, where $N_1 \gg 1$, for the initial stabilization with a single atom clock, where $N_2 = 1$, we found that a combined clock operating at roughly the stability of the first ensemble is possible. Previous studies of a similar setup discussed the measurement of frequency

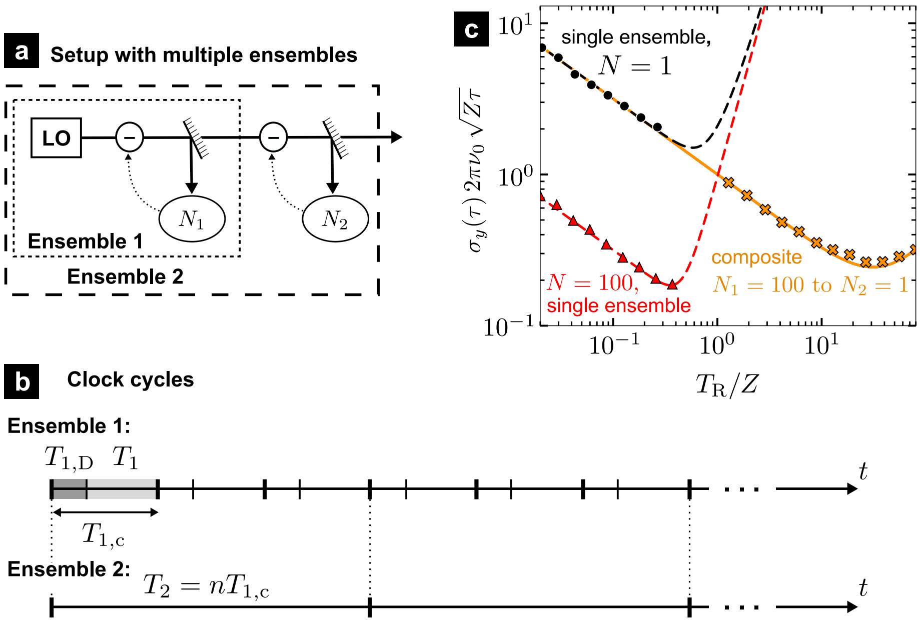
a
Setup with multiple ensembles
LO
−
N_1
−
N_2
Ensemble 1
Ensemble 2
b
Clock cycles
Ensemble 1:
$T_{1,\mathrm{D}}$
T_1
$T_{1,\mathrm{c}}$
Ensemble 2:
$T_2 = nT_{1,\mathrm{c}}$
t
t
c
$\sigma_y(\tau)\,2\pi\nu_0\,\sqrt{Z\tau}$
10^1
10^0
10^{-1}
10^{-1}
10^0
10^1
T_R/Z
single ensemble,
$N = 1$
composite
$N_1 = 100$ to $N_2 = 1$
$N = 100$,
single ensemble

Figure 3.14: **Mixed composite clocks: a** Schematic setup for a composite clock using multiple ensembles, following [BS13a]. **b** Clock cycles for the two ensembles show phase stabilization of the laser seen by ensemble 2 over several cycles of feedback operation from ensemble 1 and its servo. Each Ramsey measurement on ensemble 2 needs the phase estimates of ensemble 1 made during the longer Ramsey dark times T_2, e.g. $\check{\phi}_j^{(1)}$ for $j = 1, 2, \ldots, n$ in the first cycle. In that way only the small residual phase has to be determined for further stabilization. **c** Performance of a composite clock with $N_1 = 100$ and $N_2 = 1$ (orange marks). All values of T_2 are multiples of the Ramsey time $T_1 = 0.32 \times Z$, used for the first ensemble. We assumed $T_{1,\mathrm{D}} = 0$ so that $T_1 \equiv T_{1,\mathrm{c}}$. Red triangles and black dots show clocks with a single ensemble.

ratios only [HL16]. Figure 3.14**c** shows such an idealized setting where the stability of a single atom clock is pushed way beyond its coherence time limit almost down to the level of the large first ensemble. In this way the composite clock is limited by the QPN of the single atom over a large range of interrogation times. The difference between the minimum of the single ensemble clock and the composite clock is due to the fact that the relevant last ensemble sees different temporal correlations of the noise in the two cases. While the single ensemble clock corrects errors from a flicker frequency noise limited laser, the single atom of the composite clock effectively sees the white atomic noise of the first ensemble. Now for the correlated flicker noise the stability can be reduced more than it is possible for the uncorrelated white noise. When imagining the combination of an optical lattice clock and an ion clock with only few ions but high accuracy the result we show would mean operating the ion clock at its QPN limit, however, below the CTL restriction due to the increased interrogation time. This can push the Ramsey times up to the point where spontaneous decay of the

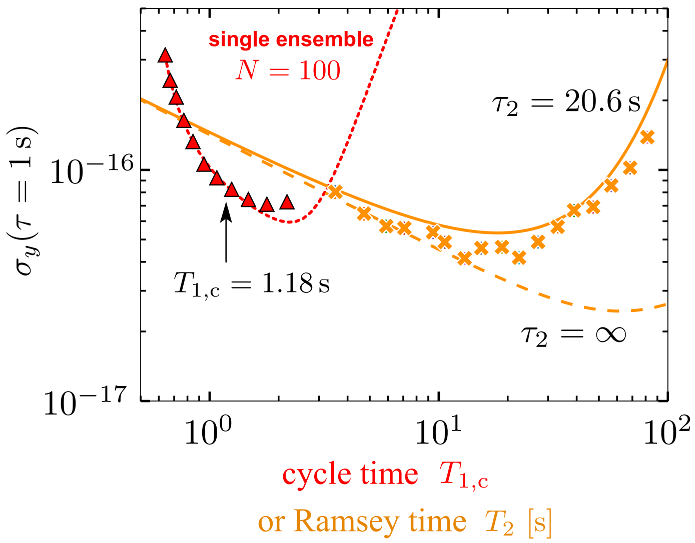

Parameter values	
N_1	100
N_2	1
$\nu_0^{(1)}$	4.29×10^{14} Hz
$\nu_0^{(2)}$	11.21×10^{14} Hz
τ_1	∞
τ_2	20.6 s
$\sigma^2_{y,\mathrm{LO}}(\tau)$	$2 \times 10^{-33}\frac{\mathrm{s}}{\tau} + 10^{-32}$ $+6 \times 10^{-35}\frac{\tau}{\mathrm{s}}$
$(g^{(1)}, g_2^{(1)}, g^{(2)})$	(0.6 0.012 0.01)
T_1	0.64 s
$T_{1,\mathrm{D}}$	0.54 s
$T_{2,\mathrm{D}}$	0 s

Figure 3.15: **A more realistic composite clock simulation:** Long term stability when including considerable dead-time in the first ensemble and finite excited state lifetime for the second ensemble. Symbols are the result of numerical simulations while lines show the analytic theory of the SDE. For the composite clock we also show the expected performance without spontaneous emission (dashed line). The table summarizes the parameter values for the numerical simulations.

excited energy level can no longer be neglected and again reduces the stability. Also in the regime of very long interrogation times other practical limitations may set in which we neglect in this thesis. Nevertheless, we find that the combined stabilization works well even when considering a more realistic example with a ^{87}Sr optical lattice clock and an ^{27}Al$^+$ ion clock. As can bee seen in Fig. 3.15, the stabilization works even with significant dead time in the first ensemble. In that case, the overall stability of the composite clock is limited by the finite lifetime of the ^{27}Al$^+$ ion at $\tau_2 = 20.6\,\mathrm{s}$. For Ramsey times longer than τ_2, a significant loss of stability can be observed compared to the expected stability without any spontaneous decay (dashed line). Recently it was also shown that using coherent dynamic decoupling interactions, instead of measurements of the phase difference, is a way to prevent much of the dead time in such a composite clock setup [DAB+19]. Applying this method may improve the stability even further than shown here.

Realistically, one should now also think about dropping the assumption of ideal references we made throughout this thesis. Because, if one of the advantages of such a composite atomic clock is to use the high stability of a lattice clock combined with the high accuracy of an ion clock, then the laser frequency that comes out of the stabilization done by the lattice clock will include the systematic shifts of the atoms therein. Although temporal correlations of the systematic shifts may be typically very small, this type of noise would still constitute to the output. It would give rise to new flicker frequency or random walk frequency noise in addition to the white measurement noise and will be seen by the ion clock. However, as this is only an outlook, the impact of limited systematic accuracy in a cascaded clock remains to be studied in detail.

Another point to note is that, as the additional ensembles in such a 'scaling down' setting will typically be QPN limited, entangled states will be more relevant here as well. In this direction of research, cascaded versions of the maximally entangled GHZ states have been proposed to build up a highly stable atomic clock [KKB+14, PS07]. While maybe most efficiently using its atomic resources, many drawbacks can be connected to GHZ states. Such as an enhanced susceptibility to external noise (environmental dephasing or spontaneous emission) which need to be considered carefully. Therefore recently also spin squeezed states have been considered in a composite clock setup [PS20]. Although not cascaded in the way presented here (the interrogation time remains the same for all ensembles), the protocol also heavily relies on forwarding the measured phase information from one ensemble to the next. This is in close similarity to the earlier work of Borregaard and Sørensen [BS13b] where an adaptive measurement scheme with weak measurements on a single ensemble effectively fulfilled the same purpose. Both studies reported stability with Heisenberg scaling, i.e. $\sigma_y^2 \propto \frac{1}{T_{\mathrm{R}} N^2}$.

3.6.2 Beating quantum projection noise in atomic clocks

For this last part we will now assume optical atomic clocks operating with negligibly small dead time or small ensemble sizes, so that they are limited entirely by the trade-off between QPN and CTL. In a coherent atomic interferometer, like the Ramsey interrogation, improved measurement sensitivity compared to the QPN have typically been expressed in terms of the squeezing parameter or a signal-to-noise ratio only (see chapter 2). This figure of merit however assumes a specific working point and characterizes the sensitivity only locally around exactly that point. As seen all throughout this chapter, such a strong assumption does simply not hold up for the optical atomic clocks in general. The servo cycle in which the feedback corrections are applied is a dynamical problem for which a broader range of phases needs to be estimated correctly due to the fluctuating frequency of the underlying laser. In the following, the phases in each interrogation cycle will be described as random samples from a single normal distribution

$$\mathscr{P}(\phi) = \frac{1}{\sqrt{2\pi V_\phi}} e^{-\frac{\phi^2}{2V_\phi}}, \tag{3.107}$$

centered around 0 and with variance $V_\phi = \chi(\gamma)\left(\frac{T_\mathrm{R}}{Z}\right)^{2+\gamma}$ as in Eq. (3.88). Note that modeling the phases by this single, simple distribution is a strong assumption. In principle the distribution could vary over different clock cycles contained in the long averaging times of the clock. Including higher moments could be relevant or the connection between the variance and the laser coherence time could be different. However, when the clock is faithfully locking the laser it is reasonable to assume that the phase distributions will be stationary and higher moments like the skewness are suppressed. This has been observed for uncorrelated atoms already [LSH+17] and is confirmed for variationally optimized protocols as well. In further agreement with Ref. [LSH+17], the variance V_ϕ of servo prediction errors at short T_R is slightly increased in the numerical simulations where servos with a gain $0 < g < 1$ lead to an effective averaging over many measurements. Nevertheless the normal distributed phases are a good approximation for many relevant values of T_R and N.

Let us now introduce the weighted phase uncertainty

$$u(T_\mathrm{R}) = \int_{-\infty}^{\infty} \mathrm{d}\phi\, \mathscr{P}(\phi)\, \mathbb{V}_\phi \tag{3.108}$$

with the variance

$$\mathbb{V}_\phi = \sum_{M=-N/2}^{N/2} \left[\phi - \check{\phi}(M)\right]^2 P(M|\phi) \tag{3.109}$$

of the phase estimator

$$\check{\phi}(M) = \left(\frac{\partial\langle M\rangle}{\partial\phi}\Big|_{\phi=0}\right)^{-1} M, \tag{3.110}$$

given a measurement outcome M. In this way $\mathbb{V}_\phi$ is the variance of the linear estimator, defined in the same way as in the treatment of the SDE, given that the true phase value was ϕ. The conditional probabilities $P(M|\phi)$ are the phase dependent measurement statistics of a spin projection, as before. When optimizing variational protocols the direction can be fixed such that only measurements of e.g. S_y need to be considered, given that the control operations of the class allow for appropriate alignment of the state before the measurement. Note that all protocols are assumed to be designed such that $\langle M\rangle\big|_{\phi=0} = 0$, to assure $\langle\check{\phi}\rangle\big|_{\phi=0} = 0$ at the center of the prior, which removes any bias of the estimator at that point. When the new local oscillator noise is uncorrelated between different cycles of the feedback loop the Allan deviation is connected to the weighted phase uncertainty as [PS20, B$^+$19b]

$$\sigma_y(\tau) = \frac{1}{2\pi\nu_0}\frac{u(T_{\mathrm{R}})}{T_{\mathrm{R}}}\sqrt{\frac{T_{\mathrm{R}}}{\tau}}. \tag{3.111}$$

This is in accord to what we had motivated in section 3.2.2. The absence of correlations has been confirmed numerically in many studies ([ASL04, BS13b, KKB$^+$14, LSH$^+$17]) and is implied by the Gaussian assumption from above. One can also check that the weighted phase uncertainty reproduces essential features of the previous stability analysis: To this end we first express the estimator variance as

$$\mathbb{V}_\phi = \left(\phi - \left(\frac{\partial\langle M\rangle}{\partial\phi}\Big|_{\phi=0}\right)^{-1}\langle M\rangle_\phi\right)^2 + \left(\frac{\partial\langle M\rangle}{\partial\phi}\Big|_{\phi=0}\right)^{-2}(\Delta M)^2_\phi. \tag{3.112}$$

At lowest order of $V_\phi \to 0$, the Gaussian reduces to a Dirac delta function $\mathscr{P}(\phi) \to \delta(\phi)$ and as $\lim_{\phi\to 0}\langle\check{\phi}\rangle = 0$ the weighted phase uncertainty

$$u(T_{\mathrm{R}} \to 0) = \mathbb{V}_{\phi=0} = \xi \tag{3.113}$$

reduced simply to the Wineland squeezing parameter. On the other hand one can extract the lowest order N independent contribution as well. For protocols without decoding, i.e $\mathcal{U}_{\mathrm{de}} = \mathbb{1}$, it turns out that $\langle\check{\phi}\rangle = \sin(\phi)$. Plugging this into Eq. (3.108) and evaluating the Gaussian integral shows that

$$\lim_{N\to\infty} u(T_{\mathrm{R}}) = \frac{5}{12}V_\phi^3 + \mathcal{O}(V_\phi)^4 \tag{3.114}$$

to lowest order in the width of the phase prior. This reproduces the scaling law of the CTL derived in Eq. (3.92) from the stochastic differential equation up to the pre-factor.

With the weighted phase uncertainty replacing the squeezing parameter ξ in the Allan deviation it becomes clear that, rather than optimizing the squeezing parameter only, an atomic clock works best when the weighted estimator variance $\frac{u(T_{\mathrm{R}})}{T_{\mathrm{R}}}$ per interrogation time is minimized. Following the approach of section 2.4 a large class of protocols can be constructed from OAT and collective rotations. In contrast to the main results of chapter 2, which extensively explored optimal scenarios with very few interactions, minimizing the weighted estimator variance can also be considered as a variational problem which allows more layers of interactions for encoding and decoding the state. Thus general strategies, like the ones introduced in section 2.4, can be introduced by

$$\mathcal{U}_{\mathrm{en}} = R_x(\alpha_{n_{\mathrm{en}}})R_y(\theta_{n_{\mathrm{en}}})T(\mu_{n_{\mathrm{en}}})\ldots R_x(\alpha_1)R_y(\theta_1)T(\mu_1) \tag{3.115}$$

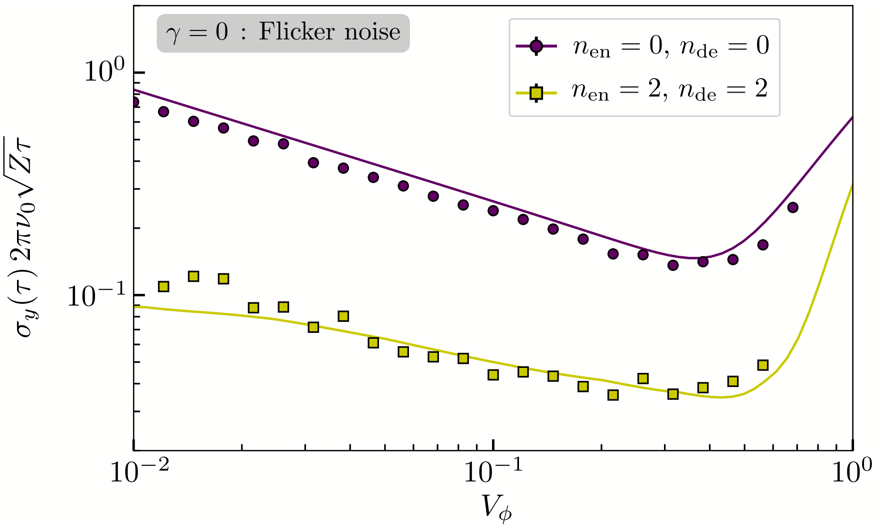

Figure 3.16: **Variationally Optimized Stability:** Long-term clock stability as a function of the width V_ϕ of the phase prior for $N = 256$ atoms. The comparison shows the standard Ramsey protocol with uncorrelated atoms, where $n_{\mathrm{en}} = n_{\mathrm{de}} = 0$, and protocols that result from the variational optimization when $n_{\mathrm{en}} = n_{\mathrm{de}} = 2$. The local oscillator experiences flicker frequency noise only. Solid lines are the prediction of Eq. (3.111) for the optimized protocols, while symbols are full numerical simulations of the clock. The optimized variational parameters of the protocols were determined by R. Kaubruegger, D. Vasilyev and P. Zoller (private communication).

with n_{en} layers encoding the initial state onto $|\psi_0\rangle = |\mathrm{x}\rangle$, where $T(\mu) \equiv T_\mu$ is the OAT interaction (see 2.4.2), and

$$\mathcal{U}_{\mathrm{de}} = R_x(\beta_{n_{\mathrm{de}}}) R_y(\vartheta_{n_{\mathrm{de}}}) T(\nu_{n_{\mathrm{de}}}) \ldots R_x(\beta_1) R_y(\vartheta_1) T(\nu_1) \tag{3.116}$$

to decode the phase information before the measurement. The full protocol is then described in terms of the set of variational parameters $\boldsymbol{\alpha}, \boldsymbol{\theta}, \boldsymbol{\mu}, \boldsymbol{\beta}, \boldsymbol{\vartheta}, \boldsymbol{\nu}$. The variational protocols stated here were designed by R. Kaubruegger, D. Vasilyev and P. Zoller. We note that a method for the full minimization of the weighted phase uncertainty $u(T_{\mathrm{R}})$ in Eq. (3.108) was developed by K. Macieszczak et al. [MFDD14], including an analytic optimization of the measurement operators. Beyond the scope of this thesis it would be interesting to compare the performance of the variational protocols with the optimal protocols.

Even at relatively small variational cost significant improvements in the QPN limited regime, and also on the overall stability, can be achieved. In most cases the gain from the model-based optimization of the weighted phase uncertainty transfers nicely to simulations of the full feedback loop without requiring any further assumptions. Comparing to the simulated clock stability, no additional drawbacks due to fringe hops were found in the most optimal protocols down to $N = 4$ particles. Figure 3.16

shows one example, highlighting the achievable enhancement in stability for variationally optimized clock protocols. The optimal parameters for the protocols were provided by R. Kaubruegger in a private communication. The results presented in Figure 3.16 show excellent agreement between the theoretical predictions of the simplified stability in Eq. (3.111) and the simulated instabilities, proving the applicability of the model in this case. For the CSS it can be seen that the predicted instability is a slightly too pessimistic prediction. This is due to assuming unity gain in the estimator, Eq. (3.110), which can degrade the stability compared to the numerics which typically run with a smaller gain factor for improved stability of the feedback loop. One way to circumvent this problem is to replace the weighted phase variance by e.g. the posterior variance of an optimized linear estimator, as considered by Leroux *et al.* [LSH+17], which should then rather be a lower bound on the numerical data. Nonetheless, looking at the improved instability of the simulated clock we find an overall gain of 5.8 dB or a factor of 3.8 at the optimal interrogation time. The results presented in this outlook establish the variational protocols as a promising new component of entanglement enhanced optical atomic clocks.

4

Designed interactions for quantum metrology with trapped ions

Summarizing the results of the two preceding chapters we found that on the one hand weak spin squeezing is useful for optical atomic clocks with small particle numbers and on the other hand static phase estimation can be enhanced with generalized echo protocols even for strong one-axis-twisting strengths. Both results have in common that they rely on an implementation of the one-axis-twisting interaction to generate spin-spin interactions. As emphasized before, generating such interactions is possible with trapped ions, one of the leading experimental platforms for optical atomic clocks and precision measurements. This section focuses in the first part on driving a high fidelity entangling gate between two ions using oscillating magnetic field gradients in the near-field regime of a microwave conductor embedded in a surface-electrode ion trap. We will see that the resulting gate dynamics can be designed in the form of the one-axis-twisting interaction.

The main result that this section then features, is the calculation of an error budget, establishing what are the limiting factors to the fidelity of such two-qubit gates in a state-of-the-art system. Instabilities of the motional mode are found to be the largest cause of errors. Building on this first result we then show the theoretical improvement in fidelity when employing amplitude modulation, which allows for an efficient suppression of errors caused by mode instabilities. Both results are theory complements to experimental work done by H. Hahn, G. Zarantonello, J. Morgner, A. Bautista-Salvador and C. Ospelkaus at the Physikalisch Technische Bundesanstalt in Braunschweig (PTB). Part of the results presented in this chapter, along with results from the experiment, are contained in Ref. [HZS$^+$19] and Ref. [ZHM$^+$19], paving way to entangling gates with demonstrated infidelity around 10^{-3}, performed at PTB (see [ZHM$^+$19]).

The same type of sideband interaction which drives the quantum gate is also useful for detection schemes with single particles in Penning traps. For the rather exotic (anti-)proton, the spin degree can not be detected directly due to the lack of any electronic transitions. However, coupling the spin of the (anti-)proton with its motion can then allow to facilitate an effective measurement of the spin state via a measurement of the axial motion of the ion. In the end, precision spectroscopy of the Larmor frequency can be envisioned in this way, testing fundamental symmetries of matter and antimatter. Thus the possibility to drive resonant sideband interactions with low errors is discussed in section 4.2, by using the existing feature of precision Penning traps to have regions with a strong magnetic field gradient and by adding a rf-driving field. The scheme we put forward in Nitzschke *et al.* [NSN+20] was motivated by a similar proposal for ions in a Paul trap by Mintert and Wunderlich [MW01].

4.1 Analysis of error sources in a microwave near-field entangling gate

4.1.1 Setup and Hamiltonian

To start the discussion of ion based quantum gates, a review of some classic results regarding the degrees of freedom of trapped ions as well as their interaction with oscillating electric or magnetic fields is given first. Parts of this discussion share an approach similar to the one of Sepiol [Sep16]. The results presented next form the basis to discuss sideband interactions, connecting the spin and motional degrees of freedom of a trapped ion, which are used in the Mølmer-Sørensen gate (see section 4.1.2).

Ion motion Consider a string of ions trapped in the electromagnetic field of a conventional Paul trap [MGW05, WMI+98]. In general, Paul traps produce a static electric quadrupole field, providing confinement of the ions along one spatial direction, along with another oscillating electric quadrupole field, at radio-frequencies, which traps the ions in the transverse (radial) direction. They have been constructed in a large variety of designs but at the level of abstraction needed here, all we are concerned with is the general feature of these traps: The ions perform small oscillations with extension $\boldsymbol{r}_j$ (for ion j) around their equilibrium positions $\boldsymbol{\mathcal{R}}_j$, which are the local potential minima for the sum of the electromagnetic potential generated by the Paul trap and the Coulomb potential of all other ions in the trap [Jam98a]. A typical configuration is the linear ion crystal, where a strong radial confinement of the trapping fields causes all ions to align along one particular axis of the trap (the y-direction in this section), so that $\boldsymbol{\mathcal{R}}_j = \mathcal{Y}_j \boldsymbol{e}_{\boldsymbol{y}}$. As each ions position determines the potential felt by the other ions, it is clear that their motion will be coupled. Indeed, in a standard harmonic approximation of the potential it turns out that N ions exhibit $3N$ collective normal modes with angular oscillation frequencies $\omega_{l,k}$. Here $l = \{x, y, z\}$ denotes the spatial orientation of the relevant trap axis and $k = 1, 2, \ldots, N$ labels the N normal modes within each direction. Note that the basis referred to by l may differ from the basis $\tilde{x}, \tilde{y}, \tilde{z}$ that comes natural from the geometry of the ion trap and the static magnetic field, setting the quantization axis. Especially for surface traps, which will be considered in this section, the two radial modes will generically not be parallel and perpendicular to the chip surface. However, a transformation between the two bases can always be obtained by simply rotating the coordinate system so we are not too concerned about the specific directions here. For future reference it is only noted that the weak axial direction has $\tilde{y} = y$ in this study. The corresponding eigenvectors $\boldsymbol{b}^{(l,k)}$ of the potential energy give the normalized amplitudes for each ion and thus the shape of the collective oscillation. For example in a two-ion crystal they are

$$\boldsymbol{b}^{(l,1)} = \frac{1}{\sqrt{2}} \begin{pmatrix} 1 \\ 1 \end{pmatrix}, \qquad \boldsymbol{b}^{(l,2)} = \frac{1}{\sqrt{2}} \begin{pmatrix} 1 \\ -1 \end{pmatrix} \tag{4.1}$$

along each trap axis l. These vectors describe center-of-mass motion and an out-of-phase oscillating mode (also called stretch-mode). The projections of any small oscillation $\boldsymbol{r}$ of the entire crystal onto the normal modes are $q_{l,k} = \boldsymbol{b}^{(l,k)} \cdot \boldsymbol{r}$. In turn, the displacement of ion n in direction l can be expressed as $r_n^{(l)} = \sum_p q_{l,p} \boldsymbol{b}_n^{(l,p)}$ via the normal modes. In a standard treatment of quantum mechanical harmonic oscillators, introducing creation and annihilation operators $a_{l,k}^\dagger$, $a_{l,k}$ allows to express position and momentum for the normal modes as

$$q_{l,k} = \frac{1}{\sqrt{2}} \ell_{l,k} (a_{l,k}^\dagger + a_{l,k}), \tag{4.2}$$

$$p_{l,k} = \frac{i}{\sqrt{2}} \frac{\hbar}{\ell_{l,k}} (a_{l,k}^\dagger - a_{l,k}), \tag{4.3}$$

where $\ell_{l,k} = \sqrt{\frac{\hbar}{m\omega_{l,k}}}$ with the ions mass m and (secular) oscillation frequencies $\omega_{l,k}$. These creation and annihilation operators diagonalize the Hamiltonian for the ion motion, which is then given by

$$H_{\text{mot}} = \sum_{l=\{x,y,z\}} \sum_{k=1}^{N} \hbar\omega_{l,k} \, a_{l,k}^\dagger a_{l,k}, \tag{4.4}$$

neglecting the constant zero point energy contribution.

The two-level system Reducing the complex electronic structure of atoms to only two relevant energy levels is commonly possible for many trapped ion species. Be it two states connected by a narrow quadrupole E2-transitions in the optical regime (e.g. $^{40}\mathrm{Ca}^+$), or two hyperfine ground states for which coherent interactions have been achieved either via Raman lasers (e.g. in $^{171}\mathrm{Yb}^+$) and oscillating magnetic fields (e.g with $^{9}\mathrm{Be}^+$ or $^{43}\mathrm{Ca}^+$). All these systems have in common that they can be described analogously to a pseudospin-1/2 particle, so in terms of Pauli matrices or collective spins operators in the case of many ions. The basic Hamiltonian is

$$H_s = \sum_{j=1}^{N} \frac{\hbar\omega_0}{2}\,\sigma_z^{(j)} = \hbar\omega_0 S_z \tag{4.5}$$

with the qubit transition frequency ω_0 and collective spin operator S_z (cf. 2.2.1). The special case we consider in this section is the transition between the two hyperfine states $|F=2, m_F=1\rangle \equiv |\downarrow\rangle \equiv |0\rangle \leftrightarrow |F=1, m_F=1\rangle \equiv |\uparrow\rangle \equiv |1\rangle$ in the $^2\mathrm{S}_{1/2}$ manifold of $^{9}\mathrm{Be}^+$. At a particular static magnetic field strength, this transition frequency becomes in lowest order insensitive to the strength of the magnetic field [L$^+$05a], meaning that

$$\langle 1|\boldsymbol{\mu}_z|1\rangle - \langle 0|\boldsymbol{\mu}_z|0\rangle = 0 \tag{4.6}$$

with $\boldsymbol{\mu}_z$ the magnetic dipole moment in z-direction. So in this case the magnetic field induced shifts of the two states are identical around $|\boldsymbol{B_0}| = 22.3\,\mathrm{mT}$ [Wah16]. This ensures long coherence times [L$^+$05a], as required for many tasks in quantum computation, quantum simulation, or quantum metrology. Note the similarity to the concept of magical wavelengths for the light shifts caused by optical lattices in atomic clocks.

Interaction with an oscillating field If one adds an oscillating magnetic field $\boldsymbol{B}(\mathbf{R},t) = \boldsymbol{B}(\mathbf{R})\cos(\omega t - \phi)$ at the position of the ion, the ion-field interaction for the hyperfine qubits is given by the magnetic dipole Hamiltonian

$$H_{\mathrm{int}} = -\sum_{j=1}^{N} \boldsymbol{\mu}\cdot\mathbf{B}(\mathbf{R_j})\,\cos(\omega t-\phi), \tag{4.7}$$

where $\boldsymbol{\mu}$ is the vector of magnetic dipole moments and $\mathbf{R_j}$ the position of ion j. Expressing H_{int} by the spin algebra gives

$$\begin{aligned} H_{\mathrm{int}} &= -\sum_{j=1}^{N}\Big[H_{11}|1\rangle\langle 1| + H_{01}|0\rangle\langle 1| + H_{10}|1\rangle\langle 0| + H_{00}|0\rangle\langle 0|\Big] \\ &= -\sum_{j=1}^{N} H_{01}\,\sigma_x^{(j)} + \frac{1}{2}(H_{11}-H_{00})\,\sigma_z^{(j)} \end{aligned} \tag{4.8}$$

in terms of the matrix elements $H_{ab} = \langle a|\boldsymbol{\mu}\cdot\mathbf{B}(\mathbf{R_j}, t)|b\rangle$. In the derivation of Eq. (4.8) it is assumed that $H_{01} = H_{10}$ is real and in going to the second line a constant energy offset $\frac{1}{2}(H_{11} + H_{00})\mathbb{1}$ was dropped. When addressing transitions with $\Delta m = 0$, such as $|0\rangle \leftrightarrow |1\rangle$ introduced above, the only relevant matrix elements are $\langle a|\boldsymbol{\mu}_{\tilde{\boldsymbol{z}}}|b\rangle$. So the transition is driven by the component $\boldsymbol{B}_{\tilde{\boldsymbol{z}}}$, which is the projection of the oscillating field along the quantization axis $\tilde{\boldsymbol{z}}$, thus ideally requiring linear polarization in that direction. In this case the term proportional to $\sigma_z^{(j)}$ in H_{int} vanishes for the field insensitive qubit, where $H_{11} - H_{00} = 0$ following from Eq. (4.6). Additionally, the selection rules give

$$H_{01} = -\mu B_{\tilde{z}} \cos(\omega t - \phi) \tag{4.9}$$

where $\mu \equiv \langle 0|\boldsymbol{\mu}_{\tilde{\boldsymbol{z}}}|1\rangle$. Overall, the interaction Hamiltonian is thus

$$H_{\text{int}} = \mu \cos(\omega t - \phi) \sum_{j=1}^{N} \boldsymbol{B}_{\tilde{z}}(\mathbf{R}_j)\, \sigma_x^{(j)}\,. \tag{4.10}$$

As emphasized above, entangling the ions works when the spin-spin interaction is mediated by the collective ion motion. So in order to see motional sideband transitions in H_{int} one expands $\boldsymbol{B}_{\tilde{\boldsymbol{z}}}$ in a Taylor series around the ion positions. Up to linear order in the small displacement the Hamiltonian is

$$H_{\text{int}} = \mu \cos(\omega t - \phi) \sum_{j=1}^{N} \left(\boldsymbol{B}_{\tilde{z}}(\boldsymbol{\mathcal{R}}_j) + \sum_{l=\{x,z\}} \frac{\partial \boldsymbol{B}_{\tilde{z}}}{\partial l}\Big|_{\boldsymbol{\mathcal{R}}_j} \sum_{k=1}^{N} \boldsymbol{b}_j^{(l,k)} \frac{1}{\sqrt{2}} \ell_{l,k} (a_{l,k}^\dagger + a_{l,k}) \right) \sigma_x^{(j)} \tag{4.11}$$

where the magnetic field and the gradient are evaluated at the equilibrium position $\boldsymbol{\mathcal{R}}_j$ of the ions. In this result we used the approximation that the gradient $\frac{\partial \boldsymbol{B}_{\tilde{z}}}{\partial y}$ of the magnetic field in y-direction, i.e along the ion string, vanishes to a high degree, due to the geometry of the trap. This is because for the experiments we aim to describe the weak trapping axis (y-direction) runs along the microwave conductor generating the oscillating field, which eliminates coupling to modes in that spatial direction. Only couplings to the radial modes remain for that setup.

Sideband interactions The full Hamiltonian of the system at this point is

$$H = H_s + H_{\text{mot}} + H_{\text{int}}, \tag{4.12}$$

combining Eq. (4.4), Eq. (4.5) and Eq. (4.11). In the end we will be interested in oscillating fields with $\omega = \omega_0 \pm (\omega_{l',k'} + \delta)$, detuned close to one of the motional sidebands. We assume the frequency hierarchy $|\delta| \ll \omega_{l',k'} \ll \omega_0$. Going to the interaction picture with respect to $H_s + H_{\mathrm{mot}}$ (denoting the transformed Hamiltonian with a tilde) gives

$$\begin{aligned}\tilde{H} =& \sum_{j=1}^{N} \Bigg\{ \frac{\hbar\Omega_j^C}{2} e^{-i[(\omega-\omega_0)t-\phi]} \sigma_+^{(j)} \\ &+ \sum_{l=\{x,z\}} \sum_{k=1}^{N} \frac{\hbar\Omega_{j,l,k}}{2} \left(\sigma_+^{(j)} a_{l,k} e^{-i[(\omega-\omega_0+\omega_{l,k})t-\phi]} + \sigma_+^{(j)} a_{l,k}^\dagger e^{-i[(\omega-\omega_0-\omega_{l,k})t-\phi]} \right) \Bigg\} + h.c.\end{aligned} \tag{4.13}$$

where terms oscillating with frequencies $\approx 2\omega_0$ are neglected in the standard rotating wave approximation. We define the Rabi frequencies

$$\Omega_j^C \equiv \frac{1}{\hbar} \mu \, \boldsymbol{B}_{\tilde{z}}(\boldsymbol{\mathcal{R}}_j), \tag{4.14}$$

$$\Omega_{j,l,k} \equiv \frac{1}{\hbar} \frac{1}{\sqrt{2}} \mu \, \boldsymbol{b}_j^{(l,k)} \ell_{l,k} \frac{\partial \boldsymbol{B}_{\tilde{z}}}{\partial l} \Big|_{\boldsymbol{\mathcal{R}}_j} . \tag{4.15}$$

The term in the first line of Eq. (4.13) and its Hermitian conjugate correspond to carrier transitions which become resonant for $\omega = \omega_0$. For the operation of the quantum gate, where $\omega = \omega_0 \pm (\omega_{l',k'} + \delta)$, these would be unwanted contributions to the dynamics. Carrier transitions will be neglected in the subsequent theoretical model due to the fact that they are far off-resonant and, by design, the ion trap generates a large magnetic field gradient with simultaneously low residual field amplitude [WHZ+17]. At $\omega = \omega_0 - \omega_{l,k}$ one finds the red sideband, containing terms with $\sigma_+^{(j)} a_{l,k}$ or $\sigma_-^{(j)} a_{l,k}^\dagger$, to be resonant. This creates (removes) motional excitation while simultaneously flipping the spin state to (from) the state $|0\rangle$. At $\omega = \omega_0 + \omega_{l,k}$ the blue sideband is resonant, which has $\sigma_+^{(j)} a_{l,k}^\dagger$ and $\sigma_-^{(j)} a_{l,k}$ interactions, thus creating (removing) simultaneously spin and motional excitations. Counter-rotating terms from the off-resonantly driven other sideband will be neglected in both cases as they are oscillating on a fast timescale when $|2\omega_{l,k}| \gg \delta$.

4.1.2 The Mølmer-Sørensen gate

The interaction proposed by Mølmer and Sørensen [SM99, SM00] is based on a bichromatic drive detuned close to the red and blue sidebands of one motional mode, say l', k'. These weakly off-resonant interactions with a mode of the collective motion of the ion Coulomb crystal can mediate long range spin-spin interactions. In the combination of one red and one blue sideband, the entangling gate described here will then only drive *collective* spin flips of any two ions resonantly. The resulting gate operations were first introduced as an essential component in quantum information processing [CZ95], but can also be used to create metrologically useful entangled spin states [PSO+18]. Spin squeezed states are among them, as we will see. The original idea for gates using microwave near-field gradients was put forward by D. J. Wineland *et al.* [WMI+98] and later on in more detail by C. Ospelkaus *et al.* [OLA+08].

With two driving fields, one at $\omega = \omega_0 + (\omega_{l',k'} + \delta^B)$ and the other at $\omega = \omega_0 - (\omega_{l',k'} + \delta^R)$, the full Hamiltonian can be written as

$$H_{\mathrm{MS}}(t) = \frac{1}{2}\sum_{j,k=1}^{N}\sum_{l=\{x,z\}}\Big\{\hbar\Omega^B_{j,l,k}(t)\Big(\sigma_+^{(j)}a^\dagger_{l,k}e^{-i(\delta^B_{l,k}t-\phi^B)} + \sigma_-^{(j)}a_{l,k}e^{i(\delta^B_{l,k}t-\phi^B)}\Big) \\ + \hbar\Omega^R_{j,l,k}(t)\Big(\sigma_+^{(j)}a_{l,k}e^{i(\delta^R_{l,k}t+\phi^R)} + \sigma_-^{(j)}a^\dagger_{l,k}e^{-i(\delta^R_{l,k}t+\phi^R)}\Big)\Big\}. \tag{4.16}$$

Here $\delta^{(R,B)}_{l,k} \equiv \omega - (\omega_0 \pm \omega_{l,k}) = \pm(\omega_{l',k'} - \omega_{l,k} + \delta^{(R,B)})$ gives the detuning of the driving field to any motional mode l, k. Equation (4.16) is quite general. It allows for the (possibly different) Rabi frequencies $\Omega^{(R,B)}_{j,l,k}(t)$ to be time-dependent and also still consider all motional modes. It is worth highlighting that a Hamiltonian in the form of Eq. (4.16) can also be obtained for other types of qubits and driving fields, not only the special case of near-field microwave gates in $^9\mathrm{Be}^+$ motivated in this section. The same sideband interactions can be obtained with direct laser driving of quadrupole transitions [Jam98a, SKHR+03] or via Raman coupling [MMK+95b, MMK+95a, LBD+05]. Note, however, that the noise effects treated in section 4.1.3 are chosen specifically for the near-field microwave gates performed at PTB [HZS+19, ZHM+19]. Other implementations may be limited by different physical processes. For example spontaneous photon scattering is relevant for gates with Raman coupling [O+07] but not for the microwave near-field approach. We also add that in principle a time-dependence of the phases ϕ^R, ϕ^B is possible. However, an exact analytic treatment is no longer possible in that case, as spin projections at different times no longer commute (generally causing the Magnus expansion in Eq. (4.20) to not terminate at second order), which makes a discussion of such control techniques difficult.

To reduce the complexity of Eq. (4.16) and reveal the desired spin-spin interactions of the gate more easily, some assumptions can be made. First of all, when the detuning is close to a single motional mode, all other modes may be neglected for now. Thus the sums over l and k reduce to a single sum for which we drop mode labels, so $a^\dagger_{l,k}, a_{l,k} \rightarrow a^\dagger, a$ and $\delta^{(R,B)}_{l,k} \rightarrow \delta^{(R,B)}$. Assuming equal coupling of the two driving fields gives the additional replacements $\Omega^B_{j,l,k}(t) = \Omega^R_{j,l,k}(t) \equiv \Omega_j(t)$ and $\delta^R = \delta^B \equiv \delta$. Under these assumptions the resulting Hamiltonian

$$H_{\mathrm{MS}}(t) = \sum_{j=1}^{N}\hbar\Omega_j(t)\sigma^{(j)}_{\bar{\phi}}\left(ae^{i\delta t}e^{-i\frac{\Delta\phi}{2}} + a^\dagger e^{-i\delta t}e^{i\frac{\Delta\phi}{2}}\right) \tag{4.17}$$

is simplified considerably. The basis of the spin projection

$$\sigma_{\overline{\phi}}^{(j)} = \frac{1}{2}\left(\sigma_x^{(j)}\cos(\overline{\phi}) - \sigma_y^{(j)}\sin(\overline{\phi})\right) \tag{4.18}$$

is determined by the mean phase $\overline{\phi} = \frac{1}{2}(\phi^B + \phi^R)$. Note that we include the factor 1/2 in the definition of $\sigma_{\overline{\phi}}^{(j)}$ so that $(\sigma_{\overline{\phi}}^{(j)}, \sigma_{\overline{\phi}-\pi/2}^{(j)}, \frac{1}{2}\sigma_z^{(j)})$ fulfill the commutation relations of angular momentum. Other conventions, where the spin operators do not fulfill this property, are, however, also used in the literature. The phase difference $\Delta\phi = \phi^B - \phi^R$ affects the initial direction of the spin-dependent displacement in phase space. In the following we will assume $\Delta\phi = 0$ due to the high level of control over the phase of the microwave driving fields, which gives

$$H_{\mathrm{MS}}(t) = \sum_{j=1}^{N} \hbar\Omega_j(t)\sigma_{\overline{\phi}}^{(j)}\left(ae^{i\delta t} + a^\dagger e^{-i\delta t}\right). \tag{4.19}$$

Equation (4.19) can be identified as the dynamics of a driven harmonic oscillator with a spin-dependent force. When driving closed curves in the oscillators phase space, effective spin-spin interactions are induced by the geometric (Berry) phase. For completeness we note that related concepts for geometric phase gates have been proposed [L+03, MSJ00, SdMFZ99].

The effect of $H_{\mathrm{MS}}(t)$ can be nicely seen from the unitary time evolution. The exact propagator $\mathcal{U}(t)$ for the ideal gate with the Hamiltonian in Eq. (4.19) can be derived analytically: Expressing $\mathcal{U}(t)$ in terms of the Magnus expansion [Mag54]

$$\mathcal{U}(t) = \exp\left(\sum_{k=1}^{\infty}(-i/\hbar)^k \zeta_k(t)\right), \tag{4.20}$$

where

$$\zeta_1(t) = \int_0^t \mathrm{d}t_1\, H_{\mathrm{MS}}(t_1), \tag{4.21}$$

$$\zeta_2(t) = \frac{1}{2}\int_0^t \mathrm{d}t_1 \int_0^{t_1} \mathrm{d}t_2 \left[H_{\mathrm{MS}}(t_1),\, H_{\mathrm{MS}}(t_2)\right], \tag{4.22}$$

$$\begin{aligned}\zeta_3(t) = \frac{1}{6}\int_0^t \mathrm{d}t_1 \int_0^{t_1} \mathrm{d}t_2 \int_0^{t_2} \mathrm{d}t_3 \Big(&\left[H_{\mathrm{MS}}(t_1), \left[H_{\mathrm{MS}}(t_2), H_{\mathrm{MS}}(t_3)\right]\right] + \\ &\left[H_{\mathrm{MS}}(t_3), \left[H_{\mathrm{MS}}(t_2), H_{\mathrm{MS}}(t_1)\right]\right]\Big),\end{aligned} \tag{4.23}$$

$$\vdots$$

one can use the very convenient fact that for the interaction Hamiltonian in Eq. (4.19) the series terminates after the second order. The resulting propagator is

$$\mathcal{U}(t) = e^{\sum_{j=1}^{N}\sigma_{\overline{\phi}}^{(j)}\left(\alpha_j(t)a^\dagger - \alpha_j^*(t)a\right)}\, e^{-i\sum_{j,n=1}^{N}\Phi_{jn}(t)\sigma_{\overline{\phi}}^{(j)}\sigma_{\overline{\phi}}^{(n)}} \tag{4.24}$$

with the time-dependent displacement

$$\alpha_j(t) = -i \int_0^t \mathrm{d}t_1 \, \Omega_j(t_1) e^{i\delta t_1} \tag{4.25}$$

and geometric phases

$$\begin{aligned}\Phi_{jn}(t) &= \frac{-i}{2} \int_0^t \mathrm{d}t_1 \int_0^{t_1} \mathrm{d}t_2 \, \Omega_j(t_1)\Omega_n(t_2) \left\{ e^{i\delta(t_1-t_2)} - e^{-i\delta(t_1-t_2)} \right\} \\ &= \int_0^t \mathrm{d}t_1 \int_0^{t_1} \mathrm{d}t_2 \, \Omega_j(t_1)\Omega_n(t_2) \sin\big(\delta(t_1-t_2)\big) \, . \end{aligned} \tag{4.26}$$

In order to have pure spin-spin interactions in $\mathcal{U}(t)$, the displacement of the motional mode needs to be zero at the end of the gate. When t_g is the duration for which the gate drive is applied, the requirement is $\alpha_j(t_g) = 0$. On the other hand, the geometric phases $\Phi_{jn}(t_g)$ should take on stable, nonzero values. In that way when driving the gate with one of the center-of-mass modes, which have $b_j = \frac{1}{\sqrt{N}}$ for all j so that $\Omega_j \equiv \Omega$, and assuming for simplicity $\overline{\phi} = 0$, one finds the propagator

$$\mathcal{U}(t) = e^{-i\Phi(t_g) S_x^2} \tag{4.27}$$

which is exactly the one-axis-twisting dynamics we introduced in section 2.4.2. Here in the x-basis, i.e. with the collective spin operator $S_x = \frac{1}{2}\sum_{j=1}^N \sigma_x^{(j)}$ instead of the z-basis we considered before, but this is equivalent up to a collective spin rotation or a rotation of the Bloch sphere.

Instead of the center-of-mass mode, the gate that was realized in Ref. [HZS⁺19] operated with a radial stretch mode of the two-ion crystal, where $\boldsymbol{b}^{l',k'} = \frac{1}{\sqrt{2}}(1,-1)^T$. Nevertheless, it can be shown that at an appropriate gate time, such that $\Phi(t_g) = \frac{\pi}{2}$, the maximally entangled state

$$|\Psi\rangle = \mathcal{U}(t_g)|00\rangle = \frac{e^{i\pi/4}}{\sqrt{2}}\big(|11\rangle - i|00\rangle\big) \tag{4.28}$$

is generated [HZS+19, Hah19]. The state $|\Psi\rangle$ can be used as a benchmark to test the quality of the gate operation. Looking at the fidelity $\mathscr{F} = \langle\Psi|\rho(t_g)|\Psi\rangle$ between the state $\rho(t_g)$, which is generated at time t_g, and the ideal entangled state $|\Psi\rangle$ provides a measure of how well the ideal dynamics is applied [S+00]. Respectively, the infidelity $1 - \mathscr{F}$ quantifies the impact of parasitic interactions. For details on the measurements of the fidelity which we will refer to later, the reader is referred to Refs. [HZS+19, Hah19]. A comparison of different methods to infer $\mathscr{F}$ from the measurement data can be found in Ref. [Zar20].

4.1.3 Error budget from experimental parameters

For actual gate operations many kinds of perturbations need to be considered. Especially in the regime of small infidelities the selection can become very diverse, with each noise source contributing some fraction to the overall low error. In order to identify the current infidelity contributions when producing the maximally entangled state $|\Psi\rangle$, we simulate the dynamics of the system using a master equation which includes one of the noise terms and feed it with experimentally determined input parameters. The treatment of a master equation becomes necessary as the exact propagator can no longer be obtained analytically in the presence of some of the error sources. The selection of error sources presented below is certainly not complete. It is based on the most relevant effects observed in the characterization of the specific experimental setup and is thus aimed at capturing the largest limitations of the measured gate infidelity. Each perturbation is evaluated in isolation, allowing to clearly identify which physical causes need to be addressed in order to improve the quality of the gate.

The full master equation is given by

$$\dot{\rho} = -i[H, \rho] + \mathcal{L}_h \rho + \mathcal{L}_d \rho, \tag{4.29}$$

where the Hamiltonian is $H = H_{\text{MS}} + H_m + H_z + H_{\text{spec}}$. With

$$H_{\text{MS}} = \frac{\hbar}{2} \sum_{j=1}^{N} (\Omega^B(t) \sigma_j^+ a_{x,2}^\dagger e^{-i\delta t} + \Omega^R(t) \sigma_j^- a_{x,2} e^{i\delta t}) + \text{H.c.} \tag{4.30}$$

being a particular case of the light matter interaction in Eq. (4.16) and an extension to the ideal gate interaction presented in Eq. (4.19). This Hamiltonian is adjusted to include the most relevant measured error sources only. The gate operates on one of the radial stretch modes at $\omega_{x,2}$. This mode was chosen as it exhibits the largest coupling to the field gradient and is expected to show a lower heating rate than the center-of-mass oscillation [Jam98b, KWM+98]. Further,

$$H_m = \hbar \delta_\epsilon(t) a_{x,2}^\dagger a_{x,2} \tag{4.31}$$

describes shifts of the motional mode frequency addressed by the gate drive and

$$H_z = \frac{\hbar \Delta_\epsilon(t)}{2} \sum_j \sigma_z^{(j)} \tag{4.32}$$

gives the uncompensated A.C. Zeeman shift of the transition frequency. Couplings to other off-resonant motional modes in the radial plane are included by the term

$$H_{\text{spec}} = \sum_{(l,k) \neq (l',k')} \sum_{j=1}^{N} \frac{\hbar \Omega_{l,k}}{2} (\sigma_j^+ + \sigma_j^-)(a_{l,k} e^{i\delta_{l,k} t} + a_{l,k}^\dagger e^{-i\delta_{l,k} t}). \tag{4.33}$$

In addition to the unitary dynamics of the Hamiltonian H, incoherent processes also disturb the gate operation. Anomalous heating of the secular motion and loss of coherence for the qubit are characteristic for quantum gates with trapped ion. The exact mechanisms of heating is complex, but fluctuating electric fields, originating from the surface of the trap electrodes, are suspected to drive the noise, making this process challenging to eliminate [HCW+13, BKRB15]. In the theoretical model, heating of the motional mode to a thermal state with $\overline{n}_{th} \gg 1$ and decoherence of the qubit are considered by the Lindblad terms [SM00]

$$\mathcal{L}_h \rho = \hbar\gamma_h (\mathcal{D}[a_{x,2}]\rho + \mathcal{D}[a^\dagger_{x,2}]\rho) \tag{4.34}$$

with the heating rate γ_h and

$$\mathcal{L}_d \rho = \frac{\hbar\gamma_d}{2} \sum_j \mathcal{D}[\sigma_z^{(j)}]\rho \tag{4.35}$$

with the decoherence rate γ_d respectively, where

$$\mathcal{D}[\hat{O}]\rho = \hat{O}\rho\hat{O}^\dagger - \frac{1}{2}\hat{O}^\dagger\hat{O}\rho - \frac{1}{2}\rho\hat{O}^\dagger\hat{O}. \tag{4.36}$$

Table 4.1 lists all contributions to the infidelity $1-\mathscr{F}$ for the different error sources considered in this thesis. With the exception of the off-resonant carrier excitation, all are contained in the dynamics of Eq. (4.29). The largest infidelity contribution at 1.3×10^{-2}, due to motional mode instabilities, is in good agreement with the experimentally measured infidelity of $1.8\% \pm 1.2\%$. The remainder of this section is dedicated to a more detailed discussion of the evaluation of the infidelity contributions.

Gate parameters First we specify the fixed parameters of the gate reported in Ref. [HZS+19]. As this was performed in an $N = 2$ ion crystal with an approximately rectangular pulse, where ideally

$$\Omega^R(t) = \Omega^B(t) = \begin{cases} \Omega_g & 0 \leq t < t_g \\ 0 & \text{else} \end{cases}, \tag{4.37}$$

the time-dependent displacement and phase (see Eq. (4.25) and Eq. (4.26)) are

$$\alpha(t) = \frac{\Omega_g}{\delta}\left(e^{-i\delta t} - 1\right), \tag{4.38}$$

$$\Phi(t) = \frac{\Omega_g^2}{\delta^2}\left(\delta t - \sin(\delta t)\right). \tag{4.39}$$

Consequently, the displacement vanishes at gate times and detunings with

$$\delta\, t_g = L\, 2\pi, \tag{4.40}$$

Effect	Parameter	Infidelity
mode instability	$\sqrt{\langle(\delta_\epsilon/\delta)^2\rangle} = 1.1 \times 10^{-2}$ $0.3\,\mathrm{Hz}/\mu\mathrm{s}$ chirp for $600\mu\mathrm{s}$	1.3×10^{-2}
spectator mode	$\Delta\nu = 2\pi \times 42.5\,\mathrm{kHz}$ with $\bar{n}_{z,2} = 0.27$	5.2×10^{-3}
motional heating	$\gamma_h = \dot{\bar{n}}_{x,2} = 28$ ph/s	3.8×10^{-3}
off-resonant carrier excitation	- (measured infidelity)	$< 2.3 \times 10^{-3}$
qubit decoherence	$\tau_d = 1/\gamma_d > 0.5\,\mathrm{s}$	$< 9.3 \times 10^{-4}$
pulse shape	see main text	6.3×10^{-4}
ACZS fluctuations	$\sqrt{\langle(\Delta_\epsilon/\Delta_z)^2\rangle} = 8 \times 10^{-4}$	1.1×10^{-4}
Rabi frequency imbalance	$\frac{\Omega_R - \Omega_B}{\Omega_B} = 2.33 \times 10^{-2}$	4.1×10^{-6}

Table 4.1: **Error budget:** Infidelity contributions from different sources of imperfections. All infidelity values, except for the off-resonant carrier excitation, result from numerical simulations of the quantum dynamics, according to Eq. (4.29). In each case, the respective noise effect is included with a strength given by the measured parameter specified in the second column.

where the integer $L \in \mathbb{N}$ counts the number of loops that are covered in phase space. With Eq. (4.40), the requirement on the geometric phase, $\Phi(t_g) = \frac{\pi}{2}$, can be expressed as

$$\Phi(t_g) = \frac{\Omega_g^2}{\delta^2} L\, 2\pi = \frac{\pi}{2} \quad \Leftrightarrow \quad \delta = 2\Omega_g\sqrt{L}. \tag{4.41}$$

The relations presented above have three free parameters (t_g, δ, Ω_g) for two equations, so one can be chosen freely, which then determines the other two from Eq. (4.40) and Eq. (4.41) for each L. Typically it is the Rabi frequency which is fixed and chosen as large as possible to apply the gate as fast as possible. Limitations can come either from the available laser power, undesired broadening effects or through the energy that is dissipated into the small conducting structures on the surface electrode trap, as in the setup at PTB. There, the Rabi frequency was measured to be $\Omega_g = 2\pi \times 1.071\,\mathrm{kHz}$, resulting in $\delta = 2\pi \times 3.71\,\mathrm{kHz}$ and $t_g = 808\,\mu s$. A deviation to the experimentally determined optimal detuning $\delta_{\mathrm{exp}} = 2\pi \times 3.4\,\mathrm{kHz}$ is likely due to a systematic offset in the measurement of motional frequencies and the reported motional instability. Sideband cooling of the motional mode driving the gate was performed. The final state after cooling was close to the motional ground state with a residual mean phonon number $\bar{n} = 0.11$. While the gate is under ideal conditions independent of $\bar{n}$, we will soon see that the susceptibility of the fidelity to other imperfections is, however, increased for larger values of $\bar{n}$. See Eq. (4.43) for a particular example.

The infidelity values in the error budget of Table 4.1 result from analytic calculations or numerical simulations of the quantum dynamics according to Eq. (4.29) considering the ideal gate parameters described so far with addition of the corresponding noise in the form stated above. All simulations were done with QuTiP [QuT16] and used a truncated Hilbert space for the motional mode. For our analysis, including the first 25 Fock states was sufficient, given the low initial thermal distribution with a measured mean occupation of $\bar{n} = 0.11$ and the small motional displacement during the dynamics. In the following, the error sources are presented in the order of their respective contribution to the overall infidelity.

Motional instability The largest error according to our investigation results from frequency instability of the two-ion rocking mode, which establishes the gate dynamics[1]. This effect consists of two parts: On the one hand, normally distributed variations of the frequency with a standard deviation of $\sqrt{\langle(\delta_\epsilon/\delta)^2\rangle} = 1.1 \times 10^{-2}$, inferred from a full width at half maximum (FWHM) linewidth of $2\pi \times 101\,\mathrm{Hz}$ in a calibration scan directly before the gate measurement. On the other hand, there is a frequency chirp within each gate. We model this effect by a linear increase of the secular frequency $\omega_{l,k}(t)$ of $0.3\,\mathrm{Hz}/\mu\mathrm{s}$ within the first $600\,\mu\mathrm{s}$ and a constant frequency afterwards, based on an observed saturation behaviour [Hah19]. Such frequency chirps have also been observed in other experiments using near-field gradients [HSA$^+$16] and are presumed to be inherent to warm-up processes in the microwave-generating structures.

The infidelity for the shot-to-shot fluctuations of the mode frequency can be studied exactly. Considering the propagator

$$\mathcal{U}(\alpha, \Phi) = \exp\Big(S_{\overline{\phi}}(\alpha a^\dagger - \alpha^* a) - i\Phi S_{\overline{\phi}}^2\Big) \tag{4.42}$$

with $S_{\overline{\phi}} = \sum_{j=1}^{N} \sigma_{\overline{\phi}}^{(j)}$ for general displacement α and phase Φ. The corresponding fidelity is

$$\mathscr{F}(\alpha, \Phi) = \frac{1}{8}\left\{3 + e^{-4|\alpha|^2(\bar{n}+\frac{1}{2})} + 4\sin(\Phi)e^{-|\alpha|^2(\bar{n}+\frac{1}{2})}\right\}. \tag{4.43}$$

This shows how the fidelity is reduced when the conditions $|\alpha(t_g)| = 0$ and $\Phi(t_g) = \frac{\pi}{2}$ are not met exactly. When going to another interaction picture with respect to $H_m = \hbar\delta_\epsilon a_{x,2}^\dagger a_{x,2}$ it becomes clear that the effect of shot-to-shot fluctuations of the mode frequency is equivalent to changes of the detuning $\delta \to \delta + \delta_\epsilon$. So making this replacement in Eq. (4.38) and Eq. (4.39) and using the two expression in Eq. (4.43) produces an exact result for the fidelity with respect to the dimensionless parameter δ_ϵ/δ. Assuming some distribution $P(\delta_\epsilon/\delta)$ for the relative deviation from the nominal mode frequency allows to calculate the average fidelity

---

[1] Referred to as the 'high-frequency rocking mode' in the original publication.

$$\langle \mathscr{F} \rangle = \int_{-\infty}^{\infty} \mathrm{d}(\delta_\epsilon/\delta)\, P(\delta_\epsilon/\delta) \mathscr{F}(\delta_\epsilon/\delta). \tag{4.44}$$

The FWHM for the Lorentzian lineshape in a calibration frequency scans reveals the strength of fluctuations on the timescale of the gate duration. The distribution $P(\delta_\epsilon/\delta)$ is approximated here by a Gaussian with standard deviation $s = \frac{\mathrm{FWHM}}{2\sqrt{2 \ln 2}}$ of the measured FWHM to calculate the average fidelity[2].

For the time-dependent frequency chirp, numerical simulations are required to calculate the infidelity. In this process the gate detuning is numerically optimized to give the lowest infidelity for the combination of frequency chirp and mode fluctuations. A change of the optimal detuning occurs because the chirp will favour a detuning which is lower than the theory value so that over the course of the gate duration the effective detuning moves closer to the theory value due to the chirp. Combining the two effects (again with $\sqrt{\langle (\delta_\epsilon/\delta)^2 \rangle} = 1.1 \times 10^{-2}$) the expected infidelity of both processes is evaluated to 1.3×10^{-2}. This turned out to be the dominant noise contribution to the gate. Addressing this issue via pulse shaping techniques is briefly discussed in section 4.1.4. Figure 4.1 shows the combination of the average infidelity $1 - \langle \mathscr{F} \rangle$ and the contribution of a frequency chirp as a function of the width $s = \sqrt{\langle (\delta_\epsilon/\delta)^2 \rangle}$ of the distribution $P(\delta_\epsilon/\delta)$ and for varying duration T_{chirp} of the linear frequency chirp.

Coupling to the nearest motional mode Another error is caused by driving the identical spin-spin interaction via other motional modes of the two-ion crystal, as shown in the derivation of the Mølmer-Sørensen Hamiltonian. As both the displacement of these other modes as well as the additional geometric phases depend inversely on their detuning with respect to the driving fields, the discussion is limited here to the closest mode only, which contributes the largest error of this kind. It turns out that the relevant mode is the additional ('low-frequency') rocking mode $a_{z,2}$, oscillating in the second radial normal mode direction. This was measured to have an almost identical Rabi frequency, which is why $\Omega_{z,2} = \Omega_g$ is used for the simulations. The relevant contribution to the Hamiltonian is

$$H_{\mathrm{spec}} = \hbar \Omega_{z,2} S_x (a_{z,2} e^{i(\Delta\nu + \delta)t} + a_{z,2}^\dagger e^{-i(\Delta\nu+\delta)t}). \tag{4.45}$$

---

[2] Statistical moments for a Lorentzian distribution are not well defined and the approximation as a Gaussian is quite good.

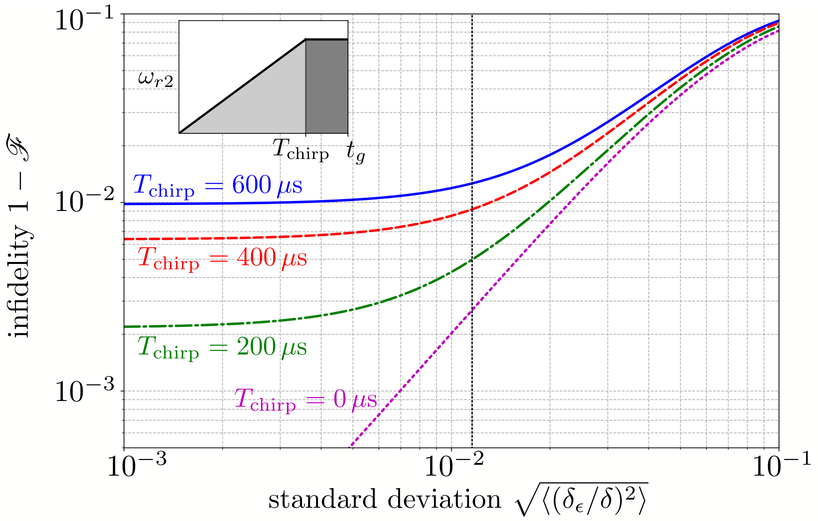

Figure 4.1: **Infidelity from mode instability:** Combined contribution for shot-to-shot fluctuations of the motional mode frequency with standard deviation $\sqrt{\langle(\delta_\epsilon/\delta)^2\rangle}$ and a time-dependent frequency chirp of duration T_{chirp} within each gate. The inset gives a visual of the assumed shape for the frequency chirp over the gate time t_g. The instability reported in the error budget, Table 4.1, is given by the intersection of the blue solid line with the vertical dashed line. Figure taken from Hahn *et al.* [HZS+19].

where the measured frequency spacing was $\Delta\nu = \omega_{z,2} - \omega_{x,2} = 2\pi \times 42.5\,\text{kHz}$. Ground state cooling to $\bar{n}_{x,2} = 0.27$ was applied for this mode as well, resulting in an infidelity of 5.2×10^{-3} due to the competing gate dynamics.

Heating of the driven motional mode and qubit decoherence Heating of the motion and decoherence of the spin qubits contribute an infidelity of 0.38% and $\approx 0.1\%$ respectively. This was inferred from simulations with the heating rate $\gamma_h = \dot{\bar{n}}_{\text{x},2} \simeq 28\,\text{ph/s}$ and the lower limit $\tau_d = 1/\gamma_d > 0.5\,\text{s}$ to the qubit coherence time.

Off-resonant carrier excitation The infidelity contribution due to off-resonant excitation of the carrier transition is included in the error budget of this thesis for completeness only. Due to the large frequency differences between the detuning of the gate and the carrier frequency, no direct simulation of this effect was possible as in that case two very different timescales need to both be included. On the one hand the extremely fast timescale of the off-resonant oscillations from the excitation of the carrier transition and on the other hand the much slower gate duration of almost 1 ms. Following the procedure developed in Ref. [HSA+16, Sep16], the error for a single qubit was estimated to be below 2.3×10^{-3} in Refs. [HZS+19, Hah19].

Pulse shape and Rabi frequency imbalance In the Hamiltonian, Eq. (4.30), equal Rabi frequencies and phases for both ions were assumed, which is true in the experiment as far as measurements could tell. The relative strength of the red and blue sideband, however, may differ because of an imbalance in the pulse envelope amplitude of the two driving fields. Treating general Ω^B and Ω^R allows to include an imbalance in the two sideband Rabi frequencies, which is treated here as a static miscalibration. For a relative error $\dfrac{\Omega_R - \Omega_B}{\Omega_B} = 2.33 \times 10^{-2}$ the infidelity is calculated to be 4.1×10^{-6}, which is by far the lowest contribution in the error budget. Similarly, distortions of the pulse shape for the microwave drive, affecting the temporal profiles $\Omega^R(t), \Omega^B(t)$, result in errors when the gate time and detuning are calculated based on an ideal pulse shape (e.g. assuming a rectangular pulse as was done here). Small infidelities below 6.3×10^{-4} were found in the simulations including such distortions of the pulse shape. In these distortions we combined the influence of adiabatic switching, ramping the driving field on and off over $2\,\mu$s following an error function profile, as well as small changes of the Rabi frequency $\Omega_g(t)$ and the A.C. Zeeman shift $\Delta_\epsilon(t)$ during the pulses, which result from power transients on the ideally rectangular signal.

Residual A.C. Zeeman shift Shifts of the qubit transition frequency due to the driving oscillating fields, the A.C. Zeeman shifts, are an effect that is specific to microwave near-field gates. Although conceptually similar A.C. Stark shifts can occur for laser driven gates. As the shifts of the red and blue detuned fields generally do not cancel each other, the gates are typically operated with some set value for this shift. In the implementation discussed here this was measured to be $\Delta_z = 2\pi \times 4.37\,\mathrm{kHz}$ prior to the gate operation. When calibrated exactly and kept constant over a full experimental run the shifted qubit frequency poses no limitation. The only change is that the driving rf-frequencies $\omega^{(R,B)} = \omega_0 + \Delta_z \pm (\omega_{l',k'} + \delta)$ must include a correction to the A.C. Zeeman shift of the qubits. Note that also the Hamiltonian H in Eq. (4.29) is in an interaction picture with respect to $H_s = (\omega_0 + \Delta_z) S_z$, containing the shifted natural transition frequency. However, residual shifts from fluctuations in the power of the applied driving fields is a cause of error. To account for this perturbation, a term proportional to Δ_ϵ is included (see Eq. (4.32)), which allows the simulation of shot-to-shot fluctuations of the residual A.C. Zeeman shift. The average infidelity in this case was determined by sampling 650 independent runs, each with a shift Δ_ϵ which is drawn from a normal distribution with standard deviation $\sqrt{\langle(\Delta_\epsilon/\Delta_z)^2\rangle} = 8 \times 10^{-4}$, measured from the actual experiment. Fluctuations of the residual A.C. Zeeman shift had been a limitation in previous microwave near-field entangling gates [HSA+16], requiring the additional use of dynamic decoupling to suppress this noise. In the experiments referred to in this thesis, stabilization of the microwave power allowed to reduce the shot-to-shot fluctuations of the A.C. Zeeman shift to such an extent that the simulated infidelity of 1.1×10^{-4} contributes only insignificantly.

4.1.4 Pulse shaping to reduce infidelity

With the motional instability identified as the main limitation of the standard entangling gate, one can now look for ways to specifically counteract this class of perturbations. Of course improving the physical stability of the radial modes in the experiment is one way to diminish the impact, but may prove to be technically challenging at the required level of accuracy. On the other hand, a collection of approaches using coherent quantum control have been proposed and demonstrated in the past which also address fluctuations of the motional frequencies [HCD+12, HM16, SSM+18, WWC+18, GB15, FOL+19]. The underlying idea for many of these schemes is to keep the displacement of the motional state close to the initial state at the end of the gate application. From an optimization point of view the additional control techniques would try to achieve

$$\frac{\partial \alpha(t_g)}{\partial \delta} = 0, \qquad \frac{\partial \Phi(t_g)}{\partial \delta} = 0 \tag{4.46}$$

while simultaneously keeping $\alpha(t_g) = 0$ and $\Phi(t_g) = \frac{\pi}{2}$ over a broad range of detunings. Consequently, the final displacement and geometric phase would be only weakly affected by changes of the detuning.

One special feature of the microwave driving fields is the high degree of control over amplitude and phase that comes with this established technology. So techniques involving the modulation of amplitudes or phases as a resource are well fitted. A practical limitation is, however, set by the energy that can be dissipated into the electrodes generating the trapping fields. This is directly related to constraints on the power and duration of the microwave fields, making a resource efficient approach highly desirable.

As shown in the following, modulation of the amplitudes turns out to be very successful in both regards. Consider for example an adjustment of the pulse envelope to the rf-fields in such a way that the Rabi frequency of the gate is

$$\Omega_g(t) = \Omega \sin^2\left(\frac{\pi t}{t_g}\right). \tag{4.47}$$

In principle there is a lot of room for variations of this simple pulse shape alone. The exponent could be changed or the argument could be replaced by $m\pi/t_g$, so that $m \in \{1, 2, 3, \dots\}$ oscillations are performed in one gate pulse. Only the conditions $\Omega(0) = \Omega(t_g) = 0$ must be met, due to the technical necessity of turning the microwave drive on and off. Despite this great diversity, in this thesis we only follow results for the pulse shape in Eq. (4.47). Further variations were investigated in the thesis of G. Zarantonello [Zar20]. Starting from the $\sin^2$ pulse shape of Eq. (4.47), the displacement and geometric phase

$$\alpha(t) = -\frac{\Omega}{\delta}\frac{2\pi^2(e^{i\delta t}-1)}{4\pi^2-(\delta t)^2}, \tag{4.48}$$

$$\Phi(t) = \frac{\Omega^2}{\delta^2}\frac{32\pi^4\delta t - 20\pi^2(\delta t)^3 + 3(\delta t)^5 - 32\pi^2\sin(\delta t)}{8\big(4\pi^2-(\delta t)^2\big)^2} \tag{4.49}$$

can be calculated directly from Eq. (4.25) and Eq. (4.26). The relations $\alpha(t_g) = 0$ and $\Phi(t_g) = \frac{\pi}{2}$ for generating a GHZ state are fulfilled when

$$t_g = \frac{2\pi\,(k+1)}{\delta}, \tag{4.50}$$

$$\delta = \Omega\sqrt{\frac{(k+1)(3k(k+2)+1)}{2k(k+2)}}, \tag{4.51}$$

where $k = 1, 2, 3, \ldots$ characterizes the order of the modulated gate, similar to the way L described the number of loops for a rectangular pulse shape (see **Gate parameters** in 4.1.3). In the second line we used the connection between δ and t_g given in Eq. (4.50) to simplify the geometric phase $\Phi(t)$ and thus the relation between δ and Ω.

To see how the amplitude modulation influences the fidelity, one can first evaluate the residual phase-space displacement, generated from a detuning $\delta + \delta_\epsilon$ which has an error δ_ϵ to the ideal value. Let us consider the lowest order in δ_ϵ/δ only, which quantifies the relative mode frequency deviations. For the rectangular pulse (with $\Omega_g \equiv \Omega$) this is

$$|\alpha(t_g)|^2 = \pi^2 L\left(\frac{\delta_\epsilon}{\delta}\right)^2 + \mathcal{O}\left(\frac{\delta_\epsilon}{\delta}\right)^3, \tag{4.52}$$

based on Eq. (4.38) and the relations (4.40), (4.41). In contrast, the $\sin^2$ pulse has

$$|\alpha(t_g)|^2 = \frac{\pi^2(k+1)^2(k+1)(3k(k+2)+1)}{2k^3(k+2)^3}\left(\frac{\delta_\epsilon}{\delta}\right)^2 + \mathcal{O}\left(\frac{\delta_\epsilon}{\delta}\right)^3. \tag{4.53}$$

From the two equations it can be concluded that the $\sin^2$ pulse efficiently suppresses parasitical displacements for higher orders k, as $|\alpha(t_g)|^2 \sim \frac{1}{k}$. In contrast the usual multi-loop rectangular pulse has $|\alpha(t_g)|^2 \sim L$. The residual displacement as a function of the order k or L, respectively, is shown in Fig. 4.2**a**. Combined with the result of Eq. (4.43) for the fidelity, it becomes evident that the reduced parasitic displacement also corresponds directly to a higher fidelity, assuming the same values for $\overline{n}$ and Φ.

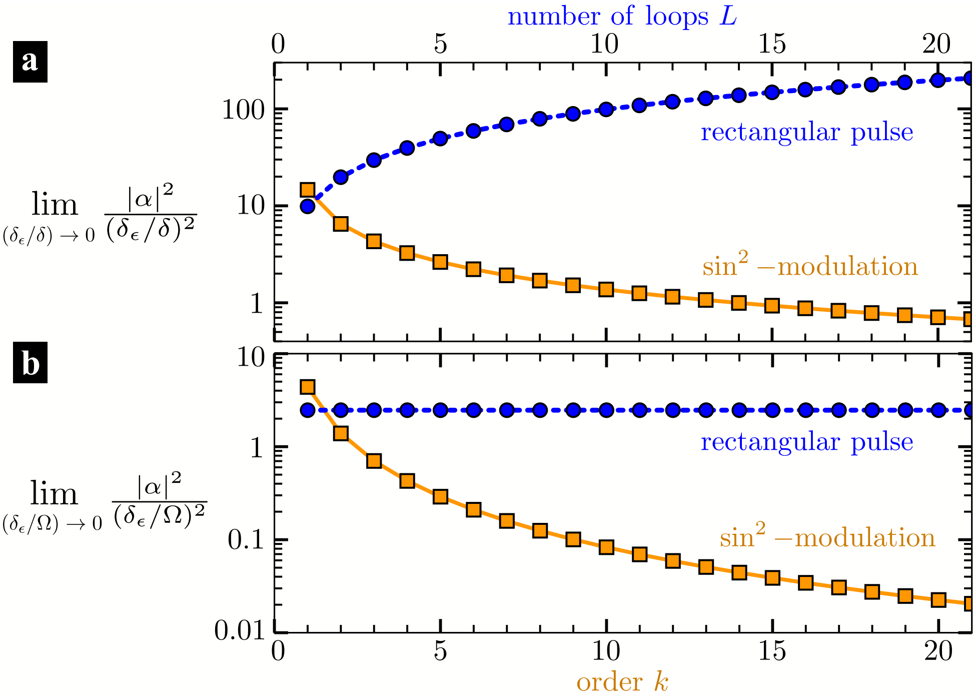

Figure 4.2: **Residual displacement:** Pre-factor to the lowest order residual displacement for relative detuning errors δ_ϵ/δ (part **a**) or δ_ϵ/Ω (part **b**). For gates using a rectangular pulse shape (blue dashed) this is given as a function of the number of loops L and for $\sin^2$-modulation (orange solid) in terms of the order k.

While the above discussion is valuable for a study of the infidelity when the detuning is kept constant and the Rabi frequency is adjusted, this does not necessarily have to be the case. Instead, Ω can be kept constant and δ changes with the order k or L, as it would be e.g. when the maximal Rabi frequency is constraint. In this case we should alter the analysis from above, as now the scales δ_ϵ/δ change with the order k or L. Looking at the pre-factor to this can then be misleading when comparing gates with different k, L. For a fair comparison one should rather consider the residual displacement in orders of δ_ϵ/Ω which is then a fixed scale, quantifying the error in the motional frequency. If we do so, the residual displacement is

$$|\alpha(t_g)|^2 = \frac{\pi^2}{4}\left(\frac{\delta_\epsilon}{\Omega}\right)^2 + \mathcal{O}\left(\frac{\delta_\epsilon}{\Omega}\right)^3, \tag{4.54}$$

for the rectangular pulse and

$$|\alpha(t_g)|^2 = \frac{\pi^2(k+1)^2}{k^2(k+2)^2}\left(\frac{\delta_\epsilon}{\Omega}\right)^2 + \mathcal{O}\left(\frac{\delta_\epsilon}{\Omega}\right)^3. \tag{4.55}$$

for the $\sin^2$-modulation. From this the respective scaling $|\alpha(t_g)|^2 \sim 1$ and $|\alpha(t_g)|^2 \sim \frac{1}{k^2}$ for higher orders L, k can be inferred. The lowest order displacement when Ω is fixed is shown in Fig. 4.2**b**.

Considering the average fidelity over normal distributed fluctuations, Eq. (4.44), produces the results of Fig. 4.3, using the same methods introduced in **Motional instability** (see 4.1.3) but with the displacement and phase from Eq. (4.48) and Eq. (4.49) for the $\sin^2$ amplitude modulation. For comparison, another coherent control method which is specifically designed to reduce errors from mode frequency fluctuations is included in that figure. The Walsh-modulation technique [HCD+12] divides the gate time into multiple intervals where the Rabi frequency is constant (each interval with a specific duration) and then features appropriate sign changes to cancel out residual displacements. The modulation functions will always perform 2^k loops in phase space so that the integer k can be used to label the order. Changes of the sign of the Rabi frequency are applied when a loop closes and spin and motion disentangle. For the lowest orders ($k = 1, 2, 3$) of Walsh modulation $\Omega(t) = \Omega\, W(2^k, t/t_g)$, with[3]

$$W(2, t/t_g) = \begin{cases} 1 & 0 \leq t/t_g < 1/2 \\ -1 & 1/2 \leq t/t_g \leq 1 \end{cases}, \tag{4.56}$$

$$W(4, t/t_g) = \begin{cases} 1 & 0 \leq t/t_g < 1/4 \\ -1 & 1/4 \leq t/t_g < 3/4 \\ 1 & 3/4 \leq t/t_g \leq 1 \end{cases}, \tag{4.57}$$

$$W(8, t/t_g) = \begin{cases} 1 & 0 \leq t/t_g < 1/8 \\ -1 & 1/8 \leq t/t_g < 3/8 \\ 1 & 3/8 \leq t/t_g < 4/8 \\ -1 & 4/8 \leq t/t_g < 5/8 \\ 1 & 5/8 \leq t/t_g < 7/8 \\ -1 & 7/8 \leq t/t_g \leq 1 \end{cases}, \tag{4.58}$$

the displacement and geometric phase are

$$\alpha_2(t) = \frac{\Omega}{\delta}\left(e^{\frac{i\delta t}{2}} - 1\right), \tag{4.59}$$

$$\alpha_4(t) = \frac{\Omega}{\delta}\left(1 - e^{\frac{i\delta t}{4}}\right)^3\left(1 + e^{\frac{i\delta t}{4}}\right), \tag{4.60}$$

$$\alpha_8(t) = \frac{\Omega}{\delta}\left(e^{\frac{i\delta t}{8}} - 1\right)^4\left(1 + e^{\frac{i\delta t}{8}}\right)^2\left(e^{\frac{i\delta t}{4}} + 1\right) \tag{4.61}$$

and

$$\Phi_2(t) = \frac{\Omega^2}{\delta^2}\left(\delta t - 4\sin\left(\frac{\delta t}{2}\right) + \sin(\delta t)\right), \tag{4.62}$$

$$\Phi_4(t) = \frac{\Omega^2}{\delta^2}\left(\delta t - 4\sin\left(\frac{\delta t}{4}\right) - 4\sin\left(\frac{\delta t}{2}\right) + 4\sin\left(\frac{3\delta t}{4}\right) - \sin(\delta t)\right), \tag{4.63}$$

---

[3] The Walsh functions in [HCD+12] are labeled by $2^k - 1$ instead of 2^k but are the same otherwise.

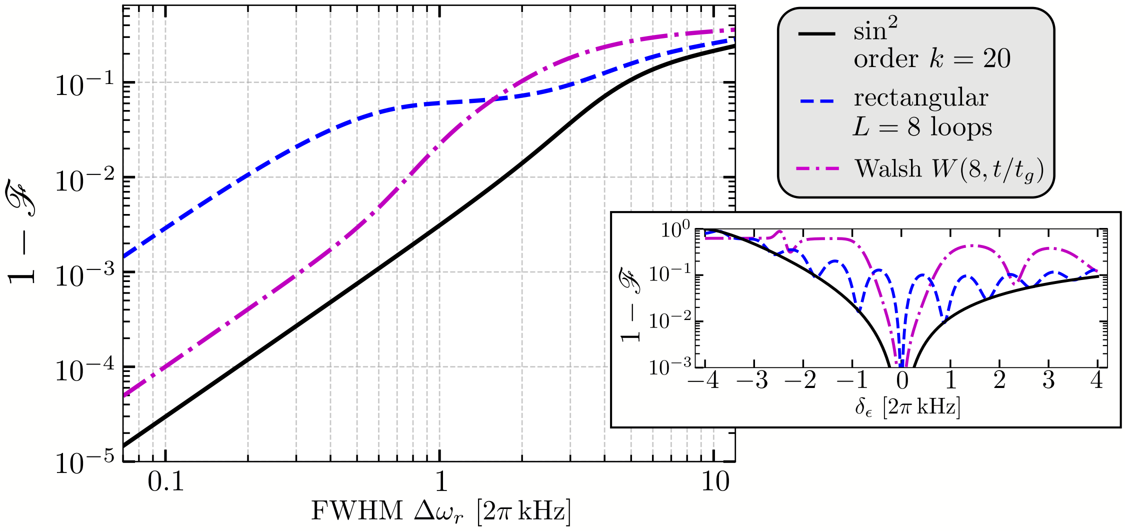

Figure 4.3: **Infidelity with modulation:** Average infidelity for shot-to-shot mode frequency fluctuations as a function of the full width at half maximum $\Delta\omega_r$ of the distribution for secular frequency deviations. The comparison features a $\sin^2$ amplitude modulated gate (black, solid line), a standard rectangular Rabi frequency with $L = 8$ loops (blue, dashed) and Walsh-modulation onto a gate which also performs in total 8 loops (magenta, dash-dotted). The inset shows the infidelity as a function of a fixed frequency error δ_ϵ. This gives an explanation for why the simple rectangular gate is superior to the Walsh-modulation when the FWHM becomes larger than a few kHz. While Walsh-modulation is designed to reduce the infidelity for small values of δ_ϵ it performs worse at rather large deviations. The model applied here considers mode frequency fluctuations with the free parameters $\Omega = 2\pi \times 1.18\,\mathrm{kHz}$ and $\overline{n} = 0.4$; no other error sources are included.

$$\Phi_8(t) = \frac{\Omega^2}{\delta^2}\left(\delta t + \sum_{n=1}^{8} a_n \sin\left(\frac{n\delta t}{8}\right)\right), \tag{4.64}$$

with $a_n = (-12, -4, 12, -12, 4, 4, -4, 1)$. The exact form of these results is not too important. What is to note is that, at $t_g = \frac{2^k 2\pi}{\delta_k}$ and $\delta_k = \Omega\, 2^{\frac{k+2}{2}}$, any residual displacement caused by small perturbations δ_ϵ as above is largely suppressed. This feature is also seen in the inset of Fig. 4.3.

What makes the $\sin^2$ pulse shape extremely interesting is that it is not only easy to implement in the microwave setting, but also very efficient in terms of the energy dissipated into the microwave conductor. Figure 4.3 provides a comparison where the dissipated energy was chosen to be practically equal for all schemes. This shows that under an additional relevant resource constraint the $\sin^2$ amplitude modulation is the most useful between the control techniques considered here. An even larger collection of schemes is considered in Ref. [Zar20], using the same theoretical methods presented here. Interestingly, the result of the larger comparison is the same. The gain in fidelity which was quantified here has been confirmed qualitatively by the experimental implementation presented in Ref. [ZHM+19]. There, an increased gate fidelity using the $\sin^2$ amplitude modulation technique was observed over a large range of motional instabilities. A newly included stabilization of the secular mode frequency, set up by J. Morgner and G. Zarantonello, along with the $\sin^2$ modulation allowed for the measurement of a two-qubit gate infidelity in the range of 10^{-3}. The remaining infidelity for the gate is now expected to be limited by uncontrolled AC Zeeman shifts. For details on the experimental side we again refer to Refs. [ZHM+19, Zar20].

4.2 Laser-less quantum logic for (anti-)protons in Penning traps

Single tapped (anti-)protons are an exciting but also challenging subject for precision metrology. In particular, they allow tests of the fundamental charge, parity, time reversal (CPT) invariance through precise determination of their respective g-factors. To determine the g-factor for an ion in a Penning trap, measurements of the cyclotron and Larmor frequency are required. Especially for the Larmor frequency this has proven to be difficult. In parallel to the progress in trapping single (anti-)protons in Penning traps, laser based manipulation and state readout has become the standard method for trapped ions over the last decades. With the development of quantum logic spectroscopy [SRL+05, WBB+02] even unconventional ions, for which a direct measurement of the spin state is not possible, could be investigated by adding a second, well controllable logic ion. Among the major successes of this method is the use of $^{27}\mathrm{Al}^+$ as a high accuracy optical atomic clock [R+07, CHK+10, BCH+19] and the precision spectroscopy of individual highly charged ions like $^{40}\mathrm{Ar}^{13+}$ [MLK+20]. However, single (anti-)protons do not possess any electronic structure, which makes direct measurements of the Larmor frequency inaccessible. While the laser-driven implementation of quantum-logic spectroscopy fails, the general idea still applies. As long as a SWAP operation of the form

$$\big(c_\uparrow|\uparrow\rangle + c_\downarrow|\downarrow\rangle\big)\otimes|0\rangle_z \to |\downarrow\rangle\otimes\big(c_\uparrow|1\rangle_z + c_\downarrow|0\rangle_z\big), \tag{4.65}$$

between the spin of the (anti-)proton and e.g. the axial motion can be performed faithfully, the motional state can be read out via a $^9\mathrm{Be}^+$ logic ion. For this purpose a motional sideband on the (anti-)proton and subsequent measurement of the motional state on the $^9\mathrm{Be}^+$ ion has to be performed. Instead of utilizing lasers for the SWAP gate, radio frequency and microwave fields are a suitable alternative for (anti-)protons. This method has recently gained renewed attention for trapped ions (see also the entangling gate discussed in section 4.1). For example, proposals have been made for conventional ions in Paul traps to induce the relevant Jaynes-Cummings interaction by static magnetic field gradients and rf-fields [MW01]. However, due to the low mass of the (anti-)proton and the relatively small magnetic moment, it is not a priori clear that this strategy can be easily transferred. In particular, it was unclear what distortions of the motional modes would go along with such a scheme. In this sense it was an open question which kind of restrictions need to be placed on the system parameters and quantum states for a faithful SWAP operation. These aspects are described in the following, according to the published work by Nitzschke *et al.* [NSN+20].

4.2.1 Penning trap with longitudinal magnetic field gradient and transverse oscillating field

Conventional Penning trap The quantum mechanical treatment of a particle in a standard Penning trap is well-known [BG86, CGV17]. Compared to the Paul trap that was discussed in the previous section, the Penning trap features only static electric fields and a static magnetic field for radial confinement. While the electric quadrupole potential

$$V(\boldsymbol{r}) = V_{\mathrm{R}} C_2 (z^2 - \frac{x^2}{2} - \frac{y^2}{2}), \tag{4.66}$$

specified in terms of the voltage V_{R} and a geometric factor C_2, confines the particle in z-direction. A constant magnetic field

$$\boldsymbol{B}_0(\boldsymbol{r}) = B_0 \begin{pmatrix} 0 \\ 0 \\ -1 \end{pmatrix}, \tag{4.67}$$

with vector potential

$$\boldsymbol{A}_0(\boldsymbol{r}) = \frac{B_0}{2} \begin{pmatrix} y \\ -x \\ 0 \end{pmatrix} \tag{4.68}$$

keeps the ion from escaping in the radial-direction, i.e. the x-y-plane. The minimal coupling Hamiltonian

$$H_{\mathrm{mot}} = \frac{(\boldsymbol{p} - q\boldsymbol{A}_0)^2}{2m} + qV,$$

of a particle with charge q and mass m describes the motion of the ion. Here $\boldsymbol{p}$ is the usual canonical momentum operator. Under this field configuration the motion in Cartesian coordinates r_k $(k = x, y, z)$ is coupled, but diagonalizing the Hamiltonian reveals that the motion actually decouples into three independent harmonic oscillators. The resulting Hamiltonian

$$H_{\mathrm{mot}} = \hbar\omega_z \left(a_z^\dagger a_z + \frac{1}{2} \right) + \hbar\omega_+ \left(a_c^\dagger a_c + \frac{1}{2} \right) - \hbar\omega_- \left(a_m^\dagger a_m + \frac{1}{2} \right) \tag{4.69}$$

thus describes one harmonic oscillation along z (axial direction) and two in the radial direction. The oscillation frequencies for the axial, modified cyclotron and magnetron motion are

$$\omega_z = \sqrt{2V_\mathrm{R}C_2\frac{q}{m}}, \qquad \omega_+ = \frac{\omega_c}{2} + \Omega_c, \qquad \omega_- = \frac{\omega_c}{2} - \Omega_c, \tag{4.70}$$

where $\omega_c = -qB_0/m$ is the cyclotron frequency and $\Omega_c > 0$ is defined by $\Omega_c^2 = \omega_c^2/4 - \omega_z^2/2$. For common Penning trap parameters these frequencies obey the hierarchy $\omega_+ \gg \omega_z \gg \omega_-$. The creation and annihilation operators obey the standard relation $[a_k, a_l^\dagger] = \delta_{kl}$ for $k, l = z, c, m$. Explicitly $a_c = (a_x + ia_y)/\sqrt{2}$ and $a_m = (a_x - ia_y)/\sqrt{2}$ so they are constructed as linear combinations of the Cartesian operators ($k = x, y, z$)

$$a_k = \frac{1}{\sqrt{2}}\left(\frac{1}{\ell_k}r_k + \frac{i\ell_k}{\hbar}p_k\right), \tag{4.71}$$

where $\ell_z = \sqrt{\hbar/m\omega_z}$ and $\ell_x = \ell_y \equiv \sqrt{\hbar/m\Omega_c}$ are the zero point fluctuations.

The magnetic dipole energy for a spin-1/2 particle with magnetic moment $\boldsymbol{\mu}$ and gyromagnetic factor g is

$$H_\mathrm{spin} = -\boldsymbol{\mu}\cdot\boldsymbol{B}_0 = \frac{\hbar}{2}\omega_\mathrm{L}\sigma_z, \qquad \omega_\mathrm{L} = \frac{g}{2}\omega_c, \tag{4.72}$$

which also establishes the determination of $g = \frac{2\omega_\mathrm{L}}{\omega_c}$ from the Larmor frequency ω_L and cyclotron frequency ω_c. Combining the spin and motion gives the full Hamiltonian

$$H_0 = H_\mathrm{mot} + H_\mathrm{spin},$$

of a particle in the conventional Penning trap.

Longitudinal gradient and transverse oscillating field If there is an additional gradient present in the static magnetic field, such that $\boldsymbol{B}(\boldsymbol{r}) = \boldsymbol{B}_0 + \boldsymbol{B}_1$ with

$$\boldsymbol{B}_1(\boldsymbol{r}) = b\begin{pmatrix} x/2 \\ y/2 \\ -z \end{pmatrix}, \tag{4.73}$$

this will lead primarily to a Stern-Gerlach splitting of the two spin states $|\uparrow\rangle, |\downarrow\rangle$. Looking at all additional terms (with $2\Omega_c \approx \omega_c$)

$$\begin{aligned} H_1 = {} & \hbar\omega_c\epsilon\left(a_z + a_z^\dagger\right)\left(\frac{g}{2}\sigma_z + 1 + 2a_c^\dagger a_c + a_c a_m + a_c^\dagger a_m^\dagger\right) \\ & - \hbar\omega_c\frac{g\epsilon}{2}\sqrt{\frac{\omega_z}{\omega_c}}\left(\sigma^+\left(a_m + a_c^\dagger\right) + \sigma^-\left(a_c + a_m^\dagger\right)\right) \\ & + \hbar\omega_c\epsilon^2\left(a_z + a_z^\dagger\right)^2(a_c^\dagger + a_m)(a_m^\dagger + a_c), \end{aligned} \tag{4.74}$$

which add to H_0 when including $\boldsymbol{B}_1$ (and the corresponding vector potential $\boldsymbol{A}_1$), this splitting is identified as the spin-dependent displacement $\propto (a_z + z_z^\dagger)\sigma_z$ in the first line. The size of the spin-dependent displacement and an additional mean displacement, which is still present in this form, are characterized by

$$\eta = \frac{\epsilon g \omega_c}{\omega_z}, \qquad \alpha = \frac{\omega_c \epsilon}{\omega_z}. \tag{4.75}$$

The dimensionless parameter

$$\epsilon = \frac{b \ell_z}{2\sqrt{2} B_0} \tag{4.76}$$

generally characterizes the relative change of the magnetic field per zero point fluctuation. While the overall separation of the two spin states for current magnetic field gradients is likely too small to measure the spin state directly (see Table 4.2), this still constitutes a first interaction between spin and ion motion. Adding an oscillating field

$$\boldsymbol{B}_2(t) = B_2 \begin{pmatrix} -\cos(\omega t) \\ -\sin(\omega t) \\ 0 \end{pmatrix} \tag{4.77}$$

to this setting can produce resonant interactions between spin and the axial harmonic oscillation: Under a suitable unitary transformation and in a rotating frame with the frequency ω of the oscillating field we find the most relevant terms of the overall Hamiltonian to be [NSN$^+$20]

$$\bar{H} = \frac{\hbar \Delta}{2}\sigma_z + \hbar \omega_z a_z^\dagger a_z + \frac{\hbar \Omega}{2}(\sigma^+ + \sigma^-) + \frac{\hbar \Omega \eta}{2}(\sigma^+ - \sigma^-)(a_z^\dagger - a_z) + \bar{H}_{\text{rest}}, \tag{4.78}$$

where

$$\Delta = \omega_{\text{L}} - 2 g \epsilon \alpha \omega_c - \omega, \tag{4.79}$$

is the detuning of the transverse oscillating field from the effective spin transition frequency and the Rabi frequency was defined as

$$\Omega = \frac{-q g B_2}{2m}. \tag{4.80}$$

Looking at Eq. (4.78), many of the terms underlying the controlled phase gate of section 4.1 can be identified here as well. The carrier drive (third term on the RHS) becomes resonant at $\Delta = 0$ while the red and blue sideband interactions in the form of the Jaynes-Cummings Hamiltonian (fourth term on the RHS) become resonant for $\Delta = \pm\omega_z$ respectively. One can also see the motivation of η being a Lamb-Dicke parameter as the sidebands are driven with an effective Rabi frequency $\eta\Omega$. While for the quantum gate the trap was designed specifically to create strong sideband transitions with a small residual carrier drive, this is commonly not the case with Penning traps used for precision measurements. On the one hand, all terms in

$$\begin{aligned}\bar{H}_{\text{rest}} = {} & \hbar(\omega_+ + \omega)a_c^\dagger a_c - \hbar(\omega_- + \omega)a_m^\dagger a_m + \hbar\omega_z\eta^2 J_z^2 - \hbar\omega_c\epsilon\Big\{ g\eta J_z\sigma_z \\ & + \frac{g}{2}\sqrt{\frac{\omega_z}{\omega_c}}\big(\sigma^-(a_c + a_m^\dagger) + \text{h.c.}\big) - \big(a_z + a_z^\dagger - 2\eta J_z - 2\alpha\big)\big(2a_c^\dagger a_c + a_c a_m + a_c^\dagger a_m^\dagger\big) \\ & + g\big(a_m^\dagger a_m - a_c^\dagger a_c\big)\big(a_z^\dagger + a_z\big)\Big\} + \hbar\omega_c\epsilon^2\big(a_z + a_z^\dagger - 2\eta J_z - 2\alpha\big)^2(a_c^\dagger + a_m)(a_m^\dagger + a_c).\end{aligned} \tag{4.81}$$

disturb the dynamics at different levels. The notion of total angular momentum $J_z = (L_z + S_z)/\hbar = a_m^\dagger a_m - a_c^\dagger a_c + \sigma_z/2$, which is a conserved quantity in the Penning trap, was used here to shorten the equation. These perturbation terms indicate that increasing the effective sideband Rabi frequency by an increased gradient (raising the value of η and ϵ) comes at the cost of mode mixing and non-linearity terms scaling also with the strength of the gradient. On the other hand there is a trade-off between unwanted carrier excitation and increased speed of the sideband dynamics with larger Rabi frequency. When driving sidebands at $|\Delta| = \omega_z$ the carrier drive should still be well off-resonant, meaning that $\Omega/\omega_z \ll 1$ must be fulfilled. In this sense there are clearly compromises to be made regarding the free parameters. To identify the relevant parameter regimes we perform numerical case studies, simulating the dynamics of a single (anti-)proton in this field configuration.

4.2.2 Numerical case studies

The numerical case studies presented here will first examine what is possible with currently achievable parameter values and then look at extensions of the parameter regime. We show that the sideband transitions introduced above can be implemented faithfully and with only small errors due to the perturbation terms for attainable parameter values. This analysis employs the numerical values for the antiproton ($q = -e_0 = -1.6 \cdot 10^{-19}\,\text{C}$, $m_p = 1.67 \cdot 10^{-27}\,\text{kg}$, $g = 5.5857$), but our conclusions remain valid for the proton as well [NSN+20].

As a first step the time evolution of the spin state and axial motion are studied: Assume the (anti-)proton is prepared in the spin state $|\uparrow\rangle$ and in its overall ground state of motion $|0, 0, 0\rangle$, expressing the number of excitations in the z, cyclotron and magnetron mode. Ideally, a pulse in the transverse direction of duration

$$\tau = \frac{\pi}{\Omega\eta} \tag{4.82}$$

and oscillating at a detuning $\Delta = \omega_z$ from the shifted spin resonance frequency will effectively convert the spin excitation into z motion without affecting the other modes,

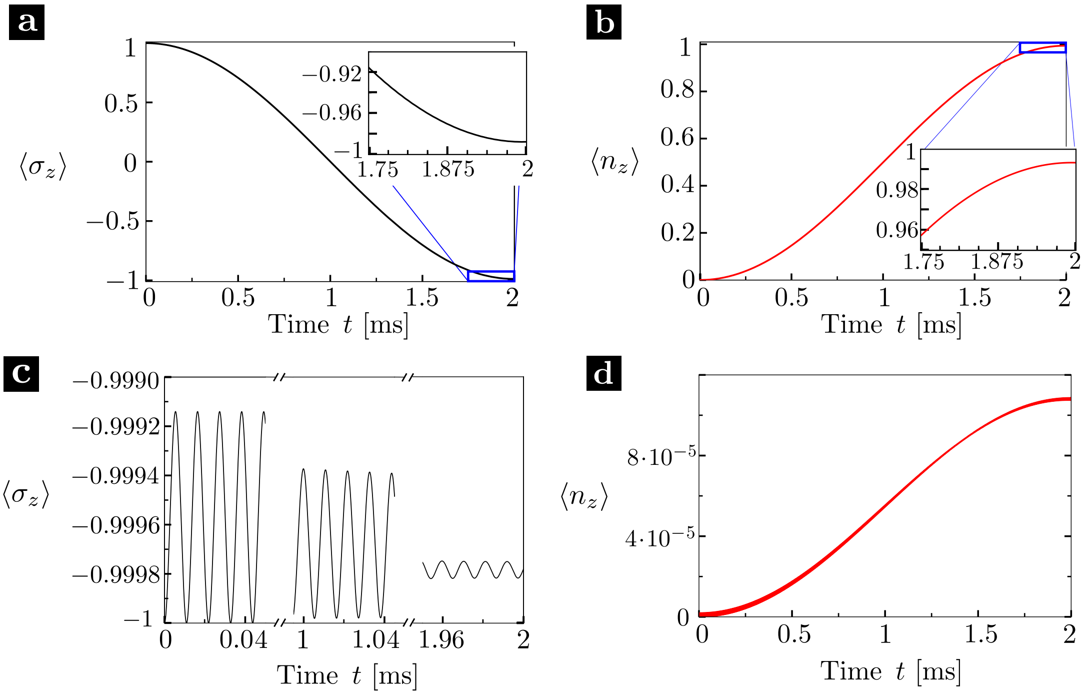

Figure 4.4: **Red sideband SWAP dynamics:** Time traces for the spin polarization $\langle\sigma_z\rangle$ (black) and average quanta in the axial mode $\langle n_z\rangle$ (red) when driving a red sideband, i.e. $\Delta = \omega_z$. At the start of the dynamics, all motional modes are in their ground state. We show the dynamics starting from $|\uparrow\rangle \otimes |0\rangle_z$ in parts **a-b** and $|\downarrow\rangle \otimes |0\rangle_z$ in parts **c-d**. The parameters are as shown in Table 4.2. Figure reproduced from Nitzschke *et al.* [NSN+20].

$|\uparrow\rangle \otimes |0,0,0\rangle \to |\downarrow\rangle \otimes |1,0,0\rangle$. At the same time, if the spin was initially in state $|\downarrow\rangle$, no coupling to motion occurs, i.e. $|\downarrow\rangle \otimes |0,0,0\rangle \to |\downarrow\rangle \otimes |0,0,0\rangle$, as here the red sideband requires to remove a phonon, which is not possible in the ground state. Given the parameters presented in Table 4.2 we find that it is possible to exploit sideband transitions, as described by the Hamiltonian in Eq. (4.78), without having significant contributions from the coupling to cyclotron and magnetron mode from the terms in the Hamiltonian given by Eq. (4.81).

To illustrate this point, Fig. 4.4 shows the result of a numerical solution of the Schrödinger equation for the complete Hamiltonian in Eq. (4.78), including even the terms of second order in the Lamb-Dicke parameter, that is $(\hbar\Omega\eta^2/4)(a_z^\dagger - a_z)^2(\sigma^+ + \sigma^-)$. This is a precautionary measure, since with an effective Lamb thickness parameter $\eta = 0.13$ the higher order terms may not be simply neglected. However, we did not find a significant influence of these terms here. Within the simulations we truncate the Hilbert space of each motional mode at Fock state 5. This was found to be sufficient as the dynamics is limited to the lowest Fock states only and convergence of the simulation was reached already at this low cutoff. Figure 4.4 shows the spin po-

	Parameter	Symbol	Value	Unit	Eq.
Independent trap parameters	Longitudinal magnetic field	B_0	3.00	T	(4.67)
	Longitudinal trap frequency	ω_z	91.49	2π kHz	(4.70)
	Magnetic field gradient	b	1200.00	T/m	(4.73)
Derived trap parameters	Cyclotron frequency	ω_c	45745.13	2π kHz	(4.70)
	Modified cyclotron frequency	ω_+	45745.04	2π kHz	(4.70)
	Magnetron frequency	ω_-	91.49	2π Hz	(4.70)
	Relative field gradient per zero point fluctuation	ϵ	$4.68 \cdot 10^{-5}$	-	(4.76)
	Mean displacement in z per zero point fluctuation	α	$2.34 \cdot 10^{-2}$	-	(4.75)
	Effective Lamb-Dicke parameter	η	$1.31 \cdot 10^{-1}$	-	(4.75)
	Gradient induced shift of spin resonance	$2g\epsilon\alpha\omega_c$	558.95	2π Hz	(4.79)
Pulse parameters	Rabi frequency	Ω	1.91	2π kHz	(4.78)
	Effective Rabi frequency for sideband transition	$\eta\Omega$	250.00	2π Hz	(4.78)
	Spurious coupling of spin to cyclotron/magnetron mode	$\epsilon\omega_c$	2.14	2π kHz	(4.81)
	Pulse duration for π-pulse	τ	2.00	ms	(4.82)
	Suppression of carrier transition	Ω/ω_z	$2 \cdot 10^{-2}$	-	

Table 4.2: **(Anti-)proton parameter values:** Case study for sideband pulses coupling spin and motion of an (anti-)proton. Table adapted from Nitzschke *et al.* [NSN+20].

larization $\langle \sigma_z(t) \rangle$ and the average number of quanta $\langle n_z(t) \rangle$ in the axial mode versus time for the initial state $|\uparrow\rangle \otimes |0,0,0\rangle$ (in parts **a** and **b**) and $|\downarrow\rangle \otimes |0,0,0\rangle$ (in parts **c** and **d**), respectively. Figure 4.4**a** and Figure 4.4**b** clearly show the spin excitation oscillating over to the motional degree of freedom within a time $\pi/\eta\Omega = 2\,\mathrm{ms}$ for the pulse parameters given in Table 4.2. Up to very small errors (see the zoom-ins around $t = 2\,\mathrm{ms}$) this corresponds exactly to the expected sideband dynamics. The population of excited states in the cyclotron and magnetron mode were found to be insignificantly small and are therefore not shown. In contrast, the other initial state, $|\downarrow\rangle \otimes |0,0,0\rangle$, has no resonant transitions that can be driven. This state should ideally remain unchanged. Figure 4.4**c** and Figure 4.4**d** thus illustrate the effects of spurious dynamics from coupling to cyclotron and magnetron motion. The errors consist of small residual excitation of spin and axial motion, on the order of ϵ, with rapid oscillations on a timescale $\sim 2\pi/\omega_z$, so roughly on the order of the axial frequency.

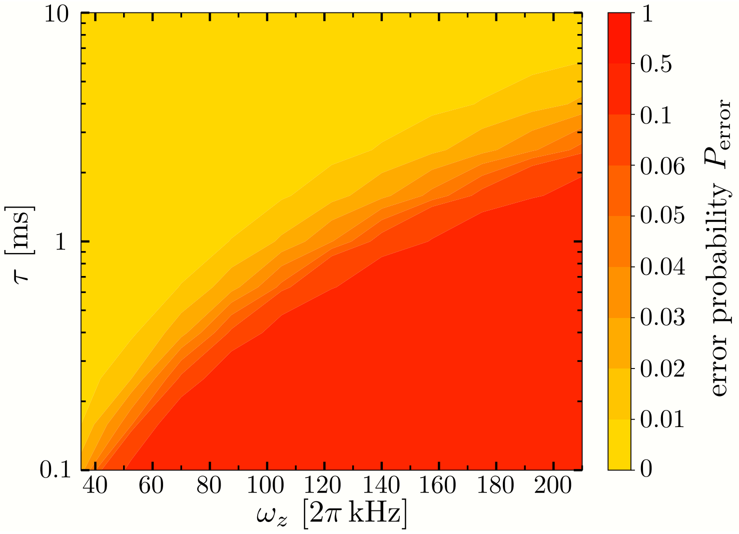

Figure 4.5: **Extended parameter scan:** Error probability for a spin measurement based on the sideband SWAP as a function of the duration τ and axial frequency ω_z. The non-linear color scale shows two major regimes of operation. In the bottom right, the red region signals unfeasible SWAP operations with errors beyond 50%. In the top left, the yellow region corresponds to SWAP interactions with error probabilities at most 1%. This should be viewed as an upper bound to the readout error as for this figure the numerical simulations considered the spin and axial motion only. We are thus not calculating the exact error but only an upper bound. Figure reproduced from Nitzschke *et al.* [NSN⁺20].

When using the SWAP gate to effectively perform spin measurements, as in Eq. (4.65), one can quantify the intrinsic imperfections of the SWAP gate by studying the error probability of the readout. Specifically, readout errors occur with probability $P(n_z = 0|\uparrow)$ when starting with the spin in the excited state and with probability

$P(n_z \neq 0|\downarrow)$ when starting in the ground state. The two cases describe, respectively, the absence of state transfer from the excited spin state or the faulty measurement of an excitation in the z mode by off-resonant driving. We define the total error probability as $P_{\text{error}} = \big(P(n_z = 0|\uparrow) + P(n_z \neq 0|\downarrow)\big)/2$, where an equal *a priori* probability for both spin states was assumed. Figure 4.5 shows the total error probability versus pulse duration τ and longitudinal confinement ω_z. The Rabi frequency is scaled such that $\eta\Omega\tau = \pi$, to always assure a proper state swap. So in this case reducing the SWAP duration τ also means increasing the Rabi frequency, which of course finds its limitations when the condition $\Omega/\omega_z \ll 1$ for off-resonant carrier driving is weakened. This can be clearly seen in Fig. 4.5 by the drastic increase of the readout error in the lower right half of the plot. Nevertheless we identify also large regions where low readout errors are possible, which highlights the prospects of this method.

4.3 Conclusion and outlook

Over the course of this section we have presented promising results on the laser-less control of trapped ions. The spin-spin and spin-motion interactions established here form a basis for quantum computation, quantum simulation and quantum metrology.

Concerning the microwave driven phase gates we were able to calculate the error budget for a state-of-the-art system with integrated control electrodes in a surface electrode ion trap. In a combination of analytical modelling and numerical simulations of the gate dynamics, we evaluated the infidelity contributions for a variety of noise processes based on experimentally determined input values. Instability of the radial mode, mediating the interaction, was identified as the main source of error. We found good agreement between the calculated errors and the measured infidelity. To improve the gates, a comparison of different coherent control methods was made. In particular, modulation of the amplitude according to a $\sin^2$ function allows to drastically reduce errors originating from fluctuations of the secular oscillation frequency. This approach, which fits particularly well to the capabilities of microwave controls, also turns out to be efficient with respect to the input energy of the driving field.

Given the high quality of gate operations that were finally achieved, applications in quantum computation or quantum simulation can now be envisioned. One challenge is certainly the scaling to larger ion crystals while maintaining the high quality of the interactions. To study the relevant sources of errors for larger numbers of ions the methods presented here are generally still appropriate. However, they may need to be re-evaluated for what kind of perturbations can be characterized in the measurements. Further applications of the phase gates are in quantum metrology, as discussed in previous chapters of this thesis. Unfortunately, the special case of $^9\text{Be}^+$ is less relevant as an atomic clock. Although a high stability can be expected due to the magnetic field-insensitive qubit, at $\omega_0 = 1082.55$ MHz it is still a microwave transition. Therefore it will be difficult for an atomic clock based on $^9\mathrm{Be}^+$ to compete with the relative frequency stability of optical atomic clocks, where $\omega_0 \sim 10^{15}$ Hz. More interesting would then be the question whether measurements on the $^9\mathrm{Be}^+$ hyperfine qubit can provide information about new physics in some other respect.

As the theoretical model of the gate dynamics is quite general, the methods described here can still be used for the investigation of quantum gates on other transitions. For example to study the generation of entanglement on optical qubits, where an improved stability of high-precision atomic clocks can actually be expected (see chapter 3). Finally, with regard to the last chapter, it should be noted that accurate control of $^9\mathrm{Be}^+$ ions is also extremely important for hybrid systems in which $^9\mathrm{Be}^+$ is used as logic ions.

In the last section, the quantum mechanical dynamics of a single (anti-)proton in a Penning trap with a magnetic field gradient and an oscillating field in transverse direction was investigated. From the theoretical analysis, the Jaynes-Cummings dynamic between the spin and the axial oscillation mode of the ion results on the one hand, and on the other hand a multitude of further interactions between spin and motion as well as among the different modes of motion is found. Using case studies it was shown that the sidebands for the axial motion can be specifically addressed without being limited by spurious terms. In particular, the trap parameters and strength of the magnetic field gradient are compatible with the design of Penning traps for precision measurements, where high magnetic field gradients are already present when a magnetic bottle is created. The laser-less sideband interactions we have analyzed could enable quantum-logic based readout for the spin state of single (anti-)protons in the future.

In a step towards the realisation of this protocol further aspects need to be considered. In this thesis only the overall ground state of motion was considered at the start of the sideband interaction. Continuing in this direction, we have seen that weak thermal excitations in the motional modes can have a considerable influence on the dynamics. While a small population in the first excited state of the axial motion did not reduce the quality of an effective spin readout, population of excited states of the cyclotron and magnetron mode had a drastic effect [NSN+20]. Achieving ground state cooling for all motional modes is certainly a challenging task. Nevertheless, key methods of cooling all motional modes in a Penning trap have been shown. The overall cooling process may be achieved through sympathetic cooling to the ground state on the axial mode [GSTS16] and mode coupling between the radial and axial modes [CWBP90]. Note that only axial cooling to near the ground state is strictly necessary for the quantum logic scheme. However, changes of the total angular momentum, which come with cyclotron and magneton excitation, cause significant shifts of the effective transition frequency. In this sense the scheme could still be possible if the angular momentum is kept sufficiently stable. Another point to address is preparing the ion at the position of the strong magnetic field gradient. Only a minimal model for ion transport was discussed in Nitzschke *et al.* [NSN+20]. More detailed studies of the ion transport in a Penning trap would certainly be required to understand the possibilities and restrictions it poses on the presented scheme. Finally, we note that the relatively long SWAP duration may at some point be problematic if there are competing noise sources, like anomalous heating of the modes. So far extremely low heating rates were measured in state-of-the-art Penning traps [B+19a], so the SWAP gate may actually not be limited by heating. However, a detailed study including heating remains an open task.

5

Summary and closing statements

This thesis was motivated by the quest to explore new theoretical concepts for entanglement enhanced quantum metrology, contributing to improved optical atomic clocks and similar precision measurements with atoms. Progress in this direction is envisioned to guide our understanding of fundamental physical principles as a long term goal. The three main parts of this thesis considered entanglement enhanced Ramsey interferometry, the trade-off between laser noise and quantum projection noise for entanglement enhanced strategies in optical atomic clocks, and the robust generation of spin-spin and spin-motion interactions with trapped ions.

The first part treated atomic phase measurements, a task which is ubiquitous in precision metrology and often carried out via Ramsey interferometry. The applications of this method range from spectroscopy to magnetometry, gravimetry and frequency metrology (atomic clocks), making Ramsey interferometry an interesting case study. Prior to the results of this thesis, some entangled states were known to enhance the sensitivity beyond the quantum projection noise limit of uncorrelated atoms [KU93]. Even fundamental limits to the sensitivity of Ramsey interferometry were developed [GLM11, PSO$^+$18], showing that in principle large sensitivity is possible. However, generating the required optimal states and complex measurement operations may be difficult to implement and thus prohibit the use of such protocols. Any noise, which perturbs the spin-spin interaction, is troublesome as well, reducing the achievable sensitivity, especially for highly entangled states. With experiments in quantum metrology approaching a 'NISQ-like' [Pre18] era, where noisy entangling interactions on up to hundreds of ions or $\sim 10^4$ neutral atoms comes into reach [PSO$^+$18], it becomes ever more important to look for classes of robust protocols which still provide significant enhancement. The guiding research questions identified for chapter 2 were thus: Can Ramsey protocols be robustly enhanced with minimal requirements for measurements and interactions? Are there any alternatives to the known protocols if only specific controls are allowed?

The answers to these questions, and the core results of Chapter 2, can be summarized as follows. First, extensions to standard Ramsey interferometry were constructed by altering the initial interferometer state and also allowing another entangling interaction before applying the final spin measurement. Particular cases of this class have been considered frequently throughout this thesis. With regard to practical interactions, we focused on protocols which make use of one-axis-twisting, which has already been demonstrated in experiments with trapped ions [LBS+04, GBSN+17], cold atoms [HKEK16] and spinor Bose-Einstein condensates [LSM+16]. We demonstrated in chapter 2 that an exact evaluation of the variational class with one squeezing interaction before and one after the signal imprint and otherwise only rotations of the collective spin is possible. Within this class of generalized Ramsey protocols we discovered only one previously unknown protocol, which features an unusual double inversion of the dynamics. This was found by analytic calculation of the sensitivity, combined with an optimization of the geometric degrees of freedom, related to the signal and measurement direction. The new over-un-twisting protocols exhibit Heisenberg scaling of the sensitivity and stand out by reaching the fundamental quantum Fisher information limit as well. Interestingly, the Heisenberg scaling persists when adding collective or individual dephasing noise during the one-axis-twisting interactions. So the new protocols identified here are also robust to relevant experimental imperfections, one of the goals set above. The presented theory can be viewed as a step to approach the elusive Heisenberg limit, despite noise and imperfections.

While we explored the generalized Ramsey protocols with any interaction strength, the optimal points can be difficult to reach in some experiments. In cases where there is a constraint to the strength or duration of the one-axis-twisting, e.g. from the way that the interactions are generated, restrictions on the parameter regimes need to be taken into account. It would then be interesting to increase the complexity of the entangling or decoding interactions to see if there exist different protocol types with only small levels of interaction in a larger variational class. Rather than a restriction of the parameter space, the constraint may instead be incorporated into the cost function of the optimization, based on the physical origin of the constraint. Similarly, bringing the protocols closer to a specific application, it seems interesting to see how the landscapes which were derived here change for different cost functions, which then include distinctive features of that application.

After identifying generalized Ramsey protocols which improve over quantum projection noise, chapter 3 considered a specific application of phase measurements, namely the optical atomic clock. At the start of our research it was already known that ideal optical atomic clocks are mainly limited between quantum projection noise and phase noise from the fluctuating laser frequency. It had further been shown that weakly squeezed states, reducing quantum projection noise without affecting the effective laser coherence time, can improve the stability [ASL04] just as extended designs with multiple cascaded ensembles can, by sequentially prolonging the laser coherence time [BS13a]. Another limitation due to finite dead time and the resulting Dick effect had been characterised long ago [Dic88] but remains a relevant practical limitation for current optical lattice clocks. Building on known stability models we aimed at establishing a minimal theoretical model which captures the essential features of an atomic clock. Given this model we then answer the guiding research question: Under which conditions can the stability of realistic optical atomic clocks, in the simplest architecture, be improved by weakly entangled squeezed states? This directly relates to the question if entangled states should be employed in a given atomic clock.

As the main result of this study a particle number independent bound to the long term stability was identified. This means that for ensembles larger than some critical atom number the stability can no longer be increased with squeezed states. Our newly developed model provides an investigation, in which parameter regimes laser noise is not the most stringent limitation, so squeezing can improve the stability, and in which cases laser noise is dominant and needs to be overcome by other means before squeezing provides an advantage. With current clock parameters the critical number is around 1000 atoms and improved lasers would raise the number to around 10.000 for the next generation of clocks. In the process of these results we also developed a novel analysis of fringe hops from the stochastic differential equation. Looking towards the future it is found that the known cascaded clock setup is compatible with an asymmetric setup of one large atomic ensemble and one single atom clock, even under practical assumptions. This can allow to push interrogation times of the single atom to a regime where limitations from the finite excited state lifetime need to be considered. The results we have presented in that direction provide answers to how much extended clock architectures can circumvent the limits we established for a conventional setup. In cases with insignificant dead time we report first hints of an improved stability from variationally optimised interrogation protocols, in the spirit of the generalized Ramsey protocols developed in chapter 2.

Of course we have made some basic assumptions when modelling the clock instability. Subsequent studies may explore the consequence of e.g. limited atomic coherence, limited excited state lifetime or constraints to the Ramsey time. With the stability bounds established in chapter 3, it would now be interesting to consider the consequences for some of the potential applications of optical atomic clocks. Under which circumstances can entanglement enhanced protocols improve task in navigation, communication or geodesy? Or are the main applications in laboratory settings only, such as tests of fundamental physics and in the definition of the SI second? It is intriguing to wonder if other architectures of clocks would have advantages in that regard. Proceeding the idea of cascaded operation with multiple ensembles, it would be curious to see at which point systematic shifts of the transition frequency in one ensemble lead to limitations on the final stability of the composite system.

With small scale systems identified as promising candidates for entanglement enhanced metrology, chapter 4 explores the robust generation of spin-spin and spin-motion interactions for trapped ions. We have aimed in particular at answering the question: How can the necessary interactions for improved metrology be faithfully implemented in the case of trapped ions? Entanglement of ions following the classic Mølmer-Sørensen gate [SM00] has long been demonstrated [S$^+$00]. Scaling up the number of ions, however, remains a challenging task. Surface-electrode ion traps provide a feasible solution to this problem, especially when adding integrated microwave control to drive the quantum gates. A state-of-the-art setup of this type is considered in chapter 4, where the corresponding experimental goal was to perform a maximally entangled state with high-fidelity. Conventional gates with the microwave near-field gradient had been performed previously [OLA$^+$08, HSA$^+$16], but little had been known on coherent quantum control, exploiting the particular benefits of a microwave drive. In the theory contribution of chapter 4 we first calculated an error budget based on experimentally measured imperfections to predict the gate infidelity and find the limiting noise sources. The results nicely reproduced the observed infidelity of the gate and show instabilities of the motional mode as the largest error source. Extending this first work, different methods of coherent quantum control were studied to further reduce errors. As a core result amplitude modulation of the driving fields stood out as an effective and resource efficient method allowing gates with infidelity in the $\sim 10^{-3}$ range.

High fidelity gates, like the ones analysed in chapter 4, are also relevant to perform tasks in quantum information and quantum simulation. Given the unique scaling opportunities of micro-fabricated traps, studies of more complicated many-body dynamics, dissipative (open) dynamics, or small scale quantum algorithms can be envisioned.

The last part of the thesis established a new method of laser-less spin-motion coupling, focusing in particular on the application for single (anti-)protons in Penning traps. This is a direct answer to the guiding research question: Can one design readout schemes for exotic particles without optical transitions, like single trapped (anti-)protons?

Measuring key properties, like the g-factor of protons and antiprotons, provides insights into fundamental symmetries between matter and antimatter. However, the fact that the (anti-)proton can not be manipulated by using some internal electronic structure, as would be conventional for other ions, but only by the spin degree of freedom makes the system challenging to study on its own. Methods of quantum logic spectroscopy [SRL+05] are applicable, so long as coherent interactions between the spin and one motional mode can be carried out. To this end, we successfully identified parameter regimes for which a sideband SWAP, in the form of the Jaynes-Cummings interaction, can be applied faithfully using an in-build magnetic field gradient and rf-fields. The approach bears similarities to the microwave near field entangling gates and found inspiration in a comparable proposal for quantum information processing by Mintert and Wunderlich [MW01]. Our results provide a step towards quantum logic spectroscopy in yet another exotic system with high relevance to searches for violations of CPT symmetry and Lorentz symmetry. One pressing open question is, if there exist more resilient designs to induce the same interaction, which are e.g. less prone to the initial motion of the ion.

Overall, we hope that the results of this thesis will eventually contribute to the larger goal of establishing quantum mechanical entanglement in a variety of precision measurements. It would be a great success of this branch of research to see an entanglement enhanced atomic physics experiment detect some trace of extensions to our current model of physics. Until now, entanglement enhanced protocols with atomic systems have mostly been shown as proof-of-principle experiments, far from the parameter regimes of the best detectors of this kind. However, given the continuous improvement and the steady removal of technical limitations in this discipline, a growing number of experiments will soon be limited by the influence of quantum mechanical measurement noise. We were able to show this explicitly in chapter 3 for optical atomic clocks. While typical optical lattice clocks are not yet limited by quantum projection noise, the situation is different for smaller ensembles. Especially for the well-established ion clocks, which are now evolving from a complicated, large-scale laboratory system to user-oriented instruments. When aiming at an improved stability with a handful of atoms, methods to reduce the quantum projection noise are essential. The same applies to the newly emerging clocks of neutral atoms in optical tweezers and also for lattice clocks once the clock lasers and dead times improve further. It is therefore encouraging to see that robust Ramsey interferometry can be achieved with reasonable expenditure of established resources (cf. Chapter 2). We believe that the results of this thesis promote the use of entangled states in state-of-the-art precision measurements already in the near future and not only as a long-term goal. Besides the more or less passive adaptation of protocols, an extended view of our results should also include active methods of noise suppression. Decoherence-free subspaces, dynamic decoupling or coherent control can be used to realize robust interactions and prolong the coherence of transitions despite external error sources. The transfer of these control mechanisms to the highly stable optical clock transitions is an open goal and the demonstration of entanglement enhanced protocols a milestone even for a few ions. One of the links between the three parts of this thesis would indeed be the study of robust entanglement generation, as in chapter 4, in the particular case of the highly stable optical clock transitions, cf. chapters 2 and 3. Understanding what the unique challenges and limitations are in that case is an important next step. From the theoretical side, this would require to combine a detailed description of e.g. ion traps, lattice clocks, atoms in tweezer arrays or others, including their systematic shifts and relevant imperfections, with the desired spin-spin interactions. In the end, we placed a lot of emphasis on the search for new physics when motivating the results of this thesis. Entanglement enhanced atomic sensors are certainly envisioned to establish even tighter constraints on parameters involved in some of the models which aim at extending our current understanding of the laws of physics. It would therefore be interesting to quantify more precisely to which level effects of e.g. dark matter or dark energy could be excluded or possibly even detected when using entanglement.

A

Signal and noise from spin characteristic functions

The matrices M and Q, introduced in section 2.6 can be conveniently evaluated when transforming to the spherical basis S_+, S_z, S_- and using the characteristic function approach of Arecchi et al. [ACGT72]. The first part of this appendix shows a detailed derivation of the expectation values contained in M and Q for the noiseless case, while in the rest of this appendix we extend the calculations to include collective and individual dephasing.

A.1 Without dephasing

The spherical basis S_+, S_z, S_- for a collective spin of length $S = N/2$ includes the angular momentum ladder operators $S_\pm = S_x \pm i\, S_y$, introduced in section 2.2.1. In the following, we aim at calculating expectation values with respect to the spin coherent states $|\theta,\varphi\rangle = e^{-i\theta(S_x \sin\varphi - S_y \cos\varphi)}|-S\rangle_z$, where the special case $\varphi = 0$, $\theta = \pi/2$ is the initial state $|\mathrm{x}\rangle$ of a standard Ramsey protocol after the first $\pi/2$-pulse. Anti-normally ordered expectation values in the spherical basis, meaning that S_- is always left of S_z and both to the left of S_+, of the general form $\langle\theta,\varphi|S_-^c e^{\mathfrak{c}S_-} S_z^b e^{\mathfrak{b}S_z} S_+^a e^{\mathfrak{a}S_+}|\theta,\varphi\rangle$, with integers a, b, c as well as arbitrary coefficients $\mathfrak{a}, \mathfrak{b}, \mathfrak{c}$, can be calculated via derivatives of a spin characteristic function [ACGT72]. Explicitly,

$$\langle\theta,\varphi|S_-^c e^{\mathfrak{c}S_-} S_z^b e^{\mathfrak{b}S_z} S_+^a e^{\mathfrak{a}S_+}|\theta,\varphi\rangle = \partial_\alpha^a\, \partial_\beta^b\, \partial_\gamma^c\; X_A(\alpha,\beta,\gamma)\big|_{\alpha=\mathfrak{a},\beta=\mathfrak{b},\gamma=\mathfrak{c}} \tag{A.1}$$

with the anti-normally ordered spin characteristic function [ACGT72]

$$\begin{aligned} X_A(\alpha,\beta,\gamma) &= \langle\theta,\varphi|e^{\gamma S_-} e^{\beta S_z} e^{\alpha S_+}|\theta,\varphi\rangle \qquad \text{(A.2)} \\ &= \left[e^{-\frac{\beta}{2}}\cos^2\left(\frac{\theta}{2}\right) + e^{\frac{\beta}{2}}\left(\sin\left(\frac{\theta}{2}\right)e^{-i\varphi} + \alpha\cos\left(\frac{\theta}{2}\right)\right)\left(\sin\left(\frac{\theta}{2}\right)e^{i\varphi} + \gamma\cos\left(\frac{\theta}{2}\right)\right)\right]^{2S}. \end{aligned}$$

Using the transformation matrix

$$A = \begin{pmatrix} \frac{1}{2} & 0 & \frac{1}{2} \\ \frac{1}{2i} & 0 & -\frac{1}{2i} \\ 0 & 1 & 0 \end{pmatrix} \tag{A.3}$$

and

$$M_s = i \begin{pmatrix} \langle [S_+(\mu), S_+(\nu)] \rangle & \langle [S_+(\mu), S_z(\nu)] \rangle & \langle [S_+(\mu), S_-(\nu)] \rangle \\ \langle [S_z(\mu), S_+(\nu)] \rangle & \langle [S_z(\mu), S_z(\nu)] \rangle & \langle [S_z(\mu), S_-(\nu)] \rangle \\ \langle [S_-(\mu), S_+(\nu)] \rangle & \langle [S_-(\mu), S_z(\nu)] \rangle & \langle [S_-(\mu), S_-(\nu)] \rangle \end{pmatrix}, \tag{A.4}$$

the matrix M is related to its counterpart M_s -in the spherical basis- via $M = AM_sA^T$. In the same way the covariance variance Q can be expressed as $Q = AQ_sA^T$ with

$$Q_s = \frac{1}{2} \begin{pmatrix} \langle [S_+(\nu), S_+(\nu)]_+ \rangle & \langle [S_+(\nu), S_z(\nu)]_+ \rangle & \langle [S_+(\nu), S_-(\nu)]_+ \rangle \\ \langle [S_z(\nu), S_+(\nu)]_+ \rangle & \langle [S_z(\nu), S_z(\nu)]_+ \rangle & \langle [S_z(\nu), S_-(\nu)]_+ \rangle \\ \langle [S_-(\nu), S_+(\nu)]_+ \rangle & \langle [S_-(\nu), S_z(\nu)]_+ \rangle & \langle [S_-(\nu), S_-(\nu)]_+ \rangle \end{pmatrix} - \boldsymbol{j}\,\boldsymbol{j}^T,$$

where $\boldsymbol{j} = \big(\langle S_+(\nu)\rangle, \langle S_z(\nu)\rangle, \langle S_-(\nu)\rangle\big)^T$ and $[\cdot,\cdot]_+$ denotes the anti-commutator.

To calculate the expectation values therein, the spin operators must be brought into anti-normal order before applying Eq. (A.1). For this we use that the transformed operators $S_{(+,z,-)}(\mu) = T_\mu^\dagger S_{(+,z,-)} T_\mu$ are

$$S_z(\mu) = S_z \tag{A.5}$$

and

$$S_\pm(\mu) = e^{i\mu/2} S_\pm e^{\pm i\mu S_z} = e^{-i\mu/2} e^{\pm i\mu S_z} S_\pm. \tag{A.6}$$

Furthermore, the transformations

$$e^{i\mu S_z} S_\pm e^{-i\mu S_z} = e^{\pm i\mu} S_\pm, \qquad e^{-i\mu S_z} S_\pm e^{i\mu S_z} = e^{\mp i\mu} S_\pm \tag{A.7}$$

$$\Rightarrow S_+ e^{\pm i\mu S_z} = e^{\mp i\mu}\ e^{\pm i\mu S_z} S_+, \qquad e^{\pm i\mu S_z} S_- = e^{\mp i\mu}\ S_- e^{\pm i\mu S_z} \tag{A.8}$$

are applied to obtain anti-normal ordering. With these transformations, we find for the first order moments

$$\langle S_+(\nu)\rangle = e^{-i\nu/2} \langle e^{i\nu S_z} S_+ \rangle = e^{-i\nu/2} \partial_\alpha X_A \big|_{\alpha=\gamma=0,\beta=i\nu}, \tag{A.9}$$

$$\langle S_z(\nu)\rangle = \langle S_z \rangle = \partial_\beta X_A \big|_{\alpha=\beta=\gamma=0}, \tag{A.10}$$

$$\langle S_-(\nu)\rangle = e^{i\nu/2} \langle S_- e^{-i\nu S_z} \rangle = e^{i\nu/2} \partial_\gamma X_A \big|_{\alpha=\gamma=0,\beta=-i\nu}, \tag{A.11}$$

where all expectation values are with respect to the coherent spin state $|\theta, \varphi\rangle$. For the symmetric second order moments:

$$\begin{aligned}\langle [S_+(\nu), S_+(\nu)]_+\rangle &= 2\langle S_+(\nu) S_+(\nu)\rangle \\ &= 2e^{-i2\nu}\langle e^{i2\nu S_z} S_+^2\rangle \\ &= 2e^{-i2\nu}\partial_\alpha\partial_\alpha X_A\big|_{\alpha=\gamma=0,\beta=i2\nu},\end{aligned} \tag{A.12}$$

$$\begin{aligned}\langle [S_+(\nu), S_z(\nu)]_+\rangle &= \langle S_+(\nu) S_z + S_z S_+(\nu)\rangle \\ &= e^{-i\nu/2}\langle 2\, S_z e^{i\nu S_z} S_+ - e^{i\nu S_z} S_+\rangle \\ &= e^{-i\nu/2}\Big\{2\partial_\beta\partial_\alpha X_A\big|_{\alpha=\gamma=0,\beta=i\nu} - \partial_\alpha X_A\big|_{\alpha=\gamma=0,\beta=i\nu}\Big\},\end{aligned} \tag{A.13}$$

$$\begin{aligned}\langle [S_+(\nu), S_-(\nu)]_+\rangle &= \langle [S_+, S_-]_+(\nu)\rangle \\ &= 2\langle S_- S_+ + S_z\rangle \\ &= 2\Big\{\partial_\gamma\partial_\alpha X_A\big|_{\alpha=\beta=\gamma=0} + \partial_\beta X_A\big|_{\alpha=\beta=\gamma=0}\Big\},\end{aligned} \tag{A.14}$$

$$\langle [S_z(\nu), S_+(\nu)]_+\rangle = \langle [S_+(\nu), S_z(\nu)]_+\rangle, \tag{A.15}$$

$$\begin{aligned}\langle [S_z(\nu), S_z(\nu)]_+\rangle &= 2\langle S_z^2\rangle \\ &= 2\partial_\beta\partial_\beta X_A\big|_{\alpha=\beta=\gamma=0},\end{aligned} \tag{A.16}$$

$$\begin{aligned}\langle [S_z(\nu), S_-(\nu)]_+\rangle &= \langle S_z S_-(\nu) + S_-(\nu) S_z\rangle \\ &= e^{i\nu/2}\langle 2S_- S_z e^{-i\nu S_z} - S_- e^{-i\nu S_z}\rangle \\ &= e^{i\nu/2}\Big\{2\partial_\beta\partial_\gamma X_A\big|_{\alpha=\gamma=0,\beta=-i\nu} - \partial_\gamma X_A\big|_{\alpha=\gamma=0,\beta=-i\nu}\Big\},\end{aligned} \tag{A.17}$$

$$\langle [S_-(\nu), S_+(\nu)]_+\rangle = \langle [S_+(\nu), S_-(\nu)]_+\rangle, \tag{A.18}$$

$$\langle [S_-(\nu), S_z(\nu)]_+\rangle = \langle [S_z(\nu), S_-(\nu)]_+\rangle, \tag{A.19}$$

$$\begin{aligned}\langle [S_-(\nu), S_-(\nu)]_+\rangle &= 2\langle S_-(\nu) S_-(\nu)\rangle \\ &= 2e^{i2\nu}\langle S_-^2 e^{-i2\nu S_z}\rangle \\ &= 2e^{i2\nu}\partial_\gamma\partial_\gamma X_A\big|_{\alpha=\gamma=0,\beta=-i2\nu}.\end{aligned} \tag{A.20}$$

Finally, the moments for the commutators are:

$$\begin{aligned}\langle [S_+(\mu), S_+(\nu)]\rangle &= \langle S_+(\mu) S_+(\nu) - S_+(\nu) S_+(\mu)\rangle \\ &= e^{-i(\mu+\nu)/2}(e^{-i\nu} - e^{-i\mu})\langle e^{i(\mu+\nu)S_z} S_+^2\rangle \\ &= e^{-i(\mu+\nu)/2}(e^{-i\nu} - e^{-i\mu})\partial_\alpha\partial_\alpha X_A\big|_{\alpha=\gamma=0,\beta=i(\mu+\nu)}\end{aligned} \tag{A.21}$$

$$\begin{aligned}\langle [S_+(\mu), S_z(\nu)]\rangle &= \langle S_+(\mu) S_z - S_z S_+(\mu)\rangle \\ &= -e^{-i\mu/2}\langle e^{i\mu S_z} S_+\rangle \\ &= -e^{-i\mu/2}\partial_\alpha X_A\big|_{\alpha=\gamma=0,\beta=i\mu}\end{aligned} \tag{A.22}$$

$$\begin{aligned}
\langle[S_+(\mu),S_-(\nu)]\rangle &= \langle S_+(\mu)S_-(\nu)-S_-(\nu)S_+(\mu)\rangle \\
&= e^{-i(\mu-\nu)/2}\langle 2S_z e^{i(\mu-\nu)S_z} + (e^{-i(\mu-\nu)}-1)\,S_- e^{i(\mu-\nu)S_z}S_+\rangle \\
&= e^{-i(\mu-\nu)/2}\Big\{2\partial_\beta X_A\big|_{\alpha=\gamma=0,\beta=i(\mu-\nu)} \\
&\qquad\qquad + (e^{-i(\mu-\nu)}-1)\partial_\gamma\partial_\alpha X_A\big|_{\alpha=\gamma=0,\beta=i(\mu-\nu)}\Big\}
\end{aligned} \tag{A.23}$$

$$\begin{aligned}
\langle[S_z(\mu),S_+(\nu)]\rangle &= \langle S_zS_+(\nu)-S_+(\nu)S_z\rangle \\
&= -\langle[S_+(\nu),S_z]\rangle \\
&= e^{-i\nu/2}\partial_\alpha X_A\big|_{\alpha=\gamma=0,\beta=i\nu}
\end{aligned} \tag{A.24}$$

$$\langle[S_z(\mu),S_z(\nu)]\rangle = \langle[S_z,S_z]\rangle = 0 \tag{A.25}$$

$$\begin{aligned}
\langle[S_z(\mu),S_-(\nu)]\rangle &= \langle S_zS_-(\nu)-S_-(\nu)S_z\rangle \\
&= -e^{i\nu/2}\langle S_-e^{-i\nu S_z}\rangle \\
&= -e^{i\nu/2}\partial_\gamma X_A\big|_{\alpha=\gamma=0,\beta=-i\nu}
\end{aligned} \tag{A.26}$$

$$\begin{aligned}
\langle[S_-(\mu),S_+(\nu)]\rangle &= \langle S_-(\mu)S_+(\nu)-S_+(\nu)S_-(\mu)\rangle \\
&= e^{i(\mu-\nu)/2}\langle (1-e^{i(\mu-\nu)})\,S_-e^{-i(\mu-\nu)S_z}S_+ - 2S_ze^{-i(\mu-\nu)S_z}\rangle \\
&= e^{i(\mu-\nu)/2}\Big\{(1-e^{i(\mu-\nu)})\partial_\alpha\partial_\gamma X_A\big|_{\alpha=\gamma=0,\beta=-i(\mu-\nu)} \\
&\qquad\qquad - 2\partial_\beta X_A\big|_{\alpha=\gamma=0,\beta=-i(\mu-\nu)}\Big\}
\end{aligned} \tag{A.27}$$

$$\begin{aligned}
\langle[S_-(\mu),S_z(\nu)]\rangle &= -\langle[S_z,S_-(\mu)]\rangle \\
&= e^{i\mu/2}\langle S_-e^{-i\mu S_z}\rangle \\
&= e^{i\mu/2}\partial_\gamma X_A\big|_{\alpha=\gamma=0,\beta=-i\mu}
\end{aligned} \tag{A.28}$$

$$\begin{aligned}
\langle[S_-(\mu),S_-(\nu)]\rangle &= \langle S_-(\mu)S_-(\nu)-S_-(\nu)S_-(\mu)\rangle \\
&= e^{i(\mu+\nu)/2}(e^{i\mu}-e^{i\nu})\langle S_-^2e^{-i(\mu+\nu)S_z}\rangle \\
&= e^{i(\mu+\nu)/2}(e^{i\mu}-e^{i\nu})\partial_\gamma\partial_\gamma X_A\big|_{\alpha=\gamma=0,\beta=-i(\mu+\nu)}
\end{aligned} \tag{A.29}$$

With the characteristic function

$$X_A(0,\pi/2) = \Big[\frac{1}{2}e^{-\beta/2} + \frac{1}{2}e^{\beta/2}\big(1+\alpha\big)\big(1+\gamma\big)\Big]^{2S} \tag{A.30}$$

we then find

$$\begin{pmatrix}\langle S_+(\nu)\rangle\\ \langle S_z(\nu)\rangle\\ \langle S_-(\nu)\rangle\end{pmatrix} = \begin{pmatrix}q_0\\ 0\\ q_0\end{pmatrix} \tag{A.31}$$

with $q_0 = S\,\cos^{2S-1}(\frac{\nu}{2})$. Likewise one finds

$$Q_s = \begin{pmatrix} q_2 & i\,q_3 & q_1\\ i\,q_3 & q_4 & -i\,q_3\\ q_1 & -i\,q_3 & q_2\end{pmatrix} - \begin{pmatrix}q_0\\ 0\\ q_0\end{pmatrix}\big(q_0,0,q_0\big) \tag{A.32}$$

and thus

$$Q = AQ_sA^T = \begin{pmatrix} \frac{1}{2}(q_1+q_2)-q_0^2 & 0 & 0 \\ 0 & \frac{1}{2}(q_1-q_2) & q_3 \\ 0 & q_3 & q_4 \end{pmatrix} \tag{A.33}$$

as well as

$$M_s = \begin{pmatrix} n_2 & i\,n_3 & n_1 \\ i\,n_4 & 0 & -i\,n_4 \\ n_1 & -i\,n_3 & n_2 \end{pmatrix} \tag{A.34}$$

and

$$M = AM_sA^T = \begin{pmatrix} \frac{1}{2}(n_1+n_2) & 0 & 0 \\ 0 & \frac{1}{2}(n_1-n_2) & n_3 \\ 0 & n_4 & 0 \end{pmatrix}. \tag{A.35}$$

The components are

$$\begin{aligned} q_0 &= \frac{N}{2}\cos^{N-1}\left(\frac{\nu}{2}\right), \\ q_1 &= \frac{N(N+1)}{4}, \\ q_2 &= \frac{N(N-1)}{4}\cos^{N-2}(\nu), \\ q_3 &= \frac{N(N-1)}{4}\sin\left(\frac{\nu}{2}\right)\cos^{N-2}\left(\frac{\nu}{2}\right), \\ q_4 &= \frac{N}{4}. \end{aligned}$$

and

$$\begin{aligned} n_1 &= \frac{N(N-1)}{2}\sin\left(\frac{\mu-\nu}{2}\right)\cos^{N-2}\left(\frac{\mu-\nu}{2}\right), \\ n_2 &= -\frac{N(N-1)}{2}\sin\left(\frac{\mu-\nu}{2}\right)\cos^{N-2}\left(\frac{\mu+\nu}{2}\right), \\ n_3 &= -\frac{N}{2}\cos^{N-1}\left(\frac{\mu}{2}\right), \\ n_4 &= \frac{N}{2}\cos^{N-1}\left(\frac{\nu}{2}\right). \end{aligned}$$

A.2 Expectation values with dephasing

This section contains details on calculating spin expectation values with dephasing noise. The OAT dynamics in the case of collective dephasing is given by the master equation

$$\dot{\rho} = -i[H,\rho] + \gamma_C\mathcal{L}_C[\rho] \tag{A.36}$$

with $H = \chi S_z^2$, $\mathcal{L}_C[\rho] = S_z \rho S_z - \frac{1}{2} S_z^2 \rho - \frac{1}{2} \rho S_z^2$ and the dephasing rate γ_C. Likewise, individual dephasing is described by the master equation

$$\dot{\rho} = -i[H, \rho] + \gamma_I \mathcal{L}_I[\rho] \tag{A.37}$$

with $H = \chi S_z^2$ and $\mathcal{L}_I[\rho] = \sum_{k=1}^N \sigma_z^{(k)} \rho \sigma_z^{(k)} - \rho$ where $\gamma_I > 0$ is the individual dephasing rate, equal for all particles. The formal solution for collective dephasing is

$$\rho(t) = T_\mu e^{\sigma \frac{|\mu|}{2} \mathcal{L}_C} [\rho_0] T_\mu^\dagger = e^{\sigma \frac{|\mu|}{2} \mathcal{L}_C} [T_\mu \rho_0 T_\mu^\dagger] \tag{A.38}$$

from an initial state ρ_0 and with $\sigma = |\gamma_C|/|\chi|$. For individual dephasing we find

$$\rho(t) = T_\mu e^{\Sigma \frac{|\mu|}{2} \mathcal{L}_I} [\rho_0] T_\mu^\dagger = e^{\Sigma \frac{|\mu|}{2} \mathcal{L}_I} [T_\mu \rho_0 T_\mu^\dagger], \tag{A.39}$$

where $\Sigma = |\gamma_I|/|\chi|$. Expectation values of any operator A are then

$$\langle A \rangle = \mathrm{tr}\, [A \rho(t)] = \mathrm{tr} \left[A e^{\sigma \frac{|\mu|}{2} \mathcal{L}_C} [T_\mu \rho_0 T_\mu^\dagger] \right] = \mathrm{tr} \left[T_\mu^\dagger e^{\sigma \frac{|\mu|}{2} \mathcal{L}_C^\dagger} [A] T_\mu \, \rho_0 \right] \tag{A.40}$$

or the same expression with $\sigma \to \Sigma$ and $\mathcal{L}_C \to \mathcal{L}_I$ for individual dephasing. Here, $\mathcal{L}^\dagger$ is the adjoint Lindblad operator, defined via

$$\mathrm{tr}\, [A \, \mathcal{L}[B]] = \mathrm{tr} \left[\mathcal{L}^\dagger [A] \, B \right] \tag{A.41}$$

so that

$$\mathcal{L}^\dagger [A] = L^\dagger A L - \frac{1}{2} L^\dagger L A - \frac{1}{2} A L^\dagger L \tag{A.42}$$

given

$$\mathcal{L}[A] = L A L^\dagger - \frac{1}{2} L^\dagger L A - \frac{1}{2} A L^\dagger L. \tag{A.43}$$

For both, collective and individual dephasing, this simplifies to $\mathcal{L}_C^\dagger = \mathcal{L}_C$ and $\mathcal{L}_I^\dagger = \mathcal{L}_I$. For the protocols of chapter 2, this allows to evaluate the expectation values

$$\langle S_-^{k_-} S_z^{k_z} S_+^{k_+} \rangle \big|_{\phi=0} = \mathrm{tr} \left[T_\nu^\dagger e^{\sigma \frac{|\mu|}{2} \mathcal{L}_C} \left[e^{\sigma \frac{|\nu - \mu|}{2} \mathcal{L}_C} \left[S_-^{k_-} S_z^{k_z} S_+^{k_+} \right] \right] T_\nu \, \rho_0 \right] \tag{A.44}$$

required for the spin covariance matrix as well as the slope

$$\begin{aligned} \frac{\partial \langle S_{\boldsymbol{m}} \rangle}{\partial \phi} \Big|_{\phi=0} &= \frac{\partial}{\partial \phi} \left(\sum_k \mathrm{tr} \left[m_k S_k e^{\sigma \frac{|\nu - \mu|}{2} \mathcal{L}_C} \left[T_{\nu - \mu} e^{-i\phi \sum_l n_l S_l} e^{\sigma \frac{|\mu|}{2} \mathcal{L}_C} \left[T_\mu \rho_0 T_\mu^\dagger \right] e^{i\phi \sum_l n_l S_l} T_{\nu - \mu}^\dagger \right] \right] \right) \Bigg|_{\phi=0} \\ &= i \sum_{l,k} n_l M_{lk} m_k \end{aligned}$$

with

$$M_{l,k} = \mathrm{tr} \left[T_\mu^\dagger e^{\sigma \frac{|\mu|}{2} \mathcal{L}_C} \left[[S_l, \, T_{\nu - \mu}^\dagger e^{\sigma \frac{|\nu - \mu|}{2} \mathcal{L}_C} [S_k] T_{\nu - \mu}] \right] T_\mu \rho \right]. \tag{A.45}$$

The same applies for individual dephasing with $\sigma \leftrightarrow \Sigma$ and $\mathcal{L}_C \leftrightarrow \mathcal{L}_I$. The expectation values presented here can now be reduced to their noiseless version by explicitly evaluating the transformed operators. At this point however we have to separate collective and individual dephasing. For collective dephasing the following holds: First, it is clear that $e^{\sigma\frac{|\mu|}{2}\mathcal{L}_C}[S_z] = S_z$ and from the commutation relations (2.7) it follows that $e^{\sigma\frac{|\mu|}{2}\mathcal{L}_C}[S_\pm] = e^{-\sigma\frac{|\mu|}{4}}S_\pm$. Repeated application of the commutation relations then also gives

$$e^{\sigma\frac{|\mu|}{2}\mathcal{L}_C}[S_\pm^2] = e^{-\sigma|\mu|}S_\pm^2, \tag{A.46}$$

$$e^{\sigma\frac{|\mu|}{2}\mathcal{L}_C}[S_\pm S_z] = e^{-\sigma\frac{|\mu|}{4}}S_\pm S_z, \tag{A.47}$$

$$e^{\sigma\frac{|\mu|}{2}\mathcal{L}_C}[S_z S_\pm] = e^{-\sigma\frac{|\mu|}{4}}S_z S_\pm, \tag{A.48}$$

$$e^{\sigma\frac{|\mu|}{2}\mathcal{L}_C}[S_\pm S_\mp] = S_\pm S_\mp, \tag{A.49}$$

which allows to express all expectation values to the ones with $\sigma = 0$ and appropriate exponential damping factors. With this, we find

$$\begin{pmatrix} \langle S_+(\nu)\rangle \\ \langle S_z(\nu)\rangle \\ \langle S_-(\nu)\rangle \end{pmatrix} = \begin{pmatrix} \tilde{q}_0 \\ 0 \\ \tilde{q}_0 \end{pmatrix} \tag{A.50}$$

with, again, $\tilde{q}_0 = e^{-\sigma\frac{|\nu-\mu|+|\mu|}{4}}S\cos^{2S-1}(\frac{\nu}{2})$.
Likewise one finds

$$\tilde{Q}_s = \begin{pmatrix} \tilde{q}_2 & i\,\tilde{q}_3 & \tilde{q}_1 \\ i\,\tilde{q}_3 & \tilde{q}_4 & -i\,\tilde{q}_3 \\ \tilde{q}_1 & -i\,\tilde{q}_3 & \tilde{q}_2 \end{pmatrix} - \begin{pmatrix} \tilde{q}_0 \\ 0 \\ \tilde{q}_0 \end{pmatrix} \big(\tilde{q}_0, 0, \tilde{q}_0\big) \tag{A.51}$$

and thus

$$\tilde{Q} = A\tilde{Q}_s A^T = \begin{pmatrix} \frac{1}{2}(\tilde{q}_1+\tilde{q}_2) - \tilde{q}_0^2 & 0 & 0 \\ 0 & \frac{1}{2}(\tilde{q}_1-\tilde{q}_2) & \tilde{q}_3 \\ 0 & \tilde{q}_3 & \tilde{q}_4 \end{pmatrix} \tag{A.52}$$

with

$$\begin{aligned} &\tilde{q}_1 = q_1 = S^2 + \frac{S}{2}, \quad \tilde{q}_2 = e^{-\sigma(|\nu-\mu|+|\mu|)}\frac{S}{2}(2S-1)\cos(\nu)^{2S-2}, \\ &\tilde{q}_3 = e^{-\sigma\frac{|\nu-\mu|+|\mu|}{4}}\frac{S}{2}(2S-1)\cos(\frac{\nu}{2})^{2S-2}\sin(\frac{\nu}{2}) \quad \text{and} \quad \tilde{q}_4 = q_4 = \frac{S}{2}. \end{aligned} \tag{A.53}$$

Finally,

$$\tilde{M}_s = \begin{pmatrix} \tilde{n}_2 & i\,\tilde{n}_3 & \tilde{n}_1 \\ i\,\tilde{n}_4 & 0 & -i\,\tilde{n}_4 \\ \tilde{n}_1 & -i\,\tilde{n}_3 & \tilde{n}_2 \end{pmatrix} \tag{A.54}$$

and

$$\tilde{M} = A\tilde{M}_s A^T = \begin{pmatrix} \frac{1}{2}(\tilde{n}_1+\tilde{n}_2) & 0 & 0 \\ 0 & \frac{1}{2}(\tilde{n}_1-\tilde{n}_2) & \tilde{n}_3 \\ 0 & \tilde{n}_4 & 0 \end{pmatrix} \tag{A.55}$$

with

$$\tilde{n}_1 = e^{-\sigma\frac{|\nu-\mu|}{4}} S(2S-1)\sin(\frac{\mu-\nu}{2})\cos(\frac{\mu-\nu}{2})^{2S-2}, \tag{A.56}$$
$$\tilde{n}_2 = -e^{-\sigma(\frac{|\nu-\mu|}{4}+|\mu|)} S(2S-1)\sin(\frac{\mu-\nu}{2})\cos(\frac{\mu+\nu}{2})^{2S-2}, \tag{A.57}$$
$$\tilde{n}_3 = -e^{-\sigma\frac{|\mu|}{4}} S\cos(\frac{\mu}{2})^{2S-1}, \tag{A.58}$$
$$\tilde{n}_4 = e^{-\sigma\frac{|\nu-\mu|+|\mu|}{4}} S\cos(\frac{\nu}{2})^{2S-1}. \tag{A.59}$$

A similar study shows that for individual dephasing the operators transform as

$$e^{\Sigma\frac{|\mu|}{2}\mathcal{L}_I}[S_z] = S_z, \tag{A.60}$$
$$e^{\Sigma\frac{|\mu|}{2}\mathcal{L}_I}[S_\pm] = e^{-\Sigma|\mu|}S_\pm, \tag{A.61}$$
$$e^{\Sigma\frac{|\mu|}{2}\mathcal{L}_I}[S_\pm^2] = e^{-2\Sigma|\mu|}S_\pm^2, \tag{A.62}$$
$$e^{\Sigma\frac{|\mu|}{2}\mathcal{L}_I}[S_\pm S_z] = e^{-\Sigma|\mu|}S_\pm S_z, \tag{A.63}$$
$$e^{\Sigma\frac{|\mu|}{2}\mathcal{L}_I}[S_z S_\pm] = e^{-\Sigma|\mu|}S_z S_\pm, \tag{A.64}$$
$$e^{\Sigma\frac{|\mu|}{2}\mathcal{L}_I}[S_\pm S_\mp] = e^{-2\Sigma|\mu|}\left[S_\pm S_\mp + \left(\frac{N}{2} \pm S_z\right)\left(e^{2\Sigma|\mu|}-1\right)\right]. \tag{A.65}$$

With this, we find

$$\begin{pmatrix} \langle S_+(\nu)\rangle \\ \langle S_z(\nu)\rangle \\ \langle S_-(\nu)\rangle \end{pmatrix} = \begin{pmatrix} q_0' \\ 0 \\ q_0' \end{pmatrix} \tag{A.66}$$

with $q_0' = e^{-\Sigma(|\nu-\mu|+|\mu|)}q_0$.
Further

$$Q_s' = \begin{pmatrix} q_2' & i\,q_3' & q_1' \\ i\,q_3' & q_4' & -i\,q_3' \\ q_1' & -i\,q_3' & q_2' \end{pmatrix} - \begin{pmatrix} q_0' \\ 0 \\ q_0' \end{pmatrix}\left(q_0', 0, q_0'\right) \tag{A.67}$$

and thus

$$Q' = AQ_s'A^T = \begin{pmatrix} \frac{1}{2}(q_1'+q_2') - q_0'^2 & 0 & 0 \\ 0 & \frac{1}{2}(q_1'-q_2') & q_3' \\ 0 & q_3' & q_4' \end{pmatrix} \tag{A.68}$$

with

$$q_1' = e^{-2\Sigma(|\nu-\mu|+|\mu|)}q_1 + N/2(1-e^{-2\Sigma(|\nu-\mu|+|\mu|)}), \tag{A.69}$$
$$q_2' = e^{-2\Sigma(|\nu-\mu|+|\mu|)}q_2, \tag{A.70}$$
$$q_3' = e^{-\Sigma(|\nu-\mu|+|\mu|)}q_3, \tag{A.71}$$
$$q_4' = q_4. \tag{A.72}$$

Finally,

$$M_s' = \begin{pmatrix} n_2' & i\,n_3' & n_1' \\ i\,n_4' & 0 & -i\,n_4' \\ n_1' & -i\,n_3' & n_2' \end{pmatrix} \tag{A.73}$$

and

$$M' = AM'_sA^T = \begin{pmatrix} \frac{1}{2}(n'_1 + n'_2) & 0 & 0 \\ 0 & \frac{1}{2}(n'_1 - n'_2) & n'_3 \\ 0 & n'_4 & 0 \end{pmatrix} \tag{A.74}$$

with

$$n'_1 = e^{-\Sigma(|\nu-\mu|+2|\mu|)}\ n_1, \tag{A.75}$$

$$n'_2 = e^{-\Sigma(|\nu-\mu|+2|\mu|)}\ n_2, \tag{A.76}$$

$$n'_3 = e^{-\Sigma|\mu|}\ n_3, \tag{A.77}$$

$$n'_4 = e^{-\Sigma(|\nu-\mu|+|\mu|)}\ n_4. \tag{A.78}$$

B

Optimal interrogation time

In this appendix we additionally show the optimal Ramsey times corresponding to Fig. 3.9 in section 3.3. These are the interrogation times which minimize the overall instability, modelled in our work according to Eq. (3.44), for each N. The results are shown in Fig. B.1. Overall they follow the same general trend as the instabilities presented in section 3.3. This is again due to the fact that in the regime of large particle number and long dead times the instability is limited by the trade-off between Dick effect and CTL which reaches its minimum at an N-independent interrogation time. For smaller particle numbers the optimal interrogation time actually depends on N. There, spin squeezed states require reduced Ramsey times compared to the

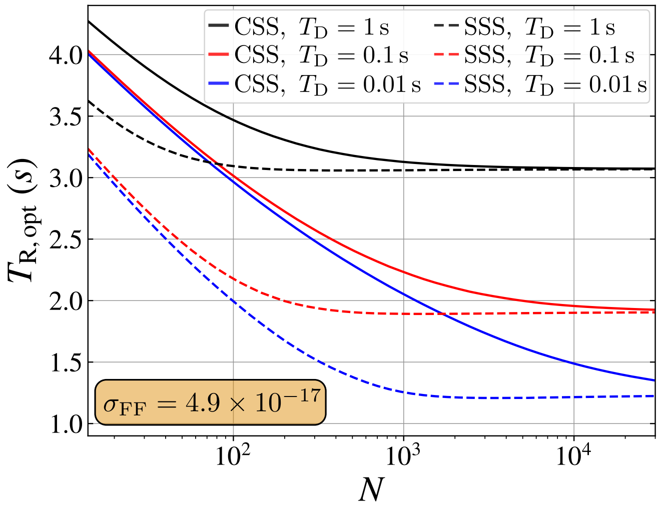

Figure B.1: **Optimal interrogation times:** Optimal Ramsey times which are required for the results on dead time limited clocks in Figure 3.9. Based on the logic of section 3.3 the optimal interrogation times follow the same overall trend as the instability. For the chosen laser noise parameters (see Table 3.2) they are all on the order of a few seconds.

uncorrelated states as the minimum between QPN and CTL shifts to smaller values of T_{R} when the projection noise is reduced. Considering a fixed particle number one finds that as the dead time increases, a longer optimal Ramsey time is required. This is because the observed fraction of the interrogation cycle is increased in order to reduce the Dick effect. In the same way, a shorter dead time is accompanied by a reduced $T_{\mathrm{R,opt}}$. A reduction of the dead time therefore also reduces the relevance of fringe-hops. Looking at Fig. 3.12 of the main text, the lowered $T_{\mathrm{R,opt}}$ means moving further left into the blue region of fringe-hop-free clock operation. However, fringe-hops remain relevant for very small ensembles, $N < 10$, even at $T_{\mathrm{D}} = 0$ because of the strong influence of the quantum projection noise [LSH+17].

List of Figures

2.1 Bloch sphere visualization . . . 7
2.2 Example Wigner functions . . . 10
2.3 Single qubit Ramsey protocol . . . 13
2.4 Distribution with QPN . . . 15
2.5 Ramsey interferometer with N atoms . . . 17
2.6 Overview of one-axis-twisting states . . . 21
2.7 Generalized Ramsey protocols . . . 27
2.8 Landscapes for larger N . . . 30
2.9 Sensitivity with dephasing . . . 33
2.10 Overview of sensitivity with collective dephasing . . . 34
2.11 Scaling of the sensitivity with N . . . 35
2.12 Effects of individual dephasing . . . 36
2.13 Illustration of over-un-twisting protocols . . . 37
2.14 Over-un-twisting signal . . . 38
2.15 G-asymmetry . . . 41
2.16 Extended Protocols . . . 43

3.1 Setup and noise processes . . . 47
3.2 A typical noisy signal . . . 51
3.3 Stability analysis . . . 53
3.4 Example clock laser stability . . . 57
3.5 Measurement distributions and sampling . . . 63
3.6 Asymptotic stability . . . 69
3.7 A lower bound to the clock stability . . . 70
3.8 Minimal clock stability . . . 71
3.9 Approaching the optimal stability . . . 73
3.10 Scaling of the critical particle number . . . 74
3.11 Stability with and without a double integrator . . . 81
3.12 Fringe-hops and interrogation time . . . 87
3.13 Modeling fringe-hops . . . 89
3.14 Mixed composite clocks . . . 93
3.15 A more realistic composite clock simulation . . . 94

3.16 **Variationally Optimized Stability** 98

4.1 **Infidelity from mode instability** 115
4.2 **Residual displacement** 119
4.3 **Infidelity with modulation** 121
4.4 **Red sideband SWAP dynamics** 127
4.5 **Extended parameter scan** 129

B.1 **Optimal interrogation times** 149

List of Tables

3.1 Noise contributions to the Allan variance 56
3.2 Laser parameters 58

4.1 Error budget 112
4.2 (Anti-)proton parameter values 128

Bibliography

[A$^+$19a] M. Abdel-Hafiz et al. Guidelines for developing optical clocks with 10^{-18} fractional frequency uncertainty. *arXiv e-prints*, page arXiv:1906.11495, Jun 2019. `arXiv:1906.11495`.

[A$^+$19b] F. Acernese et al. Increasing the astrophysical reach of the advanced Virgo detector via the application of squeezed vacuum states of light. *Phys. Rev. Lett.*, 123:231108, Dec 2019. URL: `https://link.aps.org/doi/10.1103/PhysRevLett.123.231108`, `doi:10.1103/PhysRevLett.123.231108`.

[ACGT72] F. T. Arecchi, E. Courtens, R. Gilmore, and H. Thomas. Atomic coherent states in quantum optics. *Phys. Rev. A*, 6:2211–2237, Dec 1972. URL: `https://link.aps.org/doi/10.1103/PhysRevA.6.2211`, `doi:10.1103/PhysRevA.6.2211`.

[Aga81] G. S. Agarwal. Relation between atomic coherent-state representation, state multipoles, and generalized phase-space distributions. *Phys. Rev. A*, 24:2889–2896, Dec 1981. URL: `https://link.aps.org/doi/10.1103/PhysRevA.24.2889`, `doi:10.1103/PhysRevA.24.2889`.

[All66] D. W. Allan. Statistics of atomic frequency standards. *Proceedings of the IEEE*, 54(2):221–230, 1966.

[And05] A. André. *Nonclassical states of light and atomic ensembles: Generation and new applications.* PhD thesis, Harvard University, Cambridge Massachusetts, May 2005.

[APS97] G. S. Agarwal, R. R. Puri, and R. P. Singh. Atomic Schrödinger cat states. *Phys. Rev. A*, 56:2249–2254, Sep 1997. URL: `https://link.aps.org/doi/10.1103/PhysRevA.56.2249`, `doi:10.1103/PhysRevA.56.2249`.

[APSK18] F. Anders, L. Pezzé, A. Smerzi, and C. Klempt. Phase magnification by two-axis countertwisting for detection-noise robust interferometry. *Phys. Rev. A*, 97:043813, Apr 2018. URL: `https:`

//link.aps.org/doi/10.1103/PhysRevA.97.043813, doi:10.1103/PhysRevA.97.043813.

[ASL04] A. André, A. S. Sørensen, and M. D. Lukin. Stability of atomic clocks based on entangled atoms. *Phys. Rev. Lett.*, 92:230801, Jun 2004. URL: https://link.aps.org/doi/10.1103/PhysRevLett.92.230801, doi:10.1103/PhysRevLett.92.230801.

[B+71] J. A. Barnes et al. Characterization of frequency stability. *IEEE Transactions on Instrumentation and Measurement*, IM-20(2):105–120, May 1971. URL: https://doi.org/10.1109/tim.1971.5570702, doi:10.1109/tim.1971.5570702.

[B+19a] M. J. Borchert et al. Measurement of ultralow heating rates of a single antiproton in a cryogenic Penning trap. *Phys. Rev. Lett.*, 122:043201, Jan 2019. URL: https://link.aps.org/doi/10.1103/PhysRevLett.122.043201, doi:10.1103/PhysRevLett.122.043201.

[B+19b] B. Braverman et al. Near-unitary spin squeezing in ^{171}Yb. *Phys. Rev. Lett.*, 122:223203, Jun 2019. URL: https://link.aps.org/doi/10.1103/PhysRevLett.122.223203, doi:10.1103/PhysRevLett.122.223203.

[BC94] S. L. Braunstein and C. M. Caves. Statistical distance and the geometry of quantum states. *Phys. Rev. Lett.*, 72:3439–3443, May 1994. URL: https://link.aps.org/doi/10.1103/PhysRevLett.72.3439, doi:10.1103/PhysRevLett.72.3439.

[BCH+19] S. M. Brewer, J.-S. Chen, A. M. Hankin, E. R. Clements, C. W. Chou, D. J. Wineland, D. B. Hume, and D. R. Leibrandt. ^{27}Al^{+} quantum-logic clock with a systematic uncertainty below 10^{-18}. *Phys. Rev. Lett.*, 123:033201, Jul 2019. URL: https://link.aps.org/doi/10.1103/PhysRevLett.123.033201, doi:10.1103/PhysRevLett.123.033201.

[BCN+14] J. G. Bohnet, K. C. Cox, M. A. Norcia, J. M. Weiner, Z. Chen, and J. K. Thompson. Reduced spin measurement back-action for a phase sensitivity ten times beyond the standard quantum limit. *Nature Photonics*, 8:731–735, Jul 2014. URL: https://doi.org/10.1038/nphoton.2014.151.

[BDF$^+$08] S. Boixo, A. Datta, S. T. Flammia, A. Shaji, E. Bagan, and C. M. Caves. Quantum-limited metrology with product states. *Phys. Rev. A*, 77:012317, Jan 2008. URL: `https://link.aps.org/doi/10.1103/PhysRevA.77.012317`, `doi:10.1103/PhysRevA.77.012317`.

[BFCG07] S. Boixo, S. T. Flammia, C. M. Caves, and J.M. Geremia. Generalized limits for single-parameter quantum estimation. *Phys. Rev. Lett.*, 98:090401, Feb 2007. URL: `https://link.aps.org/doi/10.1103/PhysRevLett.98.090401`, `doi:10.1103/PhysRevLett.98.090401`.

[BG86] L. S. Brown and G. Gabrielse. Geonium theory: Physics of a single electron or ion in a Penning trap. *Rev. Mod. Phys.*, 58:233–311, Jan 1986. URL: `https://link.aps.org/doi/10.1103/RevModPhys.58.233`, `doi:10.1103/RevModPhys.58.233`.

[BHS18] L. Barsotti, J. Harms, and R. Schnabel. Squeezed vacuum states of light for gravitational wave detectors. *Reports on Progress in Physics*, 82(1):016905, December 2018. URL: `https://doi.org/10.1088/1361-6633/aab906`, `doi:10.1088/1361-6633/aab906`.

[BHW13] D. W. Berry, M. J. W. Hall, and H. M. Wiseman. Stochastic Heisenberg limit: Optimal estimation of a fluctuating phase. *Phys. Rev. Lett.*, 111:113601, Sep 2013. URL: `https://link.aps.org/doi/10.1103/PhysRevLett.111.113601`, `doi:10.1103/PhysRevLett.111.113601`.

[BIWH96] J. J . Bollinger, W. M. Itano, D. J. Wineland, and D. J. Heinzen. Optimal frequency measurements with maximally correlated states. *Phys. Rev. A*, 54:R4649–R4652, Dec 1996. URL: `https://link.aps.org/doi/10.1103/PhysRevA.54.R4649`, `doi:10.1103/PhysRevA.54.R4649`.

[BKRB15] M. Brownnutt, M. Kumph, P. Rabl, and R. Blatt. Ion-trap measurements of electric-field noise near surfaces. *Rev. Mod. Phys.*, 87:1419–1482, Dec 2015. URL: `https://link.aps.org/doi/10.1103/RevModPhys.87.1419`, `doi:10.1103/RevModPhys.87.1419`.

[BKV18] B. Braverman, A. Kawasaki, and V. Vuletić. Impact of non-unitary spin squeezing on atomic clock performance. *New Journal of Physics*, 20(10):103019, Oct 2018. URL: `https://doi.org/10.1088/1367-2630/aae563`, `doi:10.1088/1367-2630/aae563`.

[BS13a] J. Borregaard and A. S. Sørensen. Efficient atomic clocks operated with several atomic ensembles. *Phys. Rev. Lett.*, 111:090802, Aug 2013. URL: `https://link.aps.org/doi/10.1103/PhysRevLett.111.090802`, `doi:10.1103/PhysRevLett.111.090802`.

[BS13b] J. Borregaard and A. S. Sørensen. Near-Heisenberg-limited atomic clocks in the presence of decoherence. *Phys. Rev. Lett.*, 111:090801, Aug 2013. URL: `https://link.aps.org/doi/10.1103/PhysRevLett.111.090801`, `doi:10.1103/PhysRevLett.111.090801`.

[BSB$^+$19] S. C. Burd, R. Srinivas, J. J. Bollinger, A. C. Wilson, D. J. Wineland, D. Leibfried, D. H. Slichter, and D. T. C. Allcock. Quantum amplification of mechanical oscillator motion. *Science*, 364(6446):1163–1165, Jun 2019. URL: `https://doi.org/10.1126/science.aaw2884`, `doi:10.1126/science.aaw2884`.

[Bur69] D. Bures. An extension of Kakutani's theorem on infinite product measures to the tensor product of semifinite w^*-algebras. *Transactions of the American Mathematical Society*, 135:199–199, 1969. URL: `https://doi.org/10.1090/s0002-9947-1969-0236719-2`, `doi:10.1090/s0002-9947-1969-0236719-2`.

[BW08] R. Blatt and D. J. Wineland. Entangled states of trapped atomic ions. *Nature*, 453(7198):1008–1015, Jun 2008. URL: `https://doi.org/10.1038/nature07125`, `doi:10.1038/nature07125`.

[CGV17] F. Crimin, B. M. Garraway, and J. Verdú. The quantum theory of the Penning trap. *Journal of Modern Optics*, 65(4):427–440, Nov 2017. URL: `https://doi.org/10.1080/09500340.2017.1393570`, `doi:10.1080/09500340.2017.1393570`.

[CGWT16] K. C. Cox, G. P. Greve, J. M. Weiner, and J. K. Thompson. Deterministic squeezed states with collective measurements and feedback. *Phys. Rev. Lett.*, 116:093602, Mar 2016. URL: `https://link.aps.org/doi/10.1103/PhysRevLett.116.093602`, `doi:10.1103/PhysRevLett.116.093602`.

[CHK$^+$10] C. W. Chou, D. B. Hume, J. C. J. Koelemeij, D. J. Wineland, and T. Rosenband. Frequency comparison of two high-accuracy Al$^+$ optical clocks. *Phys. Rev. Lett.*, 104:070802, Feb 2010. URL: `https://link.aps.org/doi/10.1103/PhysRevLett.104.070802`, `doi:10.1103/PhysRevLett.104.070802`.

[CHT+11] C. W. Chou, D. B. Hume, M. J. Thorpe, D. J. Wineland, and T. Rosenband. Quantum coherence between two atoms beyond $Q = 10^{15}$. *Phys. Rev. Lett.*, 106:160801, Apr 2011. URL: `https://link.aps.org/doi/10.1103/PhysRevLett.106.160801`, `doi:10.1103/PhysRevLett.106.160801`.

[CSP09] A. D. Cronin, J. Schmiedmayer, and D. E. Pritchard. Optics and interferometry with atoms and molecules. *Rev. Mod. Phys.*, 81:1051–1129, Jul 2009. URL: `https://link.aps.org/doi/10.1103/RevModPhys.81.1051`, `doi:10.1103/RevModPhys.81.1051`.

[CWBP90] E. A. Cornell, R. M. Weisskoff, K. R. Boyce, and D. E. Pritchard. Mode coupling in a Penning trap: π pulses and a classical avoided crossing. *Physical Review A*, 41(1):312–315, Jan 1990. URL: `https://link.aps.org/doi/10.1103/PhysRevA.41.312`, `doi:10.1103/PhysRevA.41.312`.

[CZ95] J. I. Cirac and P. Zoller. Quantum computations with cold trapped ions. *Phys. Rev. Lett.*, 74:4091–4094, May 1995. URL: `https://link.aps.org/doi/10.1103/PhysRevLett.74.4091`, `doi:10.1103/PhysRevLett.74.4091`.

[D+17] P. Delva et al. Test of special relativity using a fiber network of optical clocks. *Phys. Rev. Lett.*, 118:221102, Jun 2017. URL: `https://link.aps.org/doi/10.1103/PhysRevLett.118.221102`, `doi:10.1103/PhysRevLett.118.221102`.

[DAB+19] S. Dörscher, A. Al-Masoudi, M. Bober, R. Schwarz, R. Hobson, U. Sterr, and C. Lisdat. Dynamic decoupling of laser phase noise in compound atomic clocks. *arXiv e-prints*, page arXiv:1911.13146, Nov 2019. `arXiv:1911.13146`.

[DAS94] J. P. Dowling, G. S. Agarwal, and W. P. Schleich. Wigner distribution of a general angular-momentum state: Applications to a collection of two-level atoms. *Phys. Rev. A*, 49:4101–4109, May 1994. URL: `https://link.aps.org/doi/10.1103/PhysRevA.49.4101`, `doi:10.1103/PhysRevA.49.4101`.

[DBSS16] E. Davis, G. Bentsen, and M. Schleier-Smith. Approaching the Heisenberg limit without single-particle detection. *Phys. Rev. Lett.*, 116:053601, Feb 2016. URL: `https://link.aps.org/doi/10.1103/PhysRevLett.116.053601`, `doi:10.1103/PhysRevLett.116.053601`.

[DDKG12] R. Demkowicz-Dobrzański, J. Kołodyński, and M. Guţă. The elusive Heisenberg limit in quantum-enhanced metrology. *Nature Communications*, 3(1):1063, Jan 2012. URL: `https://doi.org/10.1038/ncomms2067`, `doi:10.1038/ncomms2067`.

[Dev86] L. Devroye. *Non-Uniform Random Variate Generation*. Springer New York, 1986. URL: `https://doi.org/10.1007/978-1-4613-8643-8`, `doi:10.1007/978-1-4613-8643-8`.

[Dic88] G. J. Dick. Local oscillator induced instabilities in trapped ion frequency standards. In *Proceedings of the 19th Annu. Precise Time and Time Inverval Meeting, Redendo Beach, 1987*, pages 133–147. U.S. Naval Observatory, 1888. `http://tycho.usno.navy.mil/ptti/1987/Vol%2019_13.pdf`.

[DL13] P. Delva and J. Lodewyck. Atomic clocks: New prospects in metrology and geodesy. *Acta Futura*, 7:67–78, 2013. Proceedings of the Workshop "Relativistic Positioning Systems and their Scientific Applications" held in Brdo near Kranj, Slovenia, 19-21 September 2012. `doi:10.2420/AF07.2013.67`.

[DPGM90] G. J. Dick, J. D. Prestage, C. A. Greenhall, and L. Maleki. Local oscillator induced degradation of medium-term stability in passive atomic frequency standards. In *22nd Annual Precise Time and Time Interval (PTTI) Applications and Planning Meeting*, pages 487–508, May 1990.

[DTW17] K. Duivenvoorden, B. M. Terhal, and D. Weigand. Single-mode displacement sensor. *Phys. Rev. A*, 95:012305, Jan 2017. URL: `https://link.aps.org/doi/10.1103/PhysRevA.95.012305`, `doi:10.1103/PhysRevA.95.012305`.

[EdMFD11] B. M. Escher, R. L. de Matos Filho, and L. Davidovich. General framework for estimating the ultimate precision limit in noisy quantum-enhanced metrology. *Nature Physics*, 7(5):406–411, Mar 2011. URL: `https://doi.org/10.1038/nphys1958`, `doi:10.1038/nphys1958`.

[FOL+19] C. Figgatt, A. Ostrander, N. M. Linke, K. A. Landsman, D. Zhu, D. Maslov, and C. Monroe. Parallel entangling operations on a universal ion-trap quantum computer. *Nature*, 572(7769):368–372, Jul 2019. URL: `https://doi.org/10.1038/s41586-019-1427-5`, `doi:10.1038/s41586-019-1427-5`.

[Fra16] M. Fraas. An analysis of the stationary operation of atomic clocks. *Communications in Mathematical Physics*, 348(2):363–393, Sep 2016. doi:10.1007/s00220-016-2761-1.

[FSD16] F. Fröwis, P. Sekatski, and W. Dür. Detecting large quantum Fisher information with finite measurement precision. *Phys. Rev. Lett.*, 116:090801, Mar 2016. URL: https://link.aps.org/doi/10.1103/PhysRevLett.116.090801, doi:10.1103/PhysRevLett.116.090801.

[FSKD14] F. Fröwis, M. Skotiniotis, B. Kraus, and W. Dür. Optimal quantum states for frequency estimation. *New Journal of Physics*, 16(8):083010, Aug 2014. URL: https://doi.org/10.1088/1367-2630/16/8/083010, doi:10.1088/1367-2630/16/8/083010.

[G$^+$18] J. Grotti et al. Geodesy and metrology with a transportable optical clock. *Nature Physics*, 14(5):437–441, Feb 2018. URL: https://doi.org/10.1038/s41567-017-0042-3, doi:10.1038/s41567-017-0042-3.

[Gar09] C. W. Gardiner. *Stochastic Methods*, volume 13 of *Springer Series in Synergetics*. Springer-Verlag, Berlin, 4 edition, 2009. URL: https://www.springer.com/de/book/9783540707127.

[GB15] T. J. Green and M. J. Biercuk. Phase-modulated decoupling and error suppression in qubit-oscillator systems. *Phys. Rev. Lett.*, 114:120502, Mar 2015. URL: https://link.aps.org/doi/10.1103/PhysRevLett.114.120502, doi:10.1103/PhysRevLett.114.120502.

[GBSN$^+$17] M. Gärttner, J. G. Bohnet, A. Safavi-Naini, M. L. Wall, J. J. Bollinger, and A. M. Rey. Measuring out-of-time-order correlations and multiple quantum spectra in a trapped-ion quantum magnet. *Nature Physics*, 13(8):781–786, May 2017. URL: https://doi.org/10.1038/nphys4119, doi:10.1038/nphys4119.

[GKP01] D. Gottesman, A. Kitaev, and J. Preskill. Encoding a qubit in an oscillator. *Phys. Rev. A*, 64:012310, Jun 2001. URL: https://link.aps.org/doi/10.1103/PhysRevA.64.012310, doi:10.1103/PhysRevA.64.012310.

[GLM06] V. Giovannetti, S. Lloyd, and L. Maccone. Quantum metrology. *Phys. Rev. Lett.*, 96:010401, Jan 2006. URL: https://link.aps.org/

doi/10.1103/PhysRevLett.96.010401, doi:10.1103/PhysRevLett.96.010401.

[GLM11] V. Giovannetti, S. Lloyd, and L. Maccone. Advances in quantum metrology. *Nature Photonics*, 5(4):222–229, Mar 2011. URL: https://doi.org/10.1038/nphoton.2011.35, doi:10.1038/nphoton.2011.35.

[GMB+14] L. I. R. Gil, R. Mukherjee, E. M. Bridge, M. P. A. Jones, and T. Pohl. Spin squeezing in a Rydberg lattice clock. *Phys. Rev. Lett.*, 112:103601, Mar 2014. URL: https://link.aps.org/doi/10.1103/PhysRevLett.112.103601, doi:10.1103/PhysRevLett.112.103601.

[GSP19] M. Gessner, A. Smerzi, and L. Pezzé. Metrological nonlinear squeezing parameter. *Phys. Rev. Lett.*, 122:090503, Mar 2019. URL: https://link.aps.org/doi/10.1103/PhysRevLett.122.090503, doi:10.1103/PhysRevLett.122.090503.

[GSTS16] J. F. Goodwin, G. Stutter, R.C. Thompson, and D.M. Segal. Resolved-sideband laser cooling in a Penning trap. *Physical Review Letters*, 116(14):143002, Apr 2016. URL: https://link.aps.org/doi/10.1103/PhysRevLett.116.143002, doi:10.1103/PhysRevLett.116.143002.

[GZ15] C. Gardiner and P. Zoller. The quantum world of ultra-cold atoms and light book II: The physics of quantum-optical devices. In *Cold Atoms*, pages 1–524. Imperial College Press, Apr 2015. URL: https://doi.org/10.1142/9781783266784, doi:10.1142/9781783266784.

[Hah19] Henning Hahn. *Two-qubit microwave quantum logic gate with* $^9Be^+$ *ions in scalable surface-electrode ion traps.* PhD thesis, Gottfried Wilhelm Leibniz Universität, Hannover, Jul 2019.

[Hai18] S. A. Haine. Using interaction-based readouts to approach the ultimate limit of detection-noise robustness for quantum-enhanced metrology in collective spin systems. *Phys. Rev. A*, 98:030303, Sep 2018. URL: https://link.aps.org/doi/10.1103/PhysRevA.98.030303, doi:10.1103/PhysRevA.98.030303.

[Har16] S. Hartmann. Generalized Dicke states. *Quantum Inf. Comput.*, 16(15&16):1333–1348, 2016. URL: http://www.rintonpress.com/xxqic16/qic-16-1516/1333-1348.pdf.

[HB93] M. J. Holland and K. Burnett. Interferometric detection of optical phase shifts at the Heisenberg limit. *Phys. Rev. Lett.*, 71:1355–1358, Aug 1993. URL: `https://link.aps.org/doi/10.1103/PhysRevLett.71.1355`, `doi:10.1103/PhysRevLett.71.1355`.

[HBB$^+$07] B. L. Higgins, D. W. Berry, S. D. Bartlett, H. M. Wiseman, and G. J. Pryde. Entanglement-free Heisenberg-limited phase estimation. *Nature*, 450(7168):393–396, Nov 2007. URL: `https://doi.org/10.1038/nature06257`, `doi:10.1038/nature06257`.

[HCD$^+$12] D. Hayes, S. M. Clark, S. Debnath, D. Hucul, I. V. Inlek, K. W. Lee, Q. Quraishi, and C. Monroe. Coherent error suppression in multiqubit entangling gates. *Phys. Rev. Lett.*, 109:020503, Jul 2012. URL: `https://link.aps.org/doi/10.1103/PhysRevLett.109.020503`, `doi:10.1103/PhysRevLett.109.020503`.

[HCW$^+$13] D.A. Hite, Y. Colombe, A.C. Wilson, D.T.C. Allcock, D. Leibfried, D.J. Wineland, and D.P. Pappas. Surface science for improved ion traps. *MRS Bulletin*, 38(10):826–833, Oct 2013. URL: `https://doi.org/10.1557/mrs.2013.207`, `doi:10.1557/mrs.2013.207`.

[HEKK16] O. Hosten, N. J. Engelsen, R. Krishnakumar, and M. A. Kasevich. Measurement noise 100 times lower than the quantum-projection limit using entangled atoms. *Nature*, 529(7587):505–508, Jan 2016. URL: `https://doi.org/10.1038/nature16176`, `doi:10.1038/nature16176`.

[Hel69] C. W. Helstrom. Quantum detection and estimation theory. *Journal of Statistical Physics*, 1(2):231–252, 1969. URL: `https://doi.org/10.1007/bf01007479`, `doi:10.1007/bf01007479`.

[HHV$^+$20] S. Häfner, S. Herbers, S. Vogt, C. Lisdat, and U. Sterr. Transportable interrogation laser system with an instability of mod $\sigma_y = 3 \times 10^{-16}$. *Optics Express*, 28(11):16407, May 2020. URL: `https://doi.org/10.1364/oe.390105`, `doi:10.1364/oe.390105`.

[HKEK16] O. Hosten, R. Krishnakumar, N. J. Engelsen, and M. A. Kasevich. Quantum phase magnification. *Science*, 352(6293):1552–1555, Jun 2016. URL: `https://doi.org/10.1126/science.aaf3397`, `doi:10.1126/science.aaf3397`.

[HL16] D. B. Hume and D. R. Leibrandt. Probing beyond the laser coherence time in optical clock comparisons. *Phys. Rev. A*, 93:032138, Mar 2016. URL: `https://link.aps.org/doi/10.1103/PhysRevA.93.032138`, `doi:10.1103/PhysRevA.93.032138`.

[HM16] F. Haddadfarshi and F. Mintert. High fidelity quantum gates of trapped ions in the presence of motional heating. *New Journal of Physics*, 18(12):123007, Dec 2016. URL: `https://doi.org/10.1088/1367-2630/18/12/123007`, `doi:10.1088/1367-2630/18/12/123007`.

[HMP$^+$97] S. F. Huelga, C. Macchiavello, T. Pellizzari, A. K. Ekert, M. B. Plenio, and J. I. Cirac. Improvement of frequency standards with quantum entanglement. *Phys. Rev. Lett.*, 79:3865–3868, Nov 1997. URL: `https://link.aps.org/doi/10.1103/PhysRevLett.79.3865`, `doi:10.1103/PhysRevLett.79.3865`.

[HPM$^+$19] P. He, M. A. Perlin, S. R. Muleady, R. J. Lewis-Swan, R. B. Hutson, J. Ye, and A. M. Rey. Engineering spin squeezing in a 3D optical lattice with interacting spin-orbit-coupled fermions. *Phys. Rev. Research*, 1:033075, Nov 2019. URL: `https://link.aps.org/doi/10.1103/PhysRevResearch.1.033075`, `doi:10.1103/PhysRevResearch.1.033075`.

[HSA$^+$16] T. P. Harty, M. A. Sepiol, D. T. C. Allcock, C. J. Ballance, J. E. Tarlton, and D. M. Lucas. High-fidelity trapped-ion quantum logic using near-field microwaves. *Phys. Rev. Lett.*, 117:140501, Sep 2016. URL: `https://link.aps.org/doi/10.1103/PhysRevLett.117.140501`, `doi:10.1103/PhysRevLett.117.140501`.

[HSL$^+$16] N. Huntemann, C. Sanner, B. Lipphardt, Chr. Tamm, and E. Peik. Single-ion atomic clock with 3×10^{-18} systematic uncertainty. *Phys. Rev. Lett.*, 116:063001, Feb 2016. URL: `https://link.aps.org/doi/10.1103/PhysRevLett.116.063001`, `doi:10.1103/PhysRevLett.116.063001`.

[Hüb92] M. Hübner. Explicit computation of the Bures distance for density matrices. *Physics Letters A*, 163(4):239–242, Mar 1992. URL: `https://doi.org/10.1016/0375-9601(92)91004-b`, `doi:10.1016/0375-9601(92)91004-b`.

[HW12] M. J. W. Hall and H. M. Wiseman. Does nonlinear metrology offer improved resolution? Answers from quantum information theory. *Phys. Rev. X*, 2:041006, Oct 2012. URL: `https://link.aps.org/doi/10.1103/PhysRevX.2.041006`, `doi:10.1103/PhysRevX.2.041006`.

[HZL+18] J. Huang, M. Zhuang, B. Lu, Y. Ke, and C. Lee. Achieving Heisenberg-limited metrology with spin cat states via interaction-based readout. *Phys. Rev. A*, 98:012129, Jul 2018. URL: `https://link.aps.org/doi/10.1103/PhysRevA.98.012129`, `doi:10.1103/PhysRevA.98.012129`.

[HZS+19] H. Hahn, G. Zarantonello, M. Schulte, A. Bautista-Salvador, K. Hammerer, and C. Ospelkaus. Integrated $^9\mathrm{Be}^+$ multi-qubit gate device for the ion-trap quantum computer. *npj Quantum Information*, 5(1), Aug 2019. URL: `https://doi.org/10.1038/s41534-019-0184-5`, `doi:10.1038/s41534-019-0184-5`.

[Jam98a] D. F. V. James. Quantum dynamics of cold trapped ions with application to quantum computation. *Applied Physics B: Lasers and Optics*, 66(2):181–190, Feb 1998. URL: `https://doi.org/10.1007/s003400050373`, `doi:10.1007/s003400050373`.

[Jam98b] D. F. V. James. Theory of heating of the quantum ground state of trapped ions. *Phys. Rev. Lett.*, 81:317–320, Jul 1998. URL: `https://link.aps.org/doi/10.1103/PhysRevLett.81.317`, `doi:10.1103/PhysRevLett.81.317`.

[Joz94] R. Jozsa. Fidelity for mixed quantum states. *Journal of Modern Optics*, 41(12):2315–2323, Dec 1994. URL: `https://doi.org/10.1080/09500349414552171`, `doi:10.1080/09500349414552171`.

[Kae90] F. X. Kaertner. Analysis of white and $f^{-\alpha}$ noise in oscillators. *International Journal of Circuit Theory and Applications*, 18(5):485–519, Sep 1990. URL: `https://doi.org/10.1002/cta.4490180505`, `doi:10.1002/cta.4490180505`.

[KBC+15] R. Kohlhaas, A. Bertoldi, E. Cantin, A. Aspect, A. Landragin, and P. Bouyer. Phase locking a clock oscillator to a coherent atomic ensemble. *Physical Review X*, 5(2):021011, Apr 2015. URL: `https://doi.org/10.1103/physrevx.5.021011`, `doi:10.1103/physrevx.5.021011`.

[KBK+19] J. Keller, T. Burgermeister, D. Kalincev, A. Didier, A. P. Kulosa, T. Nordmann, J. Kiethe, and T. E. Mehlstäubler. Controlling systematic frequency uncertainties at the 10^{-19} level in linear Coulomb crystals. *Phys. Rev. A*, 99:013405, Jan 2019. URL: `https://link.aps.org/doi/10.1103/PhysRevA.99.013405`, `doi:10.1103/PhysRevA.99.013405`.

[KKB+14] E. M. Kessler, P. Kómár, M. Bishof, L. Jiang, A. S. Sørensen, J. Ye, and M. D. Lukin. Heisenberg-limited atom clocks based on entangled qubits. *Phys. Rev. Lett.*, 112:190403, May 2014. URL: `https://link.aps.org/doi/10.1103/PhysRevLett.112.190403`, `doi:10.1103/PhysRevLett.112.190403`.

[KKB+19] J. Keller, D. Kalincev, T. Burgermeister, A. P. Kulosa, A. Didier, T. Nordmann, J. Kiethe, and T.E. Mehlstäubler. Probing time dilation in Coulomb crystals in a high-precision ion trap. *Phys. Rev. Applied*, 11:011002, Jan 2019. URL: `https://link.aps.org/doi/10.1103/PhysRevApplied.11.011002`, `doi:10.1103/PhysRevApplied.11.011002`.

[KMR+01] D. Kielpinski, V. Meyer, M. A. Rowe, C. A. Sackett, W. M. Itano, C. Monroe, and D. J. Wineland. A decoherence-free quantum memory using trapped ions. *Science*, 291(5506):1013–1015, Jan 2001. URL: `https://doi.org/10.1126/science.1057357`, `doi:10.1126/science.1057357`.

[KSK+19] R. Kaubruegger, P. Silvi, C. Kokail, R. van Bijnen, A. M. Rey, J. Ye, A. M. Kaufman, and P. Zoller. Variational spin-squeezing algorithms on programmable quantum sensors. *Phys. Rev. Lett.*, 123:260505, Dec 2019. URL: `https://link.aps.org/doi/10.1103/PhysRevLett.123.260505`, `doi:10.1103/PhysRevLett.123.260505`.

[KU93] M. Kitagawa and M. Ueda. Squeezed spin states. *Phys. Rev. A*, 47:5138–5143, Jun 1993. URL: `https://link.aps.org/doi/10.1103/PhysRevA.47.5138`, `doi:10.1103/PhysRevA.47.5138`.

[KWM+98] B. E. King, C. S. Wood, C. J. Myatt, Q. A. Turchette, D. Leibfried, W. M. Itano, C. Monroe, and D. J. Wineland. Cooling the collective motion of trapped ions to initialize a quantum register. *Phys. Rev. Lett.*, 81:1525–1528, Aug 1998. URL: `https://link.aps.org/doi/10.1103/PhysRevLett.81.1525`, `doi:10.1103/PhysRevLett.81.1525`.

[L+03] D. Leibfried et al. Experimental demonstration of a robust, high-fidelity geometric two ion-qubit phase gate. *Nature*, 422(6930):412–415, Mar 2003. URL: `https://doi.org/10.1038/nature01492`, `doi:10.1038/nature01492`.

[L+05a] C. Langer et al. Long-lived qubit memory using atomic ions. *Phys. Rev. Lett.*, 95:060502, Aug 2005. URL: `https://link.aps.org/doi/10.1103/PhysRevLett.95.060502`, `doi:10.1103/PhysRevLett.95.060502`.

[L+05b] D. Leibfried et al. Creation of a six-atom 'Schrödinger cat' state. *Nature*, 438(7068):639–642, Dec 2005. URL: `https://doi.org/10.1038/nature04251`, `doi:10.1038/nature04251`.

[L+19] H. Levine et al. Parallel implementation of high-fidelity multi-qubit gates with neutral atoms. *Phys. Rev. Lett.*, 123:170503, Oct 2019. URL: `https://link.aps.org/doi/10.1103/PhysRevLett.123.170503`, `doi:10.1103/PhysRevLett.123.170503`.

[LBD+05] P. J. Lee, K-A Brickman, L. Deslauriers, P. C. Haljan, L.-M. Duan, and C. Monroe. Phase control of trapped ion quantum gates. *Journal of Optics B: Quantum and Semiclassical Optics*, 7(10):S371–S383, Sep 2005. URL: `https://doi.org/10.1088/1464-4266/7/10/025`, `doi:10.1088/1464-4266/7/10/025`.

[LBS+04] D. Leibfried, M. D. Barrett, T. Schaetz, J. Britton, J. Chiaverini, W. M. Itano, J. D. Jost, C. Langer, and D. J. Wineland. Toward Heisenberg-limited spectroscopy with multiparticle entangled states. *Science*, 304(5676):1476–1478, Jun 2004. URL: `https://doi.org/10.1126/science.1097576`, `doi:10.1126/science.1097576`.

[LBY+15] A. D. Ludlow, M. M. Boyd, J. Ye, E. Peik, and P. O. Schmidt. Optical atomic clocks. *Rev. Mod. Phys.*, 87:637–701, Jun 2015. URL: `https://link.aps.org/doi/10.1103/RevModPhys.87.637`, `doi:10.1103/RevModPhys.87.637`.

[LSH+17] I. D. Leroux, N. Scharnhorst, S. Hannig, J. Kramer, L. Pelzer, M. Stepanova, and P. O. Schmidt. On-line estimation of local oscillator noise and optimisation of servo parameters in atomic clocks. *Metrologia*, 54(3):307–321, Apr 2017. URL: `https://doi.org/10.1088%2F1681-7575%2Faa66e9`, `doi:10.1088/1681-7575/aa66e9`.

[LSM+16] D. Linnemann, H. Strobel, W. Muessel, J. Schulz, R. J. Lewis-Swan, K. V. Kheruntsyan, and M. K. Oberthaler. Quantum-enhanced sensing based on time reversal of nonlinear dynamics. *Phys. Rev. Lett.*, 117:013001, Jun 2016. URL: `https://link.aps.org/doi/10.1103/PhysRevLett.117.013001`, `doi:10.1103/PhysRevLett.117.013001`.

[LSNC+18] R. J. Lewis-Swan, M. A. Norcia, J. R. K. Cline, J. K. Thompson, and A. M. Rey. Robust spin squeezing via photon-mediated interactions on an optical clock transition. *Phys. Rev. Lett.*, 121:070403, Aug 2018. URL: `https://link.aps.org/doi/10.1103/PhysRevLett.121.070403`, `doi:10.1103/PhysRevLett.121.070403`.

[LSSVac10a] I. D. Leroux, M. H. Schleier-Smith, and V. Vuletić. Implementation of cavity squeezing of a collective atomic spin. *Phys. Rev. Lett.*, 104:073602, Feb 2010. URL: `https://link.aps.org/doi/10.1103/PhysRevLett.104.073602`, `doi:10.1103/PhysRevLett.104.073602`.

[LSSVac10b] I. D. Leroux, M. H. Schleier-Smith, and V. Vuletić. Orientation-dependent entanglement lifetime in a squeezed atomic clock. *Phys. Rev. Lett.*, 104:250801, Jun 2010. URL: `https://link.aps.org/doi/10.1103/PhysRevLett.104.250801`, `doi:10.1103/PhysRevLett.104.250801`.

[Lui04] A. Luis. Nonlinear transformations and the Heisenberg limit. *Physics Letters A*, 329(1-2):8–13, Aug 2004. URL: `https://doi.org/10.1016/j.physleta.2004.06.080`, `doi:10.1016/j.physleta.2004.06.080`.

[LWL+11] J. Lodewyck, P. G. Westergaard, A. Lecallier, L. Lorini, and P. Lemonde. Frequency stability of optical lattice clocks. *New Journal of Physics*, 13(5):059501, May 2011. URL: `https://doi.org/10.1088/1367-2630/13/5/059501`, `doi:10.1088/1367-2630/13/5/059501`.

[M+17] D. G. Matei et al. 1.5 μm lasers with sub-10 mHz linewidth. *Phys. Rev. Lett.*, 118:263202, Jun 2017. URL: `https://link.aps.org/doi/10.1103/PhysRevLett.118.263202`, `doi:10.1103/PhysRevLett.118.263202`.

[M+19] W. F. McGrew et al. Towards the optical second: Verifying optical clocks at the SI limit. *Optica*, 6(4):448–454, Apr 2019. URL: `http://www.osapublishing.org/optica/abstract.cfm?URI=optica-6-4-448`, `doi:10.1364/OPTICA.6.000448`.

[Mag54] W. Magnus. On the exponential solution of differential equations for a linear operator. *Communications on Pure and Applied Mathematics*, 7(4):649–673, Nov 1954. URL: https://doi.org/10.1002/cpa.3160070404, doi:10.1002/cpa.3160070404.

[MCS+19] I. S. Madjarov, A. Cooper, A. L. Shaw, J. P. Covey, V. Schkolnik, T. H. Yoon, J. R. Williams, and M. Endres. An atomic-array optical clock with single-atom readout. *Phys. Rev. X*, 9:041052, Dec 2019. URL: https://link.aps.org/doi/10.1103/PhysRevX.9.041052, doi:10.1103/PhysRevX.9.041052.

[Mes62] A. Messiah. *Quantum mechanics*. North-Holland, Amsterdam, 1962.

[MFDD14] Katarzyna Macieszczak, Martin Fraas, and Rafał Demkowicz-Dobrzański. Bayesian quantum frequency estimation in presence of collective dephasing. *New Journal of Physics*, 16(11):113002, Oct 2014. URL: https://doi.org/10.1088/1367-2630/16/11/113002, doi:10.1088/1367-2630/16/11/113002.

[MGL+18] T. E. Mehlstäubler, G. Grosche, C. Lisdat, P. O. Schmidt, and H. Denker. Atomic clocks for geodesy. *Reports on Progress in Physics*, 81(6):064401, Apr 2018. URL: https://doi.org/10.1088/1361-6633/aab409, doi:10.1088/1361-6633/aab409.

[MGW05] F. G. Major, V. N. Gheorghe, and G. Werth. *Charged Particle Traps*. Springer-Verlag, 2005. URL: https://doi.org/10.1007/b137836, doi:10.1007/b137836.

[MHG+18] G. E. Marti, R. B. Hutson, A. Goban, S. L. Campbell, N. Poli, and J. Ye. Imaging optical frequencies with 100 μHz precision and 1.1 μm resolution. *Phys. Rev. Lett.*, 120:103201, Mar 2018. URL: https://link.aps.org/doi/10.1103/PhysRevLett.120.103201, doi:10.1103/PhysRevLett.120.103201.

[MLK+20] P. Micke, T. Leopold, S. A. King, E. Benkler, L. J. Spieß, L. Schmöger, M. Schwarz, J. R. Crespo López-Urrutia, and P. O. Schmidt. Coherent laser spectroscopy of highly charged ions using quantum logic. *Nature*, 578(7793):60–65, Jan 2020. URL: https://doi.org/10.1038/s41586-020-1959-8, doi:10.1038/s41586-020-1959-8.

[MMK+95a] C. Monroe, D. M. Meekhof, B. E. King, W. M. Itano, and D. J. Wineland. Demonstration of a fundamental quantum logic gate. *Phys. Rev. Lett.*, 75:4714–4717, Dec 1995. URL: `https://link.aps.org/doi/10.1103/PhysRevLett.75.4714`, `doi:10.1103/PhysRevLett.75.4714`.

[MMK+95b] C. Monroe, D. M. Meekhof, B. E. King, S. R. Jefferts, W. M. Itano, D. J. Wineland, and P. Gould. Resolved-sideband Raman cooling of a bound atom to the 3D zero-point energy. *Phys. Rev. Lett.*, 75:4011–4014, Nov 1995. URL: `https://link.aps.org/doi/10.1103/PhysRevLett.75.4011`, `doi:10.1103/PhysRevLett.75.4011`.

[MNH18] S. S. Mirkhalaf, S. P. Nolan, and S. A. Haine. Robustifying twist-and-turn entanglement with interaction-based readout. *Phys. Rev. A*, 97:053618, May 2018. URL: `https://link.aps.org/doi/10.1103/PhysRevA.97.053618`, `doi:10.1103/PhysRevA.97.053618`.

[MRK+01] V. Meyer, M. A. Rowe, D. Kielpinski, C. A. Sackett, W. M. Itano, C. Monroe, and D. J. Wineland. Experimental demonstration of entanglement-enhanced rotation angle estimation using trapped ions. *Phys. Rev. Lett.*, 86:5870–5873, Jun 2001. URL: `https://link.aps.org/doi/10.1103/PhysRevLett.86.5870`, `doi:10.1103/PhysRevLett.86.5870`.

[MSJ00] G. J. Milburn, S. Schneider, and D. F. V. James. Ion trap quantum computing with warm ions. *Fortschritte der Physik*, 48(9-11):801–810, Sep 2000. URL: `https://doi.org/10.1002/1521-3978(200009)48:9/11<801::aid-prop801>3.0.co;2-1`, `doi:10.1002/1521-3978(200009)48:9/11<801::aid-prop801>3.0.co;2-1`.

[MSP16] T. Macrì, A. Smerzi, and L. Pezzé. Loschmidt echo for quantum metrology. *Phys. Rev. A*, 94:010102, Jul 2016. URL: `https://link.aps.org/doi/10.1103/PhysRevA.94.010102`, `doi:10.1103/PhysRevA.94.010102`.

[MW01] F. Mintert and C. Wunderlich. Ion-trap quantum logic using long-wavelength radiation. *Phys. Rev. Lett.*, 87(25):257904, Nov 2001. URL: `http://link.aps.org/doi/10.1103/PhysRevLett.87.257904`, `doi:10.1103/PhysRevLett.87.257904`.

[MWSN11] J. Ma, X. Wang, C. P. Sun, and F. Nori. Quantum spin squeezing. *Physics Reports*, 509(2):89 – 165, 2011. URL: http://www.sciencedirect.com/science/article/pii/S0370157311002201, doi:https://doi.org/10.1016/j.physrep.2011.08.003.

[MYH08] D. Meiser, J. Ye, and M. J. Holland. Spin squeezing in optical lattice clocks via lattice-based QND measurements. *New Journal of Physics*, 10(7):073014, Jul 2008. doi:10.1088/1367-2630/10/7/073014.

[N+15] T. L. Nicholson et al. Systematic evaluation of an atomic clock at 2×10^{-18} total uncertainty. *Nature communications*, 6:6896, Apr 2015. doi:10.1038/ncomms7896.

[NC09] M. A. Nielsen and I. L. Chuang. *Quantum Computation and Quantum Information*. Cambridge University Press, 2009. URL: https://doi.org/10.1017/cbo9780511976667, doi:10.1017/cbo9780511976667.

[NKC04] K. Numata, A. Kemery, and J. Camp. Thermal-noise limit in the frequency stabilization of lasers with rigid cavities. *Phys. Rev. Lett.*, 93:250602, Dec 2004. URL: https://link.aps.org/doi/10.1103/PhysRevLett.93.250602, doi:10.1103/PhysRevLett.93.250602.

[NKDW19] A. Niezgoda, D. Kajtoch, J. Dziekańska, and E. Witkowska. Optimal quantum interferometry robust to detection noise using spin-1 atomic condensates. *New Journal of Physics*, 21(9):093037, September 2019. URL: https://doi.org/10.1088/1367-2630/ab4099, doi:10.1088/1367-2630/ab4099.

[NSH17] S. P. Nolan, S. S. Szigeti, and S. A. Haine. Optimal and robust quantum metrology using interaction-based readouts. *Phys. Rev. Lett.*, 119:193601, Nov 2017. URL: https://link.aps.org/doi/10.1103/PhysRevLett.119.193601, doi:10.1103/PhysRevLett.119.193601.

[NSN+20] D. Nitzschke, M. Schulte, M. Niemann, J. M. Cornejo, S. Ulmer, R. Lehnert, C. Ospelkaus, and K. Hammerer. Elementary laser-less quantum logic operations with (anti-)protons in Penning traps. *Advanced Quantum Technologies*, page 1900133, Jun 2020. URL: https://doi.org/10.1002/qute.201900133, doi:10.1002/qute.201900133.

[NYE+19] M. A. Norcia, A. W. Young, W. J. Eckner, E. Oelker, J. Ye, and A. M. Kaufman. Seconds-scale coherence on an optical clock transition in a tweezer array. *Science*, 366:93–97, Oct 2019. URL: https://doi.org/10.1126/science.aay0644, doi:10.1126/science.aay0644.

[O+07] R. Ozeri et al. Errors in trapped-ion quantum gates due to spontaneous photon scattering. *Phys. Rev. A*, 75:042329, Apr 2007. URL: https://link.aps.org/doi/10.1103/PhysRevA.75.042329, doi:10.1103/PhysRevA.75.042329.

[OLA+08] C. Ospelkaus, C. E. Langer, J. M. Amini, K. R. Brown, D. Leibfried, and D. J. Wineland. Trapped-ion quantum logic gates based on oscillating magnetic fields. *Phys. Rev. Lett.*, 101:090502, Aug 2008. URL: https://link.aps.org/doi/10.1103/PhysRevLett.101.090502, doi:10.1103/PhysRevLett.101.090502.

[P+20] E. Pedrozo-Peñafiel et al. Entanglement-Enhanced Optical Atomic Clock. *arXiv e-prints*, page arXiv:2006.07501, Jun 2020. arXiv:2006.07501.

[Par09] M. G. A. Paris. Quantum estimation for quantum technology. *International Journal of Quantum Information*, 07(supp01):125–137, Jan 2009. URL: https://doi.org/10.1142/s0219749909004839, doi:10.1142/s0219749909004839.

[Pre18] J. Preskill. Quantum computing in the NISQ era and beyond. *Quantum*, 2:79, Aug 2018. URL: https://doi.org/10.22331/q-2018-08-06-79, doi:10.22331/q-2018-08-06-79.

[PS07] L. Pezzé and A. Smerzi. Sub shot-noise interferometric phase sensitivity with beryllium ions Schrödinger cat states. *Europhysics Letters (EPL)*, 78(3):30004, Apr 2007. URL: https://doi.org/10.1209/0295-5075/78/30004, doi:10.1209/0295-5075/78/30004.

[PS09] L. Pezzé and A. Smerzi. Entanglement, nonlinear dynamics, and the Heisenberg limit. *Phys. Rev. Lett.*, 102:100401, Mar 2009. URL: https://link.aps.org/doi/10.1103/PhysRevLett.102.100401, doi:10.1103/PhysRevLett.102.100401.

[PS20] L. Pezzé and A. Smerzi. Heisenberg-limited noisy atomic clock using a hybrid coherent and squeezed states protocol. *arXiv e-prints*, page arXiv:2003.10943, Mar 2020. arXiv:2003.10943.

[PSO+18] L. Pezzé, A. Smerzi, M. K. Oberthaler, R. Schmied, and P. Treutlein. Quantum metrology with nonclassical states of atomic ensembles. *Rev. Mod. Phys.*, 90:035005, Sep 2018. URL: `https://link.aps.org/doi/10.1103/RevModPhys.90.035005`, `doi:10.1103/RevModPhys.90.035005`.

[PST05] E. Peik, T. Schneider, and C. Tamm. Laser frequency stabilization to a single ion. *Journal of Physics B: Atomic, Molecular and Optical Physics*, 39(1):145–158, Dec 2005. URL: `https://doi.org/10.1088/0953-4075/39/1/012`, `doi:10.1088/0953-4075/39/1/012`.

[QuT16] QuTiP: Quantum toolbox in PYTHON. `http://qutip.org/`, 2016.

[R+07] T. Rosenband et al. Observation of the $^1S_0 \rightarrow ^3P_0$ clock transition in $^{27}Al^+$. *Phys. Rev. Lett.*, 98:220801, May 2007. URL: `https://link.aps.org/doi/10.1103/PhysRevLett.98.220801`, `doi:10.1103/PhysRevLett.98.220801`.

[R+20] B. M. Roberts et al. Search for transient variations of the fine structure constant and dark matter using fiber-linked optical atomic clocks. *New Journal of Physics*, 22(9):093010, Sep 2020. URL: `https://doi.org/10.1088/1367-2630/abaace`, `doi:10.1088/1367-2630/abaace`.

[Ram50] N. F. Ramsey. A molecular beam resonance method with separated oscillating fields. *Phys. Rev.*, 78:695–699, Jun 1950. URL: `https://link.aps.org/doi/10.1103/PhysRev.78.695`, `doi:10.1103/PhysRev.78.695`.

[RB08] S. M. Roy and S. L. Braunstein. Exponentially enhanced quantum metrology. *Phys. Rev. Lett.*, 100:220501, Jun 2008. URL: `https://link.aps.org/doi/10.1103/PhysRevLett.100.220501`, `doi:10.1103/PhysRevLett.100.220501`.

[RCK+06] C. F. Roos, M. Chwalla, K. Kim, M. Riebe, and R. Blatt. 'Designer atoms' for quantum metrology. *Nature*, 443(7109):316–319, Sep 2006. URL: `https://doi.org/10.1038/nature05101`, `doi:10.1038/nature05101`.

[Rie06] F. Riehle. *Frequency Standards - Basics and Applications.* Wiley-VCH, Weinheim, 2006.

[Ril08] W. J. Riley. Handbook of frequency stability analysis. *NIST Special Publication*, 1065, 2008. URL: `https://www.nist.gov/publications/handbook-frequency-stability-analysis`.

[RL13] T. Rosenband and D. R. Leibrandt. Exponential scaling of clock stability with atom number. *arXiv e-prints*, page arXiv:1303.6357, Mar 2013. `arXiv:1303.6357`.

[Rut78] J. Rutman. Characterization of phase and frequency instabilities in precision frequency sources: Fifteen years of progress. *Proceedings of the IEEE*, 66(9):1048–1075, 1978.

[S$^+$00] C. A. Sackett et al. Experimental entanglement of four particles. *Nature*, 404(6775):256–259, Mar 2000. URL: `https://doi.org/10.1038/35005011`, `doi:10.1038/35005011`.

[S$^+$16] M. Schioppo et al. Ultrastable optical clock with two cold-atom ensembles. *Nature Photonics*, 11(1):48–52, Nov 2016. URL: `https://doi.org/10.1038/nphoton.2016.231`, `doi:10.1038/nphoton.2016.231`.

[SAL$^+$18] N. Shammah, S. Ahmed, N. Lambert, S. De Liberato, and F. Nori. Open quantum systems with local and collective incoherent processes: Efficient numerical simulations using permutational invariance. *Physical Review A*, 98(6), Dec 2018. URL: `https://doi.org/10.1103/physreva.98.063815`, `doi:10.1103/physreva.98.063815`.

[SAM$^+$98] G. Santarelli, C. Audoin, A. Makdissi, P. Laurent, G. J. Dick, and A. Clairon. Frequency stability degradation of an oscillator slaved to a periodically interrogated atomic resonator. *IEEE Transactions on Ultrasonics, Ferroelectrics, and Frequency Control*, 45(4):887–894, 1998.

[SBD$^+$18] M. S. Safronova, D. Budker, D. DeMille, Derek F. Jackson Kimball, A. Derevianko, and Charles W. Clark. Search for new physics with atoms and molecules. *Rev. Mod. Phys.*, 90:025008, Jun 2018. URL: `https://link.aps.org/doi/10.1103/RevModPhys.90.025008`, `doi:10.1103/RevModPhys.90.025008`.

[SDCZ01] A. S. Sørensen, L.-M. Duan, J. I. Cirac, and P. Zoller. Many-particle entanglement with Bose–Einstein condensates. *Nature*, 409(6816):63–66, Jan 2001. URL: `https://doi.org/10.1038/35051038`, `doi:10.1038/35051038`.

[SdMFZ99] E. Solano, R. L. de Matos Filho, and N. Zagury. Deterministic Bell states and measurement of the motional state of two trapped ions. *Phys. Rev. A*, 59:R2539–R2543, Apr 1999. URL: `https://link.aps.org/doi/10.1103/PhysRevA.59.R2539`, `doi:10.1103/PhysRevA.59.R2539`.

[Sep16] Martin Sepiol. *A high-fidelity microwave driven two-qubit quantum logic gate in* $^{43}Ca^{+}$. PhD thesis, University of Oxford, 2016.

[SGW^{+}19] A. Shankar, G. P. Greve, B. Wu, J. K. Thompson, and M. J. Holland. Continuous real-time tracking of a quantum phase below the standard quantum limit. *Phys. Rev. Lett.*, 122:233602, Jun 2019. URL: `https://link.aps.org/doi/10.1103/PhysRevLett.122.233602`, `doi:10.1103/PhysRevLett.122.233602`.

[SHL^{+}19] C. Sanner, N. Huntemann, R. Lange, C. Tamm, E. Peik, M. S. Safronova, and S. G. Porsev. Optical clock comparison for Lorentz symmetry testing. *Nature*, 567(7747):204–208, Mar 2019. URL: `https://doi.org/10.1038/s41586-019-0972-2`, `doi:10.1038/s41586-019-0972-2`.

[SJA^{+}16] J. Sastrawan, C. Jones, I. Akhalwaya, H. Uys, and M. J. Biercuk. Analytically exploiting noise correlations inside the feedback loop to improve locked-oscillator performance. *Phys. Rev. E*, 94:022204, Aug 2016. URL: `https://link.aps.org/doi/10.1103/PhysRevE.94.022204`, `doi:10.1103/PhysRevE.94.022204`.

[SKHR^{+}03] F. Schmidt-Kaler, H. Häffner, M. Riebe, S. Gulde, G. P. T. Lancaster, T. Deuschle, C. Becher, C. F. Roos, J. Eschner, and R. Blatt. Realization of the Cirac–Zoller controlled-NOT quantum gate. *Nature*, 422(6930):408–411, Mar 2003. URL: `https://doi.org/10.1038/nature01494`, `doi:10.1038/nature01494`.

[SLS^{+}19] M. Schulte, C. Lisdat, P. O. Schmidt, U. Sterr, and K. Hammerer. Prospects and challenges for squeezing-enhanced optical atomic clocks. *arXiv e-prints*, pages arXiv:1911.00882, accepted at Nat. Comm., Nov 2019. `arXiv:1911.00882`.

[SM99] A. Sørensen and K. Mølmer. Quantum computation with ions in thermal motion. *Phys. Rev. Lett.*, 82:1971–1974, Mar 1999. URL: `https://link.aps.org/doi/10.1103/PhysRevLett.82.1971`, `doi:10.1103/PhysRevLett.82.1971`.

[SM00] A. Sørensen and K. Mølmer. Entanglement and quantum computation with ions in thermal motion. *Phys. Rev. A*, 62:022311, Jul 2000. URL: `https://link.aps.org/doi/10.1103/PhysRevA.62.022311`, `doi:10.1103/PhysRevA.62.022311`.

[SML$^+$14] H. Strobel, W. Muessel, D. Linnemann, T. Zibold, D. B. Hume, L. Pezzé, A. Smerzi, and M. K. Oberthaler. Fisher information and entanglement of non-Gaussian spin states. *Science*, 345(6195):424–427, Jul 2014. URL: `https://doi.org/10.1126/science.1250147`, `doi:10.1126/science.1250147`.

[SMLSH20] M. Schulte, V. J. Martínez-Lahuerta, M. S. Scharnagl, and K. Hammerer. Ramsey interferometry with generalized one-axis twisting echoes. *Quantum*, 4:268, May 2020. URL: `https://doi.org/10.22331/q-2020-05-15-268`, `doi:10.22331/q-2020-05-15-268`.

[SMS$^+$18] R. Shaniv, T. Manovitz, Y. Shapira, N. Akerman, and R. Ozeri. Toward Heisenberg-limited Rabi spectroscopy. *Phys. Rev. Lett.*, 120:243603, Jun 2018. URL: `https://link.aps.org/doi/10.1103/PhysRevLett.120.243603`, `doi:10.1103/PhysRevLett.120.243603`.

[SRL$^+$05] P. O. Schmidt, T. Rosenband, C. Langer, W. M. Itano, J. C. Bergquist, and D. J. Wineland. Spectroscopy using quantum logic. *Science*, 309(5735):749–752, Jul 2005. URL: `http://www.sciencemag.org/cgi/content/abstract/309/5735/749`, `doi:10.1126/science.1114375`.

[SSLVac10] M. H. Schleier-Smith, I. D. Leroux, and V. Vuletić. States of an ensemble of two-level atoms with reduced quantum uncertainty. *Phys. Rev. Lett.*, 104:073604, Feb 2010. URL: `https://link.aps.org/doi/10.1103/PhysRevLett.104.073604`, `doi:10.1103/PhysRevLett.104.073604`.

[SSM$^+$18] Y. Shapira, R. Shaniv, T. Manovitz, N. Akerman, and R. Ozeri. Robust entanglement gates for trapped-ion qubits. *Phys. Rev. Lett.*, 121:180502, Nov 2018. URL: `https://link.aps.org/doi/10.1103/PhysRevLett.121.180502`, `doi:10.1103/PhysRevLett.121.180502`.

[ST58] A. L. Schawlow and C. H. Townes. Infrared and optical masers. *Phys. Rev.*, 112:1940–1949, Dec 1958. URL: `https://link.aps.org/doi/10.1103/PhysRev.112.1940`, `doi:10.1103/PhysRev.112.1940`.

[ST12] N. Shiga and M. Takeuchi. Locking the local oscillator phase to the atomic phase via weak measurement. *New Journal of Physics*, 14(2):023034, Feb 2012. URL: `https://doi.org/10.1088/1367-2630/14/2/023034`, `doi:10.1088/1367-2630/14/2/023034`.

[SWGT19] S. Saskin, J. T. Wilson, B. Grinkemeyer, and J. D. Thompson. Narrow-line cooling and imaging of Ytterbium atoms in an optical tweezer array. *Phys. Rev. Lett.*, 122:143002, Apr 2019. URL: `https://link.aps.org/doi/10.1103/PhysRevLett.122.143002`, `doi:10.1103/PhysRevLett.122.143002`.

[T$^+$19] M. Tse et al. Quantum-enhanced advanced LIGO detectors in the era of gravitational-wave astronomy. *Phys. Rev. Lett.*, 123:231107, Dec 2019. URL: `https://link.aps.org/doi/10.1103/PhysRevLett.123.231107`, `doi:10.1103/PhysRevLett.123.231107`.

[TFNT09] T. Takano, M. Fuyama, R. Namiki, and Y. Takahashi. Spin squeezing of a cold atomic ensemble with the nuclear spin of one-half. *Phys. Rev. Lett.*, 102:033601, Jan 2009. URL: `https://link.aps.org/doi/10.1103/PhysRevLett.102.033601`, `doi:10.1103/PhysRevLett.102.033601`.

[TKA$^+$19] T. R. Tan, R. Kaewuam, K. J. Arnold, S. R. Chanu, Zhiqiang Zhang, M. S. Safronova, and M. D. Barrett. Suppressing inhomogeneous broadening in a Lutetium multi-ion optical clock. *Phys. Rev. Lett.*, 123:063201, Aug 2019. URL: `https://link.aps.org/doi/10.1103/PhysRevLett.123.063201`, `doi:10.1103/PhysRevLett.123.063201`.

[TMS17] A. R. Thompson, J. M. Moran, and G. W. Swenson. *Interferometry and Synthesis in Radio Astronomy*. Springer International Publishing, 2017. URL: `https://doi.org/10.1007/978-3-319-44431-4`, `doi:10.1007/978-3-319-44431-4`.

[TTK11] M. Takamoto, T. Takano, and H. Katori. Frequency comparison of optical lattice clocks beyond the Dick limit. *Nature Photonics*, 5(5):288–292, Apr 2011. URL: `https://doi.org/10.1038/nphoton.2011.34`, `doi:10.1038/nphoton.2011.34`.

[TWC11] M. Tsang, H. M. Wiseman, and C. M. Caves. Fundamental quantum limit to waveform estimation. *Phys. Rev. Lett.*, 106:090401, Mar 2011. URL: `https://link.aps.org/doi/10.1103/PhysRevLett.106.090401`, `doi:10.1103/PhysRevLett.106.090401`.

[Uhl76] A. Uhlmann. The "transition probability" in the state space of a $*$-algebra. *Reports on Mathematical Physics*, 9(2):273–279, Apr 1976. URL: `https://doi.org/10.1016/0034-4877(76)90060-4`, `doi:10.1016/0034-4877(76)90060-4`.

[VBE$^+$17] G. Vallet, E. Bookjans, U. Eismann, S. Bilicki, R. Le Targat, and J. Lodewyck. A noise-immune cavity-assisted non-destructive detection for an optical lattice clock in the quantum regime. *New Journal of Physics*, 19(8):083002, Aug 2017. `doi:10.1088/1367-2630/aa7c84`.

[Wah16] Martina Wahnschaffe. *Engineered microwave control for trapped ions.* PhD thesis, Gottfried Wilhelm Leibniz Universität, Hannover, Jun 2016.

[WBB$^+$02] D. J. Wineland, J. C. Bergquist, J. J. Bollinger, R. E. Drullinger, and W. M. Itano. Quantum computers and atomic clocks. In *Proceedings of the 6th Symposium on Frequency Standards and Metrology,* Edited by P. Gill, pages 361–368. World Scientific, May 2002. URL: `https://doi.org/10.1142/9789812777713_0040`, `doi:10.1142/9789812777713_0040`.

[WBD10] J. D. Weinstein, K. Beloy, and A. Derevianko. Entangling the lattice clock: Towards Heisenberg-limited timekeeping. *Phys. Rev. A*, 81:030302, Mar 2010. URL: `https://link.aps.org/doi/10.1103/PhysRevA.81.030302`, `doi:10.1103/PhysRevA.81.030302`.

[WBI$^+$92] D. J. Wineland, J. J. Bollinger, W. M. Itano, F. L. Moore, and D. J. Heinzen. Spin squeezing and reduced quantum noise in spectroscopy. *Phys. Rev. A*, 46:R6797–R6800, Dec 1992. URL: `https://link.aps.org/doi/10.1103/PhysRevA.46.R6797`, `doi:10.1103/PhysRevA.46.R6797`.

[WBIH94] D. J. Wineland, J. J. Bollinger, W. M. Itano, and D. J. Heinzen. Squeezed atomic states and projection noise in spectroscopy. *Phys. Rev. A*, 50:67–88, Jul 1994. URL: `https://link.aps.org/doi/10.1103/PhysRevA.50.67`, `doi:10.1103/PhysRevA.50.67`.

[WHZ$^+$17] M. Wahnschaffe, H. Hahn, G. Zarantonello, T. Dubielzig, S. Grondkowski, A. Bautista-Salvador, M. Kohnen, and C. Ospelkaus. Single-ion microwave near-field quantum sensor. *Applied Physics Letters*, 110(3):034103, Jan 2017. URL: `https://doi.org/10.1063/1.4974736`, `doi:10.1063/1.4974736`.

[WLL10] P. Westergaard, J. Lodewyck, and P. Lemonde. Minimizing the Dick effect in an optical lattice clock. *IEEE Transactions on Ultrasonics, Ferroelectrics and Frequency Control*, 57(3):623–628, Mar 2010. URL: `https://doi.org/10.1109/tuffc.2010.1457`, `doi:10.1109/tuffc.2010.1457`.

[WMI+98] D. J. Wineland, C. Monroe, W. M. Itano, D. Leibfried, B. E. King, and D. M. Meekhof. Experimental issues in coherent quantum-state manipulation of trapped atomic ions. *Journal of Research of the National Institute of Standards and Technology*, 103(3):259, 1998.

[WWC+18] A. E. Webb, S. C. Webster, S. Collingbourne, D. Bretaud, A. M. Lawrence, S. Weidt, F. Mintert, and W. K. Hensinger. Resilient entangling gates for trapped ions. *Phys. Rev. Lett.*, 121:180501, Nov 2018. URL: `https://link.aps.org/doi/10.1103/PhysRevLett.121.180501`, `doi:10.1103/PhysRevLett.121.180501`.

[XTH13] M. Xu, D. A. Tieri, and M. J. Holland. Simulating open quantum systems by applying SU(4) to quantum master equations. *Physical Review A*, 87(6), Jun 2013. URL: `https://doi.org/10.1103/physreva.87.062101`, `doi:10.1103/physreva.87.062101`.

[Y+12] H. Yonezawa et al. Quantum-enhanced optical-phase tracking. *Science*, 337(6101):1514–1517, Sep 2012. URL: `https://doi.org/10.1126/science.1225258`, `doi:10.1126/science.1225258`.

[Zar20] Giorgio Zarantonello. *Robust high fidelity microwave near-field entangling quantum logic gate.* PhD thesis, Gottfried Wilhelm Leibniz Universität, Hannover, Jun 2020.

[ZHM+19] G. Zarantonello, H. Hahn, J. Morgner, M. Schulte, A. Bautista-Salvador, R. F. Werner, K. Hammerer, and C. Ospelkaus. Robust and resource-efficient microwave near-field entangling $^9\mathrm{Be}^+$ gate. *Phys. Rev. Lett.*, 123:260503, Dec 2019. URL: `https://link.aps.org/doi/10.1103/PhysRevLett.123.260503`, `doi:10.1103/PhysRevLett.123.260503`.

ACADEMIC CURRICULUM VITAE

Personal Data

NAME: Marius Schulte
BORN: 12 April 1993 in Papenburg, Germany
ADDRESS: Auf dem Dorn 24a, 30165 Hannover

Education

In progress	Doktor der Naturwissenschaften, Dr. rer. nat. Leibniz Universität Hannover Thesis: *Entanglement in Ramsey interferometry, optical atomic clocks and trapped ions* Supervisor: Prof. Dr. K. Hammerer
02/2017–present	PhD student at Institut für theoretische Physik, Leibniz Universität Hannover
03/2017	MASTER OF SCIENCE (PHYSICS) Leibniz Universität Hannover Thesis: *Quantum logic spectroscopy with ions* Supervisor: Prof. Dr. K. Hammerer
04/2015–03/2017	Master studies at Leibniz Universität Hannover
11/2014	BACHELOR OF SCIENCE (PHYSICS) Leibniz Universität Hannover Thesis: *Abfragestrategien in multi-ionen Uhren* Supervisor: Prof. Dr. K. Hammerer
10/2011–03/2015	Bachelor studies at Leibniz Universität Hannover
2004–2011	ABITUR Gymnasium Papenburg

Complete list of publications

M. Schulte, V. J. Martínez-Lahuerta, M. S. Scharnagl, K. Hammerer, *Ramsey interferometry with generalized one-axis twisting echoes*, Quantum 4, 268 (2020)

D. Nitzschke, **M. Schulte**, M. Niemann, J. M. Cornejo, S. Ulmer, R. Lehnert, C. Ospelkaus, K. Hammerer, *Elementary laser-less quantum logic operations with (anti-) protons in Penning traps*, Advanced Quantum Technologies 2020, 1900133 (2020)

M. Schulte, C. Lisdat, P. O. Schmidt, U. Sterr, K. Hammerer, *Prospects and challenges for squeezing-enhanced optical atomic clocks*, arXiv:1911.00882 (2019), accepted at Nature Communications

G. Zarantonello, H. Hahn, J. Morgner, **M. Schulte**, A. Bautista-Salvador, R. F. Werner, K. Hammerer, C. Ospelkaus, *Robust and resource-efficient microwave near-field entangling* ^{9}Be$^+$ *gate*, Physical Review Letters 123 (26), 260503 (2019)

H. Hahn, G. Zarantonello, **M. Schulte**, A. Bautista-Salvador, K. Hammerer, C. Ospelkaus, *Integrated* ^{9}Be$^+$ *multi-qubit gate device for the ion-trap quantum computer*, npj Quantum Information 5 (1), 1-5 (2019)

F. Wolf, C. Shi, J. C. Heip, M. Gessner, L. Pezzè, A. Smerzi, **M. Schulte**, K. Hammerer, P. O. Schmidt, *Motional Fock states for quantum-enhanced amplitude and phase measurements with trapped ions*, Nature Communications 10 (1), 2929 (2019)

M. Schulte, N. Lörch, P. O. Schmidt, K. Hammerer, *Photon-recoil spectroscopy: Systematic shifts and nonclassical enhancements*, Physical Review A 98 (6), 063808 (2018)

M. Schulte, N. Lörch, I. D. Leroux, P. O. Schmidt, K. Hammerer, *Quantum algorithmic readout in multi-ion clocks*, Physical Review Letters 116 (1), 013002 (2018)